ISSN 2518-7198 (Print)
ISSN 2663-5089 (Online)

BULLETIN
OF THE KARAGANDA UNIVERSITY

PHYSICS
Series

№ 1(105)/2022

ISSN 2663-5089 (Online)
ISSN-L 2518-7198 (Print)
Индексі 74616
Индекс 74616

ҚАРАҒАНДЫ УНИВЕРСИТЕТІНІҢ ХАБАРШЫСЫ

ВЕСТНИК КАРАГАНДИНСКОГО УНИВЕРСИТЕТА

BULLETIN OF THE KARAGANDA UNIVERSITY

ФИЗИКА сериясы

Серия ФИЗИКА

PHYSICS Series

№ 1(105)/2022

Қаңтар–ақпан–наурыз
30 наурыз 2022 ж.
Январь–февраль–март
30 марта 2022 г.
January–February–March
March 30th, 2022

1996 жылдан бастап шығады
Издается с 1996 года
Founded in 1996

Жылына 4 рет шығады
Выходит 4 раза в год
Published 4 times a year

Қарағанды, 2022
Караганда, 2022
Karaganda, 2022

Редакцияның мекенжайы: 100024, Қазақстан, Қарағанды қ., Университет к-сі, 28
Тел.: +7 701 531 4758; факс: (7212) 35-63-98.
E-mail: vestnikku@gmail.com; karabekova71@mail.ru
Сайты: physics-vestnik.ksu.kz

Қарағанды университетінің хабаршысы. «Физика» сериясы.

ISSN-L 2518-7198 (Print). ISSN 2663-5089 (Online).

Меншік иесі: «Академик Е.А. Бөкетов атындағы Қарағанды университеті» КЕАҚ.

Қазақстан Республикасы Ақпарат және қоғамдық даму министрлігімен тіркелген. 30.09.2020 ж. № KZ38VPY00027378 қайта есепке қою туралы куәлігі.

Басуға 29.03.2022 ж. қол қойылды. Пішімі 60×84 1/8. Қағазы офсеттік. Көлемі 16,5 б.т. Таралымы 200 дана. Бағасы келісім бойынша. Тапсырыс № 12. «Акад. Е.А. Бөкетов ат. Қарағанды ун-ті» КЕАҚ баспасының баспаханасында басылып шықты.

100024, Қазақстан, Қарағанды қ., Университет к-сі, 28. Тел. (7212) 35-63-16. E-mail: izd_kargu@mail.ru

Адрес редакции: 100024, Казахстан, г. Караганда, ул. Университетская, 28
Тел.: +7 701 531 4758. Факс: (7212) 35-63-98.
E-mail: vestnikku@gmail.com; karabekova71@mail.ru
Сайт: physics-vestnik.ksu.kz

Редакторы
Ж.Т. Нурмуханова, С.С. Балкеева, З.Е. Рамазанова

Компьютерная верстка
Г.Қ. Жанбосова

Вестник Карагандинского университета. Серия «Физика».
ISSN-L 2518-7198 (Print). ISSN 2663-5089 (Online).
Собственник: НАО «Карагандинский университет имени академика Е.А. Букетова».
Зарегистрирован Министерством информации и общественного развития Республики Казахстан. Свидетельство о постановке на переучет № KZ38VPY00027378 от 30.09.2020 г.

Подписано в печать 29.03.2022 г. Формат 60×84 1/8. Бумага офсетная. Объем 16,5 п.л. Тираж 200 экз. Цена договорная. Заказ № 12.
Отпечатано в типографии издательства НАО «Карагандинский университет им. акад. Е.А. Букетова». 100024, Казахстан, г. Караганда, ул. Университетская, 28. Тел. (7212) 35-63-16. E-mail: izd_kargu@mail.ru

Postal address: 28, University Str., 100024, Karaganda, Kazakhstan
Tel.: +7 701 531 4758; Fax: (7212) 35-63-98.
E-mail: vestnikku@gmail.com; karabekova71@mail.ru
Web-site: physics-vestnik.ksu.kz

Editors
Zh.T. Nurmukhanova, S.S. Balkeyeva, Z.E. Ramazanova

Computer layout
G.K. Zhanbossova

Bulletin of the Karaganda University. "Physics" Series.

ISSN-L 2518-7198 (Print). ISSN 2663-5089 (Online).

Proprietary: NLC "Karagandy University of the name of academician E.A. Buketov".

Registered by the Ministry of Information and Social Development of the Republic of Kazakhstan. Rediscount certificate No. KZ38VPY00027378 dated 30.09.2020.

Signed in print 29.03.2021. Format 60×84 1/8. Offset paper. Volume 16,5 p.sh. Circulation 200 copies. Price upon request. Order № 12.

Printed in the Publishing house of NLC "Karagandy University of the name of acad. E.A. Buketov".
28, University Str., Karaganda, 100024, Kazakhstan. Tel. (7212) 35-63-16. E-mail: izd_kargu@mail.ru

МАЗМҰНЫ — СОДЕРЖАНИЕ — CONTENT

ТЕХНИКАЛЫҚ ФИЗИКА
ТЕХНИЧЕСКАЯ ФИЗИКА
TECHNICAL PHYSICS

ЖЫЛУФИЗИКАСЫ ЖӘНЕ ТЕОРИЯЛЫҚ ЖЫЛУТЕХНИКАСЫ
ТЕПЛОФИЗИКА И ТЕОРЕТИЧЕСКАЯ ТЕПЛОТЕХНИКА
THERMOPHYSICS AND THEORETICAL THERMOENGINEERING

КОНДЕНСАЦИЯЛАНҒАН КҮЙДІҢ ФИЗИКАСЫ
ФИЗИКА КОНДЕНСИРОВАННОГО СОСТОЯНИЯ
PHYSICS OF THE CONDENSED MATTER

DOI 10.31489/2022PH1/6-14

UDC: 621.793

N. Kantay[1,2*], B.K. Rakhadilov[1], M. Paszkowski[3], A. Nabioldina [1]

[1]S. Amanzholov East Kazakhstan University, Ust-Kamenogorsk, Kazakhstan;
[2]D. Serikbayev East Kazakhstan Technical University, Ust-Kamenogorsk, Kazakhstan;
[3]Wroclaw University of Science and Technology, Wroclaw, Poland
[*]E-mail: nurgan85@mail.ru

Influence of Detonation Spray Parameters on the Formation of Mechanical and Tribological Properties of Gradient Coatings based on Alumina

Using the detonation method, the shaft was filled with a gas mixture of C_2H_2/O_2 from 53 to 68 % and an alumina-based gradient coating was obtained on the surface of the substrate. The microstructure of the coatings was studied by scanning electron microscopic analysis. By increasing the proportion of α-Al_2O_3 phase towards the surface layer of the coating by 10–15 %, a coating layer with increased strength and wear resistance was received. By X-ray structural study, changes in the α-Al_2O_3 lattice were studied by reducing the amount of gas filling in the barrel and the firing time from 1 s to 0.25 s. By reducing the amount of gas in the shaft from 68 to 53 % and the firing time from 1 s to 0.25 s, a compatible gradient coating with improved mechanical properties was obtained, the maximum value of microhardness of the gradient coating was 23.73 GPa. The tribological properties of the coatings were studied and showed that the value of the coefficient of friction of the gradient coating is about 50 % lower than that of other coatings, i.e. wear-resistant.

Keywords: aluminum oxide, detonation spraying, gradient coating, phase, microstructure, friction coefficient, tribology, microhardness.

Introduction

The service life of metal parts can be significantly extended by coating them with special performance characteristics. Taking advantage of this situation, it is possible to make floor coatings from high-quality and inexpensive materials, as only a coating will improve the critical role of the part. Various engineering materials often suffer from mechanical loads, thermal or aggressive environments every day. Coating technologies are being developed, but the physical and mechanical properties are improved, i.e. the production of low-porosity, wear-resistant, adhesive-coated coatings is one of the unresolved issues. Everyone gets different coatings on their own, and most scientists are studying the properties of multi-layer or gradient coatings using several powders. Artechnology has its own advantages and disadvantages. Most surface coating technologies cannot spray several powders at once, i.e., to obtain a multi-layer or gradient coating. One of the most rapidly developing roofing technologies in recent years is the method of thermal spraying. Through this technology, it is possible to obtain high-quality, durable coatings [1–5].

Thermal spraying method includes detonation spraying (DS) and high-speed gas-flame spraying (HVOF), which allows getting a coating with excellent adhesive strength, low porosity, density and wear-resistance [6, 7]. Obtained by general thermal methods, alumina-based coatings consist mainly of the γ phase; γ phase has lower properties than α phase, has a low level of wear resistance and strength. The formation of a large number of γ phases is a common problem in all coatings obtained by air plasma, plasma,

and gas-thermal spraying. In most cases, the raw powder consists only of α-Al_2O_3, the presence of α-Al_2O_3 after detonation spraying is due to the rapid crystallization of the molten volume of γ-Al_2O_3 because of insoluble or semi-soluble particles in the powder [8–10]. However, there are few studies on gradient coatings of aluminum oxide obtained by detonation spraying, which require further study. Therefore, we aim to obtain a gradient coating by changing the detonation parameters, studying the structural and phase state of aluminum oxide and changes in mechanical and tribological properties.

Experimental

Detonation coatings were obtained in the computerized complex of new generation detonation spraying CCDS2000 (Computer Controlled Detonation Spraying) [11, 12]. Figure 1 illustrates a general view and scheme of the detonation injection process. The shaft is filled with gases through a high-precision gas distribution system and controlled by a computer. The process begins by filling the shaft with carrier gas. Then a certain part of the explosive mixture is transferred in such a way that a layered gas medium is formed, consisting of a charge of explosive and carrier gas. Using a stream of carrier gas, it is poured into the explosion zone (using a computer-controlled feeder) and forms a cloud (fog). The mat is placed at a certain distance from the shaft. The computer beeps to start an explosion. This is done through an electric spark. The duration of explosive combustion of a charge is about 1 ms. A detonation wave is generated in the explosive mixture, which turns into a shock wave in the carrier gas. Detonation products (heated to 3500–4500 K) and carrier gas (heated to 1000–1500 k with shock waves) move at a speed higher than sound. The reaction time of gases with scattered particles is 2–5 ms. The velocity of the particles can reach 800–1200 ms^{-1} [13–15]. The method of detonation spraying was used to obtain Al_2O_3 coating. The size of the aluminum powder for spraying was 34±6 μm. The injection shaft was placed on a detonation unit "CCDS-2000" with a diameter of 20 mm and a length of 800 mm. Stainless steel **12Ch18N10T** was chosen as the lining material. The chemical composition of steel corresponds to GOST 4986–79 [16].

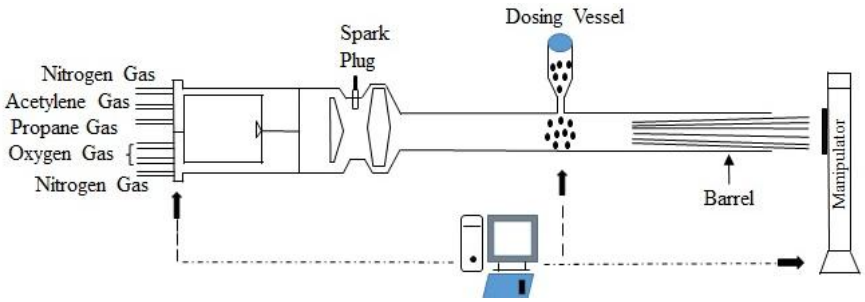

Figure 1. Schematic diagram of the computerized detonation complex CCDS200

The size of the substrate was 70x50x3 mm, the roughness of the initial surface was 0.080 μm. The surface of the substrate was sandblasted and chemically cleaned for 5–7 minutes. Sand with a grain size of about 40–60 microns was used to increase the average roughness of the dried substrate to 4.5 microns. In the production of a gradient coating based on alumina, the filling of the shaft with gas was between 53 %–68 %. The chemical composition of the substrate is shown in our previous study [17].

We obtained an Al_2O_3 coating for different volumes of barrel filling using a mixture of acetylene-oxygen as the fuel gas. As the proportion of explosive mixture increases (from 53 % to 68 % of the volume of the shaft), the temperature inside the shaft increases. In addition, changing the oxygen/fuel ratio from O_2 / C_2H_2 = 1.1 to O_2/C_2H_2 = 1.856 for low particle velocities can lead to an increase in temperature for the volume of explosive mixture. We chose O_2/C_2H_2 = 1.856 as the optimal ratio, which ensures complete melting of the powder material during injection. Table 1 shows the used process parameters.

Table 1

Technological parameters of Al_2O_3 coating

No.	O_2/C_2H_2	Barrel Filling Volume,%	Spray Distance, mm	Number of Shots
1	1.856	68, 63, 58, 53	250	20

We determined the phase composition of the sprayed coatings via the X-ray diffraction technique (XRD) applying an X'Pert PRO (Philips Corporation, Amsterdam, the Netherlands) diffractometer with Cu-Kα radiation (λ = 1.541 Å) at a voltage of 40 kV and a current of 30 mA. The diffractograms were decoded using the HighScore program. The measurements were carried out between 2°–90° with 0.02 step size and 0.5 s/step counting time. The surface roughness of the coatings was estimated according to GOST 2789–73 (ASTM D7127–05) using the Ra parameter by profilometer model 130 (JSC Plant PROTON, Moscow, Russia) [18]. We studied the mechanical properties of the coatings (microhardness) using a PMT–3M (LOMO, Saint Petersburg, Russia) microhardness tester. Microhardness was measured according to GOST 9450–76 (ASTM E384–11) [19] with a maximum load value equal to 3 N and a dwell time of 10 s. Tribological performances were evaluated in dry sliding tests performed on a high-temperature TRB3 (Anton Paar Srl, Peseux, Switzerland) using the standard ball-on-disc technique according to the ASTM G 133–95 and ASTM G99 standards [20, 21]. The sliding pair consisted of a stationary ball with a diameter of 6 mm and hardness 62±2 HRC, made of steel 100Cr6, pressed against a rotating disc made of steel **12Ch18N10T respectively** uncoated and spray-coated with 160–200 μm thick Al_2O_3 coating. The contact load amounted to 10 N and the rubbing speed to 0.2 m/s. The cycle time was 60 minutes. The tribological performance of the coatings was characterized by wear intensity and friction coefficient. To obtain results, we conducted the test on three samples from each variant. We used scanning electron microscopy (SEM) with backscattered electrons (BSE) at an accelerated voltage scanning electron microscope JSM-6390LV (Jeol, Tokyo, Japan) to study the cross-sectional morphology of the sample.

Results and Discussion

Figure 2 presents the microstructure of the cross-section for a gradient coating before and after annealing. The thickness of the coatings was 160–200 μm. The coating has a porous structure. The average pore size is 8–10 μm. Each sample was shot 5 times in each reduction, reducing the amount of gas in the barrel from 68 % to 63–58–53 %. The total number of shots was 20 times. A gradient coating was obtained by detonation spraying, reducing the volume of filling the shaft (gas) with gas (C_2H_2/O_2) from 68 % to 53 %. The roughness of the gradient coating is Ra = 0.269 μm. Based on the results of the study, it was shown that the change in the coating's roughness surface depends on the degree of gas filling of the shaft, as well as the proportion of α-Al_2O_3 and γ-Al_2O_3 phases in the coating.

Figure 3 shows the results of linear analysis of the lateral surface of the alumina-based gradient coating based on 68 %, 63 %, 58 %, 53 % of the shaft after gasification. Prior to the study of the coating, the surface of the coating was coated with carbon in a universal vacuum post, because it is difficult to see the surface morphology, as the aluminum oxide powder forms a ceramic when coated, so it was coated with a special carbon. Considering our study [17], the following gradient coating layer was obtained. On the surface of the substrate, we applied the first layer every 1 s with 68 % filling, and the second 5 layers every 0.75 seconds with 63 % filling, the third 5 layers every 0.5 seconds with 58 % filling and the fourth 5 layers every 0.25 seconds with the last 53 % filling.

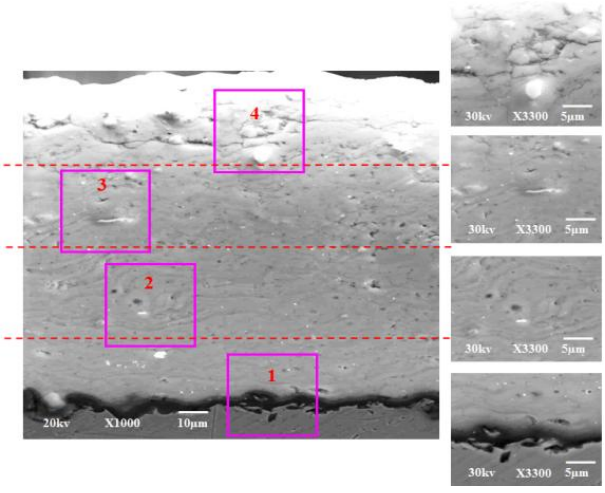

Figure 2. Microstructure of the cross-section of a gradient coating based on Al2O3:
68 % (1), 63 % (2), 58 % (3), and 53 % (4)

Figure 3a demonstrates that, in the area where the substrate is on the left side, the element Fe has more and less Ni and Cr elements. Towards the surface, one can see that the atoms of Al and O gradually increase, as shown in the right part of Figure 3a. The same process is noted in the distribution of the cardiogram elements shown in Figure 3b.

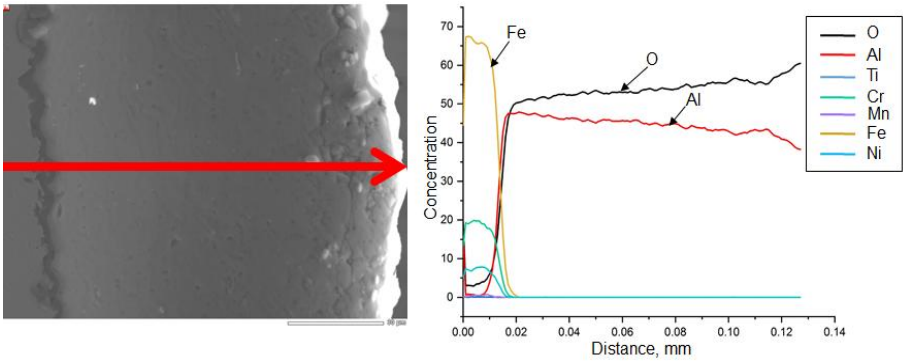

a

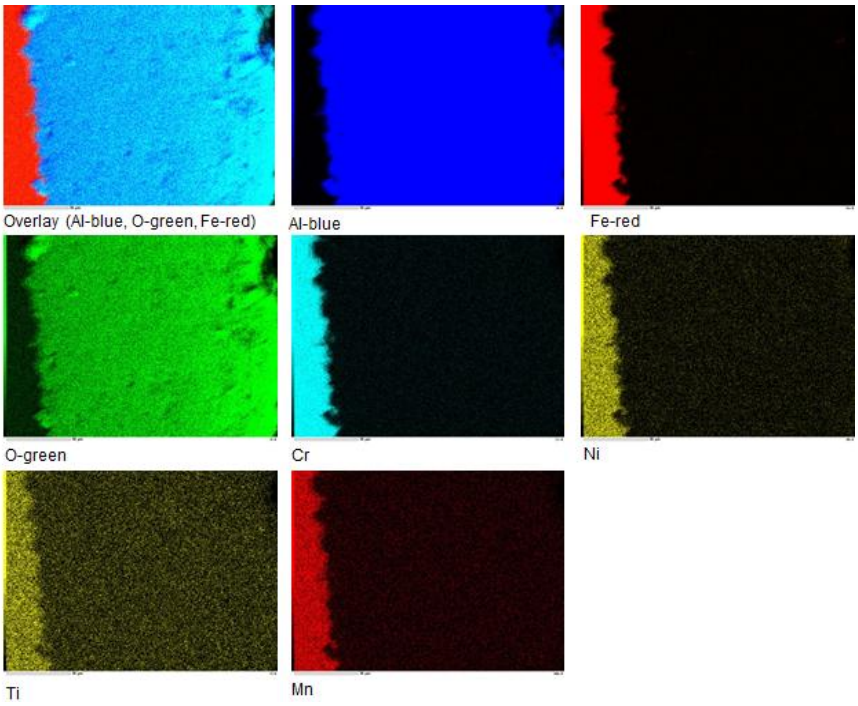

b

Figure 3. REM image taken from the cross-section of a gradient coating comprising aluminum oxide and the result of cardiogram analysis linear distribution of elements depending on the depth of the cross-section of the gradient coating Al_2O_3 (a); elemental distribution cardiogram (b)

Figure 4 shows the phase composition of the Al_2O_3 coating obtained using the given parameters. After detonation injection, alumina consisted of α-Al_2O_3 hexagonal (ICDD / JCPDS № 96–230–0376) and γ-Al_2O_3 cubic lattice (ICDD / JCPDS № 96–154–1583). Researchers [22, 23] state that Al_2O_3-based powder is capable of several modifications under the influence of high temperatures. Also, under the influence of heat, the composition of the Al_2O_3 coating changes into α, γ, δ, θ and different phases, in which the formation of α and γ phases predominates. These phases depend on the source material and the melting and cooling temperatures. Figure 4 comparatively shows the results of X-ray phase analysis of the shaft at 58 % gas filling and gradient coating. When the shaft is filled with gas up to 58 %, one can see that the proportion of the γ-Al_2O_3 phase in the alumina coating formed by the detonation explosion increases, while the proportion of the α-Al_2O_3 phase decreases (Figure 4a). We obtained the following gradient coating by regulating the phase change of the composition of aluminum oxide. First, by filling the shaft with 68 % gas on the surface

of the substrate, we laid a layer with a larger share of the γ-Al_2O_3 phase. We continued to reduce the size of the γ-Al_2O_3 phase by slightly filling the next layer (ply) by 63 %, slightly increasing the proportion of the α-Al_2O_3 phase, filling the shaft by 58 % and continuing to reduce the γ-Al_2O_3 phase in the coating. We increased the proportion of α-Al_2O_3 phase in the coating by filling the shaft by 53 % to obtain the next layer, then continued the process. Our goal is to obtain a gradient coating with a single powder (aluminum oxide) using a single dispenser, based on which a coating layer with improved mechanical and tribological properties, the γ-Al_2O_3 phase in the coating increases the plasticity and elasticity of the coating [19, 24].

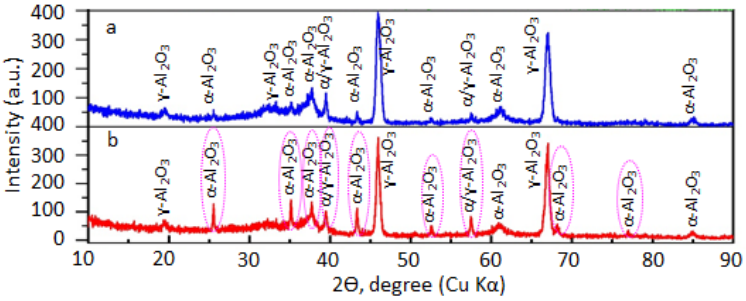

Figure 4. X-ray phase diffractogram of alumina coating obtained by filling the shaft with gas 58 % (a); 68 %, 63 %, 58 %, 53 % (b)

Figure 5 demonstrates a time graph of the coefficients of friction of the gradient coating relative to the substrate (Figure 5a) and the results of the study on the lost volume (Figure 5b). In [17], we stated that the coefficients of friction of coatings obtained during gas filling to 53–68 % were studied separately and μ = 0.52–0.59. The coefficient of friction of the pavement material was μ = 0.6–0.8, the value of the coefficient of friction of the gradient coating was μ = 0.027–0.33, i.e., the value of the coefficient of friction of the gradient coating, the wear resistance increased by 50 % compared to the pavement material. The value of the wear volume was 0.085 mm3 for the floor material, and 0.0165 mm3 for the gradient coating, i.e., it is 5 times less worn. The proposed gradient coating gives these steel products high physical, mechanical, and operational properties. In our opinion, the increase in hardness and wear resistance can be attributed to the increase in the proportion of α-Al_2O_3 phase in the coating. The α-Al_2O_3 phase has several features, including low density, relatively high melting point, excellent corrosion and wear resistance, high temperature resistance [24]. As can be seen, the wear resistance of the gradient coating was obtained by increasing the proportion of γ-Al_2O_3 phase in the substrate's vicinity and by increasing the amount of α-Al_2O_3 phase in the vicinity by reducing the degree of shaft filling from 68 to 53 % towards the surface layer. X-ray phase analysis explained this by an increase in the intensity of the diffractogram lines of the α-Al_2O_3 phase (Figure 4b).

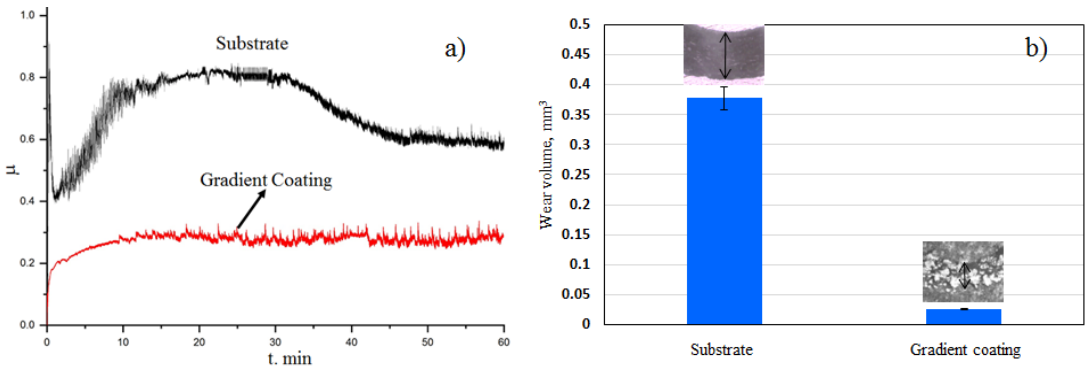

Figure 5. Results of tribological testing of Al_2O_3 coatings according to the scheme "ball-disk" a) change in the coefficient of friction; b) volumetric wear

In [17], the microhardness of the alumina coating obtained by filling the shaft with gas to 53–68 % was shown in between 16.31–20.56 GPa, the highest value of microhardness was observed at 53 % filling. The maximum value of the microhardness of the gradient coating obtained by changing the firing time with the

degree of gas filling was 23.73 GPa, i.e. the value of the microhardness increased by about 15 % compared to the filling of 53–68 %. It was found that the microhardness increases when the barrel is filled with gas by 53 % and the firing delay is 0.25 s. In addition, the abrasion wear resistance of the gradient coating was compared with that of the substrate and standard steel 45, the abrasion resistance coefficient was 1 for standard material steel 45, 0.968 for substrate material, and 6.921 for Al_2O_3-based gradient coating. It was proved that the value of the coefficient of abrasive wear of the gradient coating obtained by us is 6–7 times higher than that of standard and lining material, i.e., wear-resistant.

Depending on the amount of gas filling of the shaft, the alumina-based coatings and gradient coatings were kept in a muffle furnace at 600 °C for 100 hours. Every 10 hours we turned off the oven, cooled it with the oven, took it out and measured its mass and microhardness, thus plotting the time dependence of the heat resistance coefficient as shown in Figure 6. The coefficients of wear resistance gradually decrease after 50 hours, when filling the shaft by 58, 63, 68 %, the gradient coating has little change compared to others. From this, one can see that the quality of the gradient coating obtained by the method developed by us is good, based on the characteristics of the mechanical, tribological, and structural-phase properties of the gradient coating studied above. We consider that the reason for this is the gradual decrease in the proportion of the γ-Al_2O_3 phase to the surface with a decrease in the delay time with the amount of gas filling the shaft, and the formation of a closely spaced gradient coating under the influence of an increase in the α-Al_2O_3 phase.

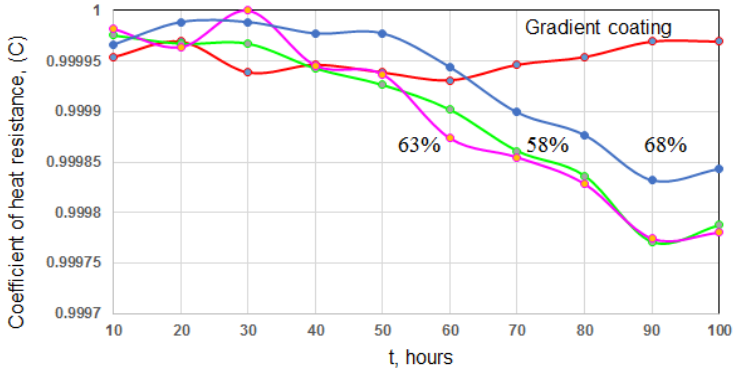

Figure 6. Graph of time dependence of Al2O3 gradient heat-resistance coefficient

Conclusions

1. A harmonious mode of obtaining a strong and dense coating layer was determined by reducing the percentage of gas filling of the detonation shaft from 68 to 53 % and regulating the formation of α-Al2O3 and γ-Al2O3 lattices of alumina-based coatings.

2. The microhardness of the alumina coating showed that the maximum value of the microhardness of the gradient coating obtained by reducing the amount of gas in the shaft from 68 to 53 % and the firing time from 1 s to 0.25 s was 23.73 GPa. The reason is the effect of increasing the volume fraction of the α-Al2O3 phase towards the surface.

3. In a tribological study of a gradient coating consisting of alumina obtained by the method developed by us, the value of the coefficient of friction was about 50 % less than that of the floor coating and other conventional coatings. The coefficient of abrasion wear resistance was 6–7 times higher than that of the lining material and steel 45, which indicates that the obtained gradient coating has a high wear resistance.

4. The value of the heat resistance coefficient of the gradient coating obtained by reducing the percentage of gas filling of the shaft from 68 to 53 % is uniform compared to other non-gradient coatings. that is, the α phase has higher physical and mechanical properties than the γ phase, i.e., it has a positive effect on temperature resistance.

Acknowledgements

The study was supported by the Ministry of Education and Science of the Republic of Kazakhstan (Grant No. AP09058615).

References

1 Vignesh S. Identifying the optimal HVOF spray parameters to attain minimum porosity and maximum hardness in iron based amorphous metallic coatings / S. Vignesh, K. Shanmugam, V. Balasubramanian, K. Sridha // Defence Technology. 13. — 2017. — P. 101–110.

2 Dhakar B. Heat treatment of plasma sprayed alumina-chromia composite coatings / B. Dhakar, A. Namdeo, S. Chatterjee, K. Sabiruddin // Surface Engineering. — 34. — 2018. — P. 737–746.

3 Алонцева Д.Л. Модификация облучением структурно-фазового состояния и свойств порошковых покрытий, нанесенных плазменной струей на стальные подложки / Д.Л. Алонцева, Н.В. Прохоренкова // Вестн. Караганд. ун-та. Сер. Физика. — 2013. — № 3 (71). — С. 4–11.

4 Ulianitsky V.Y. Detonation spraying behaviour of refractory metals: Case studies for Mo and Ta-based powders / V.Y. Ulianitsky, I.S. Batraev, A.A. Shtertser, D.V. Dudina, N.V. Bulina, I. Smurov // Advanced Powder Technology. – Vol. 29, No. 8. — 2018. — P. 1859–1864.

5 He L. Microstructure and wear properties of Al_2O_3-CeO_2/Ni- base alloy composite coatings on aluminium alloys by plasma spray / L. He, Y. Tan, X. Wang, T. Xu, X. Hong // Applied Surface Science. — 2014. — P. 760–767.

6 Vikas C. Performance of plasma sprayed Nanostructured and Conventional Coatings / C. Vikas, S.B. Singh, D. Puri, S. Prakash // Journal of the American Ceramic Society. 2. — 2008. — P. 56–62.

7 Yeskermessov D.K. Multi-component (Ti-Zr-Cr-Nb)N coatings': structure and properties / D.K. Yeskermessov, G.K. Uazyrkhanova, S.V. Plotnikov // Bulletin of the Karaganda University, Physics Series. — 2017. — No. 4 (88). — P. 8–17.

8 Monika M. Microstructural, mechanical and tribological properties of finely grained Al_2O_3 coatings obtained by SPS and S-HVOF methods / M. Monika, L. Leszek, S. Pawel, T. Filofteia-Laura, M. Hanna, D. Alain, A. Helene // Surface & Coatings Technology. — 2020. — P. 1–15.

9 Sundarajan G. The importance of coating process parameters / G. Sundarajan, D. Sen, G. Sivakumar // Wear. — 2005. — P. 377–391.

10 Saravanan P. Influence of process variables on the quality of detonation gun sprayed alumina coatings / P. Saravanan, V. Selvarajan, D.S. Rao, S.V. Joshi, G. Sundararajan // Surface & Coatings Technology. 123. — 2000. — P. 44–54.

11 Ulianitsky V.Y. Detonation spraying behavior of refractory metals: Case studies for Mo and Ta-based powders / V.Y. Ulianitsky, I.S. Batraev, A.A. Shtertser, D.V. Dudina, N.V. Bulina, I. Smurov, Detonation spraying behavior of refractory metals: Case studies for Mo and Ta-based powders // Advanced powder Technology. 29. — 2018. — P. 1859–1864.

12 Ulianitsky V.Y. The influence of the in-situ formed and added carbon on the formation of metastable Ni-based phases during detonation spraying / V.Y. Ulianitsky, D.V. Dudina, I.S. Batraev, D.K. Rybin, N.V. Bulina, A.V. Ukhina, B.B. Bokhonov // Materials Letters. — 2016. — 181. — P. 127–131.

13 Tian H.L. Tribological behaviour of a self-lubricated GO/WC-12Co thermal spray coating / H.L. Tian, M.Q. Guo, C.L. Wang, Z.H. Tang, Y.J. Cui // Surface Engineering. 34. — 2018. — P. 762–770.

14 Dudina D.V. Detonation spraying of Ti-Al Intermetallics: phase and micro-structure developments of the coatings / D.V. Dudina, I.S. Batraev, V.Y. Ulianitsky, N.V. Bulina, M.A. Korchagin, O.I. Lomovsky // Materials and Manufacturing Processes. — 2015. — P. 724–729.

15 Kantay N. Research of annealing influence on the hardness of detonation coatings from aluminum oxide / N. Kantay, B.K. Rakhadilov, M. Paszkowski, B.Tuyakbayev, Sh. Kurbanbekov, A. Nabioldina // Bulletin of the Karaganda University, Physics Series. — 2021. — P. 6–13.

16 Лента холоднокатаная из коррозионностойкой и жаростойкой стали. ГОСТ 4986–79. — М.: Государственный комитет СССР по стандартам, 2003.

17 Kantay N. Influence of Detonation-Spraying Parameters on the Phase Composition and Tribological Properties of Al_2O_3 Coatings / N. Kantay, B. Rakhadilov, S. Kurbanbekov, D. Yeskermessov, G. Yerbolatova and A. Apsezhanova // Coatings, 11. — 2021. — P. 793.

18 Шероховатость поверхности. Параметры и характеристики. ГОСТ 2789–73. — М.: Россия, 1975.

19 Измерение микротвердости методом вдавливания алмазных инструментов. ГОСТ 9450–76. — М.: Россия, 1976.

20 Standard Test Method for Linearly Reciprocating Ball-on-Flat Sliding Wear; ASTM International: West Conshohocken. ASTM G133–95, PA, USA, 1995.

21 Standard Test Method for Wear Testing with a Pin-on-Disk Apparatus; ASTM International: West Conshohocken. ASTM G99–05, PA, USA, 2005.

22 Cheng J. Microstructure and Tribocorrosion Behavior of Al_2O_3/Al Composite Coatings: Role of Al_2O_3 Additi / J. Cheng, Y. Ge, B Wang, L. Zhang, X. Hu, S. Hong, X. Liang, X. Zhang // Journal of Thermal Spray Technology. 29. — 2020. — P. 1741–1751.Kantay N. Influence of temperature on structural-phase changes and physical properties of ceramics on the basis of aluminum oxide and silicon / N. Kantay, N. Kasmamytov, B. Rakhadilov, S. Plotnikov, M. Paszkowski, Sh. Kurbanbekov // Materials Testing. — 62, Issue (7). — 2020. — P. 716–720.

24 Rakhadilov B. Experimental investigations of Al_2O_3 — and ZrO_2-based coatings deposited by detonation spraying / B. Rakhadilov, N. Kantay, Z. Sagdoldina, D. Erbolatuly, G. Bektasova, M. Paszkowski // Materials Research Express, 8. — 2021. — P. 1–12.

25 Shoja S. Calculated and experimental Schmid factors for chip flow deformation of textured CVD α-alumina coatings / S. Shoja, O. Alm, S. Norgren, H.-O. Andrén, M. Halvarsson // Surface & Coatings Technology. — 2021. — P. 412.

Н. Қантай, Б.К. Рахадилов, М. Пашковский, А. Набиолдина

Детонациялық тозаңдау параметрлерін өзгерте отырып, алюминий оксиді негізіндегі градиентті жабынды алу және оның механикалық, трибологиялық қасиеттеріне әсерін зерттеу

Детонациялық әдісті қолданып, оқпанды (ствол) 53-тен 68 %-ға дейін C_2H_2/O_2 газ қоспасымен толтыра отырып, төсеніштің (подложка) бетіне алюминий оксиді негізіндегі градиентті жабын алынды. Алынған жабындардың микроқұрылымы растрлық электронды микроскопиялық талдау көмегімен зерттелді. Жабынның беткі қабатқа қарай α-Al_2O_3 фазаның үлесін 10–15 %-ға арттыру арқылы беріктігі, тозуға тұрақтылығы жоғарылаған жабын қабаты алынды. Рентгенқұрылымдық зерттеу арқылы, оқпанды газға толтыру мөлшері мен ату кезіндегі кідіру уақытын 1с-тан 0.25 с-қа азайту кезіндегі α-Al_2O_3 торларының өзгерісі зерттелді. Оқпандағы газдың мөлшерін 68-ден 53 %-ға және ату кезіндегі кідіру уақытын 1 с-тан 0.25 с-қа азайту арқылы механикалық қасиеті жақсартылған үйлесімді градиентті жабын қабаты алынды, алынған градиентті жабынның микроқаттылықтың ең жоғары мәні 23.73 ГПа-ды көрсетті. Алынған жабындардың трибологиялық қасиеті зерттеліп, градиентті жабынның үйкеліс коэффициентінің мәні басқа жабындармен салыстырып қарағанда 50 %-дай төмен, яғни тозуға берік екенін көрсетті.

Кілт сөздер: алюминий оксиді, детонациялық тозаңдау, градиентті жабын, фаза, микроқұрылым, үйкеліс коэффициенті, трибология, микроқаттылық.

Н. Кантай, Б.К. Рахадилов, М. Пашковский, А. Набиолдина

Получение градиентного покрытия на основе оксида алюминия путем изменения параметров детонационного напыления и изучение его влияния на механические и трибологические свойства

Детонационным методом ствол был заполнен газовой смесью C_2H_2/O_2 от 53 до 68 %, и на поверхности подложки было получено градиентное покрытие на основе оксида алюминия. Микроструктура полученных покрытий была исследована с помощью растрового электронно-микроскопического анализа. За счет увеличения доли фазы α-Al_2O_3 по отношению к поверхностному слою покрытия на 10–15 % был получен слой покрытия с повышенной прочностью и износостойкостью. Путем рентгеноструктурного исследования были изучены изменения решетки α-Al_2O_3 за счет уменьшения количества газа, заполняющего ствол, и времени задержки стрельбы от 1 до 0,25 с. Из-за сокращения количества газа в стволе с 68 до 53 % и времени задержки стрельбы от 1 с до 0,25 с было получено совместимое градиентное покрытие с улучшенными механическими свойствами, максимальное значение микротвердости полученного градиентного покрытия составило 23,73 ГПа. Были изучены трибологические свойства полученных покрытий и значение коэффициента трения градиентного покрытия примерно на 50 % ниже, то есть они показывали прочность к износу, по сравнению с другими покрытиями.

Ключевые слова: оксид алюминия, детонационное напыление, градиентное покрытие, фаза, микроструктура, коэффициент трения, трибология, микротвердость.

References

1 Vignesh, S., Shanmugam, K., Balasubramanian, V., & Sridha, K. (2017). Identifying the optimal HVOF spray parameters to attain minimum porosity and maximum hardness in iron based amorphous metallic coatings, *Defence Technology, 13, 101–110.*

2 Dhakar, B., Namdeo, A., Chatterjee, S., & Sabiruddin, K. (2018). Heat treatment of plasma sprayed alumina-chromia composite coatings, *Surface Engineering, 34*, 737–746.

3 Alontseva, D.L., & Prokhorenkova, N.V. (2013). Modifikatsiia oblucheniem strukturno-fazovogo sostoianiia i svoistv poroshkovykh pokrytii, nanesennykh plazmennoi struei na stalnye podlozhki [Modification by irradiation of the structural-phase state and properties of powder coatings deposited by a plasma jet on steel substrates]. *Vestnik Karagandinskogo universiteta. Seriia Fizika — Bulletin of the University of Karaganda. Physics Series, 3, 71, 4*–11 [in Russian].

4 Ulianitsky, V.Y., Batraev, I.S., Shtertser, A.A., Dudina, D.V., Bulina, N.V., & Smurov, I. (2018). Detonation spraying behaviour of refractory metals: Case studies for Mo and Ta-based powders, *Advanced Powder Technology, 29 (8)*, 1859–1864.

5 He, L., Tan, Y., Wang, X., Xu, T., & Hong, X. (2014). Microstructure and wear properties of Al_2O_3-CeO_2 /Ni- base alloy composite coatings on aluminium alloys by plasma spray, *Applied Surface Science, 314*, 760–767.

6 Vikas, C., Singh, S. B., Puri D., & Prakash, S. (2008). Performance of plasma sprayed Nanostructured and Conventional Coatings, *Journal of the American Ceramic Society, 2*, 56–62.

7 Yeskermessov, D.K., Uazyrkhanova, G.K., & Plotnikov, S.V. (2017). Multi-component (Ti-Zr-Cr-Nb)N coatings: structure and properties. *Bulletin of the Karaganda of University-Physics, 4(88),* 8–17.

8 Monika, M., Leszek, L., Pawel, S., Filofteia-Laura, T., Hanna, M., Alain, D., & Helene, A. (2020). Microstructural, mechanical and tribological properties of finely grained Al_2O_3 coatings obtained by SPS and S-HVOF methods, *Surface & Coatings Technology, 404,* 1–15.

9 Sundarajan, G., Sen, D., & Sivakumar, G. (2005). The tribological behaviour of detonation sprayed coatings: the importance of coating process parameters, *Wear, 258,* 377–391.

10 Saravanan, P., Selvarajan, V., Rao, D.S., Joshi, S.V., & Sundararajan, G. (2000). Influence of process variables on the quality of detonation gun sprayed alumina coatings, *Surface & Coatings Technology, 123,* 44–54.

11 Ulianitsky V.Y., Batraev, I.S., Shtertser, A.A., Dudina, D.V., Bulina, N.V., Smurov, I. (2018). Detonation spraying behavior of refractory metals: Case studies for Mo and Ta-based powders. Detonation spraying behavior of refractory metals: Case studies for Mo and Ta-based powders. *Advanced Powder Technology, 29, 1859-1864.*

12 Ulianitsky V.Y., Dudina, D.V., Batraev, I.S., Rybin, D.K., Bulina, N.V., Ukhina, A.V., & Bokhonov, B.B. (2016). The influence of the in-situ formed and added carbon on the formation of metastable Ni-based phases during detonation spraying, *Materials Letters, 181,* 127–131.

13 Tian, H.L., Guo, M.Q., Wang, C.L., Tang, Z.H., & Cui, Y.J. (2018). Tribological behaviour of a self-lubricated GO/WC-12Co thermal spray coating, *Surface Engineering, 34,* 762–770.

14 Dudina, D.V., Batraev, I.S., Ulianitsky, V.Y., Bulina, N.V., Korchagin, & M.A., Lomovsky, O.I. (2015). Detonation spraying of Ti-Al Intermetallics: phase and microstructure developments of the coatings, *Materials and Manufacturing Processes, 30,* 724–729.

15 Kantay, N., Rakhadilov, B.K., Paszkowski, M., Tuyakbayev, B., Kurbanbekov, Sh., & Nabioldina, A. (2021). Research of annealing influence on the hardness of detonation coatings from aluminum oxide, *Bulletin of the Karaganda of University-Physics, 6–13.*

16 Lenta kholodnokatanaia iz korrozionnostoikoi i zharostoikoi stali [Cold-rolled band from corrosion-resistant and heat-resistant steel] (2003). HOST 4986–79. USSR State Committee for Standards. GOST 4986–79. Moscow [in Russian].

17 Kantay, N., Rakhadilov, B., Kurbanbekov, S., Yeskermessov, D., Yerbolatova, G., & Apsezhanova, A. (2021). Influence of Detonation-Spraying Parameters on the Phase Composition and Tribological Properties of Al_2O_3 Coatings. *Coatings, 11, 793.*

18 Sherokhovatost poverkhnosti. Parametry i kharakteristiki [Surface roughness. Parameters and characteristics] (1975). GOST 2789–73. Moscow: USSR State Committee for Standards [in Russian].

19 Izmerenie mikrotverdosti metodom vdavlivaniia almaznykh instrumentov [Measurement of microhardness by diamond instruments indentation] (1976). GOST 9450–76. Moscow: USSR State Committee for Standards [in Russian].

20 Standard Test Method for Linearly Reciprocating Ball-on-Flat Sliding Wear (1995). ASTM G133–95. ASTM International: West Conshohocken, PA, USA.

21 Standard Test Method for Wear Testing with a Pin-on-Disk Apparatus (2005). ASTM G99–05. ASTM International: West Conshohocken, PA, USA.

22 Cheng, J., Ge, Y., Wang, B., Zhang, L., Hu, X., Hong, S., Liang, X., & Zhang, X. (2020). Microstructure and Tribocorrosion Behavior of Al_2O_3/Al Composite Coatings: Role of Al_2O_3 Additi, *Journal of Thermal Spray Technology, 29, 1741–1751.* Kantay, N., Kasmamytov, N., Rakhadilov, B., Plotnikov, S., Paszkowski, M., & Kurbanbekov Sh. (2020). Influence of temperature on structural-phase changes and physical properties of ceramics on the basis of aluminum oxide and silicon. *Materials Testing, 62,* 716–720.

24 Rakhadilov, B., Kantay, N., Sagdoldina, Z., Erbolatuly, D., Bektasova, G., & Paszkowski, M. (2021). Experimental investigations of Al_2O_3 — and ZrO_2 -based coatings deposited by detonation spraying, *Materials Research Express, 8,* 1–12.

25 Shoja, S., Alm, O., Norgren, S., Andrén, H.-O., & Halvarsson, M. (2021). Calculated and experimental Schmid factors for chip flow deformation of textured CVD α-alumina coatings, *Surface & Coatings Technology, 412.*

DOI 10.31489/2022PH1/15-26

UDC 004.89+528-187.4

I.Yu. Cherepanska*[1], A.Yu. Sazonov[1], S.V. Kalchuk[2], O.F. Sokolovskyi [3], O.S. Sivaieva [3]

[1]National Technical University of Ukraine "Igor Sikorsky Kyiv Polytechnic Institute", Kyiv, Ukraine;
[2]Zhytomyr Polytechnic State University, Zhytomyr, Ukraine;
[3]Polissya National University, Zhytomyr, Ukraine;
*(*E-mail: cherepanskairina@gmail.com)*

Intellectual system for automated determination of the quality of natural stones surfaces processing

This automation of determination of the quality of natural stone surfaces processing is a relevant problem. It provides an intellectual system for automated determination of the quality of processing surfaces of natural stones (ISADQSS), which allows rapid assessment of the quality of stone surfaces, including roughness, with high accuracy and quick action in automatic mode and real time. The measurement result is independent of the humidity and cleanliness of the outer surface. The root mean square error of the proposed ISADQSS does not exceed 5%, the time to determine the value of the roughness is not over 2 s. ISADQSS is based on the principles of synergetic integration of various technical automation devices with different properties – artificial neural networks (ANN) (in the case of their implementation in the form of neuroprocessors), as well as the so-called registrar of main drive currents (RMDC), which is used as a sensor sensitive to changes in the rubbing force of the stone-cutting tool depending on changes in the roughness value of the machined surface. The proposed ISADQSS is an innovative and promising development that combines such advantages as high accuracy and speed, versatility and ease of use.

Keywords: artificial neural networks, roughness, quality, automation, accuracy, speed, measurement.

Introduction

Formulation of the problem. Measuring the roughness of treated surfaces, in particular natural stones, with high accuracy and speed in automatic mode without stopping the technological process, is a paramount and specific task to ensure the quality of stone production. The ever-increasing requirements of international standards for product quality determine the extreme importance and urgency of this task. Its successful solution contributes to the stability of technological processes, the required product quality and the competitiveness of modern enterprises in general.

The peculiarity of the technological process of grinding the surface of natural stone is the sequential treatment of its surface with an abrasive tool with different grain size, which gradually decreases with each subsequent operation when the final result is a polished flat surface. A sign of completion of each stage of processing is to obtain a certain microprofile evenly over the entire surface of the stone. Here, in the case of failure to achieve at any of the stages of processing the same roughness over the entire plane of the treated surface in subsequent operations, there are defects that cannot be eliminated. As a result, the quality of the finished product is lost, which obviously leads to economic losses in enterprises. Undoubtedly, it is important to measure the quality of surface treatment of stones, in particular the amount of roughness at each stage of processing. However, the problem is that high humidity, dust and dirt, which are an integral part of the technological operations of stone surface treatment, limit the application of traditional measuring devices directly in the production conditions of modern stone processing enterprises.

As a rule, at stone processing enterprises the determination of the roughness of natural stone surfaces is performed with the use of specialized laboratory equipment – gloss meters and profilometers [1, 2].The latter, according to scientists and manufacturers [1, 2] have a relatively low accuracy in determining the roughness, involve a number of time-consuming and long-term operations that significantly slow down technological processes. In particular, when using gloss meters, the accuracy of measurement is affected by the level of luminous flux of the lamp, the color of natural stone, contamination and the level of humidity of the treated surface and the test sample. Therefore, it is impossible to use gloss meters directly in production conditions. Assessment of the quality of stone surface treatment with the use of glitters requires a long-term stop of technological processes for cleaning and drying of the studied surfaces. The preparatory stage of measurement, which consists in removing grinding head from the working area and turning off the machine for the time of measuring (1-2 min), while the further washing of stone sludge residues from the treated stone surface, depending on the plate size, an average of 3 -5 minutes, and the subsequent cleaning of the surface

from residual water and drying can take up to 2-3 hours, depending on the level of humidity in the production environment. Taking into account results of the research [16], the linear speed of stone quality assessment with an optical profilometer is 20 mm/sec at a measurement distance without rearranging measuring instrument (travel range) 100 mm. In terms of a unit of standard stone facing product, the minimum dimensions of which is 300x300 mm (modular tile), the measurement time per line is 15 seconds, and in terms of tool relocation and coating the entire area of the slab is 75 sec. Accordingly, the preparatory stage is the longest in time comparing to direct measurement and data processing. The duration of the measurement is comparable to the duration of processing the obtained data.

Similar requirements for dryness and cleanliness of the investigated surface are put forward in the case of mechanical profilometers. It should be emphasized the inadmissibility of the use of profilometers due to low accuracy of measurements, due to the accumulation and increase in the error due to the registration of microirregularities formed at the contact of grains of minerals in rocks and due to vibration of grinding equipment.

Given the above, the need to improve the accuracy and speed of assessing the quality of surface treatment of natural stones in an automated mode without stopping the technological processes at stone processing enterprises is not in doubt.

One of the current ways to improve the accuracy and speed of assessing the quality of surface processing of natural stones in an automated mode without stopping technological processes at stone processing enterprises is the application and synergistic integration of the proposed ISADQSS new approaches, methods and techniques for obtaining and processing measurement information, including artificial neural networks and functional converter [3].

Despite the accumulated experience in the development and successful use of ANN for information processing in conditions of high environmental dynamics, including production, environment, their high accuracy and speed [4–8] advantages and efficiency of their application in the proposed ISADQ-OSS for rapid assessment of the quality of stone surfaces, in particular roughness, with high accuracy and speed, automated mode and real-time mode, directly during the execution of technological processes and without stopping the technological equipment, there is no doubt.

The analysis of researches and publications has shown that application of the traditional specialized laboratory equipment, particularly gloss meters and profilometers for an estimation of quality of processing of surfaces of natural stones, in particular roughness, directly in production conditions is impossible. Thus, in [1, 2, 9, 10], the principles of operation of these tools are described and the experience of application in stone processing industries, in particular in granite surface treatment, is given. The authors [9, 10] indicate the possibility of using gloss meters and profilometers only in laboratory conditions of measurements. The above information allows us to draw unequivocal conclusions about the low accuracy of measurements and speed of gloss meters and profilometers, as well as indicates the obvious limitations of their application in dynamic and continuous production processes.

The literature [11] describes the experience of using laser profilometers or scanners, which have a relatively high measurement accuracy, but their use is due to the need for the absence of dirt, sludge, and water on the surface, which is impossible in industrial conditions.

There is a method of determining the surface roughness, based on the degree of polarization of the beam reflected from the studied surface [12]. The authors indicate that the method is devoid of such disadvantages as reduced accuracy due to high humidity and contamination of the test surface, but its accuracy depends on the homogeneity of the test material. Therefore, it is used only in determining the roughness of metals, ceramics, and other homogeneous materials and can not be used to determine the roughness of stone surfaces.

The work [13] provides an application of the combined method for determination of surface roughness that combines the existing contact and non-contact methods with informational methods of processing the topographic image of the surveyed surface. The essence of the method lies in the use of mathematical methods of processing data of interference of the broken surface. The results of this research allow us to conclude that further mathematical processing increases the accuracy of shortness measurements. However, this method is not beyond the scope of laboratory research because of its sensitivity to the dryness of the stone surfaces. Also, during wet grinding of stones it becomes impossible to use the method of wavelet rendering of the obtained data described in the work [14]. In spite of the efficiency and prospects of this method of information processing, the factor of non-uniform texture and color of stones remains, and in combination with the wet and sludge clogging of the examined surface makes it impossible to use it in the production conditions of stone-processing enterprises.

Selection of unresolved parts of the problem. Thus, it can be argued that despite the significant scientific and practical achievements, the problem of defining the roughness value with high accuracy, speed, in automated mode and real-time mode when evaluating the quality of natural stone surfaces at stone processing enterprises without stopping the production process, has not yet been completely solved.

This study aims is to propose an intellectual system for automated determination of the quality of processing of surfaces of natural stones (ISADQSS) with increased accuracy and speed.

Description of the proposed intellectual system for automated determination of the quality of stone surfaces

The intellectual system for automated determination of the quality of stone surfaces (ISADQSS) was developed on the basis of the latest achievements of science and technology in the spheres of artificial neural networks, informatics, automation, and microcircuitry engineering. It is based on the principles of synergetic integration and capacity by using new methods (artificial neural network) of information processing and technical devices (artificial neural network and functional transformer). At the same time, the principles of modularity and the concept of uninfection have been observed in the construction of the tested ISADQSS, including the ANN and the functional transformer. This means using unified nodes and elements in its composition, including asynchronous motor, control mechanism, which are serially produced by the industry. This allows for interoperability and unification, which is a prerequisite for increased operating hours, improved modernization, etc.

ISADQSS combines the advantages of high accuracy and speed, a wide range of natural materials that can be studied, ease of use, and versatility, possibility of automated measuring and processing of the measuring information in real time without interruption in the technological operations on the technological equipment. In this case, the use of the ISADQSS does not require special preparation of the investigated surfaces, their preliminary cleaning and drying.

Figure 1 shows the block diagram of the ISADQSS, which includes the electronic and electromechanical subsystems. Electromechanical subsystem consists of ultrasonic sensors S1 and S2 for distance measurement, sensor S3 of current, PPM – processor power module, A – main actuator with grinding head, MC – microcontroller, functional transformer (not shown in Figure 1). Integral subsystem contains ANN – artificial neural network, implemented in the form of a specialized software add-on, and integrated into the operating system of the portable computer (PC), Wi-fi module for data transmission over a distance, PC – portable computer for displaying data and displaying them in smartphones that support Android.

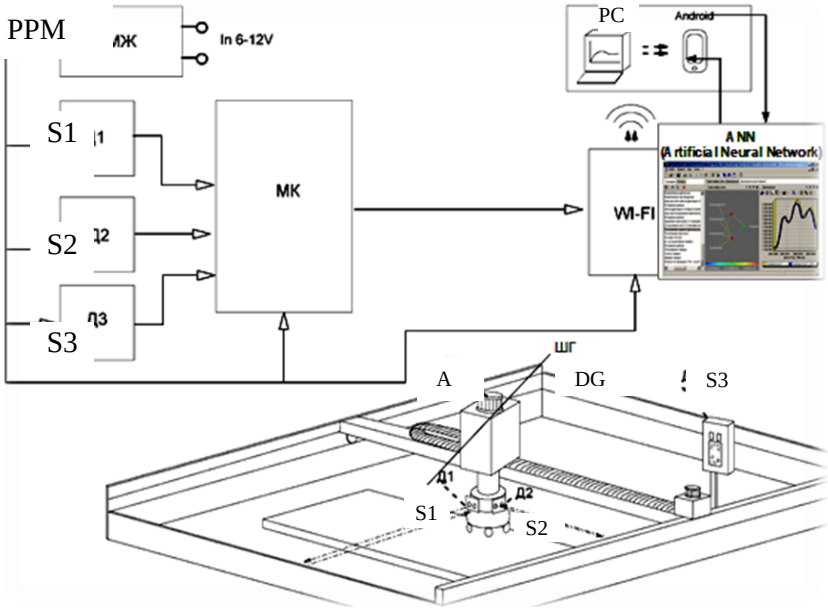

Figure 1. Structure diagram of the ISADQSS: S1, S2 – distance sensors, S3 – current sensor, PPM – processor power module, A – main actuator with grinding head DG, MC – microcontroller, Wi-fi module for distance data transmission, ANN – artificial neural network, PC – portable computer for displaying data and displaying them in smartphones that support Android

Ultrasonic distance sensors S1, S2 are used to determine the coordinates of the movement of the working shaft of the main engine and mounted directly on the machining grinding head DG drive cutting tool and form two mutually perpendicular axes of the flat coordinate system along which DG moves. When grinding or polishing the surface of natural stone, the roughness of the treated surface changes (Figure 2), which correlates with the amount of current consumed on the shaft of the main actuator A. This current is consumed by the drive of the main movement of the stone processing machine during processing of a stone surface. When the tool of the stone processing machine processes a certain area of the stone, the drive of the main movement consumes current. The magnitude of the oscillation amplitude and the instantaneous value of the current depend on the load on the drive shaft of the main motion.

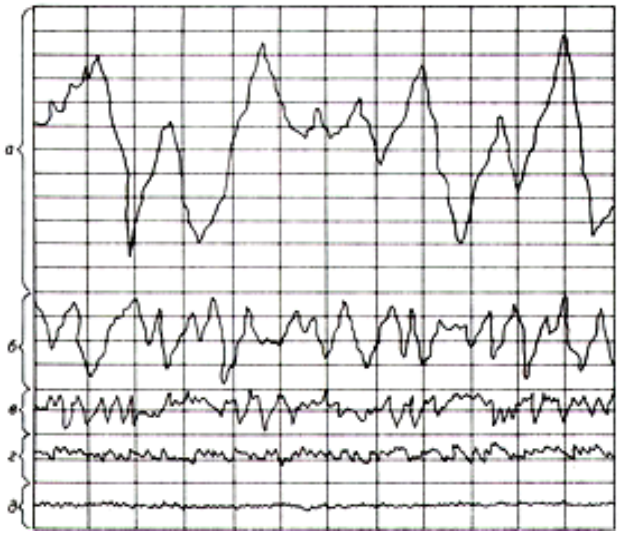

Figure 2. Change of the consumed current on a shaft of the main executive mechanism of A at various stages of processing of a granite stone by the grinding tool: a - rough grinding (peeling), b - medium grinding, c - fine grinding, d - finishing grinding (polishing), d - polishing

The load is caused by mechanical resistance from the surface of the stone, which is a function of roughness (Figure 2). Continuous measurement of the current consumption allows to monitor changes in roughness in real time. Continuous measurement of instantaneous current values is performed by the current sensor S3 and is transmitted to the implemented microcontroller, Arduino Nano V3.0 based on the Atmega328P microcontroller.

Figure 3 presents a block diagram of the electromechanical subsystem ISADQSS. The functional converter (FC), implemented using classical control methods, forms the task ofvoltage amplitude $U_{зUm}$, based on the task signal $U_{зf}$.

The voltage U_0 at zero frequency ("boost") provides a constant amount of magnetizing current and increases the overload capacity at low frequencies. Its value is chosen at the level of 6÷25 % of the nominal value [15]. The actuator is considered as an inertial link with a single gear ratio.

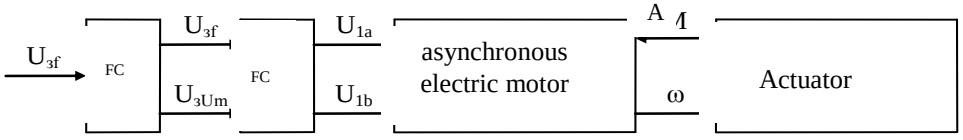

Figure 3. Block diagram of the electromechanical subsystem ISADQSS

Voltage $U_{зUm}$ applied to the input of the FC is determined by the expression (1):

$$U_{зUm} = U_0^{/} + k_{fc} U_{зf}, \tag{1}$$

where

k_{fc} – coefficient of the FC, which is determined by the expression (2);

$U_{зf}$ – task signal.

$$k_{fc} = \frac{k_f}{k_{Um}} \frac{U_{mн} - U_0}{f_н}, \tag{2}$$

where k_f, k_{Um} – frequency and voltage transfer coefficients of the converter;

$U_{mн}$, $f_н$ – rated voltage and frequency of motor supply;

U_0 – voltage at zero frequency ("boost"), $U_0 = kU_{mн}$, where k=(0,06÷0,25).

Figure 4 illustrates block diagram of the FC. Figure 5 represents the structural scheme of the FC, and its mathematical model is based on the equations of a three-phase symmetric system of voltages and transformations and is described by expressions (3) - (8).

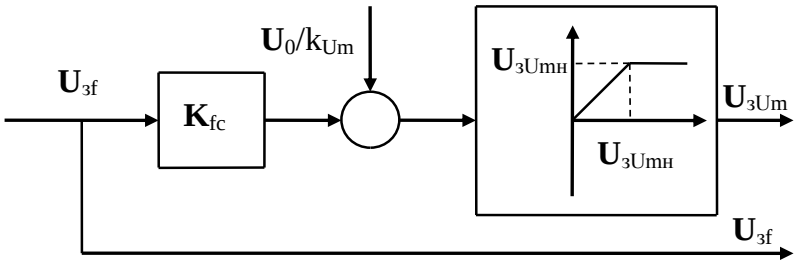

Figure 4. Block diagram of FC ISADQSS

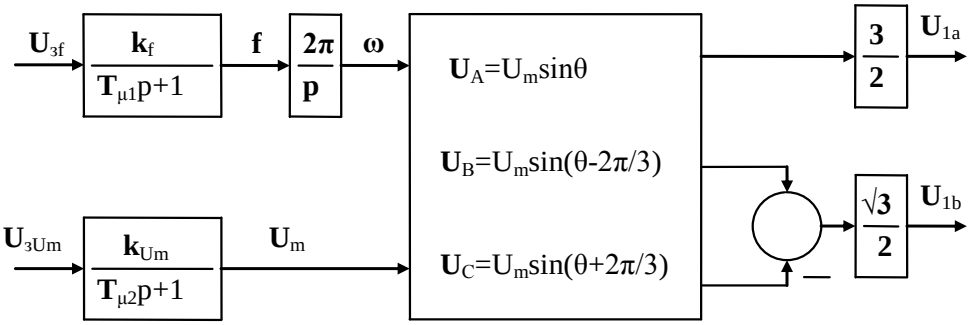

Figure 5. Block diagram of FC ISADQSS

$$U_A = U_m \sin\theta. \tag{3}$$

$$U_B = U_m \sin(\theta - 2\pi/3). \tag{4}$$

$$U_C = U_m \sin(\theta + 2\pi/3). \tag{5}$$

$$\theta = 2\pi \int_0^t f dt. \tag{6}$$

$$U_{1a} = 3U_A/2. \tag{7}$$

$$U_{1b} = \sqrt{3}(U_B - U_C)/2. \tag{8}$$

where U_A, U_B, U_C are voltages of the respective phases of the motor stator; θ – electric angle; U_{1a}, U_{1b} – projections of the stator voltage vector on the axis *a-b*of the fixed stator coordinate system.

The inertia of the transducer is approximated by aperiodic links by expressions (9), (10) in which $T_{\mu 1}$, $T_{\mu 2}$ are small uncompensated time constants.

$$f = \frac{k_f}{T_{\mu 1} p + 1} U_{зf}. \tag{9}$$

$$U_m = \frac{k_{Um}}{T_{\mu 2} p + 1} U_{зUm}. \tag{10}$$

The data received from the current sensor S3 is filtered from interference and converted into digital form. Then the difference between the maximum and minimum instantaneous values of the current in the same area of the stone is determined.

During the research, an electric motor with data [1] was used: $P_{2nom} = 11\,\text{kW}$; $\omega_{1nom} = 314\,rad/s$; $U_{1f} = 220\,V$; $f_{1nom} = 50\,Hz$; $\eta_{nom} = 0{,}88$; $\cos\phi = 0{,}9$; $s_{nom} = 0{,}03$; $x_\mu = 4{,}2\,rel.unit$; $R_1^{/} = 0{,}04\,rel.unit$; $x_1^{/} = 0{,}061\,rel.unit.$; $R_2^{//} = 0{,}025\,rel.unit$; $x_2^{//} = 0{,}12\,rel.unit$; $J_\partial = 0{,}023\,kg \cdot m^2$.

With the following parameters of the block diagram of the induction motor $I_{1nom} = 21{,}04\,A$; $R_1 = 0{,}418\,\Omega$; $R_2^{/} = 0{,}261\,\Omega$; $x_1 = 0{,}638\,\Omega$; $x_2^{/} = 1{,}25\,\Omega$; $x_{12} = 43{,}91\,\Omega$; $M_{nom} = 41{,}04\,Nm$; $L_{12} = 0{,}1398\,H$; $L_1 = 0{,}1419\,H$; $L_2 = 0{,}1438\,H$, and the following parameters of the structural diagram of the FC: $U_0 = 31{,}1V$; $k_f = 5\,Hz/V$; $k_{Um} = 31{,}1V/V$; $k_{fn} = 0{,}91/V$.

Graphs of transients in the conditions of stabilization of the speed of the drive motor of the main motion were obtained in the Simulink environment and are presented in Figure 6.

The study was conducted for 10 s. A random signal source with a normal Random Number distribution is used to simulate the moment of resistance on the shaft. The speed ω1 and the moment M1 correspond to the mode of operation of the machine during medium grinding, ω2, M2 - respectively, fine grinding of granite stone. The range of load deviations ranged from 41.42% to 70.68% relative to the nominal in the mode of medium grinding. At the penultimate stage of workpiece processing, the value of the torque of the drive motor was between the marks of 19.49% - 53.65%.

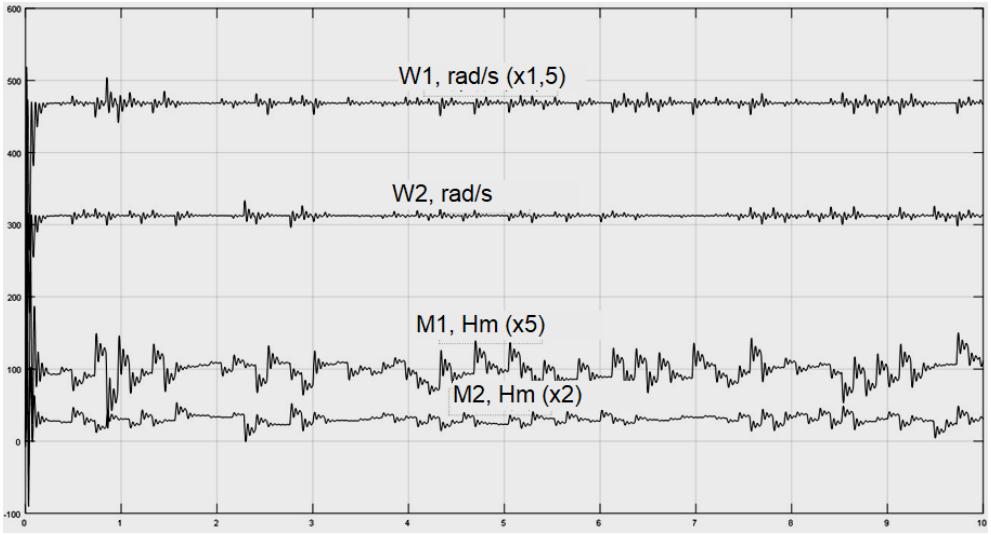

Figure 6. Graphs of transients in the conditions of stabilization of frequency of rotation of the driving engine of the main movement

Graphs of changes in the value of the output power of the main motor for the two modes of operation of the machine are shown in Figure 7.

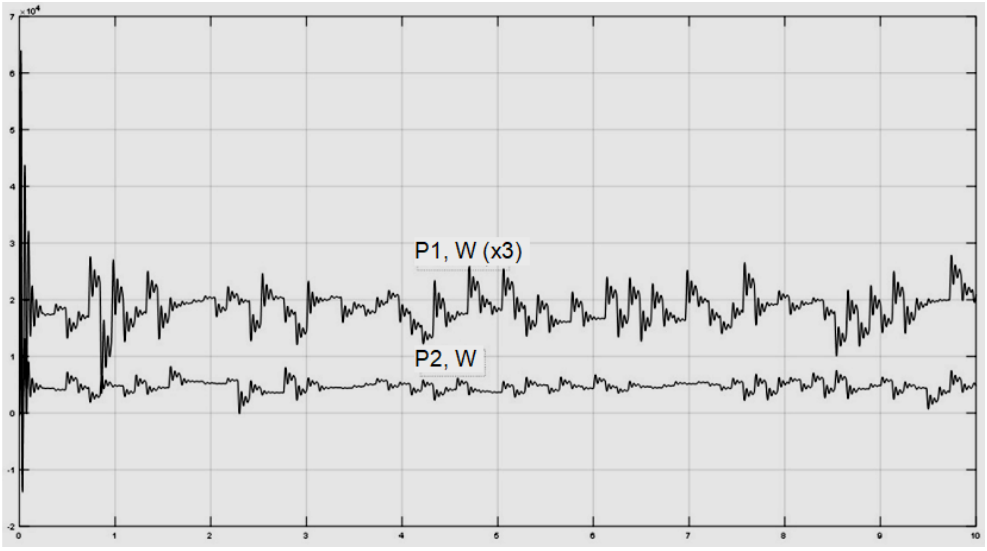

Figure 7. Graphs of change of size of output power of the electric motor of the main movement for two operating modes of the machine

The obtained voltage values are fed to the input of the ANN, which determines the quality of surface treatment of the stone. Figure 8 presents the principle of transmission of the measured roughness data when assessing the quality of stone surface treatment at the ANN input for its processing and subsequent provision of information about the quality and stage of stone surface treatment [3].

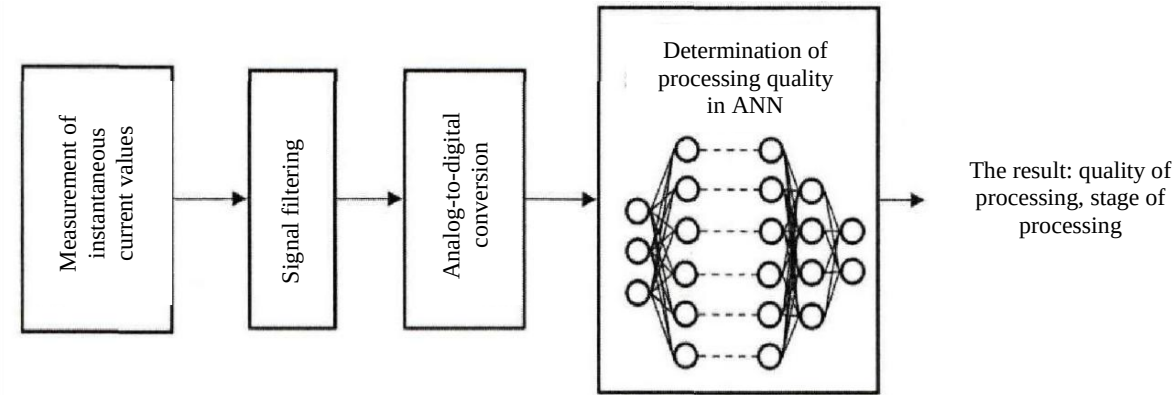

Figure 8. Block diagram of ensuring the determination of the quality of surface treatment of the stone ANN as a part of ISADQSS [3]

ANN can be implemented in one of two ways - a reprogrammed neuroprocessor or a neuroimulator, with a customizable structure of neurons according to one of the known models. At this stage of development, the ANN is implemented as a neuroimulator, which is integrated as a specialized software application to the operating system of the PC ISADQSS. The structure of the developed ANN is built on the principles of construction of a multilayer perceptron. ANN is trained by the method of "teaching with a teacher" according to the algorithm of "reverse propagation of error". The basic unit of information processing in ANN, including ANN as a structural element of ISADQSS is a neuron that produces the output OUT, forming the sum of the products of the weights *w* of the inputs *x*. The mathematical model of the neuron is represented by an expression given in [7].

Overall, the rapid assessment of the quality of surface treatment of natural stones proposed by ISADQSS is described by a rather complex mathematical model. Therefore, in general case, the problem of assessing the quality of surface treatment of natural stones, on the example of granite, can be represented as follows.

Based on the data of multiple measurements of the value of instantaneous values and the amplitude of the current consumption at different stages of grinding, the achieved quality is automatically determined dur-

ing the processing of the stone surface in real time. Figure 9 shows an example of the results of measuring the instantaneous values of current consumption by the drive of the main movement of the grinder at different quality of processing at the respective stages of grinding.

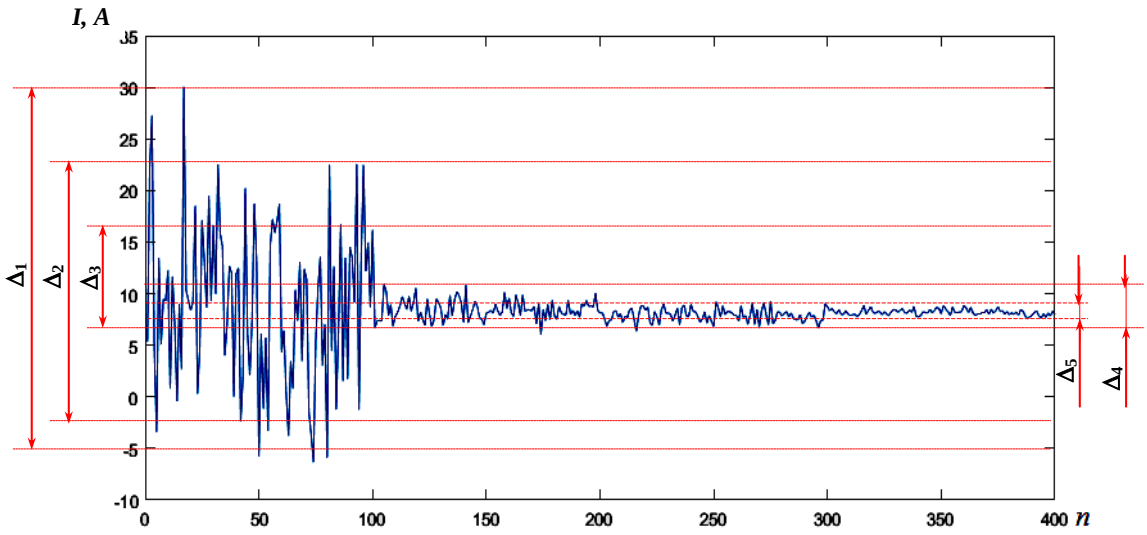

Figure 9. The result of measuring the instantaneous values of current consumption by the drive of the main motion at different quality of granite surface treatment at the appropriate stages of grinding: Δ_1 is scatter of instantaneous values of a stum at rough grinding (peeling), $\Delta_2$is scatter of instantaneous current values at average grinding,$\Delta_3$is scatter of instantaneous values of a stum at thin grinding,$\Delta_4$is scatter of instantaneous values of current at finishing grinding (ravines), $\Delta_5$is scatter of instantaneous current values during polishing

Based on the set of results of measuring the values of instantaneous values of current consumption, which were obtained by field experiment at an existing stone processing plant in the Zhytomyr region (Ukraine) was formed a database of examples for training ANN proposed ISADQSS covering many variants of scatters$\Delta_i \mid i = \overline{1; I}$ instantaneous values of current at different quality values at the respective stages of grinding. The set of scatter of instantaneous values of current consumption forms the input vector $X = \{x_n \mid n = \overline{1; N}\}$,supplied to the ANN inputs. The result is a vector of digital signal Y formed at the outputs of the ANN, which reflects the stage of processing the surface of the stone and the achieved quality: $Y = \{y_m \mid m = \overline{1; M}\}$, where y_m is the output signal of the ANN, which corresponds to the implementation of the m-th stage of grinding and the achieved quality; M is the number of grinding stages that can be determined. The maximum value of y_m at the m-th corresponding output of the ANN corresponds to the implementation of the corresponding stage of grinding and achieving a given quality. The signal from the ANN is transmitted to a PC, where automated information processing with the presentation of results in a user-friendly formis carried out.

Schematic model of ANN is shown in Figure 10. ANN is organized as a multilayer perceptron with a 3-layer structure, the number of neurons in each layer is determined by the conditions of the task. In particular, it is taken into account that the determination of the achieved quality during the processing of the stone surface in real time is carried out by ANN based on the results of continuous measurement of instantaneous values of current consumption, continuously supplied to its input.

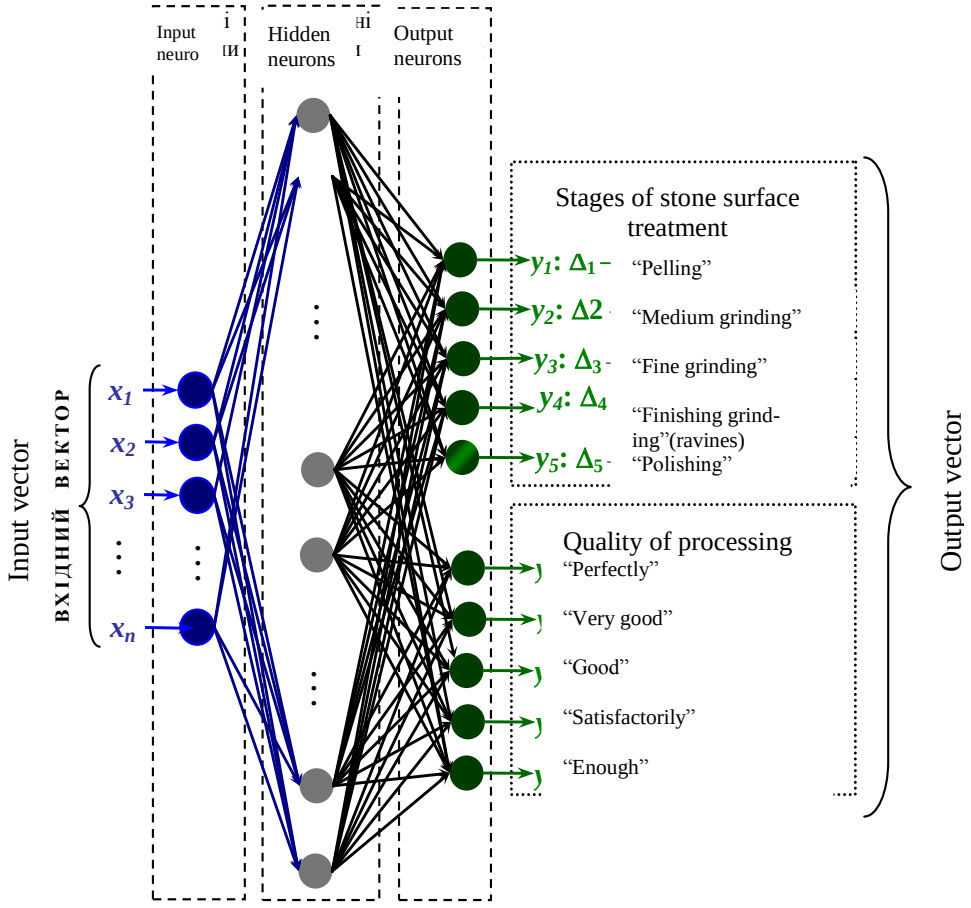

Figure 10. Schematic model of ANN of the offered ISADQSS for the automated express assessment of quality of processing of surfaces of natural stones according to a grinding stage

The number of output neurons at the output of the ANN is determined by the structure of the output vector Y. The decision on the quality achieved at the appropriate stage of grinding is made by the interpreter of the answer "winner gets everything", so the number of output signals corresponds to the number of response options which gaves the maximum signal at the output.

The hidden neurons that form the hidden layer of the ANN intermediate processing of information in such a way that the output layer of neurons is fed to linearly separated sets. The dimension of the hidden layer is determined empirically by the learning results of ANN. The value of the mean square error E, which should not exceed 0.05, is accepted as an evaluative functional of ANN training.

Computer modeling of the work of ISADQSS, in particular the developed ANN, was carried out. The obtained results indicate high speed and accuracy of work.

Thus, the time of quality assessment and determination of the stage of stone surface treatment does not exceed 2 s., which corresponds to the real time mode, and the value of the root mean square error of training and operation of ANN does not exceed the specified value - $E \leq 0{,}05$.

Conclusions

1. The description and results of experimental researches of intellectual system for automated determination of the quality of processing of surfaces of natural stones (ISADQSS) is innovative development in the field of instrument making and is intended for stone processing for express estimation of quality of processing of surfaces of stones, in particular roughness, with high accuracy in real-time and automatic mode in production conditions directly when performing technological operations of grinding and polishing.

2. According to the results of experimental studies of ISADQSS work, it was found that the value of the root-mean-square error does not exceed 0.05, and the speed does not exceed 2 s, which corresponds to the real-time mode. The measurement results do not depend on the condition of the outer surface of the stone or its humidity.

3. The proposed system has high productivity due to the use of ANN, which performs simultaneous processing of many digital data by parallel information processing, as well as a functional converter that captures the dependence of voltage on roughness in real time.

References

1 Гелета О.Л. Оцінка блиску полірованої поверхні декоративного каміння / О.Л. Гелета, І.А. Сергієнко, О.В. Горобчишин // Коштовне та декоративне каміння. — 2011. — № 3. — С. 12–15.

2 Коробійчук В. В. Оцінка якості блочної сировини та облицювальної продукції з природного каменю. Ч. І: навч. посібник / В. В. Коробійчук, А. О. Криворучко, Н. С. Ремез, К. К. Ткачук, Р. В. Соболевський. — Житомир: ЖДТУ, — 2012. — 188 с.

3 Патент на винахід 121727; МПК: (2020.01) G01B 21/30 (2006.01), B28D 1/00, B24B 5/00. Спосіб визначення якості обробки поверхні каменю / А. Ю. Сазонов, І. Ю. Черепанська, С. В. Кальчук, О.М. Безвесільна, Ю.Б. Бродський; заявник і патентоутримувач Житомирський національний агроекологічний університет. — UA 121727 C2; заявл. 15.04.2019; надр. 10.07.2020. — Бюлл. № 13.

4 Черепанська І.Ю. Інтелектуальна система вимірювання кутів. / І.Ю. Черепанська, О.М. Безвесільна, А.Ю. Сазонов // Патент України на корисну модель 127373, МПК: G 01 B 21/22 (2006.01). — 25.07.2018.

5 Cherepanska I. Artificial Neural Networks a Basic Element of the Automated Goniometric System. / I. Cherepanska, E. Bezvesilna, A. Sazonov // Recent Advances in Systems, Control and Information Technology / Proceedings of the International Conference SCIT. – 2016. – May 20–21. – P. 43–52. – 827 p. http://link.springer.com/book/10.1007 %2F978–3–319–48923–0

6 Cherepanska I. Development of artificial neural network for determining the components of errors when measuring angles using a goniometric software-hardware complex / I. Cherepanska, E. Bezvesilna, A. Sazonov, S. Nechai, O. Pidtychenko // European journal of enterprise technologies. – 2018. – Vol. 5/9 (95). – P.43–51. DOI: https://doi.org/10.15587/1729–4061.2018.141290

7 Cherepanska I. Intelligent precise goniometric system of analysis of spectral distribution intensities for definition of chemical composition of metal-containing substances / I. Cherepanska, O. Bezvesilna, Yu. Koval, A. Sazonov // Metallophysics and Advanced Technologies. – 2019. – Vol. 41. – No. 2. – P. 263 — 278. DOI: https://doi.org/10.15407/mfint.41.02.0263

8 Cherepanska I. Artificial neural network as a part of intelligent precise goniometric system of analysis of spectral distribution intensities for definition of chemical composition of metal-containing substances / I. Cherepanska, O. Bezvesilna, Yu. Koval, A. Sazonov // Metallophysics and Advanced Technologies. — 2020. — Vol. 42. — No. 10. — P. 1441–1454. DOI: https://doi.org/10.15407/mfint.42.10.1441

9 Saidi M.N. Rotational and translation-free polishing of granite: surface quality and dust particles emission and dispersion / M.N. Saidi, V. Songmene, J. Kouam, A. Bahloul // The International Journal of Advanced Manufacturing Technology. — 2018. — Vol. 98(1–4). — P. 289–303. DOI: 10.1007/s00170–018–2247–8

10 Cevheroğlu Çıra Investigation of the Effects of Marble Material Properties on the Surface Quality / Cevheroğlu Çıra, S. Dağ, A. Karakuş // Advances in Materials Science and Engineering. — 2018. — P. 1–7. DOI: 10.1155/2018/6514785

11 Saidi M.N. Experimental investigation on fine particle emission during granite polishing process / M.N. Saidi, V. Songmene, J. Kouam, A Bahloul // The International Journal of Advanced Manufacturing Technology. — 2015. — Vol. 81(9–12). — P. 2109–2121. DOI: 10.1007/s00170–015–7303-z.

12 Зиятдинов Р.Р. Система активного контроля шероховатости поверхности на основе измерения степени поляризации отраженного излучения / Р.Р. Зиятдинов, А.А. Шабаев, Р.Р. Валиахметов // Фундаментальные исследования. — 2017. — № 12–2. — С. 287–291.

13 Hunko W.S. MATLAB Image Processing as a Viable Tool to Study Low Surface Roughness / W.S. Hunko, V. Chandrasekaran, L.N. Payton // Volume 2B: Advanced Manufacturing. — 2015. — P. 1–10. DOI: 10.1115/imece2015–51672.

14 Wang, X. Using Wavelet Packet Transform for Surface Roughness Evaluation and Texture Extraction / X. Wang, T. Shi, G. Liao, Y. Zhang, Y. Hong, K. Chen // Sensors. — 2017. — Vol. 17(4). — P. 9—33. DOI: 10.3390/s17040933

15 Белов М.П. Автоматизированный электропривод типовых производственных механизмов и технологических комплексов: [учеб. для вузов] / М.П. Белов, В.А. Новиков, Л.Н. Рассудов. — М.: Изд. центр «Академия», 2007. — С. 418.

16 Tantussi, G. Analyses of stone surfaces by optical methods / G. Tantussi, M. Lanzetta, A.I. Te // Proceedings of the 8th Conference of the Italian Association of Mechanical Technology. — Ed. Del Taglia A., Dipartimento di Meccanica e Tecnologie Industriali, Università degli Studi di Firenze, Pub.: Centro Editoriale Toscano, Firenze, Italy, — 2007. — P. 27. — 97 p. ISBN: 88–7957–264–4.

И.Ю. Черепанская, А.Ю. Сазонов, С.В. Кальчук, О.Ф. Соколовский, О.С. Сиваева

Табиғи тастардың беттерін өңдеу сапасын автоматтандырылған анықтаудың интеллектуалды жүйесі

Мақала өзекті мәселеге – табиғи тастардың бетін өңдеу сапасын анықтаудың автоматтандыру деңгейін, дәлдігі мен жылдамдығын арттыруға арналған. Табиғи тастардың беткі қабатын өңдеу сапасын анықтаудың автоматтандырылған интеллектуалды жүйесі ұсынылған (ТБСАИЖ). Бұл әртүрлі сипаттағы беттерді тегістеу және жылтырату үшін тас өңдеу өнеркәсібінде қолдануға арналған аспап жасау саласындағы инновациялық әзірлеме. ТБСАИЖ тас бетін өңдеу сапасын жоғары дәлдікпен

және жылдамдықпен автоматты режимде және нақты уақыт режимінде тікелей, тегістеу және жылтырату процесінде орындауға мүмкіндік береді және технологиялық жабдықты тоқтатуды қажет етпейді. Бұл жағдайда өлшеу нәтижесі өңделген беттің ылғалдылығы мен тазалығына байланысты емес. Ұсынылған ТБСАИЖ жылтыр өлшегіштер мен профилометрлер сияқты дәстүрлі мамандандырылған зертханалық құралдарға балама болып табылады, оларды пайдалану көп еңбекті қажет етеді және қымбатқа түседі. Басқалардан айырмашылығы, ұсынылып отырған ТБСАИЖ үлкен дәлдікке ие (орташа квадраттық қателік 5%–дан аспайды) және тез әрекет етеді (кедір–бұдырлықты анықтау уақыты 2 с-тан аспайды). ТБСАИЖ әртүрлі автоматтандыру құралдарын гетерогенді қасиеттері бар синергетикалық интеграциялау қағидаттарына сәйкес құрылған – жасанды нейрондық желілер (ЖНЖ), сондай-ақ, өңделетін беттің кедір–бұдыр мөлшерінің өзгеруіне байланысты тас өңдеу құралының үйкеліс күшінің өзгеруіне сезімтал сенсор ретінде қолданылатын негізгі қозғалыс жетегінің ток тіркеушісі (НҚЖТТ). Ұсынылған ТБСАИЖ бұл жоғары дәлдік пен жылдамдық, әмбебаптылық және пайдалану жеңілдігі сияқты артықшылықтарды біріктіретін инновациялық және перспективалы даму болып табылады.

Кілт сөздер: жасанды нейрондық желілер, кедір–бұдыр, сапа, автоматтандыру, дәлдік, жылдамдық, өлшеу.

И.Ю. Черепанская, А. Ю. Сазонов, С.В. Кальчук, О.Ф. Соколовский, О.С. Сиваева

Интеллектуальная система автоматизированного определения качества обработки поверхностей природных камней

Статья посвящена актуальной проблеме – повышению уровня автоматизации, точности и быстродействия определения качества обработки поверхностей природных камней. Предложена интеллектуальная система автоматизированного определения качества обработки поверхностей природных камней (ИСАКПК). Это инновационная разработка в области приборостроения, предназначена для применения на камнеобрабатывающих производствах при шлифовании и полировании поверхностей различной природы. ИСАКПК позволяет выполнять экспресс-оценку качества обработки поверхностей камней с высокой точностью и быстродействием в автоматическом режиме и режиме реального времени непосредственно, во время выполнения технологических операций шлифования и полирования, и не требует остановки технологического оборудования. При этом результат измерения не зависит от влажности и чистоты обрабатываемой поверхности. Предложенная ИСАКПК является альтернативой традиционным специализированным лабораторным средствам, например, блескометрам и профилометрам, применение которых является трудоемким и дорогостоящим. В отличие от них, предложенная ИСАКПК имеет большую точность (средняя квадратическая погрешность не превышает 5%) и быстродействие (время определения шероховатости не более 2 с.). ИСАКПК построена по принципам синергетической интеграции разных средств автоматизации с неоднородными свойствами – искусственных нейронных сетей (ИНС), а также так называемого регистратора токов привода главного движения (РТПГД), который применяется в качестве датчика чувствительного к изменению силы трения камнеобрабатывающего инструмента в зависимости от изменения величины шероховатости обрабатываемой поверхности. Предложенная ИСАКПК является инновационной и перспективной разработкой, которая объединяет такие преимущества, как высокая точность и быстродействие, универсальность и простота использования.

Ключевые слова: искусственные нейронные сети, шероховатость, качество, автоматизация, точность, быстродействие, измерения.

References

1 Gheleta, O.L., Serghijenko, I.A., & Ghorobchyshyn, O.V. (2011). Otsenka bleska polirovannoi poverkhnosti dekorativnogo kamnia [Estimation of gloss of polished surface of decorative stone]. *Dragotsennye i dekorativnye kamni — Precious and decorative stones*, 3, 12–15 [in Ukrainian].

2 Korobijchuk, V.V., Kryvoruchko, A.O., Remez, N.S., Tkachuk, K.K., & Sobolevsjkyj, R.V. (2012). *Otsenka kachestva blochnogo syria i oblitsovochnykh izdelii iz prirodnogo kamnia. Chast I: uchebnoe posobie [Estimation of quality of block raw materials and facing products from natural stone. Part I]*. Zhytomyr: ZhDTU [in Ukrainian].

3 Sazonov, A.Yu., Cherepansjka, I.Yu., Kaljchuk, S.V., Bezvesiljna, O.M., & Brodsjkyj, Yu.B. (2020). Metod opredeleniia kachestva obrabotki poverkhnosti kamnia [Method of determining the quality of stone surface treatment]. *Patent na izobretenie — Patent for invention*, 121727; MPK: (2020.01) G01B 21/30 (2006.01), B28D 1/00, B24B 5/00 [in Ukrainian].

4 Cherepansjka, I.Yu., Bezvesiljna, O.M., & Sazonov, A.Yu. (2018). Intellektualnaia sistema izmereniia ugla [Intelligent angle measurement system]. *Patent Ukrainy na poleznuiu model — Patent of Ukraine for utility model*, 127373, MPK: G 01 B 21/22 (2006.01) [in Ukrainian].

5 Cherepanska, I., Bezvesilna, E., & Sazonov, A. (2016). Artificial Neural Network as a Basic Element of the Automated Goniometric System. *Proceedings from Recent Advances in Systems, Control and Information Technology: International Conference (May 20–21), 827* (pp. 43–52). http://link.springer.com/book/10.1007 %2F978–3-319–48923–0

6 Cherepanska, I., Bezvesilna, E., Sazonov, A., Nechai, S., & Pidtychenko, O. (2018). Development of artificial neural network for determining the components of errors when measuring angles using a goniometric software-hardware complex. *European journal of enterprise technologies,* 5/9(95), 43–51. DOI: https://doi.org/10.15587/1729–4061.2018.141290

7 Cherepanska, I., Bezvesilna, O., Koval, Yu., & Sazonov, A. (2019). Intelligent precise goniometric system of analysis of spectral distribution intensities for definition of chemical composition of metal-containing substances. *Metallophysics and Advanced Technologies*, 41(2), 263–278. DOI: https://doi.org/10.15407/mfint.41.02.0263

8 Cherepanska, I., Bezvesilna, O., Koval, Yu., & Sazonov A. (2020). Artificial neural network as a part of intelligent precise goniometric system of analysis of spectral distribution intensities for definition of chemical composition of metal-containing substances. *Metallophysics and Advanced Technologies,* 42(10), 1441–1454. DOI: https://doi.org/10.15407/mfint.42.10.1441

9 Saidi, M.N., Songmene, V., Kouam, J., & Bahloul, A. (2018). Rotational and translation-free polishing of granite: surface quality and dust particles emission and dispersion. *The International Journal of Advanced Manufacturing Technology*, 98(1–4), 289–303. DOI:10.1007/s00170–018–2247–8

10 Cevheroglu, C., Dag, S., & Karakus, A. (2018). Investigation of the Effects of Marble Material Properties on the Surface Quality. *Advances in Materials Science and Engineering*, 2018, 1–7. DOI:10.1155/2018/6514785

11 Saidi, M.N., Songmene, V., Kouam, J., & Bahloul, A. (2015). Experimental investigation on fine particle emission during granite polishing process. *The International Journal of Advanced Manufacturing Technology*, 81(9–12), 2109–2121. DOI:10.1007/s00170–015–7303-z

12 Zijatdinov, R.R., Shabaev, A.A., & Valiahmetov, R.R. (2017). Sistema aktivnogo kontrolia sherokhovatosti poverkhnosti na osnove izmereniia stepeni poliarizatsii otrazhennogo izlucheniia [Surface roughness control system based on measuring the degree of reflected light polarization]. *Fundamentalnye issledovaniia — Fundamental Research,* 12(2), 287–291 [in Russian].

13 Hunko, W.S., Chandrasekaran, V., & Payton, L.N. (2015). MATLAB Image Processing as a Viable Tool to Study Low Surface Roughness. *Advanced Manufacturing.* 2B, 1–10. DOI:10.1115/imece2015–51672

14 Wang, X., Shi, T., Liao, G., Zhang, Y., Hong, Y., & Chen, K. (2017). Using Wavelet Packet Transform for Surface Roughness Evaluation and Texture Extraction. *Sensors*, 17(4), 933. DOI:10.3390/s17040933

15 Belov, M.P. (2007). *Avtomatizirovannyi elektroprivod tipovykh proizvodstvennykh mekhanizmov i tekhnologicheskikh kompleksov: uchebnik dlia vuzov [Automated electric drive of typical production mechanisms and technological complexes: a textbook for universities]*. Moscow: Izdatelskii tsentr «Akademiia» [in Russian].

16 Tantussi, G., Lanzetta, M., & Te, A.I. (2007). Analyses of stone surfaces by optical methods. Proceedings from Ed. Del Taglia A., Dipartimento di Meccanica e Tecnologie Industriali, Università degli Studi di Firenze: *8th Conference of the Italian Association of Mechanical Technology* (p. 27). Firenze: Centro Editoriale Toscano.

DOI 10.31489/2022PH1/27-34

UDC 53.043

P.Yu. Tsyba[*1,2], O.V. Razina[1,2], N.T. Suikimbayeva[1,3]

[1]*L.N. Gumilyov Eurasian National University, Nur-Sultan, Kazakhstan*
[2]*LLP Ratbay Myrzakulov Eurasian International Centre for Theoretical Physics, Nur-Sultan, Kazakhstan*
[3]*M.Kh. Dulaty Taraz Regional University, Taraz, Kazakhstan*
([*]E-mail: pyotrtsyba@gmail.com)

Reconstruction of cosmological models are inspired by generalization of the Chaplygin gas

This paper considers models arising from the composition of the modified Gauss–Bonnet gravity (the Gauss–Bonnet invariant) and the general relativity (the Ricci scalar) against the background of a flat, homogeneous, and isotropic space-time described by the Friedmann–Robertson–Walker metric. Advantages arising from applying a theory containing higher-order invariants (Gauss–Bonnet invariant) consist in the presence of additional degrees of freedom, which makes it possible to study the influence of small-order effects on the dynamics of the system under study, which are in search and confirmed by cosmological observational data. We reconstructed two models with a power-law and exponential dependence on the Gauss–Bonnet invariant, where the model ansatz is a combination of the inverse Weierstrass elliptic function and the power-law function describing the Hubble parameter. This facilitates obtaining a quasi-Dieter law of the change of the scale factor in the initial and late epochs of the Universe. The application of the special function is inspired by generalization equation of state of the Chaplygin gas type, the Weierstrass gas. The application of the equation of state with such dependence makes allows obtaining a quasi-periodic universe. The equations of state are based on the Chaplygin gas are model equations of state and describe well the evolution of both the early and the modern universe. The obtained two particular models are investigated for the fulfillment of the energy conditions, which makes it possible to carry out analysis at a late stage of evolution of the universe and using perturbation theory covering the period of the early universe. For the power-law and exponential models, the perturbations of the Hubble parameter decrease in a finite time are shown, providing a way out of the inflationary stage of evolution of the universe.

Keywords: Friedmann equations, $f(G)$ gravity, Chaplygin gas, Weierstrass gas, energy conditions, perturbation theory, inflation, accelerated expansion.

Introduction

Cosmological observation data [1–4] testify to the discovery of the phenomenon of accelerated expansion and inform on cosmological parameters in the early epoch of the universe. To correctly understand the genesis and process of evolution of the universe, it is required to introduce changes in the classical general relativity by modifying it according to observational cosmology.

There are many possible theoretical descriptions of models responsible for this process. In particular, dark energy models [5] inspired by the modified gravity $f(R)$ have been proposed. Applying the modified theory of gravity, such as $f(R)$, gravity created the prerequisites for understanding the evolution of the universe to explain the accelerated expansion of the universe in recent times. An interesting alternative theory is the modified Gauss–Bonnet gravity [6], or $f(G)$ gravity. Concrete realistic models of $f(G)$ gravity were built to explain cosmic acceleration. By taking into account the corrections for the curvature of a higher order, the features of the future finite time are provided. To study the quantum and general theory of gravity, it is interesting to study the generalization of gravity, such as gravity $f(G)$, where G is the Gauss–Bonnet invariant. In [7], inflationary phenomenology coming from a scalar field, with quadratic curvature terms in the view of GW170817 was investigated. The dynamics of inflationary phenomenology were described and proved that theories with the Gauss–Bonnet term can be compatible with recent observations. In the work [8], de Sitter's solution in the framework of the non-minimal coupling of Gauss–Bonnet gravity with a scalar field was considered and search for the stability of de Sitter solutions, which corresponds to the minimum of the effective potential was made. In [9], inflationary phenomenology of the Einstein–Gauss–Bonnet theory corrected for k-inflation was studied and the problem of non-gaussianity under slow and constant roll conditions was considered.

In this paper, $R + f(G)$ gravity model in the framework of flat and homogeneous space-time described by the Friedmann–Robertson–Walker (FRW) metric is considered. Reconstruction of the resulting model

with a special form of the Hubble parameter inspired by the generalization of the Chaplygin gas equation of state – the Weierstrass gas, first presented in [10], is carried out with $f(G) = G^n$ и $f(G) = Ge^{\beta\frac{G}{G_0}}$. The obtained two particular models are investigated for the fulfillment of the energy dominance conditions and through perturbation theory, thus, embracing evolution in the early and late epochs of the universe.

Experimental

2. Basic of $R + f(G)$ gravity

We consider the following action, which describes General Relativity plus a function of the Gauss-Bonnet term:

$$S = \int d^4x\sqrt{-g}\left[\frac{1}{2\kappa^2}R + f(G)\right], \tag{1}$$

where $\kappa^2 = 8\pi G_N$, G_N being the Newton constant, and the Gauss-Bonnet invariant is defined as usual

$$G = R^2 - 4R_{\mu\nu}R^{\mu\nu} + R_{\mu\nu\lambda\sigma}R^{\mu\nu\lambda\sigma}. \tag{2}$$

By varying the action (1) over $g_{\mu\nu}$, the following field equations are obtained

$$0 = \frac{1}{2k^2}\left(-R^{\mu\nu} + \frac{1}{2}g^{\mu\nu}R\right) + T^{\mu\nu} + \frac{1}{2}g^{\mu\nu}f(G) - 2f_G RR^{\mu\nu} + 4f_G R^{\mu}_{\rho}R^{\nu\rho} - 2f_G R^{\mu\rho\sigma\tau}R^{\nu}_{\rho\sigma\tau}$$
$$- 4f_G R^{\mu\rho\sigma\nu}R_{\rho\sigma} + 2(\nabla^\mu\nabla^\nu f_G)R - 2g^{\mu\nu}(\nabla^2 f_G)R - 4\left(\nabla_\rho\nabla^\mu f_G\right)R^{\nu\rho} - 4\left(\nabla_\rho\nabla^\nu f_G\right)R^{\mu\rho}$$

$$+4(\nabla^2 f_G)R^{\mu\nu} + 4g^{\mu\nu}\left(\nabla_\rho\nabla_\sigma f_G\right)R^{\rho\sigma} - 4\left(\nabla_\rho\nabla_\sigma f_G\right)R^{\mu\rho\nu\sigma}, \tag{3}$$

where we made the notations $f_G = f'(G)$ and $f_{GG} = f''(G)$. We shall assume throughout the paper a spatially-flat FRW universe, whose metric is given by

$$ds^2 = -dt^2 + a^2(t)(dx^2 + dy^2 + dz^2), \tag{4}$$

In case (4), Einstein–Hilbert action (1) contains the modified Gauss–Bonnet gravity term and GR, we can rewrite as point-like action is defined by the expression:

$$S = \int dt\sqrt{-g}\left(\frac{R}{2} + \frac{f}{2} - \frac{f'}{2}\left(G - 24\frac{\dot{a}^2\ddot{a}}{a^3}\right)\right), \tag{5}$$

where $\sqrt{-g} = a^3$, $R = 6\left(2H^2 + \dot{H}\right)$ – the Ricci scalar, $G = 24\frac{\dot{a}^2\ddot{a}}{a^3} = 24H^2\dot{H} + 24H^4$ – the Gauss–Bonnet invariant, $a = a(t)$ – the scale factor, and $H = \frac{\dot{a}}{a}$ – the Hubble parameter.

From the action (5), Lagrange point takes the form

$$L = -3\dot{a}^2 a + \frac{f}{2}a^3 - \frac{f'}{2}Ga^3 - 4f''\dot{G}\dot{a}^3. \tag{6}$$

By applying Euler–Lagrange equation to the (5), we get equation of motion

$$2\dot{H} + 3H^2 = -\frac{f}{2} + \frac{f'}{2}G - 4f'''\dot{G}^2H^2 - 4f''\ddot{G}H^2 - 8f''\dot{G}H(H^2 + \dot{H}). \tag{7}$$

Accordingly, the first Friedmann $2\dot{H} + 3H^2 = -p$ equation, pressure p takes the form

$$p = \frac{f}{2} - \frac{f'}{2}G + 4f'''\dot{G}^2H^2 + 4f''\ddot{G}H^2 + 8f''\dot{G}H(H^2 + \dot{H}). \tag{8}$$

On the other hand, the total energy (Hamiltonian) corresponds to Lagrangian

$$3H^2 = -\frac{f}{2} + \frac{f'}{2}G - 4f''\dot{G}H^3. \tag{9}$$

From the second Friedmann $3H^2 = \rho$ equation, energy density ρ takes the form

$$\rho = -\frac{f}{2} + \frac{f'}{2}G - 4f''\dot{G}H^3. \tag{10}$$

3. Research methods

We can introduce energy condition in pressure p and energy density terms ρ as [11]

$$\text{NEC} \Rightarrow p + \rho \geq 0 \tag{11}$$

$$\text{WEC} \Rightarrow \rho \geq 0, p + \rho \geq 0,$$
$$\text{SEC} \Rightarrow 3p + \rho \geq 0, p + \rho \geq 0,$$
$$\text{DEC} \Rightarrow \rho \geq 0, -\rho \leq p \leq \rho.$$

To study the stability, we consider the conservation equation energy-matter perfect fluid

$$\dot{\rho} + 3H(\rho + p) = 0. \tag{12}$$

To do that, first, we have presumed a linear perturbation of the Hubble parameter as

$$H(t) = H_0(t)\big(1 + \delta(t)\big), \tag{13}$$

where $H(t)$ is the perturbed Hubble parameter and $\delta(t)$ is the perturbation term.

Energy-matter perfect fluid [12]:

$$\dot{H} = \partial_t \left(A_1 \wp^{-1}(t^2 + A_2\, exp(t)\,; g2, g3) + A_3 t^{-\frac{1}{7}} \right), \tag{14}$$

where $\dot{H} = \frac{dH}{dt}$, A_1, A_2, A_3 – arbitrary constants, $\wp^{-1}$ – inverse Weierstrass function, and $g2, g3$ – invariants. Figure 1 represents $\dot{H}$ and H time dependence.

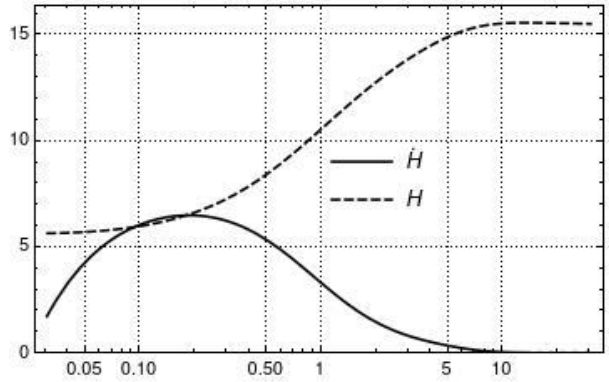

Figure 1. $\dot{H}$ and H dependence on cosmic time t at $A_1 = 10, A_2 = 0.95, A_3 = 0.8$.

Results and Discussion

4 Energy condition analysis

4.1 Power-law model

Let us consider particular case of $R + f(G)$ gravity in form $f(G) = G^n$. Take into account equations (8), (10), (14) and

$$f(G) = G^n, f'(G) = nG^{n-1}, f''(G) = n(n-1)G^{n-2}, f'''(G) = n(n-2)(n-1)G^{n-3}, \tag{15}$$

pressure p and energy density ρ in Hubble terms take the form

$$p_1 = \frac{G^n(1-n)}{2} + 4n(n-1)(n-2)G^{n-3}\dot{G}H^2 + 4n(n-1)G^{n-2}\ddot{G}H^2 + 8n(n-1)G^{n-2}\dot{G}H\big(H^2 + \dot{H}\big), \tag{16}$$

$$\rho_1 = -\frac{G^n(1-n)}{2} - 4n(n-1)G^{n-2}\dot{G}H^3, \tag{17}$$

the graphical dependence of which on the cosmic time t is shown in Figure 2 at $n = 4$. This choice of n provides a contribution to the pressure p and the energy density ρ of all terms in (16) and (17).

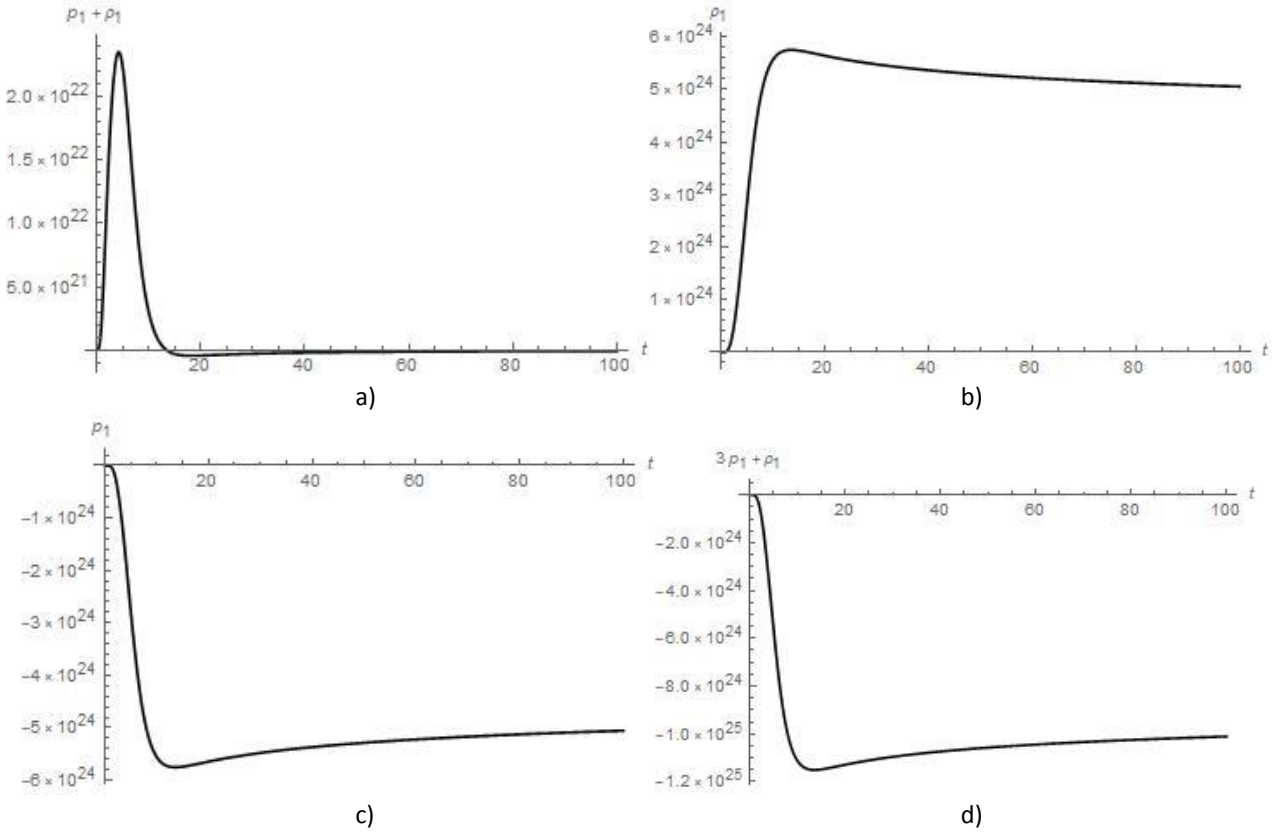

Figure 2. Dependence on cosmic time t: a) pressure p_1; b) energy density ρ_1; c) $p_1 + \rho_1$ и d) $3p_1 + \rho_1$.

Note that, with decreasing n, the values of pressure and energy density decrease, so for $n = 3$ the form of the time dependence remains, but the amplitude decreases by a factor of 10^8.

4.2 Exponential model

Let us consider another particular case $R + f(G)$ gravity in form $f(G) = f_0\left(1 - Ge^{\frac{G_0}{G}}\right)$. Take into account equation (8), (10), (14) and

$$f(G) = -f_0\left(1 - e^{\frac{G}{G_0}}\right), f'(G) = \frac{f_0}{G_0}e^{\frac{G}{G_0}}, f''(G) = \frac{f_0}{G_0^2}e^{\frac{G}{G_0}}, f'''(G) = \frac{f_0}{G_0^3}e^{\frac{G}{G_0}}. \tag{18}$$

pressure p and energy density ρ in Hubble terms take the form

$$p_2 = -\frac{f_0}{2}\left(1 - e^{\frac{G}{G_0}}\right) + 2\frac{f_0}{G_0}e^{\frac{G}{G_0}}G + 4\frac{f_0}{G_0^3}e^{\frac{G}{G_0}}\dot{G}^2H^2 + 4\frac{f_0}{G_0^2}e^{\frac{G}{G_0}}\ddot{G}H^2 + 8\frac{f_0}{G_0^2}e^{\frac{G}{G_0}}\dot{G}H(H^2 + \dot{H}), \tag{19}$$

$$\rho_2 = \frac{f_0}{2}\left(1 - e^{\frac{G}{G_0}}\right) - 2\frac{f_0}{G_0}e^{\frac{G}{G_0}}G - 4\frac{f_0}{G_0^2}e^{\frac{G}{G_0}}\dot{G}H^2, \tag{20}$$

the graphical dependence of which on the cosmological time t is shown in Figure 3.

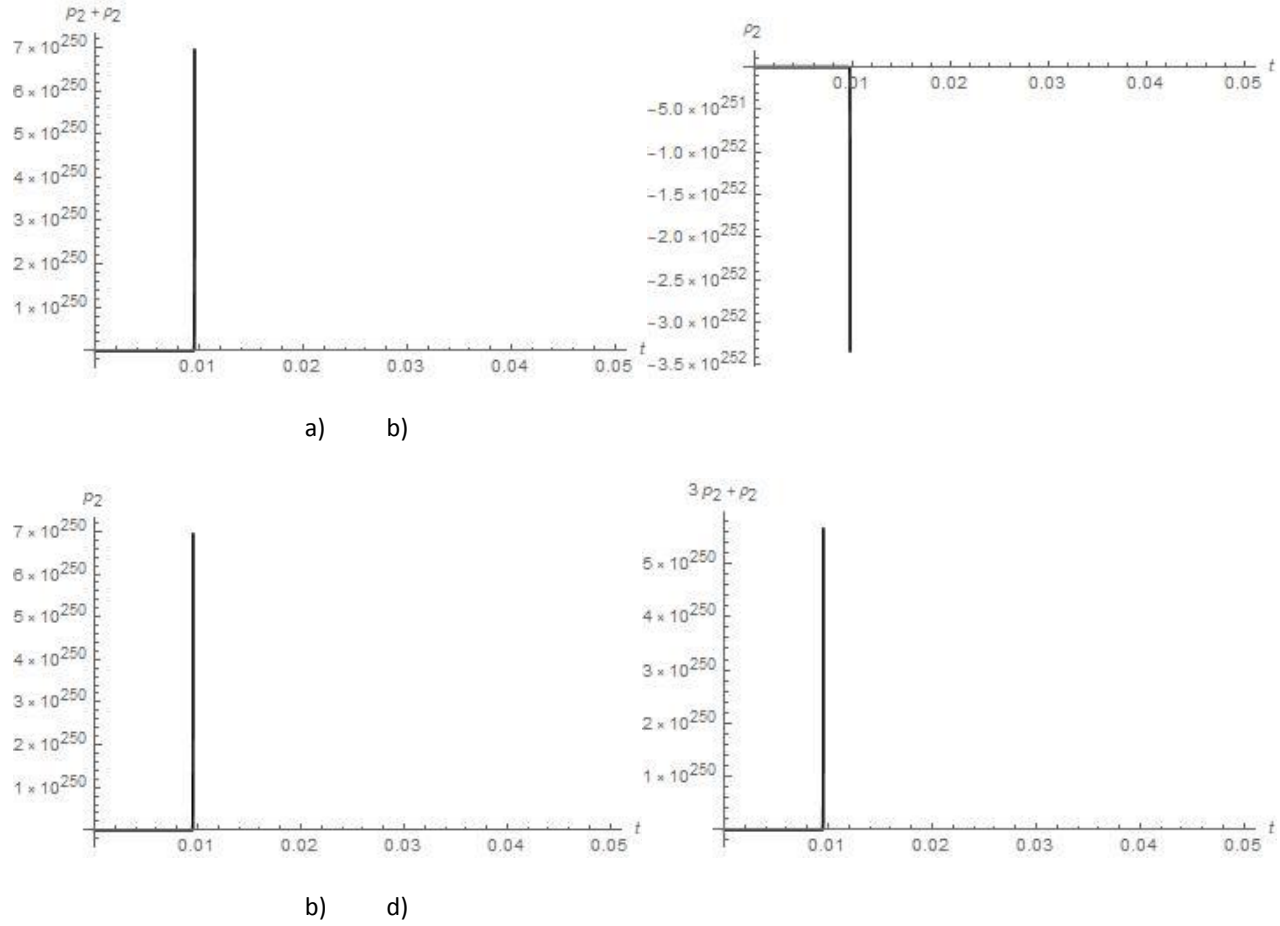

Figure 3. Dependence on cosmic time t: a) pressure p_2; b) energy density ρ_2; c) $p_2 + \rho_2$ and d) $3p_2 + \rho_2$.

5 Perturbation analysis

5.1 Power-law model

In this section, we are interested in investigating the power law's stability through perturbation analysis. Substituting in (12) (8), (10), and (13) taking into account $f(G) = G^n$, at $n = 4$, we get equation

$$H\left(\dot{H} + H^2\right)\left(\dot{G}^2 + 12\ddot{G}\left(\dot{H} + H^2\right)H^2 + 36\dot{G}H\left(\dot{H} + H^2\right)^2\right) = 0,$$

which, in the case of a search for a particular solution in terms of the Hubble parameter, transforms into a differential equation

$$\dot{H}_0(t)b(t) + H_0\dot{b}(t) + H_0^2(t)b^2(t) = 0, \tag{21}$$

where $b(t) = 1 + \delta_1(t)$. From equation (18), we obtain a particular solution describing the perturbation $\delta_4(t)$ in view

$$\frac{1}{H_0\left(1 + \delta_4(t)\right)} = t + c_1, \tag{22}$$

where H_0 is described by expression (14) and c_1 is integration constant. Solution (22) is illustrated in Figure 4.

It should be noted that at $c_1 \geq 1$ perturbation $\delta_4(t)$ takes the positive value. Perturbation $\delta_4(t)$ for the most rapidity tend to be zero at $c_1 = 1$. Perturbation $\delta_4(t)$ takes the negative value at $c_1 < 1$.

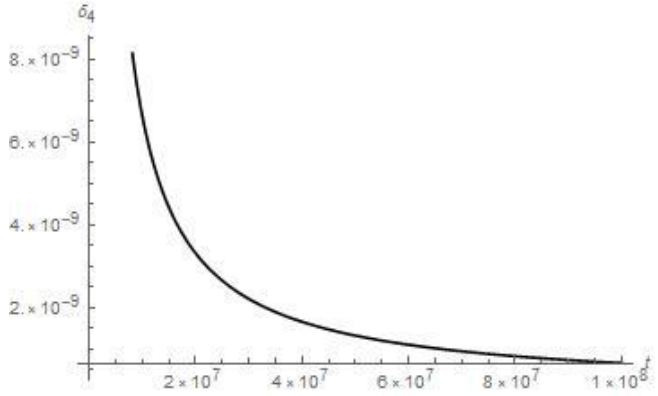

Figure 4. $\delta_4(t)$ dependence on cosmic time t at $n = 4$ and $c_1 = 1$.

5.2 Exponential model

Let us research perturbation in exponential model. Substituting in (12), (8), (10), (13) and $f(G) = f_0\left(1 - Ge^{\frac{G}{G_0}}\right)$ neglecting terms higher than the first order, we obtain the equation

$$\dot{H} = -H^2. \tag{23}$$

From equation (23), we obtain a particular solution describing the perturbation $\delta(t)$ the same as (22).

Conclusions

Here $R + f(G)$ cosmological model was considered in flat, homogeneous, and isotropic Friedmann–Robertson–Walker space-time. Power-law model and exponential model were chosen as particular cases of modified Gauss–Bonnet gravity in the $f(G)$ term. We provided energy conditions and made a perturbation analysis.

In the power-law model, the null energy condition performs, which is depicted in Figure 2a and described by $p_1 + \rho_1 \geq 0$. Weak energy condition performs and is shown in Figures 2a and 2b. It is described inequality $\rho_1 \geq 0$ and $p_1 + \rho_1 \geq 0$. Strong energy condition $p_1 + \rho_1 \geq 0$ and $3p_1 + \rho_1 \geq 0$ is represented in Figures 2a and 2d. This condition partially performs because the first inequality performs only. Violation of this condition provides accelerated expansion. Dominant energy condition $\rho_1 \geq 0, -\rho_1 \leq p_1 \leq \rho_1$ is shown in Figures 2b and 2c, and performs. The simultaneous fulfillment of weak and dominant energy conditions ensures the acceleration mode.

For the exponential model, the null energy condition $p_2 + \rho_2 \geq 0$ the same as power-law model. Weak energy condition $\rho_2 \geq 0$ and $p_2 + \rho_2 \geq 0$ partially performs because the second inequality performs only. These conditions are shown in Figures 3a and 3b. Strong energy condition $p_1 + \rho_1 \geq 0$ and $3p_1 + \rho_1 \geq 0$ is represented in Figures 3a and 3d. Figures 3a and 3c illustrate dominant energy condition $\rho_2 \geq 0, -\rho_2 \leq p_2 \leq \rho_2$. It not performs for exponential model. In this model, the energy density has a negative value, which corresponds to cosmology with a phantom field. This behavior provides a superacceleration mode.

By comparing results of energy condition models, we have $|p_1 + \rho_1| \ll |p_2 + \rho_2|$ and $|3p_1 + \rho_1| \ll |3p_2 + \rho_2|$. The power-law model $f(G)$ describes the accelerated expansion of the universe at a late stage in the evolution of the universe and this expansion will be eternal, and the results of the exponential model predict a transition to the super acceleration regime, that is, the disintegration of the universe in a finite period of time.

The analysis of the perturbation of the studied models shows that both in the power-law and exponential models, the perturbations tend to be zero. This ensures a way out of the inflationary stage at an early stage in the universe's evolution.

Acknowledgment

This study was funded by the Science Committee of the Ministry of Education and Science of the Republic of Kazakhstan AP09261147.

References

1 Perlmutter, S., Aldering, G., Goldhaber, G., Knop, R.A., Nugent, P., Castro, P.G., Deustua, S., Fabbro, S., Goobar, A., Groom, D.E., Hook, I. M., Kim, A.G., & et al. (1999). Measurements of Ω and Λ from 42 High-Redshift Supernovae. *Astrophysical Journal, 517, 2,* 564.

2 Riess, A.G., Filippenko, A.V., Challis, P., Clocchiattia, A., Diercks, A., Garnavich, P.M., Gilliland, R.L., Hogan, C.J., Jha, S., Kirshner, R.P., Leibundgut, B., Phillips, M.M., Reiss, D., Schmidt, B.P., Schommer, R.A., Smith, R.Ch., Spyromilio, J., Stubbs, Ch., Suntzeff, N.B., & Tonry, J. (1998). Observational Evidence from Supernovae for an Accelerating Universe and a Cosmological Constant. *Astronomical Journal, 116,* 3, 1009.

3 Komatsu, E., Dunkley, J., Nolta, M.R., Bennett, C.L., Gold, B., Hinshaw, G., Jarosik, N., Larson, D., Limon, M., Page, L., Spergel, D.N., Halpern, M., Hill, R.S., Kogut, A., Meyer, S.S., Tucker, G.S., Weiland, J.L., Wollack, E., & Wright, E.L. (2009). Five-Year Wilkinson Microwave Anisotropy Probe Observations: Cosmological Interpretation. *Astrophysical Journal Supplement Series, 180 (2),* 330.

4 Abraham, N., Akrami, Y., Ashdown, M., Aumont, J., Baccigalupi, C., Ballardini, M., Banday, A.J., Barriero, R.B., Bartolo, N., Basak, S., Battye, R., Benabed, K., Bernard, J.P., Bersanelli, M., Bielewicz, P., Bock, J.J., Bond, J.R., Borril, J., Bouchet, F.R., & et al. (2020). Planck 2018 results VI. Cosmological parameters. *Astronomy and Astrophysics,* 2020, *641,* A6.

5 De Felice, A., & Tsujikawa, S. (2010). $f(R)$ theories. *Living Review in Relativity, 13 (*3).

6 Baker, M.R., & Kuzmin, S. (2019). A connection between linearized Gauss-Bonnet gravity and classical electrodynamics". *International Journal Modern Physics D.,Vol. 28, №7,* 1950092.

7 Venikoudis, S.A., & Fronimos, F.P. (2021). Inflation with Gauss–Bonnet and Chern–Simons higher-curvature-corrections in the view of GW170817.

8 Vernov, S., & Pozdeeva, E. (2021). De Sitter solutions in Einstein-Gauss-Bonnet gravity. *Universe, 7(5),* 149.

9 Odintsov, S.D., Oikonomou, V.K., & Fronimos, F.P. (2021). k-Inflation-corrected Einstein-Gauss-Bonnet Gravity with Massless Primordial Gravitons. *Nuclear Physics B., 963,* 115299,

10 Bamba, K., Debnath, U., Yesmakhanova, K., Tsyba, P., Nugmanova, G., & Myrzakulov, R. (2012). Periodic Cosmological Evolutions of Equation of State for Dark Energy. *Entropy, 14(11),* 2351.

11 Bolotin, Yu.L., Yerokhin, D.A., & Lemets, O.A. (2012). Expanding Universe: slowdown or speedup? *Physics-Uspekhi, 55(9),* 941.

12 Tsyba, P., Razina, O., Barkova, Z., Bekov, S., & Myrzakulov, R. (2019). Scenario of the evolution of the universe with equation of state of the Weierstrass type gas. *Journal of Physics Conference Series, 1391,* 012162.

П.Ю. Цыба, О.В. Разина, Н.Т. Суйкимбаева

Чаплыгин газын жалпылау арқылы космологиялық модельдерді қайта құру

Мақалада Фридман–Робертсон–Уокер метрикасымен сипатталған жазық, бір текті және изотропты кеңістік–уақыт фонындағы жалпы салыстырмалық теориясының (Риччи скаляры) және Гаусс–Бонне (Гаусс-Бонне инварианты) гравитациясының модификацияланған теориясы композициясының нәтижесінде пайда болған модельдер қарастырылған. Жоғарғы ретті (Гаусс–Бонн инварианты) инварианттан тұратын теорияны есепке алу нәтижесінде пайда болатын артықшылықтар, қосымша еркіндік дәрежесінің пайда болуына негізделеді, олар космологиялық бақылаулармен нақтыланған кіші ретті эффекттердің зерттелетін жүйенің динамикасына әсерін зерттеуге мүмкіншілік береді. Авторлар Гаусс–Бонн инвариантына экспоненциалды және дәрежелі тәуелді екі моделдің қайта құрастырылуын жүзеге асырған, мұнда анзац моделі ретінде Вейерштрассаның кері эллипстік функциясының комбинациясы мен Хаббл параметрін сипаттайтын дәрежелік функциясы алынған. Бұл Әлемнің бастапқы және кейінгі дәуірлеріндегі масштаб факторының өзгеруінің квазидезитерлік заңын алуға мүмкіндік береді. Арнайы функцияны қолдану Чаплыгиндік газ түрі — Вейерштрас газының күй теңдеуін жалпылаудан туындаған. Осындай тәуелділігі бар күй теңдеуін қолдану квазипериодты Әлемді алуға мүмкіндік береді. Чаплыгин газына негізделген күй теңдеулері модельдік күй теңдеулері болып табылады және ерте және қазіргі әлемнің эволюциясын жақсы сипаттайды. Алынған екі жеке модель энергия доминантының шарттарын орындау үшін зерттелді, бұл әлемнің эволюциясының кеш кезеңінде және ерте әлемнің кезеңін қамтитын бұзылулар теориясын қолдана отырып талдау жасауға мүмкіндік береді. Дәрежелік және экспоненциалды модельдер үшін Хаббл параметрі соңғы уақытта ауытқиды, осылайша Ғалам эволюциясының инфляциялық сатысынан шығуды қамтамасыз етеді.

Кілт сөздер: Фридман теңдеуі, $f(G)$-гравитация, Чаплыгин газы, Вейерштрасс газы, энергияның доминанттылық шарттары, ұйытқу теориясы, инфляция, үдемелі кеңею.

П.Ю. Цыба, О.В. Разина, Н.Т. Суйкимбаева

Реконструкция космологических моделей, инспирированная обобщением газа Чаплыгина

В статье рассмотрены модели, возникающие в результате композиции модифицированной теории гравитации Гаусса–Бонне (инвариант Гаусса–Бонне) и общей теории относительности (скаляр Риччи) на фоне плоского, однородного и изотропного пространства–времени, описываемого метрикой Фридмана–Робертсона–Уокера. Преимущества, возникающие в результате применения теории, содержащей инварианты высшего порядка (инвариант Гаусса–Бонне), заключаются в наличии дополнительных степеней свободы, которые позволяют изучать влияние эффектов малого порядка на динамику исследуемой системы, находящихся в поиске и подтвержденных космологическими наблюдательными данными. Авторами осуществлена реконструкция двух моделей со степенной и экспоненциальной зависимостью от инварианта Гаусса–Бонне, где в качестве анзаца модели выступает комбинация обратной эллиптической функции Вейерштрасса и степенной функции, описывающей параметр Хаббла. Это позволяет получить квазидеситеровский закон изменения масштабного фактора в начальную и позднюю эпохи Вселенной. Применение специальной функции инспирировано обобщением уравнения состояния типа газа Чаплыгина – газом Вейерштрасса. Применение уравнения состояния с такой зависимостью позволяет получить квазипериодическую Вселенную. Уравнения состояния, основанные на газе Чаплыгина, являются модельными уравнениями состояния и хорошо описывают эволюцию как ранней, так и современной Вселенной. Полученные две частные модели исследованы на выполнение условий энергодоминантности, что дает возможность провести анализ в поздний этап эволюции Вселенной и с помощью теории возмущений охватывающей период ранней Вселенной. Показано, что для степенной и экспоненциальной модели возмущения параметр Хаббла уменьшается за конечное время, тем самым обеспечивая выход из инфляционной стадии эволюции Вселенной.

Ключевые слова: уравнения Фридмана, $f(G)$-гравитация, газ Чаплыгина, газ Вейерштрасса, условия энергодоминантности, теория возмущений, инфляция, ускоренное расширение.

DOI 10.31489/2022PH1/35-42

UDC 532.536

Zh.K. Akasheva[1*], A.A Kudaikulov[1], B.K. Assilbekov[1], D.A. Bolysbek[1,2]

[1]Satbayev University, Almaty, Kazakhstan;
[2]Al-Farabi Kazakh National University, Almaty, Kazakhstan
([*]E-mail: zhibek_akasheva@mail.ru)

Pore-scale modelling of fluid flow in porous media using the projection method for incompressible Navier-Stokes equations in irregular domains

This paper presents the results of numerical simulation of incompressible viscous flow in porous media, which comprise periodically arranged cylinders. This simulation is based on the numerical solution of the incompressible Navier-Stokes equations in irregular domains using the projection method on staggered grids, where the irregular boundary is represented by its level-set function at the pore-scale level. The main problem in numerical calculation of fluid flow through porous media occurs when the value of the porosity is close to 1 or is close to the threshold value since it is necessary to take a very fine numerical mesh, which requires additional computing power and increases the calculation time. There are exact analytical solutions for simple types of porous media which consist of periodically arranged cylinders. In this paper, the permeabilities of these porous media were numerically calculated and compared with the previous works based on the numerical solution of the Lattice-Boltzmann equation in irregular domains, when the fluid flow obeys Darcy's law. The comparison of numerical and theoretical values of porosity shows that this method is sufficiently accurate for porosity values φ=0.2–0.8.

Keywords: Navier-Stokes equations, numerical simulation, projection method, fibrous porous medium, permeability, porosity, grid, irregular boundary, fluid flow, geometry of pore space.

Introduction

Many of the environmental and industrial problems are related to the fluid flow in porous media. Therefore, understanding the processes that take place inside a porous medium plays a key role in science and technology.

Rabbani and Babaei [1] used pore network modeling (PNM) with a Lattice Boltzmann Method (LBM) to benefit from the strengths of both approaches. They calculated permeabilities of all throats using the LBM and substituted in the pore network model. Solving the LBM for every throat leads to an accurate representation of flow, but the algorithm is computationally expensive. LBM is used to model the steady-state incompressible fluid flow through different throat images and an Artificial Neural Network (ANN) is trained to mimic the trend of throat's permeabilities based on cross–sectional images [1].

The disadvantage of the PNM is that it cannot be applied to an inaccurate geometry. The main limitation of direct methods is the high computational cost [2], which could be a major obstacle in the case of large-sized and high-resolution volumetric images of porous material. As a solution to this size and time limitation, domain decomposition and parallel computation have been comprehensively hired to increase the models' efficiency and scalability. As another solution to deal with computational limitations, machine learning can be employed to mimic the behavior of complex solid/fluid systems. The main idea is to save the computational sources by solving a series of typical problems and extend the results to all similar cases.

With the development of high-performance computing and micro-CT technologies which allows to construct detailed geometrical description of material microstructure, it is possible to use numerical experiments for direct evaluation of material properties. In geophysical applications, such techniques are called digital rock physics and are meant to accompany and supply conventional laboratory measurements for evaluation of transport properties of rock core samples [3].

To distinguish porous media from each other, it is necessary to determine the geometry of pore space, due to microscopic pore sizes and a large number of pores per unit volume of porous medium. It is a difficult task. In most cases, statistical methods are used to determine the geometry of pore space [4, 5]. The main problem of the investigation of porous media properties is the problem of finding a relation between macroscopic parameters (e.g., permeability, elastic constants, electric or thermal conductivity) and the pore space geometry of porous media (the microstructure of porous media). For example, when the fluid flows through porous media at a low Reynolds number and it obeys Darcy's law [6]:

$$\vec{U} = \frac{K}{\mu}\nabla(p + \rho g z) \tag{1}$$

where $\vec{U}$ is the flow rate, K is the permeability of porous medium, μ is the fluid viscosity, p is the pressure in the porous medium and ρgz is the hydrostatic pressure. The main problem in this case is finding a relation between the permeability and geometrical parameters of porous media. There are only approximate solutions for simple cases of porous media comprising periodically arranged cylinders [7–11], which we consider in this paper. Mostly in practice, the Kozeny–Carman relation between the permeability and geometrical parameters of porous media is used [12, 13]:

$$K = \frac{\phi^3}{6s^2}$$

where φ is the porosity and s is the specific surface area. However, this relation was obtained for simple porous medium which constructed by the parallel capillaries with circular cross-section and this relation does not consider the microstructure of the porous medium.

This paper presents the results of numerical simulation of incompressible viscous flow in porous media at the pore-scale level. This simulation is based on the numerical solution of incompressible Navier-Stokes equations in irregular domains using the projection method on staggered grids, where the irregular boundary is represented by its level-set function [14–16]. When the fluid flow obeys Darcy's law, the permeability of these porous media was numerically calculated and compared with the previous works based on the numerical solution of the lattice-Boltzmann equation in irregular domains [17], and also the artificial compressibility relaxation algorithm was applied [18].

Experimental

Definition of the problem. A porous medium of volume V is represented in the form of the domain D which consists of two sub-domains: domain of voids D_0 with volume of fraction φ and domain of solid phases D_1 with volume of fraction 1- φ. The voids are called pores, and these pores form a pore space. Fluids that occupy these pores can flow if these pores are connected with each other [12, 13]. The minimum value of volume fraction φ at which fluid flows through a porous medium is called a threshold value [19]. A slow laminar flow through a porous medium is the problem that needs to be solved on a microscopic level. The microstructure of two-phase porous medium D is described in detail by the characteristic $I(\vec{x})$ function:

$$I(\vec{x}) = \begin{cases} 0\ for\ \vec{x} \in D_0 \\ 1\ for\ \vec{x} \in D_1 \end{cases} \tag{2}$$

The considering model is based on the numerical solution of Navier-Stokes equations for incompressible fluid flow through porous medium which is described by the $I(\vec{x})$ (equation (2)):

$$\left(\frac{\partial \vec{u}(\vec{x},t)}{\partial t} + (\vec{u}(\vec{x},t)\cdot\nabla)\vec{u}(\vec{x},t)\right) = \rho\vec{g} - \nabla p(\vec{x},t) + \mu\nabla^2\vec{u}(\vec{x},t), \vec{x} \in D_0 \tag{3}$$

$$\nabla\cdot\vec{u}(\vec{x},t) = 0, \vec{x} \in D_0 \tag{4}$$

No-slip boundary conditions are applied on the pore-matrix interface ∂D_0:

$$\vec{u}(\vec{x},t) = 0, \vec{x} \in \partial D_0 \tag{5}$$

The cubic porous medium domain D with size a is considered and the periodic boundary conditions are applied on its faces:

$$\vec{u}\left(\overrightarrow{x_C} - \frac{a}{2}, t\right) = \vec{u}\left(\overrightarrow{x_C} + \frac{a}{2}, t\right) \tag{6}$$

where $\overrightarrow{x_C}$ is the position of center of cubic domain D.

To find the permeability of porous medium, the steady state solution of equations (3, 4) with boundary conditions (5, 6) is found using the projection method on staggered grids [15]. This solution is averaged over the porous medium domain:

$$\vec{U} = \frac{\int_D \vec{u}(\vec{x})dV}{V}. \tag{7}$$

Then the Reynolds number ($Re = \frac{\rho UL}{\mu}$, where L is the characteristic length) is found below which the fluid flow in porous medium obeys Darcy's law for permeability calculation using the equation (1).

Numerical methodology. The solid surface is determined by introducing the level-set function for solid phase. For example, if the solid phase is a single sphere with diameter *d*, then its level-set function is as follows:

$$F(x,y,z) = (x-x_C)^2 + (y-y_C)^2 + (z-z_C)^2 - \frac{d^2}{4},$$

where x_C, y_C, z_C are the coordinates of the center of sphere. After introducing the level-set function for solid phase the characteristic function $I(\vec{x})$ (equation (2)) can be determined:

$$I(x,y,z) = \begin{cases} 0 \; if \; F(x,y,z) > 0, \\ 1 \; if \; F(x,y,z) \leq 1. \end{cases}$$

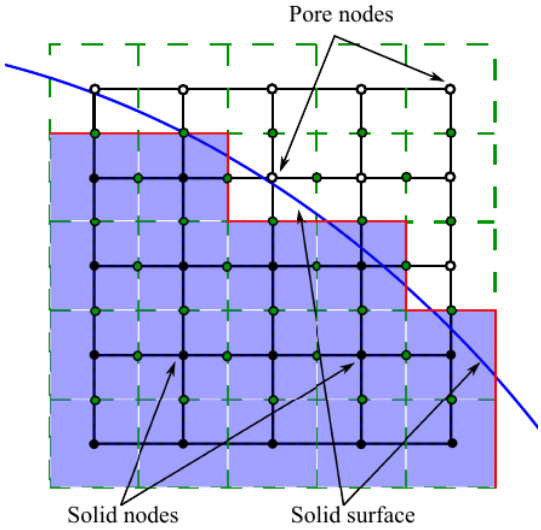

Figure 1. Representation of the staggered grid and solid surface

Porous medium domain D is approximated by generating a uniform, structured mesh that incorporates nodes of solid phase (or rock phase) D_1 and pore D_0 domains (example of the 2D structured mesh is shown in Figure 1 as black, solid lines).

The volume of solid phase of a porous medium can be calculated using the level-set function of solid phase:

$$V_{i,j,k} = \begin{cases} 0 \; if \; I(x_i, y_j, z_k) = 0 \\ \Delta^3 \; if \; I(x_i, y_j, z_k) = 1 \end{cases} \quad (8)$$

where *i*, *j*, *k* are the indexes of the mesh nodes in *x*, *y*, *z* direction, respectively, Δ and $V_{i,j,k}$ are the size and volume of the cells which circumscribed around the mesh nodes, respectively.

The total volume of the solid phase of a porous medium is:

$$V_s = \sum_{i=0}^{N_x-1} \sum_{j=0}^{N_y-1} \sum_{k=0}^{N_z-1} V_{i,j,k}, \quad (9)$$

where N_x, N_y and N_z are the number of the mesh nodes in *x*, *y*, *z* direction, respectively.

The total volume of pores of a porous medium is:

$$V_p = V - V_s.$$

The volume fraction of pores (or porosity) of a porous medium is:

$$\phi = \frac{V_p}{V} = 1 - \frac{V_s}{V}.$$

Also, the solid surface (blue line in Figure 1) can be calculated using the level-set function of solid phase:

$$S_{i,j,k} = \begin{cases} \Delta^2 \; if \; \left(I_{i+1,j,k} = 1 \; or \; I_{i,j,k} = 1\right) \; and \; I_{i+1,j,k} I_{i,j,k} = 0, \\ \Delta^2 \; if \; \left(I_{i,j+1,k} = 1 \; or \; I_{i,j,k} = 1\right) \; and \; I_{i,j+1,k} I_{i,j,k} = 0, \\ \Delta^2 \; if \; \left(I_{i,j,k+1} = 1 \; or \; I_{i,j,k} = 1\right) \; and \; I_{i,j,k+1} I_{i,j,k} = 0, \\ 0 \; otherwise. \end{cases} \quad (10)$$

The total value of the solid surface is (red line in Figure 1):

$$S = \sum_{i=0}^{N_x-1} \sum_{j=0}^{N_y-1} \sum_{k=0}^{N_z-1} S_{i,j,k} \quad (11)$$

The specific surface is:

$$s = \frac{S}{V}.$$

Calculation of the cross-sectional area and perimeter of a cylinder. The solid surface of a cylinder with the periodic structure (Figure 2) is determined by introducing the following level-set function:

$$F(x,y) = (x - x_C)^2 + (y - y_C)^2 - \frac{d^2}{4}, \quad (12)$$

where *d* is the diameter of a cylinder.

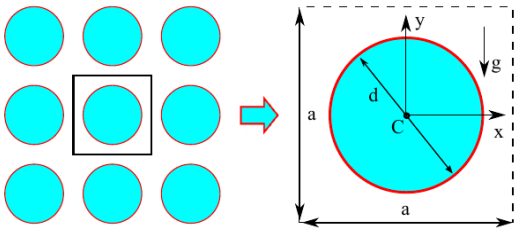

Figure 2. Two-dimensional rectangular area (*d* is the diameter of cylinder)

The area and perimeter of the cross-section of a cylinder are numerically calculated using equations (8, 9, 10, 11, 12). The comparison of numerical values of cross-sectional area and perimeter of a cylinder with exact values are shown in the Table 1, where a cylinder's diameter is *d*=0.6 (exact value of the area is $S = \frac{\pi d^2}{4} = 0.282743$ and the perimeter is $P = \pi d = 1.884956$).

The deviation between the numerical value of area and exact value is:

$$E.A. = |numerical\ value - exact\ value|.$$

The relative error is:

$$R.E.A. = \frac{E.A.}{exact\ value}.$$

Table 1

The comparison of the numerical values of cross-sectional area and perimeter of a cylinder with exact values (cylinder's diameter is d=0.6)

Number of the mesh nodes	S (cross sectional area)	E.A.	R.E.A.	P (cross-sectional perimeter)	E.P.	R.E.P.
16x16	0.269531	0.013212	0.046728	2.250000	0.365044	0.193662
32x32	0.286133	0.003389	0.011988	2.375000	0.490044	0.259977
64x64	0.281494	0.001249	0.004418	2.437500	0.552544	0.293134
128x128	0.283020	0.000277	0.000979	2.406250	0.521294	0.276555
256x256	0.282486	0.000257	0.000910	2.390625	0.505669	0.268266
512x512	0.282825	0.000082	0.000290	2.398438	0.513482	0.272411

Permeability calculation. There are many theoretical predictions of the permeability of fibrous porous media with the periodic structure [8–11].

John Happel [8] found the theoretical estimation of the permeability of these media by solving the Stokes equation for a fluid flow around a cylinder with no-slip boundary conditions at the surface of cylinder and periodic boundary conditions at the domain boundary. His theoretical prediction of the permeability of a fibrous porous medium is:

$$K_1^* = \frac{K_1}{d^2} = \frac{1}{32\varphi}\left[ln\left(\frac{1}{\varphi}\right) - \frac{1-\varphi^2}{1+\varphi^2}\right],$$

where K_1 is the permeability of fibrous porous media, d is the diameter of cylinders and $\varphi = \frac{d^2}{a^2}$, where a is the distance between centers of cylinders (see Figure 2). The main inaccuracy in his calculation is that the solution was based on solving the Stokes equation in a cylindrical coordinate system, and hence the boundary of its domain does not coincide with the real boundary.

In the work of Hasimoto [9], the exact solution of the Stokes equation for fluid flow around a cylinder in the form of infinite series is used to predict the permeability of fibrous porous media. He found the theoretical prediction of the permeability of fibrous porous media using only the terms of lowest order of this series:

$$K_2^* = \frac{K_2}{d^2} = \frac{1}{32\varphi'}\left[ln\left(\frac{1}{\varphi'}\right) - 1.476 + 2\varphi'\right] + O(\varphi'),$$

where $\varphi' = \frac{\pi d^2}{4a^2}$.

Later Sangani and Acrivos (1982) [20] improved the theoretical prediction of permeability of fibrous porous media using the terms of the highest order of the series presented in the work of Hasimoto [9]:

$$K_3^* = \frac{K_3}{d^2} = \frac{1}{32\varphi'}\left[\ln\left(\frac{1}{\varphi'}\right) - 1.476 + 2\varphi' - 1.774\varphi'^2 + 4.078\varphi'^3\right] + O\left(\varphi'^3\right).$$

The value of K_3 is close to exact value when φ' is close to 0, so the numerical value of permeability can be validated by comparing with the value of K_3 when φ' is close to 0. They also presented the numerical method to calculate the permeability for all values of the porosity in the work [10].

In the work [11], the porous medium is considered as "unit cell" and there is a unidirectional flow with a parabolic velocity profile. Their theoretical prediction of the permeability of fibrous porous medium is:

$$K_4^* = \frac{K_4}{d^2} = \frac{1}{3\varphi'} \cdot \frac{(1-\varphi)^{\frac{5}{2}}}{\left(2(\varphi+2) + 4\frac{(1-\sqrt{\varphi})(1-\varphi)^2}{\sqrt{\varphi}}\right)\frac{\sqrt{1-\varphi}}{\sqrt{\varphi}} + 12arctan\left(\frac{1+\sqrt{\varphi}}{\sqrt{1-\varphi}}\right)}.$$

The projection method on the staggered grid was applied to solve the incompressible Navier-Stokes equations and all numerical calculations were performed using PARIS simulator [21]. The results of numerical calculation of permeability were validated by comparing with theoretical estimations of the permeability of porous media like porous medium which consist of periodically arranged cylinders [7–11].

Results and Discussion

The fibrous porous medium with a periodic structure is considered in this section. Fibers are located at the same distance to each other and have the same diameter. Planar flow, that is perpendicular to the axes of cylinders, is considered. The fluid flows through this porous medium by the gravitational force. The following parameters are used: fluid density ρ=1, fluid viscosity μ=1, domain size a=1.

To find the permeability, the steady-state solution of Navier-Stokes equations is averaged over the porous medium domain (equation (7)). The permeability of fibrous porous media is numerically calculated and compared with existing theoretical estimations. For the case when the value of the porosity is close to 1, the Brinkman's estimation can be used to obtain exact solution [22].

The relation between flow rate and number of mesh nodes is shown in Table 2.

Table 2

Relation between the flow rate and number of nodes of the mesh for 2D fluid flow through the fibrous porous medium when a cylinder's diameter is *d*=0.6

Number of the mesh nodes	Flow rate
16x16	1.126954E-02
32x32	1.166258E-02
64x64	1.146031E-02
128x128	1.125835E-02

The comparison of numerical and theoretical values of the permeability of fibrous porous medium is shown in Figure 3 and Table 3.

Table 3

Numerical values of the permeability of fibrous porous medium

d (diameter of the cylinders)	φ (porosity)	s (specific surface)	$K^* = \frac{K}{d^2}$ (permeability)
0.2	0.968933	0.781250	2.076525
0.3	0.929626	1.218750	0.584678
0.4	0.874207	1.593750	0.207850
0.5	0.804138	2.031250	0.080000
0.6	0.716980	2.406250	0.030931
0.7	0.614929	2.781250	0.010859
0.8	0.496765	3.218750	0.003048
0.9	0.363464	3.593750	0.000543

Figure 3 illustrates the convergence of the flow rate (equation (7)) to the steady state value for 2D fluid flow through the fibrous porous medium.

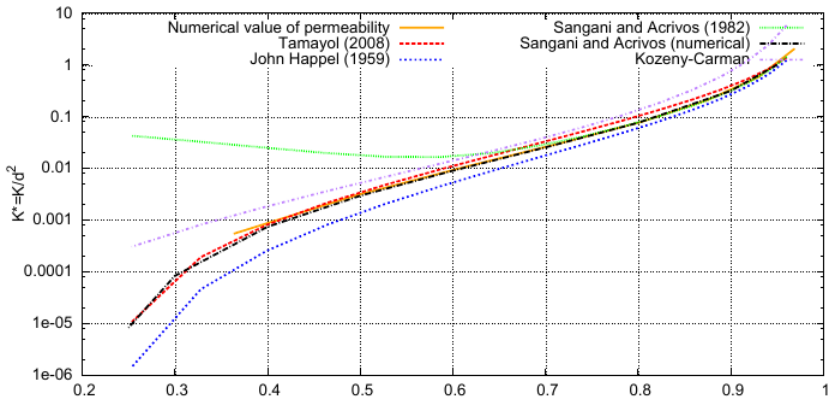

Figure 3. Comparison of the numerical and theoretical values of the permeability of fibrous porous medium

When the cylinder's diameter is small, the boundary of the domain which is considered in the work [8] almost coincide with the real boundary, so in this case the value of K_1 is close to exact value (see Figure 3).

According to Figure 3 the numerical value of the permeability is close to the value of K_3 when φ is close to 1. Thus, the error in numerical calculation of the specific surface of the fibrous porous medium has a weak effect on the numerical value of permeability.

Also, it can be seen that the numerical values of permeability presented in the work [10] are close to the numerical values of permeability for all values of the porosity where the numerical calculations were performed.

Conclusions

This paper presents the results of numerical simulation of incompressible viscous flow in porous media at the pore-scale level. To find the Reynolds number below which the fluid flow obeys Darcy's law, the incompressible Navier-Stokes equations are numerically solved using the projection method on staggered grids. The main reason for choosing this method is the possibility of finding the steady-state solution of Navier-Stokes equations more quickly than such methods as Lattice-Boltzmann, Smoothed-Particle Hydrodynamics, etc. However, this method becomes ineffective when the value of the porosity is small or is close to 1. The comparison of numerical and theoretical values of permeability shows that this method is sufficiently accurate for porosity values φ=0.2–0.8.

Acknowledgments

This research was funded by the Science Committee of the Ministry of Education and Science of the Republic of Kazakhstan (Grant No. AP08052055).

References

1 Rabbani, A., & Babaei, M. (2019). Hybrid pore-network and Lattice-Boltzmann permeability modelling accelerated by machine learning. *Advances in Water Resources, 126,* 116–128. https://doi.org/10.1016/j.advwatres.2019.02.012

2 Blunt, M.J., Bijeljic, B., Dong, H., Gharbi, O., Iglauer, S., Mostaghimi, P., Paluszny, A., & Pentland, C. (2013). Pore-scale imaging and modeling. *Advanced Water Resources, 51,* 197–216. DOI: 10.1016/j.advwatres.2012.03.003

3 Yang, C.F., & Math Phys, J. (2010). New trace formulae for a quadratic pencil of the Schrodinger operator. *Journal of Mathematical Physics*, 51, 033506–1-033506–10. DOI: 10.1063/1.3327835

4 Torquato, S. (2002). *Random Heterogeneous Materials: Microstructure and Macroscopic Properties.* New-York: Springer.

5 Anovitz, L.M., & Cole, D.R. (2015). Characterization and Analysis of Porosity and Pore Structures. R*eviews in Mineralogy & Geochemistry, 80(1),* 61–164. DOI: 10.2138/rmg.2015.80.04

6 Whitaker, S. (1986). Flow in porous media I: A theoretical derivation of Darcy's law. *Transport in Porous Media, 1,* 3–25.

7 Batchelor, G.K. (2000). *An introduction to fluid dynamics.* Cambridge: Cambridge University Press.

8 Happel, J. (1959). Viscous flow relative to arrays of cylinders. *AIChE Journal*, 5, 174–177. DOI: 10.1002/aic.690050211

9 Hasimoto, H. (1959). On the periodic fundamental solutions of the Stokes equations and their application to viscous flow past a cubic array of spheres. *Journal of Fluid Mechanics, 5(2),* 317–328. DOI: 10.1017/S0022112059000222

10 Sangani, A.S., & Acrivos, A. (1982). Slow flow past periodic arrays of cylinders with application to heat transfer. *International Journal of Multiphase Flow, 8(3),* 193–206. DOI: 10.1016/0301-9322(82)90029-5

11 Tamayol, A., & Bahrami, M. (2009). Analytical determination of viscous permeability of fibrous porous media. *International Journal of Heat and Mass Transfer, 52,* 2407–2414. DOI: 10.1016/j.ijheatmasstransfer.2008.09.032

12 Bear, J. (1972). *Dynamics of fluids in porous media*. New York: Elsevier.

13 Scheidegger, A.E. (1974). *The Physics of Flow Through Porous Media.* Toronto: University of Toronto Press.

14 Roache, P.J. (1985). Computational fluid dynamics. Albuquerque, N.M.: Hermosa Publishers.

15 Peyret, R., & Taylor, T.D. (1983). *Computational methods for fluid flow*. New York: Springer.

16 Brown, D.L., Cortez, R., & Minion, M.L. (2001). Accurate projection methods for the incompressible Navier-Stokes equations. *Journal of Computational Physics, 168(2),* 464–499. DOI: doi.org/10.1006/jcph.2001.6715

17 Cancelliere, A., Chang, C. Foti, E., Rothman, D.H., & Succi, S. (1990). The permeability of a random medium: Comparison of simulation with theory. *Physics of Fluids A: Fluid Dynamics, Vol. 2,* 2085–2088. DOI: 10.1063/1.857793

18 Chorin, A.J. (1967). A numerical method for solving incompressible viscous flow problems. *Journal of Computational Physics, 2(1).* 12–26. DOI: 10.1016/0021–9991(67)90037-X

19 Hunt, A., Ewing, R., & Ghanbarian, B. (2014). *Percolation Theory for Flow in Porous Media.* Switzerland: Springer.

20 Sangani, A.S., & Acrivos, A. (1982). Slow flow through a periodic array of spheres. *International Journal of Multiphase Flow, 8(4),* 343–360. DOI: 10.1016/0301–9322(82)90047–7

21 Zaleski, S. PARIS simulator code. *ida.upmc.fr.* Retrieved from http://www.ida.upmc.fr/ zaleski/paris.

22 Brinkman, H.C. (1949). A calculation of the viscous force exerted by a flowing fluid on a dense swarm of particles. *Applied Scientific Research,1,* 27–34. DOI: 10.1007/BF02120313

Ж.К. Акашева, А.А. Кудайкулов, Б.К. Асилбеков, Д.Ә. Болысбек

Кеуекті ортадағы сұйықтық ағынын кеуек масштабында модельдеу тұрақсыз аймақтардағы сығылмайтын сұйықтық үшін Навье-Стокс теңдеулеріне проекциялау әдісін қолдану

Мақалада периодты орналастырылған цилиндрлерден тұратын кеуекті ортадағы тұтқыр сығылмайтын сұйықтықтың ағынын сандық модельдеудің нәтижелері келтірілген. Бұл модельдеу шахмат торларындағы проекциялық әдісті қолдана отырып, тұрақты емес аудандардағы сығылмайтын сұйықтық үшін Навье–Стокс теңдеулерін сандық шешуге негізделген, мұнда тұрақты емес шекара масштабты деңгейде деңгей орнату функциясымен ұсынылған. Кеуекті орта арқылы сұйықтық ағынын сандық есептеудегі негізгі мәселе кеуектілік мәні 1 немесе шекті мәнге жақын болған кезде пайда болады. Мұндай жағдайларда қосымша есептеу қуатын қажет ететін өте аз сандық торды пайдалану керек, сонымен қатар, есептеу уақытын арттырады. Периодты орналастырылған цилиндрлермен тұратын кеуекті орта сияқты кеуекті ортаның қарапайым түрлеріне нақты аналитикалық шешімдер бар. Мақала авторлары бұл кеуекті орталардың кеуектілігін сандық түрде есептеп, оларды сұйықтық ағыны Дарси заңына бағынатын кезде біркелкі емес аймақтардағы Больцман тор теңдеуінің сандық шешіміне негізделген алдыңғы жұмыстармен салыстырған. Кеуектіліктің сандық және теориялық мәндерін салыстыру бұл әдістің φ = 0,2–0,8 кеуектілік мәндері үшін өте дәл екенін көрсетеді.

Кілт сөздер: Навье-Стокс теңдеулері, сандық модельдеу, проекция әдісі, талшықты кеуекті орта, өткізгіштік, кеуектілік, тор, тұрақсыз шекара, сұйықтық ағыны, кеуектер кеңістігінің геометриясы.

Ж.К. Акашева, А.А. Кудайкулов, Б.К. Асилбеков, Д.А. Болысбек

Поромасштабное моделирование течения жидкости в пористых средах с использованием проекционного метода для несжимаемых уравнений Навье–Стокса в нерегулярных областях

В статье представлены результаты численного моделирования течения вязкой несжимаемой жидкости в пористой среде, которая состоит из периодически расположенных цилиндров. Данное моделирование основано на численном решении уравнений Навье–Стокса для несжимаемой жидкости в нерегулярных областях с использованием проекционного метода на шахматных сетках, где нерегулярная граница представлена ее функцией установки уровня на поромасштабном уровне. Основная проблема при численном расчете течения жидкости через пористую среду возникает, когда значение пористости близко к 1 или к пороговому значению. В таких случаях необходимо использовать очень мелкую численную сетку, что требует дополнительных вычислительных мощностей, а также увеличивает время вычислений. Существуют точные аналитические решения для простых типов пористых сред, таких как пористые среды, которые состоят из периодически расположенных цилиндров. Авторами статьи пористости указанных пористых сред были численно рассчитаны и сравнены с предыдущими работами, основанными на численном решении решеточного уравнения Больцмана в нерегулярных областях, когда течение жидкости подчиняется закону Дарси. Сравнение численных и теоретических значений пористости показывает, что данный метод достаточно точен для значений пористости φ = 0,2–0,8.

Ключевые слова: уравнения Навье-Стокса, численное моделирование, проекционный метод, волокнистая пористая среда, проницаемость, пористость, сетка, нерегулярная граница, течение жидкости, геометрия порового пространства.

DOI 10.31489/2022PH1/43-57

UDC 531.133.1

S.P. Stepanenko[*1], B.I. Kotov[2], A.V. Spirin[3], V.Yu. Kucheruk[4]

[1]*National Scientific Center "Institute of Agricultural Engineering and Electrification", Ukraine;*
[2]*State Agrarian and Engineering University in Podilya, Ukraine;*
[3]*Separate structural subdivision "Ladyzhyn vocation college of Vinnytsia National Agrarian University", Ukraine;*
[4]*Vinnytsia National Technical University, Ukraine*
([*]E-mail: stepanenko_s@ukr.net)

Scientific foundations of the movement of components of grain material with an artificially formed distribution of air velocity

The article examines the study of the separation of grain materials in pneumatic channels with an artificially generated distribution of air velocity in the cross-section channel to determine the rational form and parameters of the material supply and options for grain material separation into fractions. The regularities of the weevil movement were theoretically investigated and established in the form of mathematical models of the dynamics of the movement of a solid particle in airflow, which differ from the known ones by taking into account the action of lateral forces, the concentration of the material, and the use of a power-law and an artificially formed exponential law of air distribution facilitated to increase the differences (splitting) trajectories of caryopses by 20 %. The solution of the system of nonlinear differential equations with initial conditions is performed in the Mathcad software environment in the form of trajectories of the grain in the air flow. It allows calculating their trajectories, which differ in windage coefficients and determine the rational values of the parameters of pneumo-gravity and pneumo-inertia separators. Using the obtained dependencies for the development of air separators contributes to determine the initial speed of entry and the direction of entry of the kernels into the airflow, as well as to determine the trajectories of material movement in the air channels with the bottom unloading of material.

Keywords: airflow, weevil, Zhukovsky and Magnus forces, trajectory, separation process, pneumatic separator.

Introduction

Solving the problem of dividing multicomponent grain material into separate fractions for a specific purpose (seeds, marketable grain, fodder) at the stage of primary grain processing will reduce the number and productivity of machines for secondary and special processing of conditioned grain. A promising direction for increasing the efficiency of post-harvest processing of grain in grain producers is the use of pneumatic separation machines at the first stage, the functioning of which does not depend on the initial moisture content of the grain. However, in production conditions, the separation efficiency of grain material ranges from 30 to 60 %, depending on the processing stage. The conducted research identified recommendations for the design, selection of parameters, and modes of operation of pneumatic separation channels. Nevertheless, further improvement of the quality of separation of the components of grain material (CPM) is complicated by not solving the issues of reducing the negative impact on the efficiency of separation of the irregularities of the air flow velocity fields along the width of the vertical and the height of the horizontal channels. The equalization of the velocity field with corrugated lamellar grids (at the inlet or outlet of the channel) ambiguously affects the separation efficiency and requires additional maintenance. Recently, pneumatic separators with dampers with adjustable opening angle have appeared (generators of a cascade of air jets). Establishing the optimal velocity profile for vertical and horizontal channels is the essence of the research to improve the separation efficiency of the CPM, which consists in the need to determine the influence of an artificially created velocity profile on the value of the divergence of trajectories and to determine the rational profile of the air flow velocity field in the channels.

The main conceptual provisions of the pneumatic separation of CPM into fractions during the primary processing of grain are reflected in [1]. Recent works [2–9] provide the implementation of ways to improve the efficiency of functioning and the quality of separation in air channels. To improve the separation of materials in a horizontal channel, authors of the work [2] propose to feed grain through a vertical air channel. In [3], the material is fed into the vertical channel through a multilevel cascade of guide chutes, which reduces the interaction between the grains at the entrance to the channel. Kyurchev and Kolodiy [4], for the first time, determined the separation of the CPM in the lower zone of the vertical pneumatic channel and proved the

possibility of fractionation in the vertical channel with the lower gathering of the kernels. Kharchenko and Borshch [5] used a vertical pneumatic channel with a periodically varying cross-sectional area along the height to increase the efficiency. For the first time, scientists of works [6, 7] identified the efficiency of changing the flow rate along with the height of an inclined pneumatic duct and adjusting the average air velocity in the duct. However, in the mathematical description of the movement of the weevil, they used a model with a uniform flow. At the same time, Rogovskii et al. [8] used a model of the movement of a weevil in a vertical channel with a logarithmic distribution of air velocity and assumed a decrease in the divergence of trajectories due to the unevenness of the field of air velocities. Stepanenko et al. and Rogovskii et al. [9, 10] investigated the movement of caryopses in vertical and horizontal channels with a change in the air velocity toward its movement and determined an increase in the efficiency of separation of the CPM. Nevertheless, they did not consider the effect of additional, so-called lateral (transverse) forces caused by the unevenness of the air flow velocity field. The influence of the action of lateral forces in the vertical and horizontal pneumatic separation channels is reflected in works [11–13] and the negative influence (reduction of the divergence of trajectories) of the action of lateral forces of the Magnus and Zhukovsky type is shown. Concurrently, separate studies carried out by calculating the trajectories of movement with arbitrary forms of describing the field of velocities of air flows in the channels of pneumatic separators showed the possibility of improving the quality of separation with a certain configuration of the air velocity diagram. Stepanenko et al. [13] published some data from these studies.

We formulate a mathematical description of the CPM movement in pneumatic channels with an artificially generated air velocity distribution in the channel cross-section to improve the quality of separation (differences in trajectories) of the CPM.

Experimental

Since the design features of technical means for pneumatic separation are not considered, an analytical method for studying fractionation processes by constructing a mathematical description for calculating the trajectories of the CPM and their subsequent analysis has been chosen.

Results and Discussion

Studies on the processes of separation of grain in air channels [14, 15] found that the efficiency of separation of grain material largely depends on the uniformity of the air flow in the channel. The uniformity of the flow in the air channels is characterized by the field of the flow velocity, which can be described by semi-empirical dependences. The power law of distribution is most widely used in the form of the expression [16]:

$$\upsilon(x) = \upsilon_{\max} \cdot \left[\frac{x}{b}\right]^{\frac{1}{n}}, \tag{1}$$

where $\upsilon_{\max}$ — time-variable air velocity in the center of the channel; b — half the distance between the walls of the channel; x — distance from the point under consideration to the channel wall; n — coefficient depending on the Reynolds number Re [n=7–10 at Re=2,3(10^3…10^5)].

Or a more accurate logarithmic dependence of A. Altshul [17]:

$$\frac{\upsilon(x)}{\upsilon_{\max}} = \left[1 - 2\frac{\lg\left[\frac{b}{x}\right]}{\frac{0{,}975}{\sqrt{\lambda}} + 1{,}35}\right]; \tag{2}$$

where λ — channel resistance coefficient.

The presence of an air velocity gradient in the channels causes the appearance of lateral forces [18] of the Zhukovsky type (lifting force $\overline{F}_Z$) and Magnus type (Magnus effect — $\overline{F}_M$). The action of these $\overline{F}_Z$ and $\overline{F}_M$ are directed normally to the vector of the relative flow velocity $\bar{u}$. In this case, the direction of the action of the force $\overline{F}_Z$ is directed towards an increase in the value of the air velocity in the channel section (i.e., towards the channel axis); the vector of force $\overline{F}_M$ in the direction of that side of the grain where the

vector of the air flow velocity $\overline{V}_p(x)$ coincides with the direction of rotation of the grain (with the angular velocity $\overline{\omega}$ [19]).

Thus, the force $\overline{F}_Z$ deflects the weevil in the process of its movement to the central part of the channel, where the air velocity is the greatest. The direction of action of the lateral force $\overline{F}_M$ depends on the direction of rotation of the grain: If the grain starts to rotate clockwise when leaving the feeder, then it will deviate from the centerline to the (right) wall, if the direction of rotation is opposite, the grain will deviate from the wall (right) to the channel axis. In the absence of an air velocity gradient or grain rotation, the lateral forces do not act on it; $\overline{F}_M = \overline{F}_Z = 0$. Therefore, the uniformity of the air flow rate contributes to an increase in the separation efficiency of the CPM. As the center of pressure of the air flow does not coincide with the center of gravity, a moment of aerodynamic force acts on the caryopsis and it rotates in the flow during the movement. The caryopsis differs from the shape of the ball, therefore, when turning, it changes the area of the honey section, and the resistance force, because of which the components of the reaction of the air flow appear in the horizontal plane and the trajectory of its movement becomes a spatial curve [20].

With a uniform field of air flow velocities, a further increase in the quality of CPM separation is achieved by changing the air speed in the channels in the direction of its movement, which is highlighted in [8, 9].

Since the action and direction of lateral forces to a certain extent depend on the shape of the air velocity distribution curve and, accordingly, the modulus and vector of the velocity gradient, the magnitude and direction of the action of these forces can be directed to improve the quality of the SCM separation by artificially forming the required field of air velocities in the channels.

Let us consider the process of movement of the CPM in uneven air flows with predetermined shapes of the air velocity diagram in the plane of the Cartesian rectangular coordinate system HOU under generally accepted simplifying assumptions [10–13].

Using the model of the force interaction of the CPM with an uneven air flow, we write the differential equations of the grain motion in vector form:

$$m\frac{dV}{dt} = \overline{R} + \overline{G} + \overline{F}_M(\omega) + \overline{F}_Z, \tag{3}$$

$$I\frac{d\omega}{dt} = M, \tag{4}$$

where $\overline{G} = mg$ – gravity; $\overline{R} = -mk_V\overline{u}^2(t)$ – aerodynamic drag force; $\overline{F}_Z = \frac{4}{3}\pi\rho r^2 grad V(x)\overline{u}$ – Zhukovsky's strength; $\overline{F}_M(\omega) = \frac{16}{3}\pi\rho r^3\omega\overline{u}$ – the strength of Magnus; $\overline{u} = \overline{V}_p(x) - \overline{V}$ – relative speed (flow velocity); I — moment of inertia; $m = \frac{\pi d_e^3}{6}\rho_g$ – the mass of the weevil; $d_e = 2r$ — equivalent grain diameter; ρ, ρ_g – the density of the air and the matter of the weevil, respectively; $\overline{V}$ — weevil speed; $\overline{V}_p(x)$ — air speed.

Projecting equation (3) on the XOU axis will have a system of differential equations of grain motion in coordinate form:

$$\begin{cases} m\dfrac{dV_x}{dt} = -R\sin\beta \pm \overline{F}_{Z(x)}\cos\beta \pm \overline{F}_{M(x)}\cos\beta \\ m\dfrac{dV_y}{dt} = mg - R\cos\beta \pm \overline{F}_{Z(y)}\sin\beta \pm \overline{F}_{M(y)}\sin\beta \end{cases} \tag{5}$$

where $V_x = \dfrac{dx}{dt}$; $V_y = \dfrac{dy}{dt}$; $\sin\beta = \dfrac{V_x \pm V_p(x)}{u}$; $\cos\beta = \dfrac{V_y \pm V_p(x)}{u}$; $u = \sqrt{\left(V_x \pm V_p(x)\right)^2 + \left(V_y \pm V_p(x)\right)^2}$;

u — the relative speed of the caryopsis in the stream (the speed of the flow around the caryopsis through the air);

β — the angle between the absolute velocity vector and the 0X axis.

The equations of system (5) are written in a general form in the presence of two air flows $V_p(x)$, each of which (horizontal or vertical) can be used separately.

Let us consider the process of movement of the CPM in the horizontal channel of the simplest "winnower" separator Figure 1.

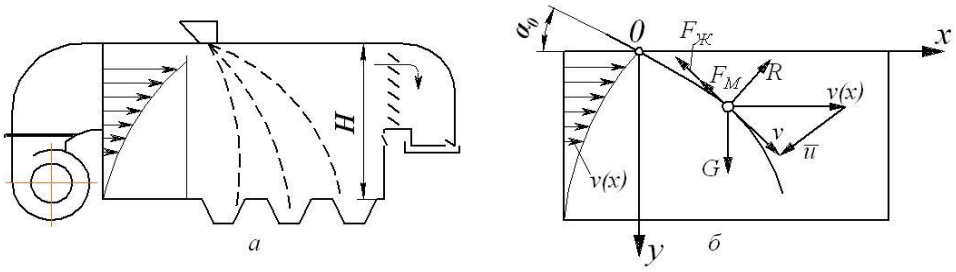

Figure 1. Scheme of the separator (a) and the force interaction of the weevil with an uneven air flow (b)

Without resorting to the details of the technical possibilities of forming a diagram of air velocities in a horizontal channel, we will accept the exponential dependence of the change in air velocity along the height of the channel:

$$V(y) = V_{\max} e^{-ky}, \tag{6}$$

It approximately characterizes the distribution of air velocity at the outlet of the centrifugal fan.

The air velocity gradient will have the opposite sign compared to the power-law distribution (1), namely:

$$grad V(x) = -kV_{\max 1} e^{-ky}, \tag{7}$$

where $V_{\max 1}$ — air velocity in the area of the upper wall of the channel.

In this case, the forces $\overline{F}_M$ and $\overline{F}_Z$ with a conventionally specified direction of rotation, directed in the direction of counteraction to motor grains, which should increase the time of its stay in the separation chamber (channel).

Projection $\overline{F}_M$ and $\overline{F}_Z$ on the coordinate axis are determined by the following dependencies:

$$\overline{F}_{Z(x)} = -\frac{4}{3}\pi\rho r^3 k V_{\max 1} e^{-ky}\left[V_{\max 1} e^{-ky} - \frac{dx}{dt}\right], \tag{8}$$

$$\overline{F}_{M(x)} = -\frac{8}{3}\pi\rho r^3 \omega(t)\left[V_{\max 1} e^{-ky} - \frac{dx}{dt}\right], \tag{9}$$

$$\overline{F}_{Z(y)} = \frac{4}{3}\pi\rho r^3 k V_{\max 1} e^{-ky}\left[\frac{dy}{dt}\right], \tag{10}$$

$$\overline{F}_{M(y)} = -\frac{8}{3}\pi\rho r^3 \omega(t)\left[\frac{dy}{dt}\right], \tag{11}$$

Substituting the values of certain components into equation (5), we get:

$$\frac{d^2x(t)}{dt^2} = k_V\left[v(y) - \frac{dx(t)}{dt}\right]\sqrt{\left[v(y) - \frac{dx(t)}{dt}\right]^2 + \left[\frac{dy(t)}{dt}\right]^2} - \frac{\left[\overline{F}_{Z(x)} + \overline{F}_{M(x)}\right]}{m}\frac{\frac{dy(t)}{dt}}{\sqrt{\left[v(y) - \frac{dx(t)}{dt}\right]^2 + \left[\frac{dy(t)}{dt}\right]^2}} \tag{12}$$

$$\frac{d^2y(t)}{dt^2} = g - k_V\left[\frac{dy(t)}{dt}\right]\sqrt{\left[v(y)-\frac{dx(t)}{dt}\right]^2+\left[\frac{dy(t)}{dt}\right]^2} - \\ -\frac{\left[\overline{F}_{Z(x)}+\overline{F}_{M(x)}\right]}{m}\frac{\left[v(y)-\frac{dx(t)}{dt}\right]}{\sqrt{\left[v(y)-\frac{dx(t)}{dt}\right]^2+\left[\frac{dy(t)}{dt}\right]^2}} \quad (13)$$

To close the system, we define the dependence $\omega(t)$:

$$I\frac{\omega(t)}{dt} = 2{,}3\pi\rho r^3\frac{h-y}{h-r}\left[\left[V_{\max}e^{-ky}-\frac{dx(t)}{dt}\right]\right], \quad (14)$$

and write the initial conditions:

$$t=0;\ \ x=0;\ \ y=0;\ \ \frac{dx(t)}{dt}=V_0\cos\alpha_0;\ \ \frac{dy(t)}{dt}=V_0\sin\alpha_0;\ \ \omega=\omega_0. \quad (15)$$

The solution of the system of equations (12)–(14) under the initial conditions (15) was calculated in the Mathcad computer environment in the form of the trajectory of the grain with different values of the hovering speed and, accordingly, the mass (Figure 2).

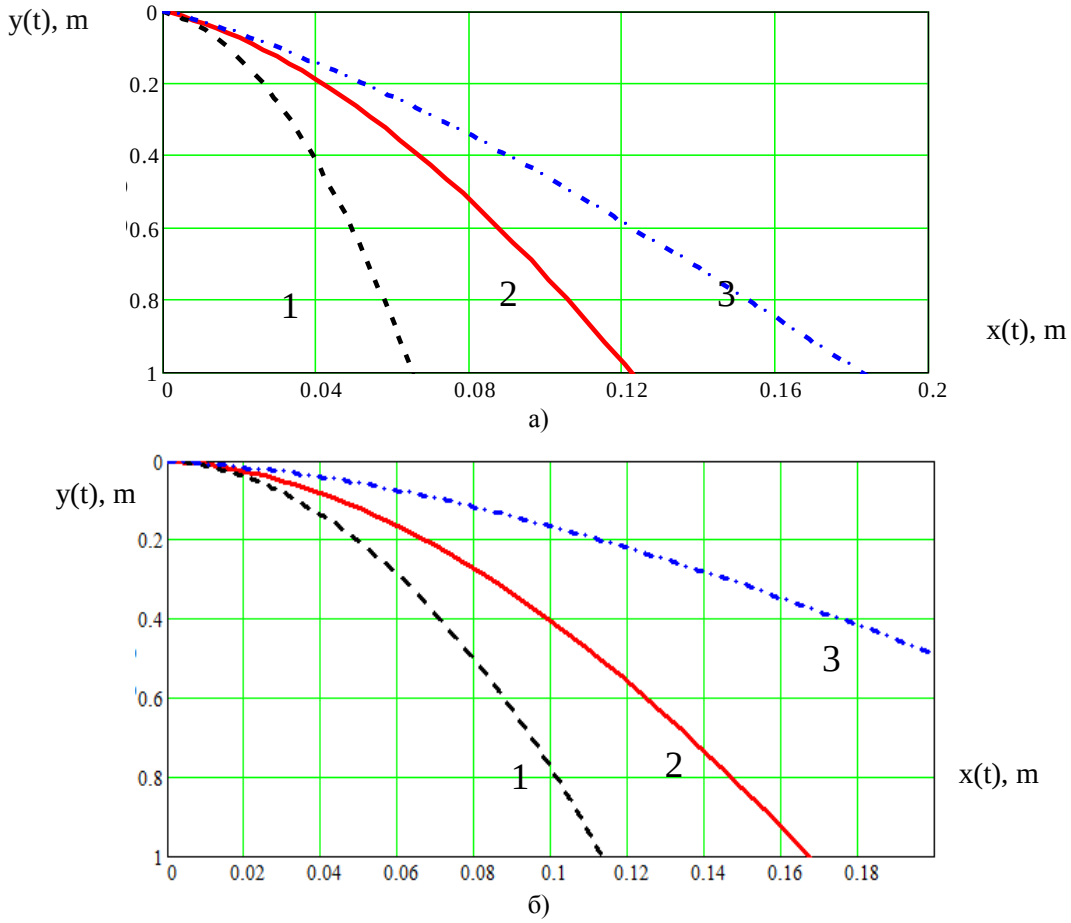

1–3, respectively $k_V = 0{,}139;\ 0{,}184;\ 0{,}392;$

Figure 2. Trajectory of movement of caryopses in a horizontal channel with uniform (a) and exponential distribution of air velocity along the height of the channel (b)

Comparing the resulting dependencies $y(x)$, it can be noted that changing the air velocity diagram in the channel contributes to increase in the divergence of the trajectories and, accordingly, in the efficiency of separating the grain material into fractions.

A promising direction for improving the quality of the separation of grain material into fractions in a horizontal flow is the use of inertial forces when the grain moves against the direction of the air flow. In this case, the speed of air flow around the caryopsis increases when entering the channel and the resistance force.

An increase in the air velocity in the zone of grain entry into the channel by changing the air velocity diagram increases both the resistance forces R and strengths $\overline{F}_M$, $\overline{F}_Z$, which will act as "lifting".

Figure 3 presents the diagram of the pneumo-inertial separator and the force interaction of the weevil with the air flow.

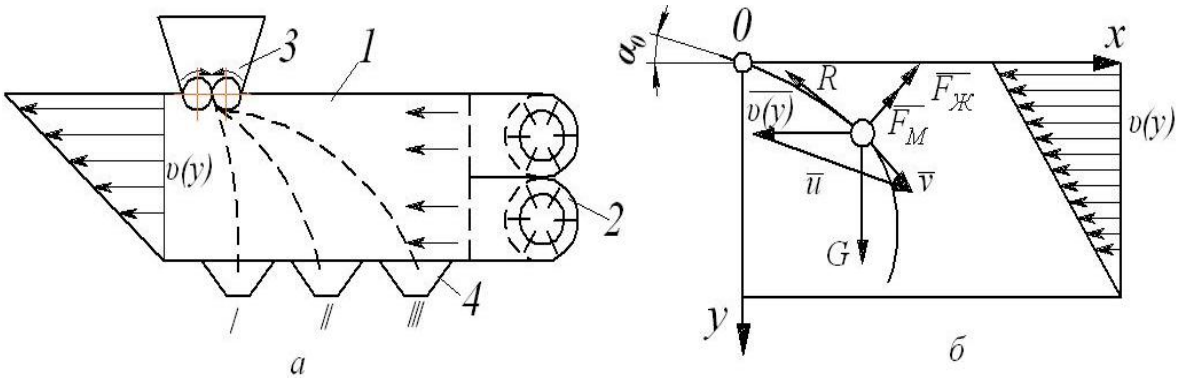

1 — pneumatic channel, 2 — fans, 3 — feed rollers, 4 — collectors of fractions.

Figure 3. Scheme of a pneumo-inertial separator (a) and the force interaction of a weevil with an air flow (b)

Let us assume a linear distribution of the air flow rate along the channel height:

$$v(y) = V_{\max} - by(t) \tag{16}$$

The system of differential equations for the movement of a grain in a horizontal uneven flow with a countercurrent feed of material in coordinate form will look like:

$$\begin{cases} m\dfrac{d^2x(t)}{dt^2} = -R\dfrac{\left[v(y)+\dfrac{dx(t)}{dt}\right]}{u} + F_{Z(x)}\dfrac{\left[\dfrac{dy(t)}{dt}\right]}{u} + F_{M(x)}\dfrac{\left[\dfrac{dy(t)}{dt}\right]}{u} \\ m\dfrac{d^2y(t)}{dt^2} = mg - R\dfrac{\left[\dfrac{dy(t)}{dt}\right]}{u} - F_{Z(y)}\dfrac{\left[-v(y)+\dfrac{dx(t)}{dt}\right]}{u} - F_{M(y)}\dfrac{\left[-v(y)+\dfrac{dx(t)}{dt}\right]}{u} \end{cases} \tag{17}$$

Where $u = \sqrt{\left[v(y)+\dfrac{dx(t)}{dt}\right]^2 + \left[\dfrac{dx(t)}{dt}\right]^2}$, $R = k_V m u^2$.

Force projections $F_{Z(x,y)}$ and $F_{M(x,y)}$ on the axis of the rectangular coordinate system XOY can be written as:

$$\overline{F}_{Z(x)} = -\frac{4}{3}\pi\rho r^3 b\left[V_{\max} - by - \frac{dx}{dt}\right], \tag{18}$$

$$\overline{F}_{M(x)} = \frac{8}{3}\pi\rho r^3 \omega\left[V_{\max} - by - \frac{dx}{dt}\right], \tag{19}$$

$$\overline{F}_{Z(y)} = -\frac{4}{3}\pi\rho r^3 b\left[\frac{dy}{dt}\right], \tag{20}$$

$$\overline{F}_{M(y)} = \frac{8}{3}\pi\rho r^3 \omega\left[\frac{dy}{dt}\right], \tag{21}$$

Substituting the value of the acting forces in equation (17), we finally get:

$$\frac{d^2x(t)}{dt^2} = \frac{-k_V\left[v(y)+\frac{dx(t)}{dt}\right]}{\sqrt{\left[v(y)+\frac{dx(t)}{dt}\right]^2+\left[\frac{dy(t)}{dt}\right]^2}} + \\ + \frac{\rho}{\rho_g}\left[V_{\max} - by - \frac{dx(t)}{dt}\right](b+2\omega)\frac{\frac{dy(t)}{dt}}{\sqrt{\left[v(y)+\frac{dx(t)}{dt}\right]^2+\left[\frac{dy(t)}{dt}\right]^2}} \tag{22}$$

$$\frac{d^2y(t)}{dt^2} = g - \frac{k_V\left[\frac{dy(t)}{dt}\right]}{\sqrt{\left[v(y)+\frac{dx(t)}{dt}\right]^2+\left[\frac{dy(t)}{dt}\right]^2}} - \\ - \frac{\rho}{\rho_g}\left[\frac{dy(t)}{dt}\right](b+2\omega)\frac{\left[v(y)+\frac{dx(t)}{dt}\right]}{\sqrt{\left[v(y)+\frac{dx(t)}{dt}\right]^2+\left[\frac{dy(t)}{dt}\right]^2}} \tag{23}$$

To close system (22) — (23), it is necessary to have the dependence $\omega = \omega(t)$. In the presence of the initial rotation speed of the weevil ω_0 (which is provided by the rollers of the feeding device (Figure 3a), rotating at different speeds.

The change in the angular velocity of rotation of the caryopsis can be determined from the equation [13]:

$$\frac{d\omega(t)}{dt} = 15\frac{\mu}{\rho r^2}\omega(t) \tag{24}$$

where μ — coefficient of dynamic viscosity of air.

On condition $t = 0;\ \omega = \omega_0;$ the change in the speed of rotation in time is determined by the dependence:

$$\omega(t) = \omega_0 e^{-15\frac{\mu t}{\rho r^2}} \tag{25}$$

To solve the system of equations, the initial conditions are formulated:

$$t = 0;\ x = 0;\ y = 0;\ \frac{dx(t)}{dt} = V_0\cos\alpha_0;\ \frac{dy(t)}{dt} = V_0\sin\alpha_0;\ \omega = \omega_0. \tag{26}$$

V_0 — the rate of introduction of grain material into the pneumatic separation channel.

The system of equations (22)–(24) with the initial conditions (26) was solved in the Mathcad computer environment. The results are presented in the form of the trajectory of movement of individual components of the grain material in Figure 4.

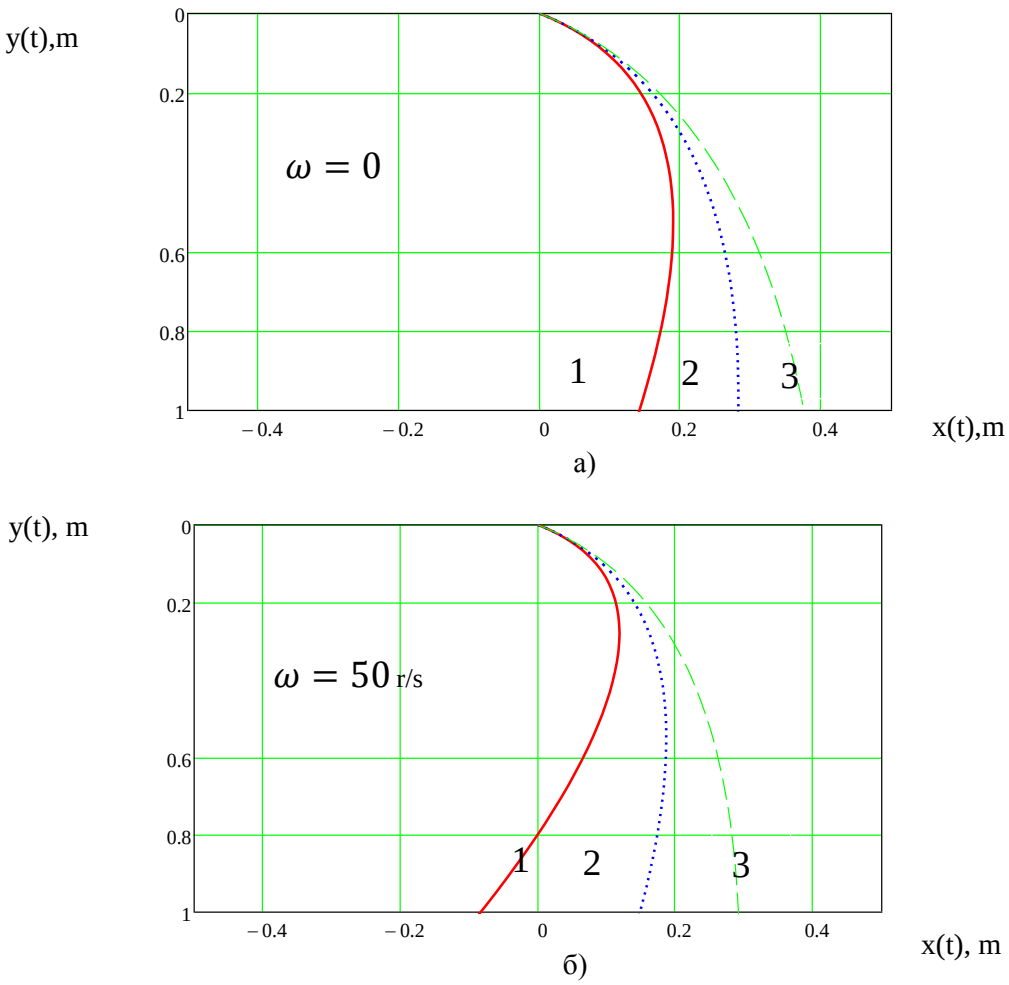

Figure 4. Trajectories of caryopses with different values of windage coefficients

The main disadvantages of vertical pneumatic separation channels of traditional rectangular cross-section, besides significant volumetric unevenness of the air flow rate, stagnant corner zones, are the imperfection of the system for feeding grain into the channel (curved pitched boards, multilevel input), which do not provide: uniform grain distribution, channel; stratification and separation of the grain stream, which in turn, leads to the jet introduction of the grain material into the air stream.

Multiple collisions of grains incorporate the involvement of small fractions in the traces of movement of larger components. As a result, some of the main fractions are carried away, while some of the trash impurities end up in the east of the commercial fractions.

Using cylindrical pneumatic channels with an annular cross-section can significantly improve separating the CPM into fractions. The use of “volumetric” feeders (conical or in the form of surfaces of revolution with a curvilinear generatrix) provides uniform along the perimeter of the channel, the introduction of grain (almost a monolayer) into the air flow, and also eliminates stagnant zones in the channel.

At the same time, it should be noted that the unevenness of the air flow velocity field in the annular channel negatively affects the separation efficiency of the grain material.

Without resorting to the details of the technical implementation of the change in the air flow velocity diagram in the annular channel, let us consider the movement of weevils in an air flow with an artificially formed air velocity irregularity. Diagrams of the pneumatic separation channel and the force interaction of the weevil with the air flow are shown in Figures 5a and 5b, respectively.

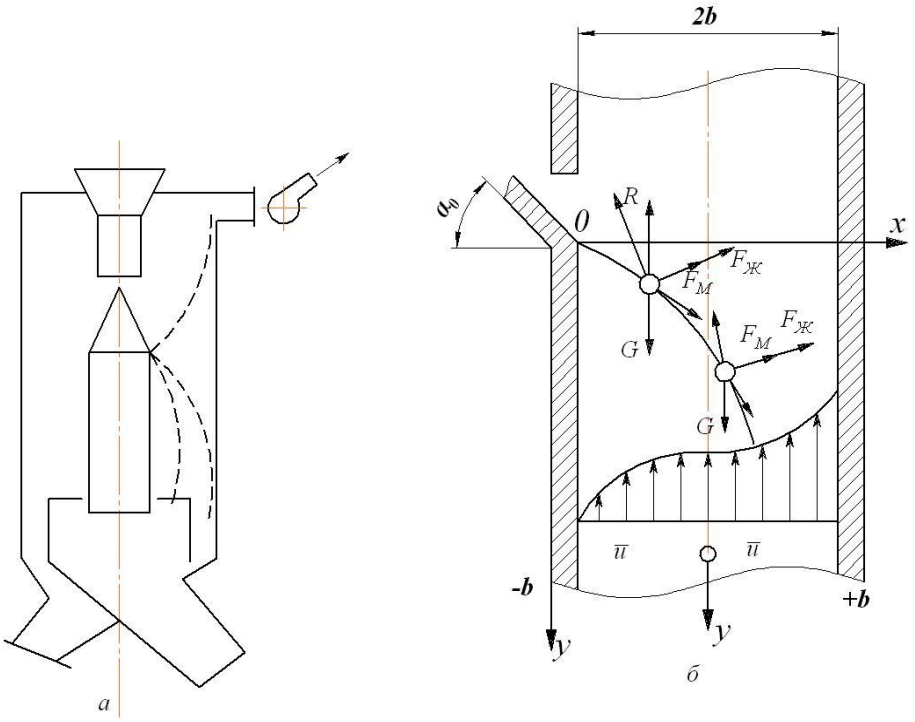

Figure 5. Scheme of a pneumo-gravity separator (a) and the force interaction of a weevil with an air flow (b)

The OS axis conventionally divides the air volume of the channel into two parts (along the axis), in which the average air flow rate is the same.

In the first part, the distribution of air velocity is described by a power law:

$$\upsilon(x) = \upsilon_{\max} \cdot \left[\frac{x}{b}\right]^{\frac{1}{10}} \tag{27}$$

and in the second part, the air velocity distribution is described by the exponential law:

$$\upsilon(x) = \upsilon_{\max} \cdot e^{k_V y} \tag{28}$$

On a weevil in an air channel except for gravity $\overline{G} = mg$, and aerodynamic resistance $R = k_V m u^2(t) = k_V m\left[V_p(x) - v(x)\right]^2$, lateral (deflecting) forces act $F_{Z(x,y)}$ and $F_{M(x,y)}$.

The equation for the dynamics of the movement of a weevil in a vertical irregular flow in the coordinate form will be as follows:

$$\begin{cases} \dfrac{d^2x(t)}{dt^2} = -k_V\left[V_p(x) - v(x)\right]^2 \cos\alpha + \dfrac{F_{Z(x)} + F_{M(x)}}{m}\sin\alpha \\ \dfrac{d^2y(t)}{dt^2} = g\sin\alpha + k_V\left[V_p(x) - v(x)\right]^2 \sin\alpha + \dfrac{F_{Z(y)} + F_{M(y)}}{m}\cos\alpha \end{cases} \tag{29}$$

From the analysis of the interaction of the forces acting on the grain and the equations of motion (29), it follows that the lateral forces $F_{Z(x,y)}$ and $F_{M(x,y)}$ deflect grains of different mass and windage in one direction throughout the entire time of movement in the channel. Moreover, one can see from the equations that less mass lateral forces have a greater effect on caryopses with a smaller mass and a less effect on caryopses of a larger mass, which contributes to the divergence of the trajectories of movement of caryopses of different fractions.

The projections of the forces acting on the weevil are determined by analogy with the previous study in the following form:

- Within the channel (- b…0):

$$\overline{F}_{Z(x)1} = \frac{4}{3}\pi\rho r^3 \frac{[V_{\max 1}]}{10b^{0,1}x^{0,9}}\left[\frac{dx(t)}{dt}\right], \tag{30}$$

$$\overline{F}_{M(x)1} = \frac{8}{3}\pi\rho r^3\omega(t)\left[\frac{dx(t)}{dt}\right],$$

$$\overline{F}_{Z(y)1} = \frac{4}{3}\pi\rho r^3 \frac{[V_{\max 1}]}{10b^{0,1}x^{0,9}}\left[[V_{\max 1}]\left[\frac{x}{b}\right]^{0,1} - \frac{dy(t)}{dt}\right], \tag{31}$$

$$\overline{F}_{M(y)1} = \frac{8}{3}\pi\rho r^3\omega(t)\left[[V_{\max 1}]\left[\frac{x}{b}\right]^{0,1} - \frac{dy(t)}{dt}\right],$$

- Within the channel (0…+b):

$$\overline{F}_{Z(x)2} = \frac{4}{3}\pi\rho r^3 k_V V_{\max 1} e^{k_V x}\left[\frac{dx}{dt}\right],$$

$$\overline{F}_{M(x)2} = \frac{8}{3}\pi\rho r^3\omega(t)\left[\frac{dx}{dt}\right],$$

$$\overline{F}_{Z(y)2} = \frac{4}{3}\pi\rho r^3 k_V V_{\max 1} e^{k_V y}\left[V_{\max 1} e^{k_V y} - \frac{dy(t)}{dt}\right], \tag{32}$$

$$\overline{F}_{M(y)2} = \frac{8}{3}\pi\rho r^3\omega(t)\left[V_{\max 1} e^{k_V y} - \frac{dy(t)}{dt}\right],$$

Initial conditions:

$$t = 0;\ \ x = -b;\ \ y = 0;\ \ \frac{dx(t)}{dt} = v_0\cos\alpha_0;\ \ \frac{dy(t)}{dt} = v_0\sin\alpha_0; \tag{33}$$

Limiting conditions:

$$\text{at} \le 0;\ \ F_{Z(x,y)}; F_{M(x,y)} = F_{Z(x,y)1}; F_{M(x,y)1} \tag{34}$$

at $\ge 0;\ \ F_{Z(x,y)}; F_{M(x,y)} = F_{Z(x,y)2}; F_{M(x,y)2}$

The solution of equations (28)–(29), taking into account (30)–(31) under the initial conditions (32) and limiting conditions (33), was obtained in the Mathcad computer environment by means of the trajectories of the caryopses in a uniform air flow (Fig. 6a) and with an artificially formed velocity field (Fig. 6b).

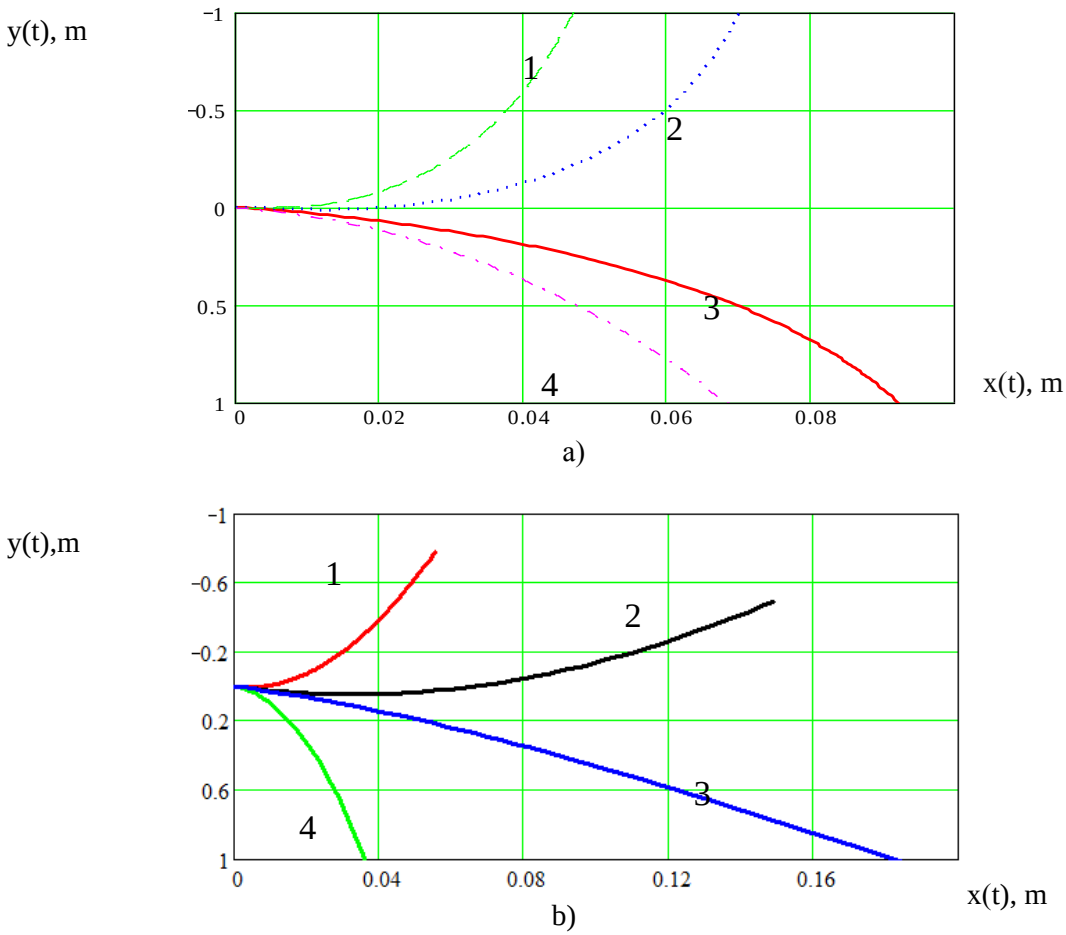

1–4, respectively $k_V = 0{,}4$; 0, 27; 0,159; 0,08

Figure 6. Trajectories of caryopsis movement in a uniform air flow
(a) and with an artificially formed velocity field (b)

As can be determined from the obtained graphical dependencies, the value of the divergence of the trajectories can be significantly increased using a rational configuration of the velocity diagram in the channel cross-section.

A further increase in the efficiency of separating caryopses according to aerodynamic properties can be achieved by distributing the air flow velocity along the channel height, namely by increasing the air velocity in the direction of its movement. For example, when the air speed (average by volumetric flow rate) changes according to a linear law:

$$V_{\max} = a - by$$

where $a = 12$, $b = 1{,}8$.

The shape of the trajectories and the magnitude of their difference change significantly, i.e., separation efficiency of CPM.

Figure 6 shows the trajectories of movement of grains of four fractions of grain material at various parameters of the air velocity diagram in the vertical section of the channel, indicating the real possibility of separating grain material into fractions in a pneumo-gravity separator.

Let us also consider the process of separating grain material into fractions in an inclined pneumatic separating channel described in [10, 12, 19–22]. Technologically, with vertical loading, the inclined channel operates in a counter-current mode and it can be considered as a pneumo-inertial separator (Figure 7), in which the inclined channel is located at an angle α to the horizon with plane-parallel walls. The air velocity along the channel height is distributed exponentially and is determined by relationship (6).

Using the model of a quasi-horizontal channel [11, 13], when the movement of the weevil is considered in a rotated α rectangular coordinate system XOУ.

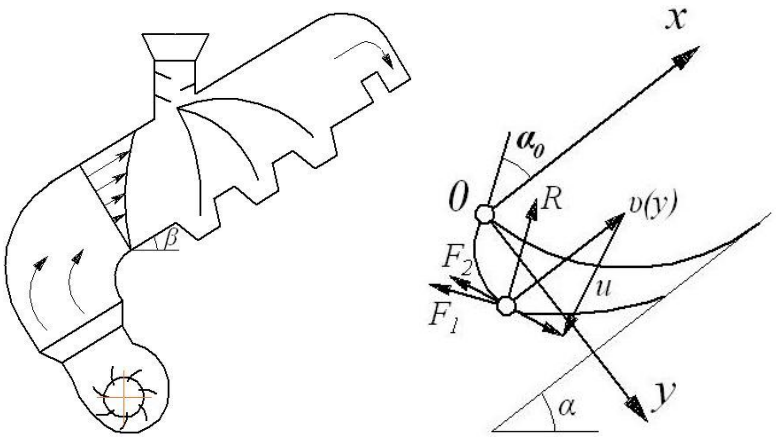

Figure 7. Diagram of an inclined pneumatic separation channel (a) and calculated scheme of action of forces (b)

In this case, we use the system of differential equations (5) in the following form:

$$\begin{cases} m\dfrac{dV_x}{dt} = R\sin\alpha - \left[F_{Z(x)} + F_{M(x)}\right]\cos\alpha - mg\sin\alpha \\ m\dfrac{dV_y}{dt} = mg\cos\alpha - R\cos\alpha - \left[F_{Z(y)} + F_{M(y)}\right]\sin\alpha \end{cases} \quad (35)$$

where $\sin\alpha = \dfrac{\dfrac{dy}{dt}}{u}$; $\cos\alpha = \dfrac{\dfrac{dy}{dt} + \dfrac{dx}{dt}}{u}$; $u = \sqrt{\left[\dfrac{dy}{dt} + \dfrac{dx}{dt}\right]^2 + \left[\dfrac{dy}{dt}\right]^2}$;

Lateral forces are determined from Eqs. (8) — (11) by replacing in (10) and (11) the sign in front of the derivative $\dfrac{dx}{dt}$ to the opposite.

Conclusions

1. The regularities of the movement of the caryopsis were theoretically investigated and established in the form of mathematical models of the dynamics of the movement of a solid caryopsis in air flow, which differs from the known ones by considering the action of lateral forces, the concentration of the material. The use of a power-law and artificially formed exponential law of air distribution made it possible to increase the discrepancy (splitting) trajectories of caryopses by 20 %.

2. The system of nonlinear differential equations with initial conditions was solved in the Mathcad software environment in the form of trajectories of the weevil in the air flow, which allows calculating their trajectories that differ in windage coefficients and determine the rational values of pneumo-gravitational and pneumo-inertial parameters.

References

1 Stepanenko S. Research pneumatic gravity separation grain materials. / *S.* Stepanenko // Agricultural Machinery, 2017. – Vol. 2. – P. 143–145.

2 Nesterenko A.V. Analytical assessment of the pneumatic separation quality in the process of grain multilayer feeding. / A.V. Nesterenko, S.M. Leshchenko, O.M. Vasylkovskyi, D.I. Petrenko // *INMATEH*-Agricultural Engineering, 2017. – Vol. 53, Iss. 3. – P. 65–70.

3 Giyevsk A.M. The application of the finite-volume method for solving the equations of hydrodynamics to substantiate certain parameters of the pneumatic system of grain cleaning machines. / A.M. Giyevsk, V.I. Orobinsky, V.A. Gulevsky, A.V. Chernyshov // Bulletin of Agrarian Science, 2017. – No. 5. – P. 65–73.

4 Кюрчев С.В. Багатокритеріальний аналіз існуючих насіннєвих сепараторів з різними робочими пристроями / С.В. Кюрчев, А.С. Колодий // Вісн. Харків. нац. техн. ун-ту сіль. господ. — 2015. — № 156 (1). — С. 86–92.

5 Харченко С. О моделировании процесса сепарации псевдоожиженной зерновой смеси на воздухопроницаемой наклонной плоскости типа «чешуйчатого» решета / С. Харченко, Ю. Борщ // Motoriz. Power Ind. Agric. — 2014. — № 16. — С. 17–23.

6 Aliev E. Modelling of mechanical and technological processes of the agricultural industry. / E. Aliev; V. Bandura; V. Pryshliak; V. Yaropu, O. Trukhanska // INMATEH-Agricultural Engineering, 2018. – Vol. 54. – P. 95–104.

7 Aliev E. Research on sunflower seeds separation by airflow. / E. Aliev; V. Yaropud; V. Dudin; V. Pryshliak; N. Pryshliak V. Ivlev // INMATEH-Agricultural Engineering, 2018. – Vol.56, No. 3. – P. 119–128.

8 Rogovskii I.L.The mathematical modeling of changes in grain moisture and heat loss on adsorption drying from parameters of grain dryer. / I.L. Rogovskii, S.P. Stepanenko, A.V. Novitskii, V.I. Rebenko // IOP Conference Series: Earth and Environmental Science 548 (2020) 082057, 2021. – Vol. 13. – P. 1–7.

9 Stepanenko S.P. Pneumonitis fractionation of grain materials in air streams of variable structure. / S.P. Stepanenko, B.I. Kotov // Machinery & Energetics. Journal of Rural Production Research. Kyiv. Ukraine, 2020. – Vol. 11, No. 1. – P. 127–132.

10 Rogovskii I. Experimental study of the process of grain cleaning in a vibro-pneumatic resistant separator with passive weeders. / I. Rogovskii , L. Titova, V.Trokhaniak , O. Trokhaniak , S. Stepanenko // Bulletin of the Transilvania University of Brasov, Series II: Forestry, Wood Industry, Agricultural Food Engineering, 2020. – Vol. 13(62), No. 1. – P. 117–128.

11 Leshchenko, S.M. Raising efficiency of pre-treatment of grain mixtures. / S.M. Leshchenko, A.N. Vasilkovsky, M.I. Vasilkovsky, V.V. Goncharov // INMATEH-Agricultural Machinery, Lutsk, 2019. – P. 230–234.

12 Kroulik M. Pneumatic conveying characteristics of seeds in a vertical ascending airstream. / M. Kroulik, J. Hula, A. Rybka, I. Honzik // Research in Agricultural Engineering, 2016. – Vol. 62(2). – P. 56–63.

13 Stepanenko S.P. Experimental studies on drying conditions of grain crops with high moisture content in low-pressure environment / S.P. Stepanenko, I.L. Rogovskii, L.L. Titova, V.I. Trokhaniak, O.V. Solomka, P.S. Popyk, V.O. Shvidia //INMATEH-Agricultural Engineering, 2019. – Vol. 57, Iss.1. – 141–146 p.

14 Гортинский В.В. Вопросы сепарирования на зерноперерабатывающих предприятиях / В.В. Гортинский, А.Б. Демский, М.А. Борискин. — М.: Колос, 1980. — 304 с.

15 Nwaizu C.C. Characterizing Airflow Paths in Grain Bulks. / C.C. Nwaizu // Master's Thesis, University of Manitoba, Winnipeg, MB, Canada, 2013.

16 Olshanskii V. About motion of grain mixture of variable porosity in the cylindrical sieve of vibrocentrifuge. / V. Olshanskii, A. Olshanskii, S. Kharchenko, F. Kharchenko // TEKA. Commission of Motorization and Energetics in Agriculture, 2016. – Vol.16, No. 3. – P. 31–34.

17 Степаненко С. П. Механіко-технологічне обґрунтування процесів і обладнання безрешітного фракціонування зернових матеріалів: автореф. ... дис. на здобуття наук. ступеня д-ра техн. наук: 05.05.11 — «Машини та засоби механизації...» / С. П. Степаненко. — Глеваха, 2021. — 50 с.

18 Тищенко Л. Моделирование динамики зерносмесей на наклонных воздухопроницаемых поверхностях пневмосепарирующих устройств зерновых сепараторов / Л. Тищенко, С. Харченко, Ю. Борщ // Eng. Nature Manag. — 2014. — С. 61–69.

19 Kuzminskyi R. Mathematical models of geometric sizes of cereal crops' seeds as dependent random variables. / R. Kuzminskyi; S. Kovalishyn; Y. Kovalchyk; R. Sheremeta // Acta Technologica Agriculturae 3, 2018. – P. 100–104.

20 Panasiewicz M. Analysis of the pneumatic separation process of agricultural materials. / M. Panasiewicz // International Agrophysics 1999. – 13(2). – P. 233–239.

21 Stepanenko S.P. Pneumonitis Fractionation of Grain Materials in Air Streams of Variable Structure. / S.P. Stepanenko, B.I. Kotov // TEKA. An International Quarterly Journal on Motorization, Vehicle Operation, Energy Efficiency and Mechanical Engineering. Lublin-Rzeszow, 2018. – Vol. 18, No. 2. – P. 69–74.

22 Badretidinov I. Mathematikcal modelling of the grain material separation in the pneumatic system of the grain cleaning machine. / I. Badretidinov, S. Mudarisov, M. Tuktarov, E. Dick, S. Arslanbekova // Journal of Applied Engineering Science, 2019. – 17(4). – P. 529–534.

С.П. Степаненко, Б.И. Котов, А.В. Спирин, В.Ю. Кучерук

Ауа жылдамдығының жасанды түрде қалыптасқан таралуымен астық материалы компоненттерінің қозғалысының ғылыми негіздері

Мақалада материалды жеткізудің ұтымды формасы мен параметрлерін және астық материалын фракцияларға бөлудің нұсқаларын анықтау үшін арнаның көлденең қимасында ауа жылдамдығын жасанды түрде бөлу арқылы пневматикалық арналардағы астық материалдарының бөлінуін зерттеу қарастырылған. Бізтұмсықтың қозғалыс заңдылықтары теориялық тұрғыдан зерттеліп, қатты бөлшектердің ауа ағынындағы қозғалысының динамикасының математикалық үлгілері түрінде анықталды, олар бүйірлік күштердің әрекетін, материалдың концентрациясын есепке алатындығымен ерекшеленетіні белгілі, сондай–ақ, қуат заңын және ауаның таралуының жасанды түрде қалыптасқан экспоненциалды заңын пайдалану дәннің траекториясының айырмашылығын (бөлінуін) 20% арттыруға мүмкіндік береді. Бастапқы жағдайлары бар сызықты емес дифференциалдық теңдеулер жүйесін шешу Mathcad бағдарламалық ортасында ауа ағынындағы астық траекториялары түрінде жүзеге асырылады, олардың желкенділік коэффициенттерімен ерекшеленетін траекторияларын есептеуге және пневматикалық гравитация және пневматикалық инерциялық сепараторлар параметрлерінің ұтымды мәндерін анықтауға мүмкіндік жасайды. Ауа сепараторларын жасау үшін алынған тәуелділіктерді қолдана отырып, бастапқы кіріс жылдамдығын және ядролардың ауа ағынына кіру бағытын есептеуге, сонымен қатар, материалды төмен босатумен ауа арналарындағы материалдың траекториясын анықтауға болады.

Кілт сөздер: ауа ағыны, бізтұмсық, Жуковский және Магнус күштері, траектория, бөлу процесі, пневматикалық сепаратор.

С.П. Степаненко, Б.И. Котов, А.В. Спирин, В.Ю. Кучерук

Научные основы движения компонентов зернового материала с искусственно сформированным распределением скорости воздуха

В статье рассмотрено исследование разделения зерновых материалов в пневматических каналах с искусственно созданным распределением скорости воздуха в поперечном сечении канала, для определения рациональной формы и параметров подачи материала и вариантов разделения зернового материала на фракции. Закономерности движения долгоносика были теоретически исследованы и установлены в виде математических моделей динамики движения твердой частицы в воздушном потоке, которые отличаются от известных тем, что учитывают действие боковых сил, концентрацию материала, а использование степенного закона и искусственно сформированного экспоненциального закона распределения воздуха позволило увеличить различия (расщепление) траекторий зерновок на 20 %. Решение системы нелинейных дифференциальных уравнений с начальными условиями выполняется в программной среде MathCad в виде траекторий зерна в воздушном потоке, позволяет рассчитать их траектории, различающиеся коэффициентами парусности, и определить рациональные значения параметров пневмогравитационного и пневмоинерционного сепараторов. Используя полученные зависимости для разработки воздушных сепараторов, можно рассчитать начальную скорость входа и направление входа ядер в воздушный поток, а также определить траекторию движения материала в воздушных каналах с нижней разгрузкой материала.

Ключевые слова: воздушный поток, долгоносик, силы Жуковского и Магнуса, траектория, процесс разделения, пневматический сепаратор.

References

1 Stepanenko, S. (2017). Research pneumatic gravity separation grain materials. *Agricultural machinery*, 2, 143–145.

2 Nesterenko, A.V., Leshchenko, S.M., Vasylkovskyi, O.M., & Petrenko, D.I. (2017). Analytical assessment of the pneumatic separation quality in the process of grain multilayer feeding. *INMATEH-Agricultural Engineering*, *53*(3), 65–70.

3 Giyevsk, A.M., Orobinsky, V.I., Gulevsky, V.A., & Chernyshov, A.V. (2017). The application of the finite-volume method for solving the equations of hydrodynamics to substantiate certain parameters of the pneumatic system of grain cleaning machines. *Bulletin of the Agrarian Science*, 5, 65–73.

4 Kyurchev, S.V., & Kolodiy, A.S. (2015). Mnogokriterialnyi analiz sushchestvuiushchikh separatorov semian s razlichnymi rabochimi ustroistvami [Multi-criterion analysis of existing seed separators with different operating devices]. *Vestnik Kharkovskogo natsionalnogo tekhnicheskogo agrarnogo universiteta — Bulletin of Kharkiv National Technical University of Agriculture*, 156 (1), 86–92 [in Ukrainian].

5 Kharchenko, S., & Borshch, Y. (2014). O modelirovanii protsessa separatsii psevdoozhizhennoi zernovoi smesi na vozdukhopronitsaemoi naklonnoi ploskosti tipa «cheshuichatogo» resheta [On modelling the process of separation of a fluidized grain mixture on an air-permeable sloping plane of the "scaly" sieve type]. Motorized Power Industry in Agriculture, 16, 17–23 [in Russian].

6 Aliev, E., Bandura, V., Pryshliak, V., Yaropu, V., & Trukhanska, O. (2018). Modelling of mechanical and technological processes of the agricultural industry. *INMATEH-Agricultural Engineering*, 54, 95–104.

7 Aliev, E., Yaropud, V., Dudin, V., Pryshliak, V., Pryshliak, N., & Ivlev, V. (2018). Research on sunflower seeds separation by airflow. INMATEH-Agricultural Engineering, 56, 119–128.

8 Rogovskii, I.L., Stepanenko, S.P., Novitskii, A.V., & Rebenko, V.I. (2020). The mathematical modeling of changes in grain moisture and heat loss on adsorption drying from parameters of grain dryer. *IOP Conference Series: Earth and Environmental Science*, 548 (082057), 13, 1–7.

9 Stepanenko, S.P., & Kotov, B.I. (2020). Pneumonitis fractionation of grain materials in air streams of variable structure. *Machinery & Energetics. Journal of Rural Production Research*, 11(1), 127–132.

10 Rogovskii, I., Titova, L., Trokhaniak, V., Trokhaniak, O., & Stepanenko, S. (2020). Experimental study of the process of grain cleaning in a vibro-pneumatic resistant separator with passive weeders. *Bulletin of the Transilvania University of Brasov, Series II: Forestry, Wood Industry, Agricultural Food Engineering*, 13(62), 1, 117–128.

11 Leshchenko, S.M., Vasilkovsky, A.N., Vasilkovsky, M.I., & Goncharov, V.V. (2009). Raising efficiency of pre-treatment of grain mixtures. *INMATEH-Agricultural Machinery*, 18, 230–234.

12 Kroulik, M., Hula, J., Rybka, A., & Honzik, I. (2016). Pneumatic conveying characteristics of seeds in a vertical ascending airstream. *Research in Agricultural Engineering*, 62(2), 56–63.

13 Rogovskii, I.L., Titova, L.L., Trokhaniak, V.I., Solomka, O.V., Popyk, P.S., Stepanenko, S.P., & Shvidia, V.O. (2019). Experimental studies on drying conditions of grain crops with high moisture content in low-pressure environment. *INMATEH-Agricultural Engineering*, 57(1), 141–146.

14 Gortinskii, V., Demskii, A., & Boriskin, M.A. (1973). *Voprosy separirovaniia na zernopererabatyvaiushchikh predpriiatiiakh[Separation Processes in Grain Processing Enterprises]*. Moscow: Kolos [in Russian].

15 Nwaizu, C.C. (2013). Characterizing Airflow Paths in Grain Bulks. *Master's Thesis,* Winnipeg.

16 Olshanskii, V., Olshanskii, A., Kharchenko, S., & Kharchenko, F. (2016). About motion of grain mixture of variable porosity in the cylindrical sieve of vibrocentrifuge. *TEKA. Commission of Motorization and Energetics in Agric*ulture, 16 (2), 31–34.

17 Stepanenko, S.P. (2021). Mekhaniko-tekhnologicheskoe obosnovanie protsessov i oborudovaniia reshetchatogo fraktsionirovaniia zernovykh materialov [Mechanical and technological substantiation of processes and equipment of lattice fractionation of grain materials] *Extended abstract of Doctor's thesis.* Glevakha [in Ukrainian].

18 Tischenko, L., Kharchenko, S., & Borshch, Yu. (2014). Modelirovanie dinamiki zernosmesei na naklonnykh vozdukhopronitsaemykh poverkhnostiakh pnevmosepariruiushchikh ustroistv zernovykh separatorov [Modelling the dynamics of grain mixtures on pitched breathable surfaces of pneumatic separating devices of grain separators]. *Eng. Nature Manag*, 2, 61–69 [in Russian].

19 Kuzminskyi, R., Kovalishyn, S., Kovalchyk, Y., & Sheremeta, R. (2018). Mathematical models of geometric sizes of cereal crops' seeds as dependent random variables. *Acta Technologica Agriculturae 3*, 100–104.

20 Panasiewicz, M. (1999). Analysis of the pneumatic separation process of agricultural materials. *International Agrophysics*, 13(2), 233–239.

21 Stepanenko, S.P., & Kotov, B.I. (2018). Pneumonitis Fractionation of Grain Materials in Air Streams of Variable Structure. *TEKA. An International Quarterly Journal on Motorization, Vehicle Operation, Energy Efficiency and Mechanical Engineering*, 18(2), 69–74.

22 Badretidinov, I., Mudarisov, S., Tuktarov, M., Dick, E., & Arslanbekova, S. (2019). Mathematical modelling of the grain material separation in the pneumatic system of the grain cleaning machine. *Journal of Applied Engineering Science*, 17(4), 529–534.

DOI 10.31489/2022PH1/58-65

UDC 533.6.011:536.24

A.Zh. Tleubergenova[*1], N.K. Tanasheva[1], K.M. Shaimerdenova[1], L.L. Minkov[2], A.N. Dyusembaeva[1], S.Zh. Uzbergenova[3]

[1] *Karaganda University of the name of academician E.A. Buketov, Kazakhstan;*
[2] *National Research Tomsk State University, Tomsk, Russia;*
[3] *Sh.Ualikhanov Kokshetau University, Kokshetau, Kazakhstan*
[*]*E-mail: shymkent.a7@mail.ru*

Study of aerodynamic parameters of the sail blade

This article studies the aerodynamic characteristics of a triangular sail blade of various parameters. For this purpose, we made a triangular sail blade with a dynamically changing surface shape. The airflow velocity varied from 3 to 12 m/s. The dependences of the aerodynamic forces of the sail blade on the flow velocity were investigated at various angles of the apex of the triangular blade. The experiments were carried out at different vertices of the angles: 0^0; 30^0; 60^0; 90^0. As a result of the experiment, it was revealed that at the vertex angle $\gamma = 90^0$, the triangular sail blade has optimal aerodynamic parameters. The dependences of the aerodynamic coefficients on the dimensionless angle of attack are obtained. It is found that the optimal number of triangular blades for a wind power plant with sailing blades is 6. It is established that at the angle of attack $\alpha = 0^0$, the maximum value of the middle section of the wind wheel to the streamlined airflow will introduce a decrease in the value of the drag coefficient with an increase in attack α. The analysis of the experiment results on the change in α from the speed of the airflow of the sail blade is carried out. When the blade position changes, drag changes relatively to the airflow. The wind wheel will change its position relative to the stream with an increase in the attack angle. With an angular position change, the area of the middle section of the wind wheel begins to decrease relative to the incoming flow. With a decrease in the middle section of the wind wheel, the drag force decreases, and the drag coefficient decreases accordingly. Thus, the total result of pressure changes on the leeward and windward surfaces of the sail can be represented as one resultant aerodynamic force directed at an angle to the line perpendicular to the wind direction.

Keywords: sail, wind turbine, flow speed, aerodynamic force, wind tunnel T-1-M, attack angle.

Introduction

The wind potential of the area primarily determines the development of the wind energy industry in Kazakhstan. The wind resource of the Republic of Kazakhstan is rich and has no territorial boundaries. Over 50 % of the country's territory has wind with speeds of 3–4 m/s, and in some open areas, one can observe higher wind speeds of 6 m/s and higher.

Foreign and domestic scientists and engineers have developed wind power plants with wind speed limits for starting work. These installations are designed for wind speeds ranging from 5–6 m/s. Based on this, an urgent issue arises in developing and studying wind power plants and their working power elements for low speeds of the air oncoming flow.

One of the representatives of wind power plants for low wind speeds is wind power plants with dynamically variable blade surfaces (a sail); the threshold speed for starting the installation is 3 m/s.

Invention [1] aims to increase the windage of the blades and increase the efficiency of using wind energy. Gandhi et al. [2] investigated the combined operation of solar photovoltaic installations with wind power installations with sail blades. A distinctive feature is that the sail blades are square-shaped.

Ghosh et al. [3] provided the study of the aerodynamic characteristics of a Cretan-type wind turbine, a wind turbine with a horizontal sail-type axis. Ignazio et al. [4] presented the pressure tendencies for different angles of attack of the sail. Finally, He et al. [5] determined the sail model's performance coefficients and the sail's optimal attack angle based on the results of tests in a wind tunnel. Jean-Baptiste [6] gave a detailed overview of various features of leeward sail flow, including the effect of separation bubbles and vortexes at the leading edge.

Blades with a dynamically changing surface shape solve the problem of increasing the wind energy utilization factor with an air incoming airflow with minimal values. The explanation for this is that when the air flows around the oncoming flow, favorable conditions are created, which, in turn, are also close to continuous flow, entailing an increase in the lift coefficient of the blades. For this purpose, the blades have the shape of a triangular sail. During the conversion of the energy of the airflow by the sailing blades into energy con-

venient for use, aerodynamic forces appear. The thrust force, which is part of the aerodynamic forces, contributes to the rotational movement of the wind power plant. The change in the value of the aerodynamic force is influenced by a change in the pressures, namely, a change in dynamic and static pressure when the blades are blown by the wind [7].

The airflow in front of the sail blade is divided into two parts: leeward and windward. The cross-section of the wind flow will be smaller than the cross-section of the initial flow from the wind side, and the speed, respectively, is greater than the actual wind speed. Considering Bernoulli's Law, the atmospheric pressure on the leeward side of the sail can be said to be less than atmospheric pressure. Most of all, the speed will increase in the front part of the sail, where there will be an area of slightest pressure, or, in other words, the most significant vacuum [8].

By similar reasoning, it is easy to establish that on the windward side of the blade, the wind speed will decrease slightly in the area of the front part of the sail. As a result, the static pressure will increase and become higher than the atmospheric pressure, i.e. there will be additional pressure above the existing atmospheric pressure. Thus, the useful work of the sail will be caused by the fact that pressures that differ in magnitude from atmospheric pressure will form on it. Their action is directed perpendicular to the sail fabric, and the value changes depending on the difference in the air flow rate at a given point.

The purpose of this work is to study the aerodynamic forces and their coefficients of the blades in the form of a triangular sail of a wind power plant.

Experimental

The authors of the work conducted laboratory experiments to study the aerodynamic forces of the sail blade. During which, the optimal linear dimensions of the triangular sail were determined. Tests of a sail blade with a movable end were carried out in the T-1-M wind tunnel (laboratory of Aerodynamic measurements), where it was fixed in the working part of the pipe. The values of the airflow velocity varied from 3 to 12 m/s.

In the proposed work, a study was carried out for an optimized blade with a dynamically variable shape, for the subsequent creation of an improved model of a wind turbine with increased efficiency. A distinctive feature is the use of nylon as a sail material.

Nylon has become one of the first synthetic fabrics in the world to be made from polyamide. In appearance, it is similar to silk — it has the same shine and smooth front surface. The fabric is strong and elastic; it is difficult to tear it. Nylon is more elastic, so it easily absorbs overloads caused by changes in wind speed values. Figure 1 illustrates an experimental sail made of nylon.

The main differences between nylon and polyester are:

1. Appearance and tactile sensations. Nylon is smooth to the touch and resembles silk. Polyester has a rough matte surface with a visible weave pattern.

2. Weight. A large nylon canvas weighs little. Polyester is also light, but it is larger than nylon.

3. Water resistance. The water-repellent properties of polyester are several times lower.

Figure 1. Experimental sail sample

According to the theory of aerodynamics, the following indicators influence the drag force and lift:

a) dynamic pressure;

b) area of the sail, m^2;

c) angle of installation of the sail relative to the wind direction;

d) linear dimensions of the sail, its profile, the fullness of the belly, etc.;

e) properties of the sail fabric, i.e. its smoothness, rigidity, ductility, density, etc.;

f) angle of inclination of the sail.

Considering the shape of the sail, it should be noted its elongation, which is directly proportional to the height of the sail H and inversely proportional to the length of the middle chord of its profile l (Figure 2) [9]. For rectangular sails, it is equal to the ratio $\frac{H}{l}$. Also, the elongation is determined by dividing the height of the sail H by its average width for a number of sails, such as guari, triangular, gaff, etc. The average width can be calculated by dividing the area of the sail S by its height H:

$$\text{Elongation} = \frac{H}{\frac{S}{H}} = \frac{H^2}{S} \tag{1}$$

The fullness of the sail, i.e. the belly of the sail is directly proportional to the magnitude of the deflection arrow and inversely proportional to the length of the chord of the sail profile l:

$$\text{Fullness} = \frac{f}{l} \tag{2}$$

The influence of all these factors can be taken into account with some remarks when determining the aerodynamic force according to certain formulas. It is established that two identical sails (in shape, cut, fabric, etc.) differ only in area and work with the same angle of attack, in any winds form aerodynamic forces proportional in magnitude to the dynamic wind pressure and sail area.

Having expressed the factors specified in paragraphs c, d, g, e in terms of the coefficient C, the aerodynamic force generated by the flow of the sail is found through the following formula:

$$F = qSC = 0,0625V_k^2SC \tag{3}$$

Where F is the aerodynamic force in kg, V_k is the wind speed in m/s, S is the windage area in m^2, C is the coefficient of aerodynamic force [7].

The characteristic of the aerodynamic qualities of the sail is the polar, which shows how the coefficient of lift varies depending on the coefficient of drag and angle of attack (Figure 3) [9].

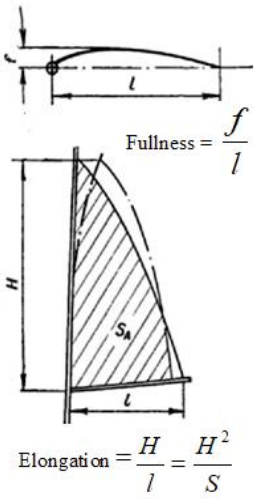

Figure 2. Puffiness and elongation of the sail

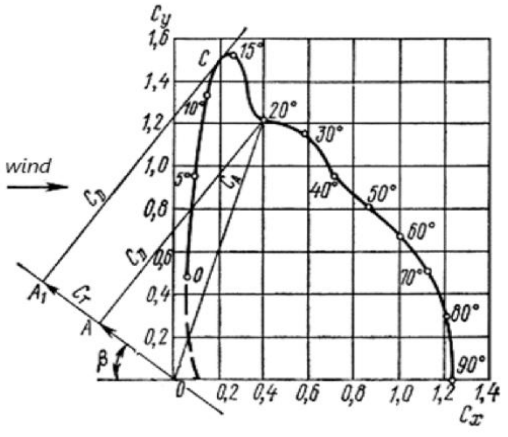

Figure 3. Polar of the sail

The coordinate axes show dimensionless coefficients Cy and Cx, so that this graph can be applied to a sail with any geometric data. The coefficients are calculated by dividing the magnitude of the measured force

by the dynamic wind pressure q, as well as by the windage area S, respectively, the coefficients will be obtained:

$$C_x, C_y \text{ or } C = \frac{X, Y or F}{qS} \quad (4)$$

With a polar, it is possible to determine the lift and drag force values and their components — the thrust force. The sail polarity allows selecting the most favorable angle for setting the sails on a given course in relation to the wind, i.e., the pulling force is at its maximum value.

Results and Discussion

The values of the lifting force obtained for a triangular sail blade with vertices angles γ (0^0; 30^0; 60^0; 90^0) at a speed range from 3 to 12 m/s are represented by the dependence shown in Figure 4. Also, under these conditions, the drag forces were determined (Figure 4).

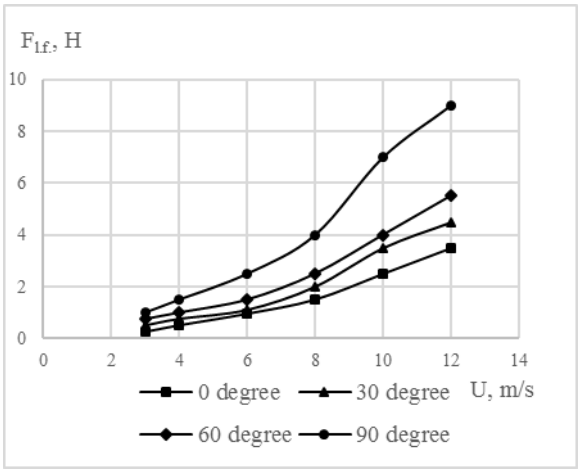

Figure 4. Graph of dependences of the lift forcing of the sail blade on the flow velocity at various angles γ of the apex of the triangular blade

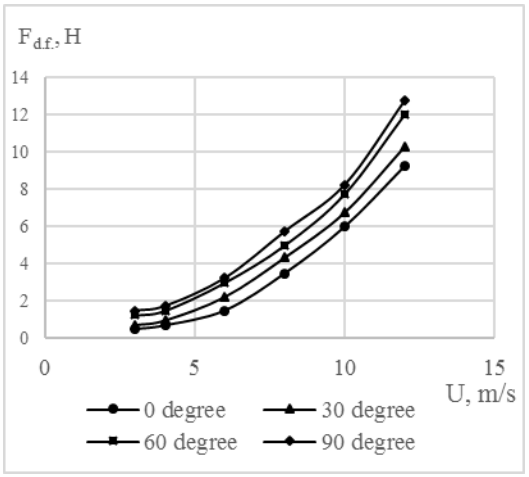

Figure 5. Graph of the dependences of the drag forces of the sail blades on the flow velocity at different angles γ of the apex of the triangular blade

From the obtained dependencies (Figures 4, 5), a proportional dependence of the blades' lift force and drag force on the flow velocity is visible. At the lowest wind speeds from 3 to 5 m/s, the appearance of lifting force is observed at values of about 2 N with a vertex angle of $\gamma = 90^0$, which proves the effectiveness of use for a range of low speeds. In a comparative analysis of the results obtained, it was found that the maximum lifting force has a sail blade with a vertex angle $\gamma = 90^0$.

Thus, a flexible sail blade with an apex angle $\gamma = 90^0$ has optimal aerodynamic characteristics.

The dependence of the change in the drag coefficient on the dimensionless angle of attack β of the wind is constructed, under the condition when the flow velocity was 5 m/s (Figure 6).

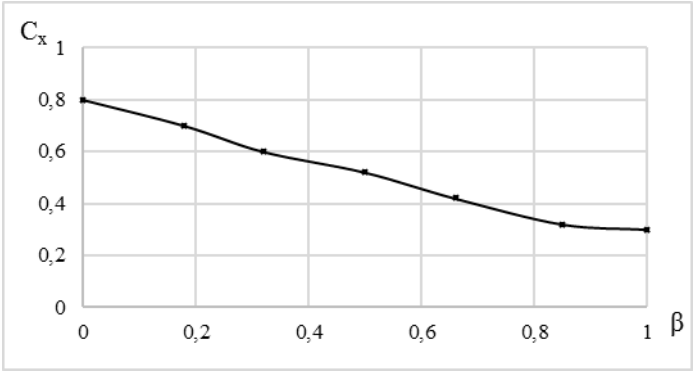

Figure 6. Dependence of the aerodynamic coefficient (drag) from β

One can see from Figure 6, the drag coefficient decreases with increasing β, this phenomenon can be explained as follows: at the attack angle $\beta = 0^0$, the Middle area of the sail blade to the streamlined air flow will be maximum. Accordingly, when the air flows around the sail blade, the resistance force will be maximum. The sail blade will change position in relation to the stream with an increase in the attack angle. With an angular position change, the area of the middle cross-section of the blade begins to decrease relative to the incoming flow. With a decrease in the middle section of the blade, the drag force decreases, and the drag coefficient decreases accordingly.

The dependence of the change in the lift coefficient on the dimensionless angle of attack β of the wind is constructed, under the condition when the flow velocity was 5 m/s (Figure 7).

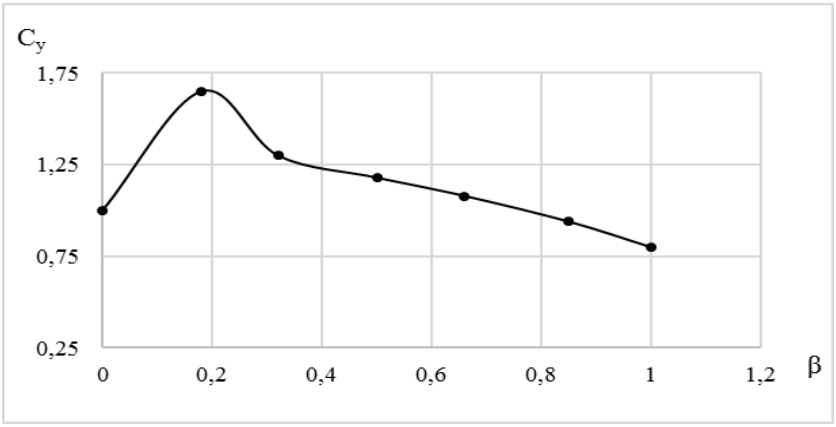

Figure 7. Dependence of the aerodynamic coefficient (lift) from β

Figure 7 demonstrates that up to $\beta = 15^0$, the value of the lift coefficient increases to 1.75, after which a sharp decline is observed. The reason for this is that up to a certain value of the angle of attack, the fullness of the belly of the sail is zero, and the sail bends, thereby increasing the pressure.

With a further increase in β, the streamlined area of the sail will decrease, which entails a decrease in lift.

Figure 8 shows the sail blade polaritites for an airflow velocity of 5 m/s.

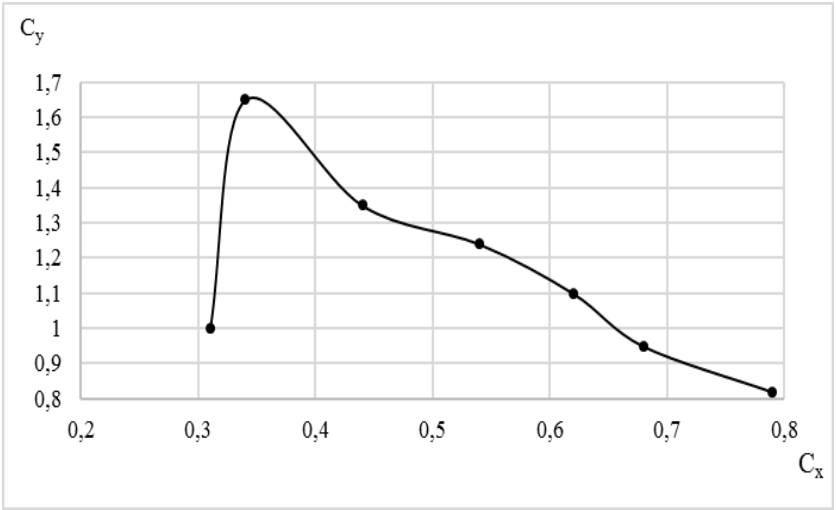

Figure 8. Sail blade polarities

Due to the fact that the ends of the triangular blade are regulated by a flexible attachment, thereby creating a dynamically changing shape of the blade surface, the drag coefficient of the sail of the authors of the work is greater than the sails, the ends of which are rigidly fixed.

Figures 9, 10 designate the dependences of the aerodynamic coefficients on n (the number of blades).

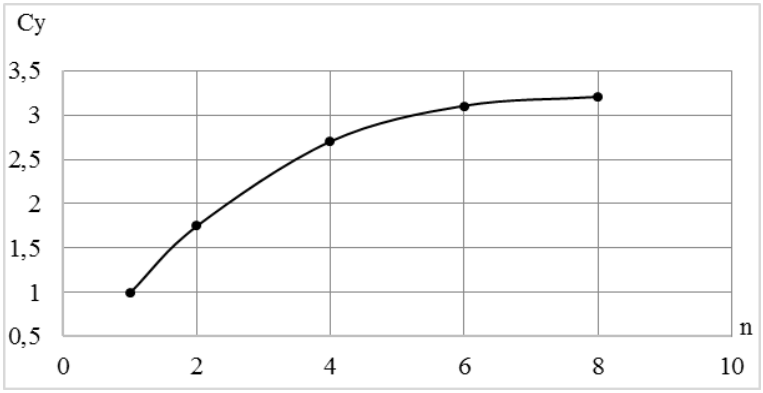

Figure 9. Dependence of the aerodynamic coefficient (lift) from n

From Figure 9, one can notice that the lift coefficient increases with an increase in n from 1 to 6. This phenomenon is observed, although the flow velocity, angle of attack, and area of the wind wheel do not change.

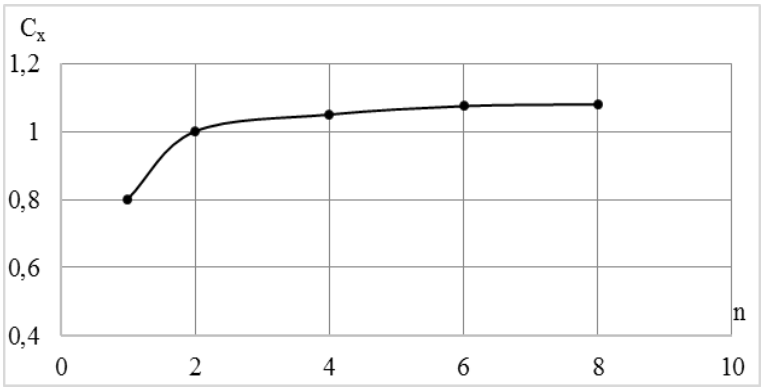

Figure 10. Dependence of the aerodynamic coefficient (drag) on n

Figure 10 represents that when the number of blades reaches 2, there is an intensive increase in the lift coefficient. When the number of blades is further increased to 8, there is a slight increase. Based on this, a further increase in the number of blades is not advisable, because the material consumption and the price of the wind turbine increases.

The task of a sailing wind wheel is to use all available power coming to the swept area. According to Bernoulli's law, when the flow velocity decreases, the pressure increases. As a result, we have increased pressure from the windward side of the wind wheel and discharge from the downwind side. It is the triggering of the energy of this pressure drop that quantifies the operation of the windmill.

From experimental data, it has been established that the optimal number of triangular blades for a wind power plant with sailing shovels is 6. Compared with winged wind turbines [10] for which the optimal number of blades is 3, in which the wind turbine has high performance, increasing the number of blades, a physical phenomenon is observed for them when the wind freely penetrates between the blades to the opposite side of the wind wheel — equalizing the pressure, resulting in reduced productivity. The error in the experiment was 4–5 %, which falls within the acceptable range.

Conclusions

We investigated the aerodynamic coefficients of a sail blade and a wind wheel made of nylon materials. Compared with the results of work [11], where polyester was used as the material of the sail blade, the lifting force of nylon is 15–20 % higher.

During the study, the following optimal results were obtained:

- The aerodynamic forces of the sail blade depend on the flow velocity at different angles of the top. It is established that at $\gamma = 90^0$ the triangular blade has the maximum values of aerodynamic forces, with a decrease in the angle to 0^0 there is a decrease, this is due to an increase in the area of resistance relative to the

air flow. This phenomenon can be explained by the fact that the drag force is directed against the speed of movement, its magnitude is proportional to the characteristic area of resistance. At the optimal angle $\gamma = 90^0$ around the triangular blade, the occurrence of air vortices is minimal, thereby leading to the prevention of disruption of vortices from the ends of the triangular blade.

- With a decrease in the mid-section of the wind wheel, the aerodynamic forces decrease, and their coefficients decrease accordingly. This is due to the fact that the reverse process of reducing the airflow velocity and increasing pressure begin behind the midsection of the sail blade. At the same time, increased pressure is created on the front side of the body, and reduced pressure is created on the backside. The boundary layer flowing around the sail blade, having passed its midsection, breaks away from the sail and, under the influence of reduced pressure behind the body, changes the direction of movement, forming a vortex. This happens both at the upper and lower points of the sail;

- The optimal number of triangular blades for a wind power plant with sailing shovels is 6.

References

1 Патент РФ № 2625080 С1. Ветроэнергетическая установка. Опубл. // Бюлл. — 2017 / Н.П. Дядченко.

2 Gandhi A.R. Design and development of sail type wind turbine with solar panel / A.R. Gandhi, A. Ravinthiran, K. Palanikumar // Materials Today: Proceedings, 2021. – Vol. 46. — Part 9. – P. 3989–3992. https://doi.org/10.1016/j.matpr.2021.02.527

3 Ghosh P. Experimental Investigations on Sail Type Wind-Turbines / P. Ghosh, M.A. Kamoji, A.W. Date, S.V. Prabhu // Wind Engineering, 2009. – Vol 33, Iss. 4. https://doi.org/10.1260/030952409789685717

4 Ignazio M.V. Sail aerodynamics: Understanding pressure distributions on upwind sails / M.V., Ignazio, G.J.F. Richard. // Experimental Thermal and Fluid Science, 2011. – Vol. 35, Iss. 8. – P. 1497–1504. https://doi.org/10.1016/j.expthermflusci.2011.06.009

5 He J. Research on sail aerodynamics performance and sail-assisted ship stability / J. He, Y.Hu, J. Juan Tang, Sh. Xue // Journal of Wind Engineering and Industrial Aerodynamics, 2015. – Vol. 146. – P. 81–89.

6 Jean-Baptiste R.G.S. Recent Advances in Numerical and Experimental Downwind Sail Aerodynamics / R.G.S. Jean-Baptiste, A. Abel, M.V. Ignazio // Journal of Sailing Technology, 2019. — Vol. 4 (01). – P. 45–65. https://doi.org/10.5957/jst.2019.4.1.45

7 Tanasheva N.K. Studying the dependence of the aerodynamic characteristics of rotating cylinders on the rake angle of air flow / N.K. Tanasheva, N.N. Shuyushbayeva, E.K. Mussenova // Technical Physics Letters, 2019. — Vol. 44 (9). – P. 787–789.

8 Tanasheva N.K. The study of the aerodynamic coefficients of rotating cylinders/ N.K. Tanasheva, A.N. Dyusembaeva, B.R. Nussupbekov, L.L. Min'kov, Zh.G. Nurgalieva, K.K. Sadenova // Bulletin of the Karaganda University, Physics Series, 2019. — Vol. 2 (94). – P. 108–113.

9 Мархай Ч. Теория плавания под парусами / Ч. Мархай. — М., 1970. — 411 с.

10 Adeyeye K.A. The effect of the number of blades on the efficiency of a wind turbine / K.A. Adeyeye, N. Ljumba, J. Colton // IOP Conference Series: Earth Environmental Science, 2021.

11 Сакипова С.Е. Анализ аэродинамических характеристик и эффективности двух макетов ветротурбины парусного типа / С.Е. Сакипова, Ж.Т. Камбарова, М.М. Тургунов, А.М. Алькенова // Вестн. Караганд. ун-та. Сер. Физика. — 2016. — № 1(81) — С. 62–68.

А.Ж. Тлеубергенова, Н.К. Танашева, К.М. Шаймерденова,
Л.Л. Миньков, А.Н. Дюсембаева, С.Ж. Узбергенова

Желкенді қалақшаның аэродинамикалық параметрлерін зерттеу

Мақалада әртүрлі параметрлердегі үшбұрышты желкенді қалақшаның аэродинамикалық сипаттамалары зерттелген. Осы мақсатта динамикалық өзгеретін беті бар үшбұрышты желкенді қалақша жасалды. Ауа ағынының жылдамдығы 3-тен 12 м/с-қа дейін өзгерді. Үшбұрышты қалақша шыңының әртүрлі бұрыштары кезінде желкенді қалақшаның аэродинамикалық күштерінің ағынның жылдамдығына тәуелділігі зерттелді. Тәжірибелер шыңдардың әртүрлі бұрыштарында жүргізілді: 0^0; 30^0; 60^0; 90^0. Шыңның бұрышы $\gamma=90^0$ кезінде үшбұрышты желкенді қалақша оңтайлы аэродинамикалық параметрлерге ие болатыны айқындалды. Аэродинамикалық коэффициенттердің шабуыл бұрышының өлшемсіз тәуелділігі алынған. Динамикалық өзгеретін бет пішіні бар қалақшалы жел турбинасы үшін қалақшаның оңтайлы саны $n=6$ екендігі анықталды. Шабуылдың $\alpha=0^0$ бұрышы кезінде желдоңғалағының миделдік ауданының максималды мәні ағылатын ауа ағынына α шабуылы артқанда маңдайлық кедергі коэффициенті мәнінің төмендеуіне әкеледі. Желкенді қалақшаның ауа ағынының жылдамдығынан α-ның өзгеруі бойынша тәжірибе нәтижелеріне талдау жүргізілген. Қалақшаның орны өзгерген сайын маңдайлық кедергі ауа ағынына қатысты өзгереді. Желдөңгелегі α мәнінің жоғарылауымен ауа ағынына қатысты өз орнын өзгертеді. Бұл жағдайда бұрыштың орны өзгерген кезде қозғалатын ағынға қатысты желдоңғалағының мидель қимасының азаюы байқалады.

Жел доңғалағының мидель қимасының төмендеуімен маңдайлық кедергі күші төмендей бастайды, сәйкесінше маңдайлық кедергі коэффициенті төмендейді. Осылайша, желкеннің ық жағы және жел жақ беттеріндегі қысымының өзгеруінің жалпы нәтижесін жел бағытының перпендикуляр сызығының кейбір бұрыштарына бағытталған, бір тең әсер ететін аэродинамикалық күш ұсынылуы мүмкін.

Кілт сөздер: желкен, желэнергетикалық қондырғысы, ағынның жылдамдығы, аэродинамикалық күш, Т-1-М аэродинамикалық құбыры, шабуыл бұрышы.

А.Ж. Тлеубергенова, Н.К. Танашева, К.М. Шаймерденова,
Л.Л. Миньков, А.Н. Дюсембаева, С.Ж. Узбергенова

Исследование аэродинамических параметров парусной лопасти

В статье изучены аэродинамические характеристики треугольной парусной лопасти различных параметров. Для данной цели была изготовлена треугольная парусная лопасть с динамически изменяемой формой поверхности. Скорость воздушного потока варьировалась, начиная 3 до 12 м/с. Была исследована зависимость аэродинамических сил парусной лопасти с разными углами вершинами от скорости потока. Эксперименты проведены при различных углах вершинах: 0^0; 30^0; 60^0; 90^0. В результате эксперимента выявлено, что при угле вершине $\gamma=90^0$ треугольная парусная лопасть обладает оптимальными аэродинамическими параметрами. Получены зависимости аэродинамических коэффициентов от безразмерного угла атаки. Обнаружено, что для ветротурбины с парусными лопастями оптимальным числом лопастей является n=6. Установлено, что при угле атаки $\alpha=0^0$ максимальное значение миделево площадь ветроколеса обтекаемому воздушному потоку введет собою к убыванию значения коэффициента лобового сопротивления с увеличением атаки α. Проведен анализ результатов эксперимента по изменению α от скорости воздушного потока парусной лопасти. При изменении положения лопасти лобовое сопротивление меняется относительно воздушного потока. Ветроколесо изменяет свое положение относительно воздушного потока, с увеличением значения α. При этом наблюдается уменьшение площади миделево сечения ветроколеса относительно к набегающему потоку при изменении углового положения. С уменьшением миделево сечения ветроколеса сила лобового сопротивления начинает убавляться, соответственно снижается коэффициент лобового сопротивления. Таким образом, суммарный результат изменения давлений на подветренной и наветренной поверхностях паруса можно представить в виде одной равнодействующей аэродинамической силы, направленной под некоторым углом к линии, перпендикулярной к направлению ветра.

Ключевые слова: парус, ветроэнергетическая установка, скорость потока, аэродинамическая сила, аэродинамическая труба Т-1-М, угол атаки.

References

1 Dyadchenko, N.P. (2017). Patent Rossiiskoi Federatsii № 2625080 C1 [Patent of Russian Federation No. 2625080 C1] [in Russian].

2 Ghandi, A.R, Ravinthiran, A., & Palanikumar, K. (2021). Design and development of sail type wind turbine with solar panel. *Materials Today: Proceedings*, *46*(9), 3989–3992. https://doi.org/10.1016/j.matpr.2021.02.527

3 Ghosh, P., Kamoji, M.A., Date, A.W., & Prabhu, S.V. (2009). Experimental Investigations on Sail Type Wind-Turbines. *Wind Engineering*, *33* (4). https://doi.org/10.1260/030952409789685717

4 Ignazio, M.V, & Richard, G.J.F. (2011). Sail aerodynamics: Understanding pressure distributions on upwind sails. *Experimental Thermal and Fluid Science*, *35*(8), 1497–1504. https://doi.org/10.1016/j.expthermflusci.2011.06.009

5 He, J., Hu, Y., Tang, J.J., & Xue, Sh. (2015). Research on sail aerodynamics performance and sail-assisted ship stability. *Journal of Wind Engineering and Industrial Aerodynamics*, 146, 81–89.

6 Jean-Baptiste, R.G.S., Abel, A., & Ignazio, M.V. (2019). Recent Advances in Numerical and Experimental Downwind Sail Aerodynamics. *Journal of Sailing Technology, 4* (01), 45–65. https://doi.org/10.5957/jst.2019.4.1.45

7 Tanasheva, N.K., Shuyushbayeva, N.N., & Mussenova, E.K (2018). Studying the dependence of the aerodynamic characteristics of rotating cylinders on the rake angle of air flow. *Technical Physics Letters*, 44 (9), 787–789.

8 Tanasheva, N.K., Dyusembaeva, A.N., Nussupbekov, B.R., Min'kov, L.L., Nurgalieva, Zh.G., & Sadenova K.K. (2019). The study of the aerodynamic coefficients of rotating cylinders. *Bulletin of the Karaganda of University-Physics*, 2(94), 108–113.

9 Markhai, Ch. (1970). Teoriia plavaniia pod parusami [Theory of sailing]. Moscow [in Russian].

10 Adeyeye K.A., Ljumba N., & Colton J. (2021). The effect of the number of blades on the efficiency of a wind turbine. IOP Conference Series: Earth Environmental Science.

11 Sakipova, S.E., Kambarova, Zh.T., Turgunov, M.M., & Alkenova, A.M. (2016). Analiz aerodinamicheskikh kharakteristik i effektivnosti dvukh maketov vetroturbiny parusnogo tipa [Analysis of aerodynamic characteristics and efficiency of two models of a sailing-type wind turbine]. *Vestnik Karagandinskogo universiteta. Seriia Fizika — Bulletin of the Karaganda of University-Physics, 1(81)*, 62–68 [in Russian].

DOI 10.31489/2022PH1/66-74

UDC 691.328

Ye.B. Utepov[1,2], A. Aniskin[3], A.S. Tulebekova[1,2], S.B. Akhazhanov[4], Sh.Zh. Zharassov[*1]

[1]L.N. Gumilyov Eurasian National University, Nur-Sultan, Kazakhstan,
[2]CSI Research & Lab, LLP, Nur-Sultan, Kazakhstan;
[3]University North, Varaždin, Croatia;
[4]Karaganda University of the name of academician E.A. Buketov, Kazakhstan
**E-mail: zhshzh95@gmail.com*

Evaluation of the Nurse-Saul method using maturity sensors for concrete strength control

The article presents the results of experimental studies on the strength of concrete grade B25 brand M350 by direct and indirect methods of control. To conduct tests, 17 cylindrical, 15 small, and 2 large cubic specimens were manufactured. 15 cylindrical specimens by 3 pieces were tested for compression in a hydraulic press on 1, 3, 7, 14, and 28 days of curing, and in the remaining two for 28 days the curing temperature was measured in order to obtain the strength-maturity relationship by the method of Nurse-Saul. The curing temperatures of the larger specimens were measured similarly, from which the concrete maturity and strength values on days 1, 3, 7, 14, and 28 were estimated. On the same days, compression tests were carried out on small specimens and by the shock pulse method on large specimens. As a result, the strength gain curves were obtained and calibration dependencies were plotted. The calibration dependencies showed a sufficiently close convergence of the results of the direct method of control (i.e., compression of small specimens) and the Nurse-Saul method of maturity, in contrast to those of the shock pulse method. The determination coefficients of these dependencies amounted to 0.9357 and 0.8965, respectively.

Keywords: maturity method, concrete strength, embedded sensors, compression test, curing temperature, shock-pulse method, calibration dependence.

Introduction

Inspection methods in modern construction increasingly overlap with information technology. Various methods and tools are used to figure out the compliance of the material with the design requirements [1, 2]. One of the frequently used and tested materials is concrete. There are many ways to determine its strength. The methods are regulated by various standards that contain a defined procedure for laboratory tests [3]. Different tools and devices can be used to identify the current and limited properties of concrete [4].

Nowadays, indirect methods of non-destructive concrete strength gain control are more popular than local destructive methods [5]. These methods give quick results and require minimal costs, with the result being made by the laboratory, but the curing time of the concrete requires intermediate solutions to complete the construction in a specified time or sooner than required by the customer [6]. Interim solutions can be formwork removal, structural loading, test scheduling, etc. The methods are based on parameters occurring during the concrete curing process, such as temperature, pressure, current conductivity, shock pulse impact, elastic rebound, plastic deformation, etc. [5].

Many standards of the CIS countries, regulating non-destructive control methods, are based on external influence. While in foreign countries, they practice such standards to determine the strength of internal pa-

rameters, which consider the temperature and curing time of concrete [7]. The method of temperature-strength control is widely used in the USA, Canada, South Africa, and European countries (Table 1).

Table 1

Foreign standards for methods of temperature-strength control of concrete [4]

No.	Standard indication	Name of the standard	Region
1	ASTM C1074	Standard Practice for Estimating Concrete Strength by Maturity Method	USA
2	ASTM C918	Standard Test Method for Measuring Early-Age Compressive Strength and Projecting Later-Age Strength	
3	ACI 318-6.2	Building Code Requirement for Structural Concrete and Commentary	
4	ACI 228.1R	In-place Methods to Estimate Concrete Strength	
5	ACI 306R	Guide to Cold Weather Concreting	
6	AASHTO T 325	Standard Method of Test for Estimating the Strength of Concrete in Transportation Construction by Maturity Tests	
7	CSA A23.1/A23.2	Concrete Materials and Methods of Concrete Construction/Test Methods and Standard Practice for Concrete	Canada
8	NCH 170	Hormigon-Requisitos generals (Concrete- General requirements)	South Africa
9	EN 206–1:2002	Concrete — Part 1: Specification, performance, production and conformity	Europe
10	BS EN 13670	Execution of concrete structures	
11	NEN 5970	Determination of Strength of Fresh Concrete with the Method of Weighted Maturity	
12	ST-NP SRO SSK-04–2013	Temperature and strength control of concrete during the construction of monolithic structures in winter	Russia

The study of temperature and strength control dates back to the 1970s by the American National Bureau of Standards. It was caused by the gradual collapse of a building under construction in Fairfax County, Virginia, which was not without casualties. According to the final inspection report, the problem was early removal of the formwork. The decision to remove the formwork was made 4 days after the concrete was poured, which was based on the average temperature readings [9]. Such cases prompted the American Occupational Safety and Health Administration to develop a standard for monitoring the curing rate over the entire 28-day period. Thus, this method has found use in several other countries, considering the specifics of the construction area and raw materials for concrete.

A good example of a country where the method of temperature-strength control regarding GOST has been developed is Russia. The standard was developed by the nonprofit partnership “Self-regulated Organization of the Union of Construction Companies of the Urals and Siberia”, owned by the Urban Building Code of the Russian Federation [10]. This standard has been in use since 2013. As stated earlier, the specifics of the territory of construction require increased attention. If we compare countries with predominantly hot climates, it is only one temperature range that affects the strength gain, while countries with sharply continental climates also take into account negative temperatures. This point is considered in [11]. The basis for the creation of the standard [10] was the thermal stress state during curing or heat treatment of concrete. The standard has only recently been introduced and not all issues have yet been covered.

The maturity method regulated by the American standard is increasingly being used in the CIS countries as well. The applicability of this approach is already being tested on domestic construction sites [12, 13]. Thus, the authors of this study have developed a measuring complex for wireless temperature monitoring and estimation of the current strength of concrete “BDM-1” [14, 15], which implements the Nurse-Saul method [16]. An important principle of BDM-1 operation is automation of temperature data acquisition since the calculation method requires particular measurements, as well as individual calculation of number and location of maturity sensors, which are reflected in construction feasibility study. To test its performance and to assess the applicability of the standard [16], many tests were carried out in this work, applying different methods.

Based on the aforementioned, this study is aimed at assessing the applicability of the Nurse-Saul maturity method for Kazakhstan construction sites in conjunction with the BDM-1 measuring complex. Thus,

the object of study is the curing temperature and strength of M350 B25 marketable concrete, produced by local manufacturers.

Experimental

The test program in this work was developed to study the process of concrete strength gain in the natural conditions using foreign [16, 17] and domestic standards [18, 19], applying different instrumentation (Table 2).

Table 2

Certified equipment used in the test program

No.	Equipment	No. of the certificate of type approval of measuring instruments	Equipment name
1	IPS-MG4.03	12148	Strength meter of building materials
2	HP-Testing	9885	Hydraulic press
3	BMD-1	3575	Wireless complex for concrete strength monitoring

Ready-mix concrete of grade B25 and brand M350 was tested (Table 3). Concrete of this grade and brand was chosen because of its wide use in the construction market [20].

Table 3

Composition of the tested concrete

No.	Component name	Consumption, kg/m^3
1	Portland cement	390
2	Washed sand	810
3	Crushed stone, fraction 5–20 mm	1080
4	Water	140
5	Chemical additive based on polycarboxylate esters HPS-3	2,73

The selected concrete mixture was used throughout the experiment. The data obtained in laboratory tests can only be used for a given concrete with the same consumable components [17, 21].

17 cylindrical specimens with a diameter and height of 15 cm each were prepared for testing by the method [16] (Fig. 1), of which 15 were tested in compression with a hydraulic press in the laboratory, by 3 specimens at 1, 3, 7, 14, and 28 days [17]. Sensors [22] were immersed in the remaining 2 specimens to measure the curing temperature of the concrete in the specimens at a frequency of 0.5 hours up to 28 days. The purpose of these tests was to derive the "strength-maturity" relationship of the concrete, where maturity is an index of temperature and time, according to the Nurse-Saul method [16, 23, 24]. This ratio was derived as a logarithmic function. It was used to calculate the current strength of concrete in a real structure, assuming the same composition was used.

Figure 1. Cylindrical specimens

The temperature-time factor was determined by the following equation [15]:

$$TTF = \sum(T_a - T_0)\Delta t; \quad (1)$$

where *TTF* — the time-temperature factor at age t (degree-days, degree-hours); Δt — time interval (days, hours); T_a — average concrete temperature during time interval (°C); T_0 — datum temperature, –10 °C.

To simulate a real structure made of the same concrete composition, two large cubic specimens sized 50x50x50 cm were prepared, in which temperature sensors were also immersed (Fig. 2 (a)). From the temperature history measured at a frequency of 0.5 hours, using the same Eq. 1, concrete maturity values (TTF) were calculated. Then, by applying these values to the derived logarithmic function, the strength values of the concrete in the structure on days 1, 3, 7, 14, and 28 of curing were estimated. On the same days, large specimens were subjected to non-destructive shock pulse testing [18] using the IPS-MG4 measuring device (Fig. 2 (b)).

In parallel with the previous tests there were molded 15 small cubic specimens of 10×10×10 cm in size, which were tested in compression by destructive method [19] on a hydraulic press, by 3 specimens on 1, 3, 7, 14, and 28 days of curing (Fig. 2 (c)).

Then, using the average strength values obtained by the three different methods, the diagrams of concrete strength gain and calibration dependencies were plotted.

a) b) c)

Figure 2. Cubic specimens: a — large specimens, b — large specimens shock pulse testing, c — small specimens

Results and Discussion

Figure 3 illustrates the results of testing cylindrical concrete specimens using the maturity method.

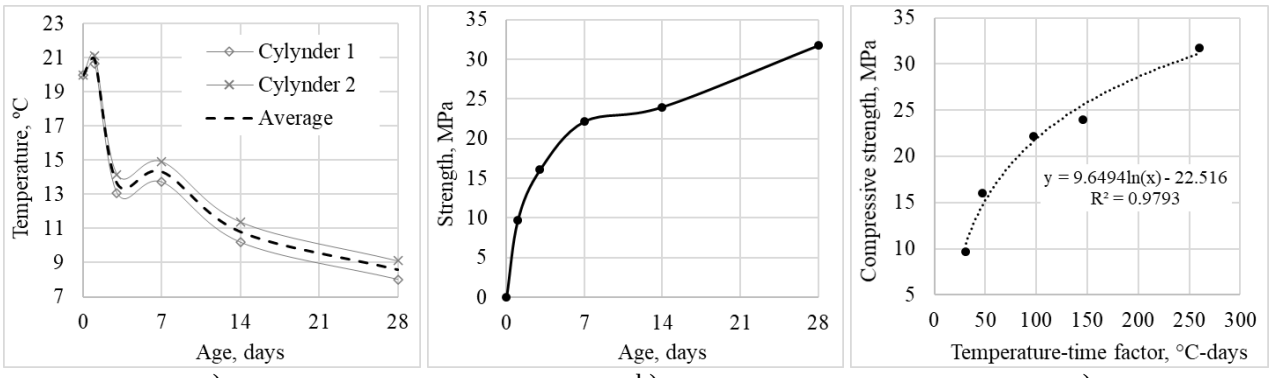

a) b) c)

Figure 3. Results of tests of cylindrical concrete specimens: a — temperature mode of curing, b — concrete strength gain diagram, c — strength-maturity relationship

Using the Nurse-Saul method, the temperature of the two cylindrical specimens was monitored for 28 days. In Fig. 3 (a), one can notice the presence of the highest curing temperature in the first 3 days (21 °C), then, there is a sharp decline with a slight increase in temperature on the 7th day. Thus, the temperature on the 28th day is about 8 °C. Fig. 3 (b) shows a diagram of the strength gain in the cylinders. The trend increases sharply in the first 3 days, after showing a gradual rise. From the cylinder curing temperature history using the equation (1), concrete maturity values at days 1, 3, 7, 14, and 28 were calculated. By plotting these values against the strength values on the same days of curing, a strength-maturity relationship was plotted (Fig. 3

(c)). It can be seen from the Figure 3 that the obtained dependence has a fairly high coefficient of determination equal to 0.9793, which indicates its further applicability in estimating the strength of the real structure (i.e. large cubic specimens) from the same composition of concrete. The test results of the large specimens are shown in Figure 4.

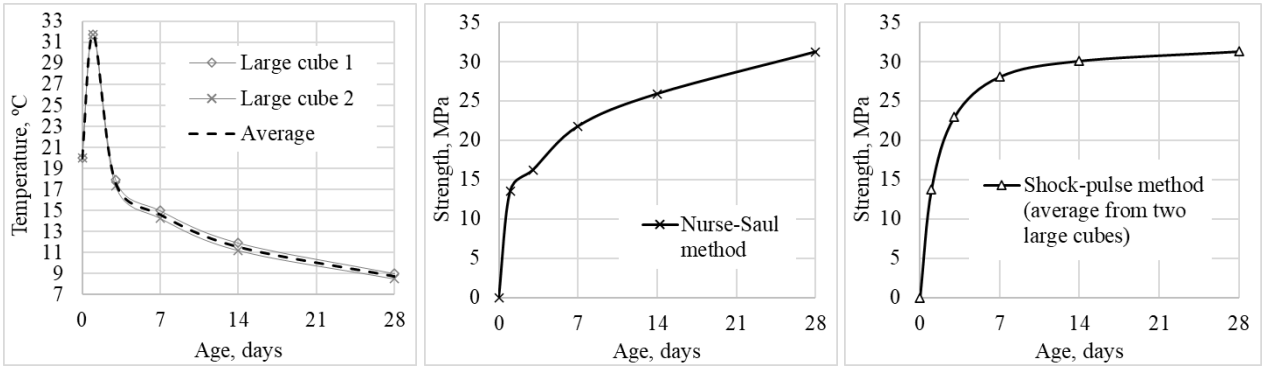

a) b) c)

Figure 4. Results of tests of large cubic concrete specimens: a — temperature mode of curing, b — Nurse-Saul strength gain curve, c — shock-pulse strength gain curve

The curing temperatures (Fig. 4 (a)) of the two large cubes for 28 days provide the average value for the Nurse-Saul strength gain curve (Fig. 4 (b)). As shown in Fig. 4 (a), compared to the curing regime of the cylinders, the temperature increase on the first day of curing of large specimens are more intense. In the first 2 days, the temperature rose to 32 °C and then decreased smoothly to 8 °C. This can be explained by the massiveness of large specimens compared to small ones. Concrete maturity values on 1, 3, 7, 14, and 28 days were calculated in a similar manner for large specimens. By applying these values to the strength-maturity relationship obtained above, the strength values for the same days were estimated, from which the strength gain diagram was plotted (Fig. 4 (b)). According to the results of tests of large specimens by shock-pulse method (Fig. 4 (c)), during the first 7 days, the strength of concrete intensively increased, after that, it smoothly passed to stabilization.

To compare the results of the indirect methods obtained above with the direct ones, a diagram of the strength gain from the tests of small cubic specimens in compression in a hydraulic press was plotted as shown in Figure 5.

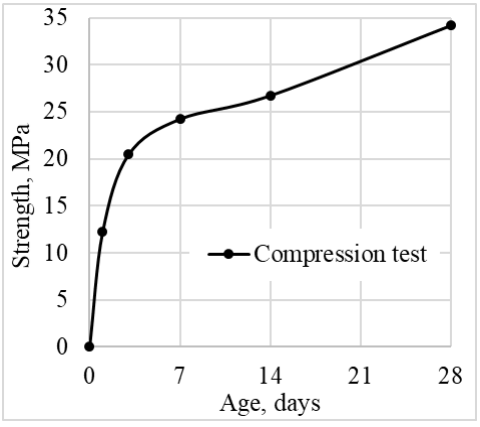

Figure 5. Results of tests of small cubic specimens by compression

The strength gain curve of small cubic specimens has a similar outline to the one obtained by the maturity method. However, the strength value at 28 days is higher. For visual comparison of the results of indirect (maturity method, shock pulse method) and direct (compression of cubic specimens) methods, their strength gain curves were combined into one diagram and calibration dependencies between these methods were derived (Fig. (6)).

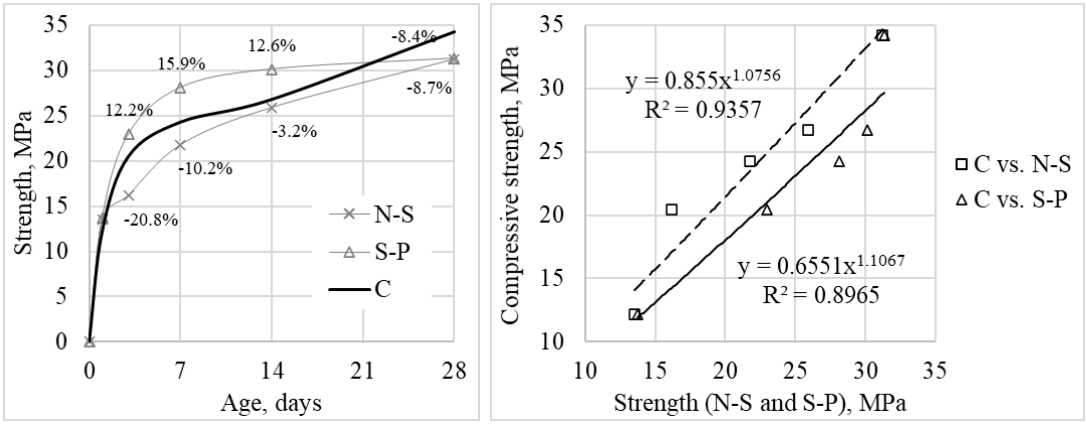

a) b)

Figure 6. Comparative analysis of the results: a — strength gain curves, b — calibration dependencies, N-S, S-P, and C — Nurse-Saul, Shock pulse methods and Compression test, respectively

According to Fig. 6 (a), on the first day, there is no difference between the strength gains, however:

– on days 3, 7, and 14, the shock pulse method values are higher than those of the compression tests by an average of 13.5 %, while on 28 day, they are lower by 8.4 %.

– values from the maturity method beginning from day 3 up to day 28 were lagging the compression test by an average of 10.7 %.

Figure 6 (b) demonstrates the calibration dependencies between the direct and indirect methods used in this study. The power functions and their coefficients of determination were derived for each of the dependencies. One can notice from Figure 6 that the coefficient of determination of the dependence between the compression test and the maturity method, equal to 0.9357, is slightly higher than those between the compression test and the shock pulse method, equal to 0.8965. This indicates that the convergence of the first two methods is greater than that of the second.

Conclusions

In this work, the authors conducted several strength tests of concrete B25 M350 by direct and indirect methods and measurements of curing temperature with specialized instrumentation and equipment. According to the results of tests and measurements, the diagrams of strength gain and temperature curing for small (10x10x10 cm) and large specimens (50x50x50 cm) were obtained, strength-maturity relationships, as well as calibration dependencies between direct and indirect methods, were plotted. The following conclusions can be drawn from the analysis of the obtained results:

- The final compressive strength of the small specimens at 28 days was higher (34 MPa) than that obtained by the maturity and shock pulse methods on large specimens, although all the specimens were kept at the same temperature and humidity conditions. This is due to their lower massiveness.

- The shock pulse method, according to the strength gain curve, looks rather idealized and does not impress sufficient confidence. There are no drops; strength gain is smooth and stable.

- The strength gain curve obtained by the Nurse-Saul maturity method has a fairly realistic outline. There are small steps and unstable gains of strength. The strength values from the Nurse-Saul method were lower than those of the others. In this regard, it can be assumed that it is more reliable and has a potential margin of safety when controlling the strength by this method.

- Comparison of the direct and indirect methods by plotting the calibration dependencies revealed a greater convergence of the maturity method with the compression test in comparison with the shock pulse method; the determination coefficients of the obtained dependencies were 0.9357 and 0.8965, respectively.

Acknowledgments

This research was funded by the Science Committee of the Ministry of Education and Science of the Republic of Kazakhstan (Grant No. AP08052033).

References

1 Liao C. Optimal Inspection Strategies for Labor Inspection in the Construction Industry / C. Liao // Journal of Construction Engineering and Management, 2015. – Vol. 141, Iss. 2. — P. 04014073.

2 Lin J. Understanding On-Site Inspection of Construction Projects Based on Keyword Extraction and Topic Modeling / J. Lin, Z. Hu, J. Li, L. Chen // IEEE Access, 2020. – No. 8. — P. 198503–198517.

3 Andersson N. Industrialization of construction: Implications on standards, business models and project orientation / N. Anderson, J. Lessing // Organization, technology and management in construction: an International Journal, 2020. – Vol. 12, No. 1. — P. 2109–2116.

4 Dovzhenko O.O. Use of extreme properties of deformation for estimation of strength of constructive concrete and reinforced concrete / O.O. Dovzhenko, V.V. Pohribnyi, Ye.V. Klymenko, M. Orešković // NEWS of the Academy of Sciences of the Republic of Kazakhstan, 2020. – Vol. 3, No. 441. — P. 32–39.

5 Malhotra V.M. Handbook on nondestructive testing of concrete / V.M. Malhotra, N.J. Carino. — CRC press. — Boca Raton. — 1991.

6 Zhang H. Building materials in civil engineering / H. Zhang. — Woodhead Publishing Limited. — 2011. — P. 440.

7 Hakan K. Determination of concrete quality with destructive and non-destructive methods / K. Hakan, T. Öztürk // Computers and Concrete, 2015. – Vol. 15, Iss. 3. — P. 473–484.

8 De Carufel S. Concrete Maturity From Theory to Application / S. De Carufel, A. Fahim, P. Ghods., A. Alizadeh. — Giatec Scientific Inc., 2018. — P. 20, 21.

9 Leyendecker E.V. Investigation of the Skyline Plaza Collapse in Fairfax Country, Virginia / E.V. Leyendecker, S.G. Fattal. — Washington D.C. — 1973.

10 СТ-НП СРО ССК-04–2013. Температурно-прочностной контроль бетона при возведении монолитных конструкций в зимний период. — УрСиб. — 2013.

11 Golovnev S.G. Normative regulation for concreting in winter / S.G. Golovnev // Academic Herald, 2014. — No. 2. — P. 70–71.

12 Lukpanov R. Performance of maturity method for estimation of concrete strength based on cubic specimens / R. Lukpanov, Sh. Zharassov, T. Mkilima, A. Aldungarova // Technobius. — 2021. — Vol. 1, No. 4. — P. 0008.

13 Utepov Y. Complex Maturity Method for Estimating the Concrete Strength Based on Curing Temperature, Ambient Temperature and Relative Humidity / Y. Utepov, A. Aniskin, A. Tulebekova, A. Aldungarova, S. Zharassov, A. Sarsembayeva // Applied Sciences, 2021. — Vol. 11, No. 16. — P. 7712.

14 Utepov Y. Prototyping an embedded wireless sensor for monitoring reinforced concrete structures / Y. Utepov, O. Khudaibergenov, Y. Kabdush, A. Kazkeev // Computers and Concrete. — 2019. — No. 24. — P. 95–102.

15 Utepov Ye. Prototyping of a concrete maturity sensor with hermetically sealed housing made of two-component plastic / Ye. Utepov, A. Tulebekova, S. Akhazhanov, Sh. Zharassov, D. Bazarbayev // Bulletin of the Karaganda University, Physics Series, 2021. — Vol. 103. — Issue 3. — P. 60–70.

16 ASTM C1074. Standard Practice for Estimating Concrete Strength by the Maturity Method. — Pennsylvania: ASTM International, 2019.

17 ASTM C192. Standard Practice for Making and Curing Concrete Test Specimens in the Laboratory. — Pennsylvania: ASTM International, 2019.

18 ГОСТ 22690. Определение прочности механическими методами неразрушающего контроля. — М.: Стандартинформ, 2015.

19 ГОСТ 10180. Методы определения прочности по контрольным образцам. — М.: Стандартинформ, 2012.

20 HomeRenovates. Concrete grade M350 class B25. — Retrieved from https://homerenovates.com/en/records/11156.

21 Bassim R. Maturity-Based Estimates of Concrete Strength for Portland Concrete Cement Pavements and Patches at Early Age of Opening to Traffic / R. Basim, M.A. Issa // ACI Materials Journal, 2020. – No. 117. — P. 197–208.

22 Kumarapu K. Thermal Remote Sensing in Early Age Concrete Strength Estimation / K. Kumarapu, M. Shashi, K. Venkata Reddy. — Springer. — Roorkee. — 2020.

23 Zhenchao D. Discussion on the Problem of Standard Deviation of Concrete Strength / D. Zhenchao // ACI Materials Journal, 2020. – No. 117(1). — P. 25–35.

24 Soutsos M. Compressive strength estimates for adiabatically cured concretes with the Modified Nurse-Saul (MNS) maturity function / M. Soutsos, M. Kanavaris // Construction and Building Materials, 2020. – No. 255. — P. 119236.

Е.Б. Утепов, А. Анискин, А.С. Тулебекова, С.Б. Ахажанов, Ш.Ж. Жарасов

Бетонның беріктігін бақылау үшін кемелдену датчиктерін қолдану арқылы Nurse-Saul әдісін бағалау

Мақалада М350 маркалы және В25 класты бетонның беріктігін тікелей және жанама бақылау әдістерімен эксперименттік зерттеулердің нәтижелері келтірілген. Сынақ жүргізу үшін 17 цилиндрлік, 15 шағын және 2 үлкен текше үлгілер дайындалған. Әрқайсысы 3 данадан тұратын 15 цилиндрлік сынама гидравликалық престе сығымдалу үшін қатайтудың 1, 3, 7, 14 және 28-ші күндерінде сыналған, ал қалған 2-уі Nurse-Saul әдісі бойынша «беріктік-кемелдену» тәуелділігін алу мақсатында

қатаю температурасы 28 күн бойы өлшенген. Үлкен үлгілердің қатаю температурасының ұқсас тәсілдері тіркелді, оған сәйкес бетонның жетілу деңгейлері және 1, 3, 7, 14 пен 28-ші күндегі беріктік мәндері есептелді. Сонымен қатар, көрсетілген тәулікте шағын үлгілерді сығуға және үлкен үлгілерді соққы-импульстік әдіспен сынау жүргізілді. Нәтижесінде беріктік қисықтары алынды және градуирлеу тәуелділіктері құрылды. Градуирлеу тәуелділіктері тікелей бақылау әдісі (яғни шағын үлгілерді сығу) нәтижелерінің және Nurse-Saul кемелдену әдісінің соққы-импульстік әдісімен салыстырғанда өте жақын ұқсастығын көрсетті. Осы тәуелділіктерді анықтау коэффициенттері сәйкесінше 0,9357 және 0,8965 болып шықты.

Кілт сөздер: кемелдену әдісі, бетонның беріктігі, кіріктірілген датчиктер, сығымдау сынағы, қатаю температурасы, импульстік–соққы әдісі, градуирлеу тәуелділігі.

Е.Б. Утепов, А. Анискин, А.С. Тулебекова, С.Б. Ахажанов, Ш.Ж. Жарасов

Оценка метода Nurse-Saul с применением датчиков зрелости для контроля прочности бетона

В статье представлены результаты экспериментальных исследований прочности бетона класса В25 марки М350 прямым и косвенным методами контроля. Для проведения испытаний было изготовлено 17 цилиндрических, 15 малых и 2 больших кубических образца. 15 цилиндрических образцов по 3 штуки испытывались на сжатие в гидравлическом прессе на 1, 3, 7, 14 и 28-е сутки твердения, а в 2-х остальных на протяжении 28-и суток измерялась температура твердения с целью получения зависимости «прочность–зрелость» по методу Nurse-Saul. Аналогичным способом фиксировалась температура твердения больших образцов, по которой вычислены уровни зрелости бетона и значения прочности на 1, 3, 7, 14 и 28-е сутки. Кроме того, в указанные сутки проводились испытания на сжатие малых образцов и ударно-импульсным методом больших образцов. В результате были получены кривые набора прочности и построены градуировочные зависимости. Градуировочные зависимости показали достаточно близкую сходимость результатов прямого метода контроля (т.е. сжатие малых образцов) и метода зрелости Nurse-Saul, в сравнении с ударно-импульсным методом. Коэффициенты детерминации данных зависимостей составили 0,9357 и 0,8965 соответственно.

Ключевые слова: метод зрелости, прочность бетона, встраиваемые датчики, испытание на сжатие, температура твердения, ударно-импульсный метод, градуировочная зависимость.

References

1 Liao, C. (2015). Optimal Inspection Strategies for Labor Inspection in the Construction Industry. *Journal of Construction Engineering and Management, 141(2),* 04014073.

2 Lin, J., Hu, Z., Lin, J., & Chen, L. (2020). Understanding On-Site Inspection of Construction Projects Based on Keyword Extraction and Topic Modeling. *IEEE Access, 8,* 198503–198517.

3 Andersson, N., & Lessing, J. (2020). Industrialization of construction: Implications on standards, business models and project orientation. *Organization, technology and management in construction: an International Journal, 12 (1),* 2109–2116.

4 Dovzhenko, O.O., Pohribnyi, V.V., Klymenko, Ye.V., & Orešković, M. (2020). Use of extreme properties of deformation for estimation of strength of constructive concrete and reinforced concrete. *NEWS of the Academy of Sciences of the Republic of Kazakhstan, 3(441),* 32–39.

5 Malhotra, V.M., & Carino, N.J. (1991). Handbook on nondestructive testing of concrete. *CRC press*.

6 Zhang, H. (2011). Building materials in civil engineering. *Woodhead Publishing Limited,* 440.

7 Hakan, K., & Öztürk, T. (2015). Determination of concrete quality with destructive and non-destructive methods. *Computers and Concrete, 15(3),* 473–484.

8 De Carufel, S., Fahim, A., Ghods, P., & Alizadeh, A. (2018). Concrete Maturity From Theory to Application. *Giatec Scientific Inc.*, 20, 21.

9 Leyendecker, E.V., & Fattal, S.G. (1973). Investigation of the Skyline Plaza Collapse in Fairfax Country, Virginia. *Washington D.C.*

10 ST-NP SRO SSK-04–2013. *Temperaturno-prochnostnoi kontrol betona pri vozvedenii monolitnikh konstruktsii v zimnii period* [*Temperature and strength control of concrete during the construction of monolithic structures in winter]* (2013). UrSyb [in Russian].

11 Golovnev, S.G. (2014). Normative regulation for concreting in winter. *Academic Herald, 2*, 70–71.

12 Lukpanov, R. Zharassov, Sh., Mkilima, T., & Aldungarova, A. (2021). Performance of maturity method for estimation of concrete strength based on cubic specimens. *Technobius, 1(4),* 0008.

13 Utepov, Y., Aniskin, A., Tulebekova, A., Aldungarova, A., Zharassov, Sh., & Sarsembayeva, A. (2021). Complex maturity method for estimating the concrete strength based on curing temperature, ambient temperature and relative humidity. *Applied Sciences, 11(16),* 7712.

14 Utepov, Y., Khudaibergenov, O., Kabdush, Y., & Kazkeev, A. (2019). Prototyping an embedded wireless sensor for monitoring reinforced concrete structures. *Computers and Concrete, 24*, 95–102.

15 Utepov, Ye. Tulebekova, A., Akhazhanov, S., Zharassov, Sh., & Bazarbayev, D. (2021). Prototyping of a concrete maturity sensor with hermetically sealed housing made of two-component plastic. *Bulletin of the Karaganda of University-Physics, 103, 3*, 60–70.

16 ASTM C1074. *Standard Practice for Estimating Concrete Strength by the Maturity Method* (2019). Pennsylvania: ASTM International.

17 ASTM C192. *Standard Practice for Making and Curing Concrete Test Specimens in the Laboratory* (2019). Pennsylvania: ASTM International.

18 GOST 22690. Opredelenie prochnosti mekhanicheskimi metodami nerazrushaiushchego kontrolia (2015) [*Determination of strength of concrete by mechanical methods of nondestructive testing]*. Moscow: Standartinform [in Russian].

19 GOST 10180. Metody opredeleniia prochnosti po kontrolnym obraztsam (2012). [*Methods for concrete strength determination using reference specimens]*. Moscow: Standartinform [in Russian].

20 HomeRenovates. Concrete grade M350 class B25. *homerenovates.com*. Retrieved from https://homerenovates.com/en/records/11156.

21 Bassim, R., & Issa, M.A. (2020). Maturity-Based Estimates of Concrete Strength for Portland Concrete Cement Pavements and Patches at Early Age of Opening to Traffic. *ACI Materials Journal, 117*, 197–208.

22 Kumarapu, K., Shashi, M., & Venkata Reddy, K. (2020). Thermal Remote Sensing in Early Age Concrete Strength Estimation, Roorkee. *Springer*.

23 Zhenchao, D. (2020). Discussion on the Problem of Standard Deviation of Concrete Strength. *ACI Materials Journal, 117(1)*, 25–35.

24 Soutsos, M., & Kanavaris, M. (2020). Compressive strength estimates for adiabatically cured concretes with the Modified Nurse-Saul (MNS) maturity function. *Construction and Building Materials, 255*, 119236.

DOI 10.31489/2022PH1/75-80

UDC 621.374: 537.524

A.K. Khassenov*, B.R. Nussupbekov, D.Zh. Karabekova,
G.A. Bulkairova, B.U. Shashubai, M.M. Bolatbekova

Karaganda University of the name of academician E.A. Buketov, Kazakhstan
**E-mail: ayanbergen@mail.ru*

Electric pulse method of processing cullet

The article considers the issue of obtaining a recycling resource during the processing cullet, which harms the environment. During the preparation of raw materials in the household waste recycling stages, the material is crushed to the right size. This is implemented in mills based on various methods of destruction. In this regard, analyses of the currently existing types of mechanical mills were carried out and their disadvantages were investigated. To solve glass recycling problem, this study presents the results of processing cullet by the electric pulse method. We provide a description of operation principle of the experimental setup and the design of the working chamber for processing the material under study. In this technology, the processing cullet is carried out with an increase in the discharge voltage of the storage from 25 kV to 35 kV, the capacitor capacity from 0,25μF to 1 μF, the number of pulse discharges from 100 to 600. By using the electric pulse method particles cullet with an initial fraction of 2 mm and 5 mm were crushed from 1 mm to 0.1 mm. The dependence of the output of the final product on the electrical parameters of the installation and the diameter of the obtained glass powder were received. The results of the grinding raw materials with the formation of pulsed electric discharges in a liquid medium allowed assessing the degree of grinding of the material. According to the obtained research data, optimal parameters of cullet grinding were established.

Keywords: electrohydraulic effect, coal powder, discharge energy, output of finished products, pulsed electrical discharges.

Introduction

In any industry, special attention is paid to the efficient use of natural resources in the production of various building materials. The problem of rational and integrated use of raw materials is closely related to the level of product development and is currently important for all industrialized countries. The creation and implementation of waste-free technologies for more complete use in the production of recycling resources and related products will improve the quality management of raw materials and final products, and reduce waste losses [1].

The cullet is one of those wastes that in natural conditions do not lose their properties for hundreds of years. The raw material is suitable for complete secondary processing with no waste. Cullet of various fractions (1–0.1 mm) is used as an additive to Portland cement and polymers. The average content of crushed glass in the composite material is about 20–50 %. These building materials are highly resistant to weather and are suitable for use as cladding materials. Another advantage of using recycled glass is that it reduces the number of landfills, contributing to reduce carbon dioxide emissions, which is an unwanted byproduct of cement production and the culprit in global warming [1–4].

The stages of processing cullet comprise processes that include crushing and grinding of raw materials. The grinding of raw materials is carried out depending on the purposes and production features of the subsequent use of the material. In these processes, various crushers are used as the main technological installations, and their intensity largely depends on the quality of products produced at the stages of recycling valuable material. The efficiency of the grinding process depends not only on the structure and technical characteristics of devices for obtaining the granulometric composition of glass powder of the required size, but also on the properties of the starting material and the solutions for obtaining the product.

For fine grinding of solids, the following equipment is most widely used [5]:

– ball mills, the productivity of material processing and energy consumption of which depend on the speed of rotation of the drum, the weight and size of the grinding bodies and the concentration of the suspension during wet grinding;

– rod mills, in which the grinding of the material is carried out by crushing, abrasion when rolling the rods in a rotating drum;

– cone crushers, based on crushing the material with the approximation of the gaps between the surfaces of internal movable and external stationary cones;

– drum mills, in which the material is crushed inside the rotating body under the action of grinding bodies or by self-grinding;

– jet mills, in which the material is crushed by feeding a jet of gas from sonic and supersonic injectors.

The above mills have several disadvantages: bulkiness, heavyweight, noise during operation, more complex and expensive design, installation complexity, high dust formation, wear of grinding bodies and contamination by-products of this wear, high energy consumption, and, as a consequence, the high energy intensity of processes [5–7]. The disadvantages of the methods used in glass recycling necessitate cause the use of improved technologies. The electrohydraulic effect can be used in the development and creation of new technologies. The essence of this method is that when carried out inside a volume of liquid in an open or closed vessel, a specially formed pulsed electric discharge is around the zone of its formation, ultra-high hydraulic pressures arise, able to commit useful mechanical work [8]. The electric pulse method finds application in the disintegration of diamond-bearing rocks, the processing of solutions for leaching uranium, the production of finely dispersed waters coal fuel, the disinfection of plant products and liquid raw materials, the descaling of heat exchangers [9–14].

The purpose of the work is to research the influence of electric discharges on the selective grinding of glass waste. We used a household cullet. The initial diameter (d_0) of the material before processing was 2 mm and 5 mm, and the obtained glass powder was d= 0,1–1 mm.

Experimental installation for crushing cullet

The experimental installation consists of a power supply unit providing constant voltage (control panel, generator, capacitors, spark gap) and a working chamber for grinding material in a liquid medium (Figure 1). The working chamber is equipped with a metal cylindrical corpus, which contains a mixture of glass fragments and industrial water (Figure 2). In the working environment, electric pulse discharges are formed between metal electrodes, with the tips of the electrodes arranged in a vertical direction against each other. The electrode (positive), powered by electric current, is fixed on the cover of the working channel made of caprolon, and the second electrode (negative) is placed on the grounded bottom of the metal vessel.

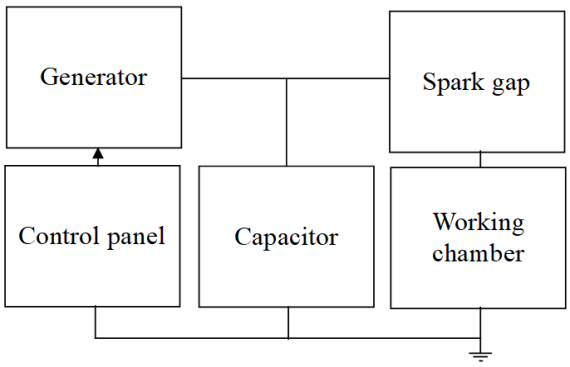

Figure 1. Flowchart of an electric pulse installation

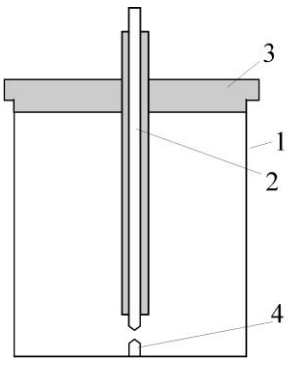

Figure 2. Working chamber: 1 — metal cylindrical corpus,
2 — positive electrode, 3 — working chamber cover, 4 — negative electrode

The installation for the grinding cullet works as follows. After the generator is powered by alternating current from the control unit, the amplified current from the generator accumulates in the capacitor until a value is reached that allows punching the air space between the metal hemispherical electrodes in the arrester. Further, the current in the form of a spark discharge formed in the spark gap is fed through a cable to the positive electrode of the working chamber. In the working chamber, when an electric explosion occurs between the ends of the positive and negative electrodes in a liquid medium, solid bodies are crushed due to shock waves and collisions of materials in them.

Methods of conducting experiments and analysis of the obtained results

The weight of the initial cullet was determined using electronic scales and for each experiment, the mass of the initial material and the volume of liquid was constant (the mass of the cullet was 100 g, the volume of industrial water – 400 ml). After drying at room temperature, the glass crushed by the electric pulse method was sieved through special standard sieves to analyze the granulometric composition of the resulting product. The yield of the required product (K, %) was determined by the ratio of the mass of the obtained product to the mass of the feedstock and was measured as a percentage.

The work on grinding cullet was carried out depending on the different values of energy and the number of pulse discharges (Figure 3). Depending on the parameters of the bank, the pulse discharge energy varied. The discharge voltage of the storage was conversed by changing the gap of the metal electrodes in the spark gap. It was noted that with an increase in the electrical parameters of the installation, the output of the finished product increases.

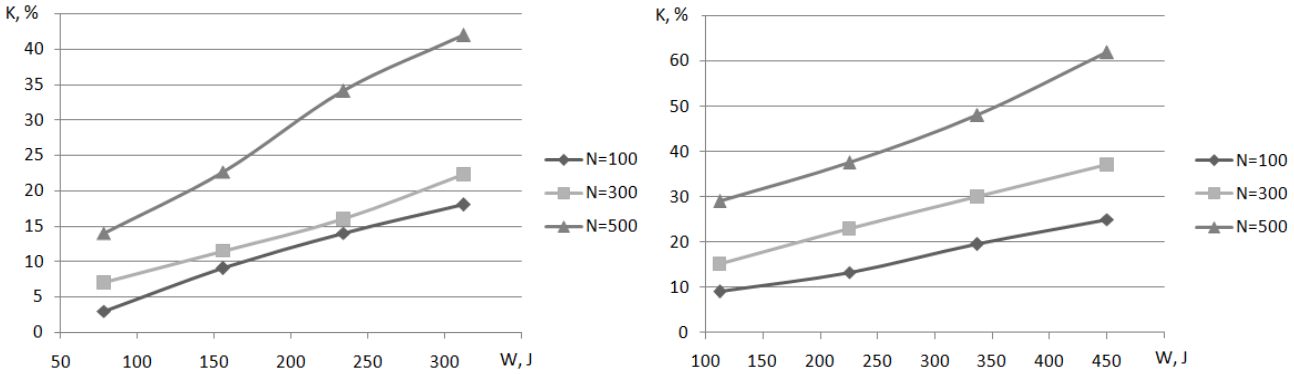

a) d_0=5 mm, d=0.2 mm, C=0.25–1μF; U=25 kV

b) d_0=5 mm, d=0.2 mm, C=0.25–1 μF; U=30 kV

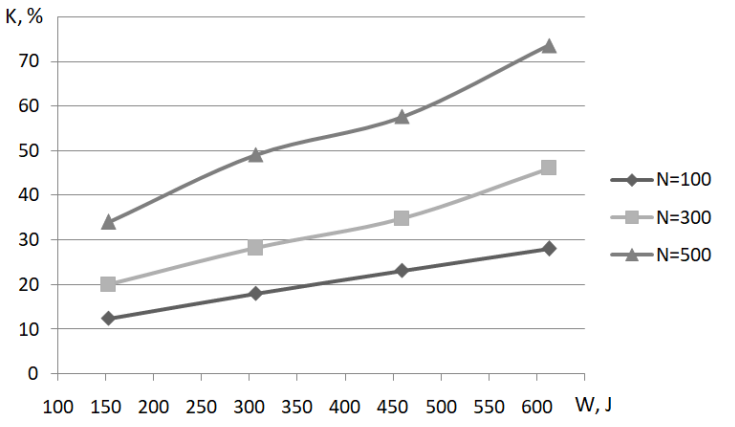

c) d_0=5 mm, d=0.2 mm, C=0.25–1 μF; U=35 kV

Figure 3. Dependence of the output of the finished product (powder diameter 0.2 mm) on the electrical parameters of the electric pulse installation

The following researches were devoted to the analysis of the granulometric composition of the material with a diameter of the initial fraction of 2 mm and 5 mm after electric pulse treatment (Figure 4). The experiment was carried out with the following parameters: storage discharge voltage is 25–35 kV, capacitance of the capacitor is 0,75μF, discharge energy is 237–459,4 J, the number of pulse discharges is 600.

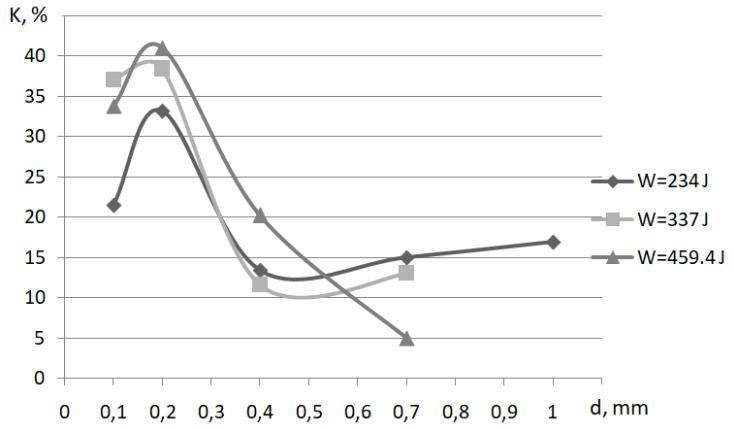

a) d_0=2mm

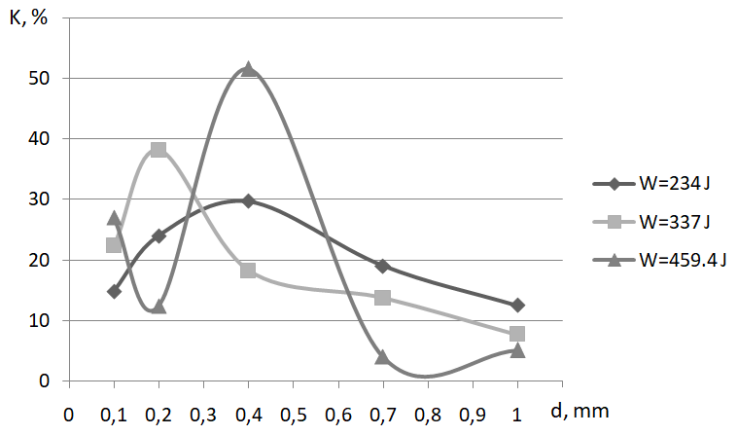

b) d_0=5 mm

Figure4. Dependence of the output of the finished product on the diameter of the obtained glass powder

Figure 4 illustrates that as the discharge energy increased, the number of crushed cullet particles increased in the range from 0,1 mm to 0,4 mm. Thus, under the action of an electric pulse shock in a liquid medium, the granulometric composition of the destruction of glass waste was changed. The conversion of the parameters of pulse discharges into different values made it possible to increase the thin classes in the coarseness of the necessary raw materials.

Conclusions

The results of the experiment showed that the electric pulse method can be used for the disintegration of cullet. Received a powder product with a diameter of 0,1–0,4 mm, used as an additive to Portland cement and polymers. The fractional composition of the material and the degree of the output of final product were regulated by the selection of parameters of pulse discharges. The following values are accepted as effective parameters of pulsed discharges when grinding glass waste: capacitor of the capacity 0,75 μF, storage discharge voltage 30 kV, discharge energy 337 J.

References

1 Павлушкина Т.К. Использование стекольного боя в производстве строительных материалов / Т.К. Павлушкина, Н.Г. Кисиленко // Стекло и керамика. — 2011. — № 5. — С. 27–34.

2 Кетов А.А. Стеклобой как сырье для получения теплоизоляционного материала / А.А. Кетов, Г.Б. Кетова, А.И. Пузанов, И.С. Пузанов, А.С. Россомагина, Д.В. Саулин // Экология и промышленность России. — 2002. — № 8. — С. 17–20.

3 Дворкин Л.И. Строительные материалы из отходов промышленности / Л.И. Дворкин, О.Л. Дворкин. — М.: Феникс, 2007. — С. 368.

4 Shevchenko V.V. ASR effect in glasses used as additives to Portland cement / V.V. Shevchenko // Glass Physics and Chemistry, 2012. — Vol. 38, Iss. 5. — P. 466–471.

5 Еренков О.Ю. Оборудование механических процессов в химической технологии / О.Ю. Еренков, А.П. Богачев. — Хабаровск: Изд-во Тихоокеан. гос. ун-та, 2014. — 80 с.

6 Пузыревская И.А. Обогащение полезных ископаемых / И.А. Пузыревская. — Благовещенск: Изд-во Амур. гос. ун-та, 2014. — 96 с.

7 Massola C.P. A discussion on the measurement of grinding media wear / C.P. Massola, A.P. Chaves, E. Albertin // Journal of Materials Research and Technology, 2016. — Vol. 5, Iss. 3. – P. 282–288.

8 Юткин Л.А. Электрогидравлический эффект и его применение в промышленности / Л.А. Юткин. — Л.: Машиностроение, 1986. — 253 с.

9 Kornev I. Pulsed electric discharge treatment of uranium leaching solutions: A method for accelerated extraction / I. Kornev, G. Osokin, N. Yavorovsky, A. Morozov, V. Litvinenko // Hydrometallurgy, 2016. — Vol. 162. — P. 37–41.

10 Мартынов Н.В. Электрогидравлическая технология дезинтеграции алмазосодержащих пород / Н.В. Мартынов, В.Н. Добромиров, Д.В. Аврамов // Обогащение руд. — 2020. — № 1(385). — С. 8–14.

11 Добромиров В.Н. Технология обеззараживания жидкостей на основе электрогидравлического эффекта / В.Н. Добромиров, Д.В. Аврамов, Н.В. Мартынов // Вода и экология. — 2019. — № 2 (78). — С. 17–23.

12 Evrendilek G.A. Configuring pulsed electric fields to treat seeds: an innovative method of seed disinfection / G.A. Evrendilek, I. Tanasov // Seed science and technology, 2017. — Vol. 45, Iss. 1. — P. 72–80.

13 Nussupbekov B.R. Coal pulverization by electric pulse method for water-coal fuel / B.R. Nussupbekov, A.K. Khassenov, D.Zh. Karabekova, U.B. Nussupbekov, M. Stoev, M.M. Bolatbekova // Bulletin of the Karaganda University, Physics Series, 2019. — No. 4 (96). — P. 80–84.

14 Khassenov A.K. Electric pulse method for producing a small-dispersed product of coal-water fuel / A.K. Khassenov, U.B. Nussupbekov, D.Zh. Karabekova, M. Stoev, M.M. Bolatbekova // Eurasian Physical Technical Journal, 2020. — Vol. 17, No. 2. — P. 96–99.

А.К. Хасенов, Б.Р. Нусупбеков, Д.Ж. Карабекова,
Г.А. Булкаирова, Б.У. Шашубай, М.М. Болатбекова

Шыны сынықтарын қайта өңдеудің электримпульстік әдісі

Мақалада қоршаған ортаға теріс әсер ететін әйнек сынықтарын өңдеу кезінде қайталама ресурстарды алу мәселесі қарастырылған. Тұрмыстық қалдықтарды өңдеу кезеңдерінде шикізатты дайындау процесінде материал қажетті мөлшерге дейін ұсақталады. Бұл әртүрлі әдістерге негізделген ұнтақтағыштарда іске асуда. Осыған байланысты қазіргі уақытта қолданыстағы механикалық диірмендердің түрлеріне талдаулар жүргізіліп, олардың кемшіліктері зерттелді. Аталған мәселені шешу үшін ғылыми жұмыста шыны сынықтарын электрлік импульсті әдіспен өңдеудің нәтижелері берілген. Тәжірибелік қондырғының жұмыс істеу принципі сипатталған, зерттелетін материалды өңдеуге арналған жұмыс камерасының құрылымы келтірілген. Аталмыш технологияда шыны сынықтарын өңдеу жинағыштың разряд кернеуін 25 кВ–тан 35 кВ–қа дейін, конденсатордың сыйымдылығын 0,25 мкФ–тан 1 мкФ–қа дейін, импульстік разрядтардың санын 100-ден 600-ге дейін арттыру арқылы орындалды. Электримпульстік әдістің көмегімен, бастапқы фракциясы — 2 және 5 мм болатын шыны бөлшектері 1 мм–ден 0,1 мм–ге дейін ұсақталды. Дайын өнімнің түсімінен электрлік параметрлік анықталды және ұсақталған шыны ұнтақтың диаметріне тәуелділігі алынды. Сұйық ортада импульстік электр разрядтарын қалыптастыру үшін шикізатты ұнтақтау нәтижелері материалды ұнтақтау дәрежесін бағалауға мүмкіндік берді. Зерттеу жұмыстарынан алынған мәліметтерге сәйкес шыны сынықтарын ұнтақтаудың оңтайлы параметрлері белгіленді.

Кілт сөздер: электргидравликалық эффект, көмір ұнтағы, разряд энергиясы, дайын өнімнің түсімі, импульстік электр разрядтары.

А.К. Хасенов, Б.Р. Нусупбеков, Д.Ж. Карабекова,
Г.А. Булкаирова, Б.У. Шашубай, М.М. Болатбекова

Электроимпульсный метод переработки стеклобоя

В статье рассмотрен вопрос получения вторичного ресурса при переработке стеклобоя, оказывающий негативное воздействие на окружающую среду. В процессе подготовки сырья на этапах переработки бытовых отходов материал измельчается до нужного размера. Данный процесс осуществляется на мельницах, основанных на различных методах разрушения. В связи с этим был проведен анализ существующих в настоящее время типов механических мельниц и исследованы их недостатки. Для решения указанной проблемы в научной работе приведены результаты обработки стеклобоя электроимпульсным методом. Описан принцип работы экспериментальной установки, приведена кон-

струкция рабочей камеры для обработки исследуемого материала. В данной технологии переработка стеклобоя выполнена с увеличением разрядного напряжения накопителя от 25 кВ до 35 кВ, емкости конденсатора от 0,25 мкФ до 1 мкФ, числа импульсных разрядов от 100 до 600. С помощью электроимпульсного метода частицы стеклобоя с исходной фракцией — 2 и 5 мм — измельчались от 1 мм до 0,1 мм. Получена зависимость выхода готового продукта от электрических параметров установки и диаметра измельченного стеклянного порошка. Результаты измельчения сырья с образованием импульсных электрических разрядов в жидкой среде позволили оценить степень измельчения материала. По полученным данным исследовательских работ установлены оптимальные параметры измельчения стеклобоя.

Ключевые слова: электрогидравлический эффект, угольный порошок, энергия разряда, выход готовой продукции, импульсные электрические разряды.

References

1 Pavlushkina, T.K., & Kisilenko, N.G. (2011). Ispolzovanie stekolnogo boia v proizvodstve stroitelnykh materialov [The use of glass cullet in the production of building materials]. *Steklo i keramika — Glass and ceramics*, 5, 27–34 [in Russian].

2 Ketov, A.A., Ketova, G.B., Puzanov, A.I., Puzanov, I.S., Rossomagina, A.S., & Saulin, D.V. (2002). Stekloboi kak syre dlia polucheniia teploizoliatsionnogo materiala [Cullet as a raw material for obtaining heat-insulating material]. *Ekologiia i promyshlennost Rossii — Ecology and industry of Russia*, 8, 17–20 [in Russian].

3 Dvorkin, L.I., & Dvorkin, O.L. (2007). Stroitelnye materialy iz otkhodov promyshlennosti [Construction materials from industrial waste]. Moscow: Feniks [in Russian].

4 Shevchenko, V.V. (2012). ASR effect in glasses used as additives to Portland cement. Glass Physics and Chemistry, 38(5), 466–471.

5 Erenkov, O. Yu., & Bogachev, A.P. (2014). Oborudovanie mekhanicheskikh protsessov v khimicheskoi tekhnologii [Equipment of mechanical processes in chemical technology]. Khabarovsk: Izdatelstvo Tikhookeanskogo gosudarstvennogo universiteta, 80 [in Russian].

6 Puzyrevskaia, I.A. (2014). Obogashchenie poleznykh iskopaemykh [Mineral enrichment]. Blagoveshchensk: Izdatelstvo Amurskogo gosudarstvennogo universiteta, 96 [in Russian].

7 Massola, C.P., Chaves, A.P., & Albertin, E. (2016). A discussion on the measurement of grinding media wear. Journal of Materials Research and Technology, 5(3), 282–288.

8 Yutkin, L.A. (1986). Elektrogidravlicheskii effekt i ego primeneniie v promyshlennosti [Electrohydraulic effect and its application in industry]. Leningrad: Mashinostroenie, 253 [in Russian].

9 Kornev, I., Osokin, G., Yavorovsky, N., Morozov, A., & Litvinenko, V. (2016). Pulsed electric discharge treatment of uranium leaching solutions: A method for accelerated extraction. Hydrometallurgy, 162, 37–41.

10 Martynov, N.V., Dobromirov, V.N., & Avramov, D.V. (2020). Elektrogidravlicheskaia tekhnologiia dezintegratsii almazosoderzhashchikh porod [Electrohydraulic technology of disintegration of diamond-bearing rocks]. *Obogashchenie rud — Ore dressing*, 1(385), 8–14 [in Russian].

11 Dobromirov, V.N., Avramov, D.V., & Martynov, N.V. (2019). Tekhnologiia obezzarazhivaniia zhidkostei na osnove elektrogidravlicheskogo effekta [Disinfection technology of liquids based on electrohydraulic effect]. *Voda i ekologiia — Water and Ecology*, 2(78), 17–23 [in Russian].

12 Evrendilek, G.A., & Tanasov, I. (2017). Configuring pulsed electric fields to treat seeds: an innovative method of seed disinfection. *Seed science and technology*, 45(1), 72–80.

13 Nussupbekov, B.R., Khassenov, A.K., Karabekova, D.Zh., Nussupbekov, U.B., Stoev, M., & Bolatbekova, M.M. (2019). Coal pulverization by electric pulse method for water-coal fuel. *Bulletin of the Karaganda of University-Physics*, 4 (96), 80–84.

14 Khassenov, A.K., Nussupbekov, U.B., Karabekova, D.Zh., Stoev, M., & Bolatbekova, M.M. (2020). Electric pulse method for producing a small-dispersed product of coal-water fuel. *Eurasian Physical Technical Journal*, 17(2), 96–99.

DOI 10.31489/2022PH1/81-88

UDC 621.74.011:669.017

E.N. Eremin

Omsk State Technical University, Omsk, Russia
E-mail: weld_techn@mail.ru

Selection of inoculant additives for modifying nickel alloys

Heat-resistant nickel alloys are widely used in the production of castings for aircraft and industrial gas turbine engines. Structural factors are the main determinants of the performance properties of cast nickel alloys. The main disadvantage of castings obtained from these alloys is the coarse-crystalline structure, uneven grain size and columnar crystals in the cross-section. Therefore, the creation of an optimal alloy structure is an important condition for obtaining high properties and ensuring the increased operability of cast parts. Obtaining a fine-grained structure has a beneficial effect on the level of mechanical and operational properties of cast metal. The most promising way to create such a structure is to introduce a small number of additives into the melt that cause heterogeneous formation of crystal nuclei, i.e. modification of the melt with dispersed particles of refractory elements and inocular compounds. To select the type of inocular particles required to initiate crystallization of a particular phase, it is necessary to have a set of data that allows one to form a theoretical understanding of the principles of such a choice. The paper provides a rationale for the selection of the type of particles of inoculators capable of causing the process of artificial changes in the structure of cast metal. For a heat-resistant nickel alloy, the use of refractory particles of ultra-dispersed titanium carbo nitride powder as inoculators are the most effective. When introduced into the melt 0.025 wt. % of such particles, a fine-grained structure of the alloy is obtained, and its ductility in comparison with the unmodified one is more than doubled.

Keywords: high-temperature nickel alloy, melt, modification, crystallization, inoculators, particles, properties, structure.

Introduction

Heat-resistant nickel alloys of various alloying degrees are widely used in many industries. They are mainly used in the production of castings of the most critical, highly loaded parts for aircraft and industrial gas turbines of engines [1, 2].

Heat-resistant cast nickel alloys are complex multi-component hetero phase systems. Structural factors, along with chemical composition, are the main factors that determine such properties of nickel alloys as ductility, heat resistance, fatigue resistance, and others [3]. The disadvantage of castings obtained from these alloys is a coarse-crystalline structure, uneven grain size and columnar crystals in the cross-section. Therefore, the creation of an optimal structure for a given alloy is an important condition for obtaining the required properties and ensuring increased material performance.

The most versatile tool that has a beneficial effect on the level of mechanical and operational properties of cast metal is to obtain a fine-grained structure [2, 3]. The greatest effect of dispersion of the primary structure should be expected when it is formed as fine equiaxed grains. To obtain such a structure, certain conditions must be created. One of these conditions is the creation of the entire volume of the melt of a minimum temperature gradient, which would be distributed within the range of crystallization of the alloy. In this case, the nucleation of crystals would occur simultaneously throughout the entire volume of the bath. The most promising way to create such crystallization centers is to introduce into the melt a small number of additives that cause heterogeneous formation of crystal nuclei, i.e. modification of the melt with dispersed particles of refractory elements and inocular compounds. This modification method is a universal way of controlling the crystal structure of cast metal [4–6].

At the same time, to select the type of inocular particles required to initiate the crystallization of a particular phase, it is necessary to have a set of data that allows one to form a theoretical understanding of the principles of such a choice. The available information is extremely contradictory. Thus, J.V. Wood [7] showed the universality of the action of only two types of particles: TiC and ZrB_2 in steels crystallizing through α- and γ- lattices. As established by J. Campbell and J.W. Bannister [8], TiC refines grain in steel with α-grid, and there are no reliable inoculators for phases with a γ-grid. G.S. Ershov and V.A. Chernyakov [9] concluded that only TiN, ZrN, and ZrB_2 can serve as stable inoculators of steel.

Ahlroth & Kettunen [10] found that as a result of the introduction of 0.3... 0.4 % of refractory metal particles (molybdenum, niobium, tungsten) into nickel alloys with a size of 200–400 microns, the metal structure changed significantly, which led to an increase in the plastic properties of the resulting castings. In [11], a similar positive effect was obtained when modifying chromium-nickel stainless steel with refractory metals.

Using the available factual material, it is possible to formulate the basic requirements for inoculating particles. They must have:

– high thermodynamic stability in the melt;

– the highest possible electrical conductivity compared to the melt;

– possibility to differ less from the melt in terms of density.

In connection with the above, the work posed substantiating the choice of the type of modifier particles capable of causing the process of artificial changes in the structure and properties of nickel alloy castings.

Experimental

Alloy Kh10N60K10V10Yu5T3M2B, which is the most prominent representative of the family of high-alloy heat-resistant nickel alloys, widely used for manufacturing parts for aviation equipment [2], was chosen as the object of research. The casting of the test ingots was carried out by vacuum induction melting, in ceramic crucibles, on a U117–7 remelting unit. The chemical composition of the cast metal is shown in Table 1.

Table 1

Alloy composition Kh10N60K10V10Yu5T3M2B by main alloying elements

Composition	Content of elements,%							
	C	Cr	Co	Al	Ti	Mo	W	Nb
Requirements for Specifications	0.13–0.19	8.0–9.0	9.0–10.1	5.1–5.7	2.0–2.6	1.2–1.7	9.5–10.1	0.8–1.1
Investigated alloy	0.18	8.5	9.9	5.6	2.4	1.6	9.8	0.9

The experiments were carried out on cast samples of alloy Kh10N60K10V10Yu5T3M2B with various additions of refractory particles in amounts used in the practice of modification. For modification, we used plasma-chemical synthesis powders with a dispersion of about 100 nm. The introduction of particles into the liquid metal was carried out using briquettes as tablets. They were obtained by mixing powder components followed by pressing at a pressure of 10–15 t/cm^2 on a PG-476 hydraulic press in a specialized press mold of the size corresponding to the tablet, ensuring its dissolution in the melt for 20–40 seconds.

The ingots were cast using the following parameters:

– Operating frequency of the generator — 25650 Hz;

– Residual pressure in the melting chamber — 10–2 mm Hg;

– Heating temperature of the melt — 1700^{o}C;

– Holding time at a given temperature (power 5 kW) — 5 min;

– Temperature of modifier input — 1650^{o}C;

– Holding time at a given temperature — 3 min;

– Cooling of the melt (power 0 kW) — 10 min.

The macrostructure of the alloy was investigated on thin sections after etching in a solution of ferric chloride and a Marble reagent. A Carl Zeiss Axio Observer Alm optical microscope was used for metallographic analysis.

Tensile tests were carried out under the requirements of GOST 1497–84.

Results and Discussion

The choice of inoculars was made based on their resistance to dissolution in the melt, and then their electrical conductivity and density were taken into account.

Analysis of the heterogenizing ability of refractory compounds of the putative modifiers shows that, from the point of view of resistance to chemical interaction and dissolution in the melt, they do not all meet the requirements. Thus, borides are not stable in nickel and its alloys because of the high diffusion mobility of boron and the ability to form low-melting boron nickelides. Oxides are the most stable in terms of re-

sistance to chemical interaction and dissolution, but they are poorly wetted by nickel alloys and can only be introduced together with thermodynamically active elements (Ca, Ba, etc.), the use of which is fraught with great difficulties. Therefore, the greatest preference when choosing modifiers, especially for high-temperature alloys, is given to inoculators in the form of nitrides, carbides and some oxides that are well wetted by melts [4, 7, 12–14] (Table 2).

Table 2

Contact angles of wetting θ in the system refractory compound — Ni *

Compound	θ*	T, °C	Environ
TiC	38/62/30	1 500/1 550/1 450	vacuum
ZrC	24/32/30	1 400/1 500/1 550	vacuum
VC	~0/-/17	1 450/-/1 380	vacuum
NbC	~0/-/18	1 450/-/1 380	vacuum
TaC	~0/-/16	1 400/-/1 380	vacuum
HfC	-/-/28	-/-/1 450	argon
TiN	70/-/98	1 550/-/1 450	argon
Si_3N_4	90/-/105	1 435/-/1 500	argon
ZrN	-/10/72	-/1 500/1 550	argon
TiB_2	64/-/39	1 480/-/1 550	helium
ZrB_2	55/-/42	1 500/-/1 500	vacuum
CrB_2	40/30/20	1 500/1 460/1 500	vacuum
Al_2O_3	128/-/-	1 500/-/-	vacuum
ZrO	118/-/-	1 500/-/-	vacuum
TiO_2	120/57/-	1 500/1 480	helium/vacuum
Cr_2O_3	0/56/-	1 400/1 500	argon/vacuum

* Work data are separated with a slash [12], [13], and [14]

The phase diagrams of Ni-C-Me (carbide-forming element) studied by H.J. Goldschmit [15] indicate that all the most stable carbides (TiC, ZrC, HfC, NbC) exhibit polymorphism in low temperatures and carbon concentrations region, can be present in the of bcc and hcp modifications, and in high temperatures and carbon concentrations region, all carbides have an fcc lattice and can serve as crystallization centers.

Polythermal section of the Ni TiC system, investigated by V.N. Eremenko, showed that it is quasi-binary and has the form of a simple diagram with a eutectic [16]. The maximum solubility of TiC in nickel occurs at a eutectic temperature of 1280°C and is 6.2 %. The solubility of carbides in liquid nickel alloys decreases in the order TiC → NbC → ZrC → HfC, but only at moderate temperatures. These carbides, as well as other interstitial phases, are characterized by a tendency to deviate from the stoichiometric composition with a deficit in carbon content, which increases the decomposition temperature of carbide systems. The deviation decreases in the following sequence [15]: $TiC_{0.28} \rightarrow ZrC_{0.28} \rightarrow HfC_{0.5} \rightarrow NbC_{0.7}$.

Deviations from stoichiometry play an important role in the kinetics of diffusion, decarburization, dissolution and oxidation processes. The vacancies in carbides can be filled with atoms of components, for example N and O. Carbonitrides, and especially oxycarbonitrides, are more stable in metal melts. However, it is known that in cermets of the MeOx-MeN type, with an increase in the proportion of MeO, the electrical resistance increases, i.e. the proportion of free electrons decreases and the wettability deteriorates. The contact angles θ of carbides with nickel alloys are low, nitrides are wetted worse, and oxides are poorly wetted (Table 2). Improvement of the wetting of refractory compounds with liquid metals occurs after a certain time of their contact due to ion-exchange reactions and mutual diffusion.

Nitrides are more stable than carbides [4, 15, 16]. At the same time, the use of nitrides for modification can lead to an increase in the nitrogen concentration in the melt and the formation of eutectic nitrides along the grain boundaries. However, a moderate increase in the nitrogen content (0.003 %) has a modifying effect on the structure of heat-resistant nickel alloys. With a further increase in its concentration, the plasticity of alloys in which there are no primary MeC carbides deteriorates, and in those alloys in which they are present, an increase in the nitrogen content worsens their morphology, which also has a negative effect on the properties of the metal.

Usually, when modifying, coarse nitride powders with a particle size of 10–200 μm are used in an amount of 0.1–0.2 % of the melt mass [4]. The dissolution of such a quantity of nitrides causes a significant increase in the nitrogen concentration in the melt and contributes to the accumulation of nitrides in the circulating charge. The use of ultrafine powders (UDP) by an order of magnitude reduces the amount of added additive (0.01–0.02 % of the melt mass) and reduces the risk of nitride accumulation [6].

Considering the above and comparing the properties of the main refractory compounds, it is possible to choose a number of inoculant additives that most fully satisfy the requirements imposed on them (Table 3).

Table 3

List of compounds that best meet the selection criteria for inoculators

Compound	Density at 1550 °C, 10^{-3} kg/cm^3	Specific electrical resistance at 1550 °C, μOhm·cm	Literary source
TiB_2	4.43	105	13
ZrB_2	5.91	66	13
WC	15.49	31	13
TiC	4.73	147	13
ZrC	6.44	175	14
NbC	7.29	120	13
HfC	12.3	140	13
TaC	13.89	112	14
TiN	5.33	132	12
ZrN	7.06	126	12
HfN	12.96	122	12
TiCN	4.9	-	17
VN	6.04	-	13
TaN	14.1	138	14
VC	5.36	-	14

Examining data from Tables 2, 3, we conclude that for the modification of nickel alloys; it is most rational to use carbides and nitrides of refractory compounds, primarily titanium as inoculants. An even greater effect can be expected from titanium carbonitride, which has the highest stability in metal melts [17, 18]. Consequently, for the castings of experimental samples, titanium carbides, nitrides, and carbonitrides were chosen as inoculant particles during modification.

The amount of refractory particles in the modifier, which ensures the optimal structure and properties of the cast metal, depends on many factors: the chemical state of the alloy, technological parameters of melting and pouring, etc., as a result of which these parameters can be determined for a specific case only experimentally.

Castings from the alloy under study have extremely low plasticity values. So, the values of the relative elongation of the cast metal obtained by vacuum induction melting are usually in the range of 3.0–3.7 %, which in many cases does not meet the production requirements [2].

The study of the influence of the type and amount of the selected particles-inoculators on the elongation (Table 4) confirmed the validity of the theoretical conclusions.

Table 4

Influence of the type and amount of selected particles on the elongation of the alloy

Inoculator	Average value of the relative elongation depending on the number of particles (weight),%				
	0.01	0.025	0.05	0.075	0.1
TiN	4.6	6.2	4.8	4.6	4.1
TiC	4.4	5.5	4.5	4.2	3.9
TiCN	4.9	7.6	6.1	4.7	4.5

The use of ultrafine powder of titanium carbonitride as particles — inoculators is the most effective. Introducing 0.025 wt.% of such particles into the melt increases the plasticity of the alloy by more than 2 times compared to unmodified, while the results are much worse when other particles are used.

Metallographic studies show that modification of the alloy Kh10N60K10V10Yu5T3M2B with titanium carbonitride manifests itself in a significant refinement of the macrograins of the alloy (Figure 1).

a) b)

a — initial; b — modified

Figure 1. Macrostructure of a microsection of alloy Kh10N60K10V10Yu5T3M2B with a diameter of 60 mm

The macrostructure of an unmodified nickel alloy ingot is characterized by large columnar grains (Figure 1a), up to 30 μm in size, in which liquation chemical inhomogeneity and pores are revealed. The modification prevented the formation of columnar grains. The structure is dominated by equiaxed grains up to 1.5 mm in size (Figure 1b).

This may be because titanium carbonitride has high stability in nickel alloys and has a density close to the carbide phase of the alloy.

In the mechanism of structure refinement during this modification, two factors can be distinguished that contribute to this process: mutual blocking and misorientation of dendrites growing in a non-uniform temperature (concentration) field; intensive separation of dendritic branches from the trunk, associated with a non-uniform concentration distribution. The first factor is realized at the growth stage, the second — during the transformation of dendrites when they coexist with the melt in a two-phase state. Introducing a dispersed solid phase into the melt distorts the local temperature and concentration field, which causes a violation of the columnar structure.

Introducing ultrafine particles of titanium carbonitride causes the creation of inclusions in the melt with a concentration and temperature different from the main melt and does not allow the formation of a columnar structure. Changes in the temperature gradient and the rate of movement of the crystallization front significantly affect not only the dendritic structure but also the morphology and topography of the components and the phase composition of heat-resistant alloys.

Conclusions

When modifying nickel alloys, using carbides and nitrides of refractory compounds, primarily titanium as inoculants, is the most rational choice. We achieved the best results when ultrafine particles of titanium carbo nitride were used as inoculators, in an amount of 0.25 wt. % providing a fine-grained structure and a twofold increase in the ductility of castings.

References

1 Reed R.C. The superalloys: fundamentals an application / R.C. Reed. — Cambridge University Press — Cambridge, 2008. — 388 p.

2 Кишкин С.Т. Литейные жаропрочные сплавы на никелевой основе [Текст] / С.Т. Кишкин, Г.Б. Строганов, А.В. Логунов. — М.: Машиностроение, 1987. — 112 с.

3 Sims C.T. Superalloys II: high-temperature materials for aerospace and industrial power / C.T. Sims, N.S. Stoloff, W.C. Hagel. — Wiley-Interscience, New York, 1987. – 640 p.

4 Бабаскин Ю.З. Структура и свойства литой стали [Текст] / Ю.З. Бабаскин. — Киев: Наук. думка, 1980. — 240 с.

5 Гольдштейн Я.Е. Инокулирование железоуглеродистых сплавов [Текст] / Я.Е. Гольдштейн, В.Г. Мизин. — М.: Металлургия, 1993. — 416 с.

6 Кузнецов М.А. Управление структурой и свойствами металлов методом модифицирования (обзор) / М.А. Кузнецов, Д.Е. Колмогоров, Е.А. Зернин // Технология машиностроения. — 2012. — № 2. — С. 5–8.

7 Wood J.Y. Nucleation in steel castings by interstitial compounds / J.Y. Wood // *International Conference: Solidification Sheffield, 1977*. — 1978. — P. 179–183.

8 Campbell J. Grain refinement of electroslaq remelted iron alloys / J. Campbell, J.W. Bannister // Metals Technology, 1975. — Vol. 2, Part 9. — P. 409–416. DOI: 10.1179/030716975803276880

9 Ершов Г.С. Строение и свойства жидких и твердых металлов [Текст] / Г.С. Ершов, В.А. Черняков. — М.: Металлургия, 1978. — 231 с.

10 Ahlroth R. Review on Ni- and Co-base composite materials for the temperature range of 1000…1100 °C / R. Ahlroth, P. Kettunen. – *Acta Polytechnica Scandivanica. Chemistry including metallurgy series*, 1973. — No. 112. — P. 32.

11 Еремин Е.Н. Применение модифицирования для повышения свойств кольцевых заготовок из азотосодержащих нержавеющих сталей, полученных способом ЦЭШЛ / Е.Н. Еремин // Современная электрометаллургия. — 2006. — № 3. — С. 3–7.

12 Самсонов Г.В. Тугоплавкие соединения: 2-е изд. [Текст] / Г.В. Самсонов, И.М. Виницкий. — М.: Металлургия, 1976. — 560 с.

13 Свойства, получение и применение тугоплавких соединений: справоч. /под ред. Т.А. Косолаповой. — М.: Металлургия, 1986. — 928 с.

14 Котельников Р.Б. Особо тугоплавкие элементы и соединения [Текст] / Р.Б. Котельников, С.Н. Башлыков, З.Г. Галиакбаров. — М.: Металлургиздат, 1968. — 376 с.

15 Гольдшмит Х. Дж. Сплавы внедрения [Текст; пер. с англ. / Х. Дж. Гольдшмит / под ред. Н.Т. Чеботарева. — Вып. 1. — М.: Мир, 1971.— 224 с.

16 Еременко В.Н. Политермический разрез системы Ni–TiC / В.Н. Еременко, З.И. Толмачева // Порошковая металлургия. — 1961. — № 2. — С. 21–29.

17 Stepanova N.N. Structure formation in “001” single crystals of a nickel-based superalloy solidified with TiCN powder addition / N.N. Stepanova, D.P. Rodinov, V.A. Sazonova, E.N. Khlystov / Materials Science and Engineering: A, 2000. — Vol. 284, Iss. 1–2. — P. 88–92 DOI:10.1016/S0921–5093(00)00763–2

18 Артемьев А.А. Влияние микрочастиц диборида титана и наночастиц карбонитрида титана на структуру и свойства наплавленного металла / А.А. Артемьев // Металловедение и термическая обработка материалов. — 2011. — № 12 (678). — С. 32–37.

Е.Н. Еремин

Никельді қорытпаларды түрлендіру үшін, оның құрамын жақсартатын қоспаларды таңдау

Ыстыққа төзімді никель қорытпалары ұшақтар мен өндірістік газ турбиналы қозғалтқыштарға арналған құю өндірісінде кеңінен қолданылады. Құрылымдық факторлар – құйылған никель қорытпаларының пайдалану қасиеттерін анықтаушы болып саналады. Бұл қорытпалардан алынған құймалардың негізгі кемшілігі – ірі түйіршікті құрылым, түйіршіктердің біркелкі еместігі және қимада бағаналы кристалдардың болуы. Сондықтан, қорытпаның оңтайлы құрылымын жасау жоғары қасиеттерді алу және құйылған бөлшектердің сапалы өнімділігін қамтамасыз етудің маңызды шарты болып табылады. Құйылған металдың механикалық және пайдалану қасиеттерінің деңгейіне пайдалы әсер ететін ең әмбебап құрал – бұл ұсақ түйіршікті құрылымды алу. Мұндай құрылымды құрудың ең перспективалы жолы – балқымаға аз мөлшерде кристалл ұйытқысының гетерогенді түзілуін тудыратын қоспаларды енгізу, яғни балқыманы баяу балқитын элементтердің дисперсті бөлшектерімен және инокулярлы–қосылыстарымен түрлендіру. Нақты бір фазаның кристалдануын бастайтын қажетті инокулярлы бөлшектердің түрін таңдау үшін, осындай таңдау принциптері туралы теориялық түсінік қалыптастыруға мүмкіндік беретін мәліметтер жиынтығы болуы керек. Жұмыста құйылған металл құрылымының жасанды өзгеру процесін тудыруы мүмкін инокуляторлар бөлшектерінің түрін таңдау негіздемесі келтірілген. Ыстыққа төзімді никель қорытпасы үшін титан карбонитридінің ультрадисперсті ұнтағының баяу балқитын бөлшектерін инокулятор ретінде қолдану тиімді екендігі көрсетілген. Балқымаға енгізгенде 0,025 салмақ, яғни мұндай бөлшектердің % –ы қорытпаның ұсақтүйіршікті құрылымын алу арқылы қамтамасыз етіледі, ал оның илемділігі түрленбегенмен салыстырғанда екі еседен астам артады.

Кілт сөздер: ыстыққа төзімді никель қорытпасы, балқыма, түрлендіру, кристалдану, инокуляторлар, бөлшектер, қасиеттері, құрылымы.

Е.Н. Еремин

Выбор инокулирующих добавок для модифицирования никелевых сплавов

Жаропрочные никелевые сплавы находят широкое применение в производстве отливок деталей авиационных и промышленных газовых турбин двигателей. Структурные факторы являются определяющими эксплуатационные свойства литых никелевых сплавов. Основным недостатком отливок, полученных из этих сплавов, являются грубокристаллическое строение, разнозернистость и наличие столбчатых кристаллов по сечению. Поэтому создание оптимальной структуры сплава является важным условием получения высоких свойств и обеспечения повышенной работоспособности литых деталей. Наиболее универсальным средством, оказывающим благоприятное влияние на уровень механических и эксплуатационных свойств литого металла, является получение мелкозернистой структуры. Наиболее перспективный путь создания такой структуры — это ввод в расплав небольшого количества добавок, вызывающих гетерогенное образование зародышей кристаллов, т.е. модифицирование расплава дисперсными частицами тугоплавких элементов и соединений-инокуляров. Для выбора типа частиц инокуляров, требуемых для инициирования кристаллизации конкретной фазы, необходимо иметь набор данных, позволяющих сформировать теоретические представления о принципах такого выбора. В работе приведено обоснование выбора типа частиц инокуляторов, способных вызывать процесс искусственного изменения структуры литого металла. Показано, что для жаропрочного никелевого сплава наиболее эффективно использование в качестве инокуляторов тугоплавких частиц ультрадисперсного порошка карбонитрида титана. При введении в расплав 0,025 вес. % таких частиц обеспечивается получение мелкозернистой структуры сплава, а его пластичность, по сравнению с немодифицированным, увеличивается более чем в два раза.

Ключевые слова: жаропрочный никелевый сплав, расплав, модифицирование, кристаллизация, инокуляторы, частицы, свойства, структура.

References

1 Reed, R.C. (2008). *The superalloys: fundamentals an application.* Cambridge University Press, Cambridge, 388.

2 Kishkin, S.T., Stroganov, G.B., & Logunov, A.B. (1987). Liteinye zharoprochnye splavy na nikelevoi osnove [Foundry heat-resistant nickel-based alloys]. Moscow: Mashinostroenie [in Russian].

3 Sims, C. T., Stoloff, N.S., & Hagel, W.C. (1987). Superalloys II: high-temperature materials for aerospace and industrial power. Wiley-Interscience, New York, 640.

4 Babaskin, Yu.Z. (1980). *Struktura i svoistva litoi stali [Cast steel structure and properties]*. Kiev: Naukova dumka [in Russian].

5 Goldshtein, Ya.E., & Mizin, V.G. (1993). *Inokulirovanie zhelezouglerodistykh splavov [Inoculation of iron-carbon alloys]*. Moscow: Metallurgiia [in Russian].

6 Kuznetsov, M.A., Kolmogorov, D.E., & Zernin, E.A. (2012). Upravlenie strukturoi i svoistvami metallov metodom modifitsirovaniia (obzor) [Management of structure and properties of metals by a modification method (review)]. *Tekhnologiia mashinostroeniia — Mechanical engineering technology*, 2, 5–8 [in Russian].

7 Wood, J.Y. (1978). Nucleation in steel castings by interstitial compounds. *International Conference: Solidification, Sheffield 1977*, 179–183.

8 Campbell, J., & Bannister, J.W. (1975). Grain refinement of electroslaq remelted iron alloys. *Metals Technology*, 2(9), 409–416. DOI: 10.1179/030716975803276880

9 Ershov, G.S., & Chernyakov, V.A. (1978). *Stroenie i svoistva zhidkikh i tverdykh metallov [Structure and properties of liquid and solid metals]*. Moscow: Metallurgiia, 231 [in Russian].

10 Ahlroth, R., & Kettunen, P. (1973). Review on Ni- and Co-base composite materials for the temperature range of 1000…1100 °C. *Acta Polytechnica Scandivanica. Chemistry including metallurgy series*, 112, 32.

11 Eremin, E.N. (2006). Primenenie modifitsirovaniia dlia povysheniia svoistv koltsevykh zagotovok iz azotosoderzhashchikh nerzhaveiushchikh stalei, poluchennykh sposobom TsEShL [The use of modification to improve the properties of annular blanks made of nitrogen-containing stainless steels obtained by the CES method]. *Sovremennaia elektrometallurgiia – Modern electrometallurgy*, 3, 3–7 [in Russian].

12 Samsonov, G.V., & Vinitskii, I.M. (1976). *Tugoplavkie soedineniia [Refractory joints]* (2d ed.). Moscow: Metallurgiia, 560 [in Russian].

13 Kosolapova, T. A. (Ed.). (1986). Svoistva, poluchenie i primenenie tugoplavkikh soedinenii: Spravochnik [Properties, production and application of refractory compounds. Cases]. Moscow: Metallurgiia, 928 [in Russian].

14 Kotelnikov, R. B., Bashlykov, S.N., & Galiakbarov, Z.G. (1968). *Osobo tugoplavkie elementy i soedineniia [Particularly refractory elements and compounds]*. Moscow: Metallurgizdat, 376 [in Russian].

15 Goldshmit, Kh.Dzh. (1971). *Splavy vnedreniia [Introduction alloys]*. Moscow: Mir, 1, 224 [in Russian].

16 Eremenko, V.N., & Tolmacheva, Z.I. (1961). Politermicheskii razrez sistemy Ni–TiC [Polythermal section of the system Ni-TiC]. *Poroshkovaia metallurgiia — Powder metallurgy, 2,* 21–29 [in Russian].

17 Stepanova, N.N., Rodionov, D.P., Sazonova, V.A., & Khlystov, E.N. (2000). Structure formation in “001” single crystals of a nickel-based superalloy solidified with TiCN powder addition. *Materials Science and Engineering: A*, 284(1–2), 88–92.

18 Artemev, A.A. (2011). Vliianie mikrochastits diborida titana i nanochastits karbonitrida titana na strukturu i svoistva naplavlennogo metalla [The effect of titanium diboride microparticles and titanium carbonitride nanoparticles on the structure and properties of the deposited metal]. *Metallovedenie i termicheskaia obrabotka materialov — Metallurgy and thermal treatment of materials, 12(678),* 32–37 [in Russian].

DOI 10.31489/2022PH1/89-98

UDC: 621.794

D.R. Baizhan[1,3*], B.K. Rakhadilov[1,2], L.G. Zhurerova[1], K. Torebek[2]

[1]*Sarsen Amanzholov East Kazakhstan University, Ust-Kamenogorsk, Kazakhstan*
[2]*Plasma Science LLP, Ust-Kamenogorsk, Kazakhstan;*
[3]*Institute of Composite Materials, Kazakhstan*
[*]*E-mail: daryn.baizhan@mail.ru*

Preparation of bio-ceramic composite coatings on Ti6Al4V titanium alloy by gas-detonation spraying

The paper presents study of a new approach to manufacturing carrier implants with a combination of bioactivity, biocompatibility, and mechanical properties, composite powders of hydroxyapatite and titanium with a mass content of 50:50 % when sprayed by gas detonation spraying. Experimental studies of the surface morphology and cross-section microstructure, phase composition and mechanical properties of HATi composite coatings are obtained. The experimental results showed that the cross-section microstructures of HATi composite coatings are typical plate structures comprising curved strips formed by well-deformed and oxidized Ti plates and limited deformed HA plates. Composite coatings' morphology and phase states were studied using scanning electron microscopy and X-ray diffractometry. It was found that the deprived coatings mainly consist of the phases HA, Ti and TiO. The elemental composition study results designated that the atomic ratio of calcium and phosphorus in the obtained coatings is Ca/P ~ 1.64, which is close to the value of the initial powder — Ca/P ~ 1.67. This indicates a limited change in the chemical composition during the coating formation.

Keywords: gas-detonation spraying, HATi composition coating, microstructure and phase composition, mechanical properties.

Introduction

In modern medicine, progress is closely linked with new drugs and treatment methods and the development of materials designed to interact with biological systems. Such materials, called biomaterials, are used mainly in restorative medicine, where they replace the tissues of a living organism as implants [1]. The modern direction in the development of implantable biomaterials is modifying their surfaces by obtaining coatings [2]. These coatings ensure the functioning implants in the environment of a living organism and promote integration with its tissues [3]. One of the most important materials widely used for this purpose is hydroxyapatite (HA) — $Ca_{10}(PO_4)_6(OH)_2$ [4]. Besides improving biocompatibility, hydroxyapatite shows high bioactivity and contributes to the intensification of osseointegration [4]. Hydroxyapatite owes such properties to its chemical and biological similarity to bones, contributing to new bone tissue [5]. Metals coated with hydroxyapatite are usually used to manufacture implants since they combine the biological properties of hydroxyapatite and the mechanical properties of metals [6]. However, the hydroxyapatite coating suffers from poor mechanical properties, such as low viscosity, fretting fatigue and resistance to abrasive wear due to the internal fragility of hydroxyapatite [7]. To coordinate the bioactivity, biocompatibility, and mechanical properties of the biomedical implant carrier, research is continuing on substrate materials [3–6], coating materials, and manufacturing technologies [1, 2]. For coating materials, amplification phases or ions are usually entered into hydroxyapatite to form composites based on hydroxyapatite [2–5]. Alloying of cati-

ons (Na^+, K^+, Mg^{2+}, Mn^{2+}, Sr^{2+}, Ba^{2+}, Cu^{2+}, Zn^{2+}, Fe^{2+}) and anions (HCO^{3-}, HPO_4^{2-}, Cl^- and F^-) is considered as an effective approach to changing the bioactivity of hydroxyapatite [4]. On the contrary, the addition of a second reinforced phase has been confirmed as an appropriate way to improve and optimize the mechanical properties of the hydroxyapatite coating [1, 2, 4]. Metals, Ti [2, 5, 6], Al [7], Co [8] and Zn [9], ceramics, including TiO_2 [3, 10], SiO_2 [11], Y_2O_3 [12], ZrO_2 [13], Al_2O_3 [14], and other materials are commonly used as the second amplified phases. Many studies [2–14] have investigated changes in the microstructure, compositional, morphological, or surface properties of such coatings and their effect on bioactivity, mechanical strength, and adhesion strength. Titanium (Ti) is a traditional biometal, which is a widely used reinforced phase for HA. When Ti particles are added to HA, the mechanical properties of composite coatings significantly improve compared to the HA coating [2, 5, 6]. The homogeneous distribution of Ti particles can strengthen the brittle HA matrix due to the mechanism of dispersion hardening [15]. Besides, Ti particles added to HA improve the melting degree and spatter plastic deformation and reduce the size of the spatter crystals of HA [16], which is favourable for the formation of the coating with a dense microstructure and better adhesive strength. The addition of Ti particles to HA can also reduce the mismatch of thermal expansion coefficients between HA-Ti coatings and metal substrates, which leads to a decrease in thermal stress inside the coatings, which favourably affects the improvement of the coating/substrate surface adhesion [17].

Given the high importance of biocompatible coatings, the selection of appropriate coating technology is therefore an important consideration. The most common coating methods include thermal spraying, immersion, dynamic mixing, sol-gel, pulsed laser deposition, and others [17–23]. Among other spraying methods, gas thermal spraying methods are widely used to obtain various biocompatible coatings. These methods include conventional plasma spraying (PS), high-velocity oxygen fuel spraying (HVOF) and cold spraying [16, 17, 21–23]. For most methods, low or intermediate adhesive strength of the coating and low crystallinity of the resulting coatings are some of the important factors limiting their application. It is necessary to develop new methods or approaches to improve the properties of coatings.

Among the coating methods by thermal spraying, gas detonation spraying (GDS) technology has been used to obtain biocompatible coatings, such as HA coatings, for orthopedic applications [17, 21, 24, 25]. Gledhill et al. conducted a comparative study of HA-based coatings obtained using air plasma spraying (APS) and GDS technologies [26]. This study demonstrated that APS coatings have higher crystallinity and lower residual stress compared to GDS coatings, which can lead to a slow dissolution rate in vitro and in vivo. The authors suggested that APS coatings are preferable to further clinical use. At the same time, Gledhill et al. studied the fatigue behavior of HA coatings obtained using the APS and GDS methods in Ringer's solution. It was shown that the APS coatings completely peeled off from the substrates after 1 million cycles in Ringer's solution, while the GDS coatings turned out to be stable even after 10 million cycles [27]. In addition, the results of another study showed that HA-based coatings obtained by the APS method exhibit low crystallinity and the appearance of a significant content of additional phases in the coatings. Such phase transformation may be the result of an extremely high temperature in the plasma atomizer of the APS approach [28]. It is important to emphasize that in the HVOF and PS methods, continuous flame or plasma spraying is used for coating [21–23]. This can lead to undesirable overheating or melting of particles and a significant increase in substrate temperature, which is the main limitation of these methods. The GDS method uses a pulsed operating mode [29, 30]. This makes it possible to minimize the aforementioned negative consequences. On the other hand, the particle velocity in the GDS method is much higher compared to the HVOF and PS methods [21], which has a positive effect on important parameters of coatings, such as adhesion strength. The results of early studies devoted to the evaluation of HA coatings obtained on Ti-based substrates were not very encouraging, mainly due to the low crystallinity [26] and high porosity of the coatings. However, recent results of Popova et al. demonstrated that uniform coatings with a regular thickness can be obtained by the GDS method using HA powders with a particle size between 50–300 μm [31]. In addition, the Ca/P ratio equal to ≈1.67 can be achieved by optimizing the parameters of the GDS process [32]. To achieve the required quality of the GDS coatings, a very careful selection of the technological regime and the automation of technological equipment are required to exclude the human factor [33, 34]. Gryshkov et al. used the GDS method to design the endoprostheses for various applications, as well as to obtain HA coatings on pure magnesium with a low melting point of 650 °C, to develop biodegradable magnesium-based implants with bioactive coatings for temporary bone fixation. Thus, the results of [33–35, 36] show that the GDS process is effective for modifying the surface of implants.

The purpose of this work is to get composite coatings based on HATi applying gas detonation spraying.

Experimental

HATi composite coatings with a thickness of about 60 microns were applied to the Ti6Al4V substrate using the CCDS2000 gas detonation complex (CCDS-2000, developed by Siberian Protective Coating Technologies LLC, Novosibirsk, Russia), the working principle is described in [37]. The general view and detonation spraying process schematic diagram are shown in Figure 1. The gun barrel is filled with gases using a high-precision gas distribution system controlled by a computer. The process begins with filling the barrel with carrier gas. After that, a particular explosive mixture is fed so that a layered gas medium consisting of an explosive charge and a carrier gas is formed. With the help of a carrier gas flow, the powder is injected into the barrel (using a computer-controlled feeder) and forms a cloud. After a part of the powder is injected, the computer signals initiate detonation. This is implemented with the help of an electric spark. The duration of the explosive combustion charge is about 1 ms. A detonation wave is formed in the explosive mixture, passing into a shockwave in the carrier gas. Detonation products (heated to 3500–4500 K) and carrier gas (heated by a shock wave to 1000–1500 K) move at supersonic speed. The interaction time of gases with sprayed particles is 2–5 ms [38]. By characterizing the phase composition of the resulting coatings HA, applied at various spraying parameters, it is possible to determine suitable spraying conditions in the GDS. Our previous studies have shown [21] that by controlling the modes of detonation spraying (the filling percentage of the barrel with an explosive gas mixture, the spraying distance), the temperature and the coating rate can be varied, respectively, this significantly affected the melting and decomposition of HA. Preliminary studies of the microstructure, phase composition and chemical structure of GDS HA coatings applied under various spraying modes and optimal spraying conditions for applying HATi composite coatings without thermally decomposed HA phase were carried out were determined (Table 1).

Table 1

Spraying conditions

Parameters	Values
Fuel/oxidizer ratio	1,856
Barrel filling volume, %	30
Spraying distance, mm	100
Shot number	10

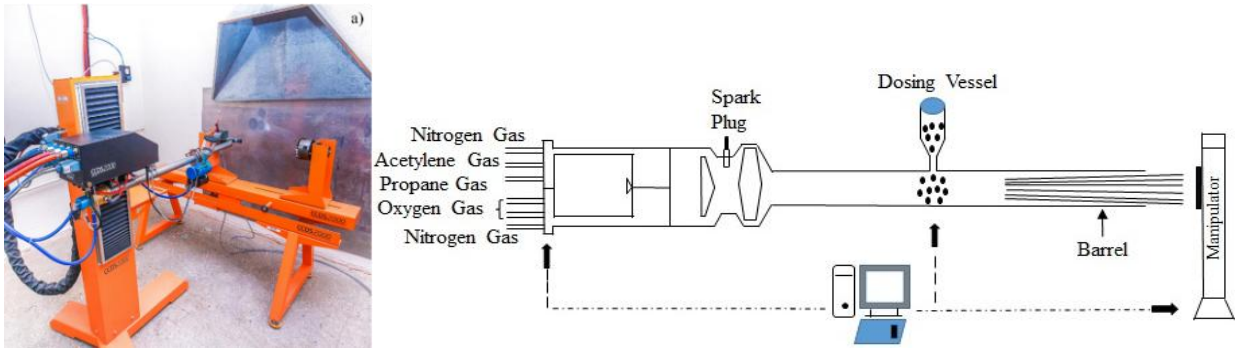

Figure 1. Schematic diagram of the CCDS2000 detonation complex

Ti6Al4V titanium alloy was used as the substrate material. The sample used to observe the microstructure was a rectangular size of 30 mm × 20mm × 3 mm. The composition of the Ti6Al4V titanium alloy is shown in Table 2. The samples were sanded (using SiC paper with a grain size of 100 to 2000). Before coating, the substrates were sandblasted with a grain size of 250–300 microns of aluminum oxide and treated with an ultrasonic bath.

Table 2

Chemical composition of Ti6Al4V alloy (weight percent).

Ti	Al	V	Fe	C	O	N	H
88,5–92,5	5,5–6,5	3,5–4,5	<0,25	<0,08	<0,13	<0,05	<0,012

Angular hydroxyapatite (HA) powder (99.95 %, produced by Sigma-Aldrich, Steinheim, Germany) with a diameter of 5–25 microns and spherical titanium powder (CL42TI) (made by Concept Laser, Germany) with a diameter of 15–45 microns were used as feedstock. HATi composite powders were obtained by mechanically mixing HA powder with Ti powder for 0.5 x using a PULVERISETTE 23 planetary ball mill. The mass ratio HA to Ti for composite powders HA-Ti was 50:50.

The sample's phase composition was studied by X-ray structural analysis on X'PertPro diffractometer using CuKα –radiation λ=2,2897 A0. The survey was carried out in the following mode: voltage across the tube U = 40 kV; tube current I = 30 мА. The decoding of diffractograms was carried out using the HighScore program. The coating's surface roughness was estimated by the parameter Ra using profilometers of model 130. The obtained coating's mechanical properties (Young's modulus, nano hardness) were studied using the NanoScan-4D Compact nanohardometer. Nano-indentation of coatings was carried out by the Oliver and Farr method using a Berkovich indenter at a load of 100 mN (ASTM E2546–07). The surface morphology and sample cross-section were studied by scanning electron microscopy (SEM) using backscattered electrons (BSE) on a TESCAN MIRA scanning electron microscope at accelerated voltages.

Results and Discussion

According to the results of scanning electron microscopy, the surface morphology of the composite coating comprises a layered-porous structure with a pronounced relief, which is typical of detonation coatings. In the resulting coatings, pores are observed that form when the coating particles melt. According to the analysis results of the coatings elemental composition, other elements besides the basic powder composition were not identified. One of the main parameters in determining bioactivity is the Ca/P ratio. The elemental analysis allows comparing the elements' concentrations that make up the coating and calculating the Ca/P ratio. The study results of the elemental composition showed that the atomic ratio of calcium and phosphorus in the sprayed coating is Ca/P ~ 1.64, which is close to the value of the initial powder — Ca/P ~ 1.67 indicates a limited change in the chemical composition during the coating formation. Figure 2 shows the SEM image and the elemental analysis of the composite coating surface.

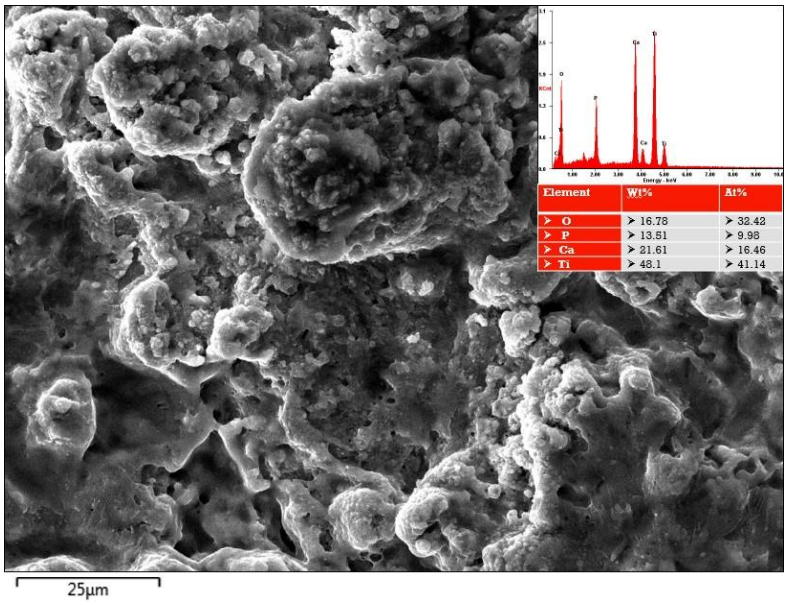

Figure 2. SEM image and EDS analysis of the HATi composite coating surface.

Plenty of scientists notes [32–37] that the coatings phase composition significantly affects the growth of bone tissue during the osseointegration of implants. The phase compositions of HATi composite powders are shown in Figure 3a. The peaks appearing at about 35°, 38°, and 40° in the Ti diffractogram (Fig. 3a) were identified as Ti crystal planes corresponding to (100), (002), and (101) [24]. Peaks appearing at approximately 26°, 32°, and 33° in the diffractogram (indicated by HA in Figure 3a) were identified as crystal planes of HA corresponding to (020), (211) and (030) [11, 38]. The characteristic sharp peaks of HA and Ti demonstrate good crystallinity of the phases of HA and Ti. In the HATi composite coatings, there was a phase of HA, Ti and TiO. However, there was no calcium oxide (CaO), tricalcium phosphate (α or β TCP) or tetra

calcium phosphate (TTCP), which are usually present in other thermal-coated HA coatings [3, 14, 23]. This confirms good phase transplantation during the formation of the HA coating by the GDS method. Compared with the corresponding composite powder, the intensity of the HA phase peaks in the coating of the HATi decreased somewhat, and some new phases formed by Ti oxidation appeared. However, the positions of the characteristic peaks of the HA phase were slightly changed. The decrease in Ti content is due to its strong oxidation during the coating formation, which was confirmed by significant titanium oxides.

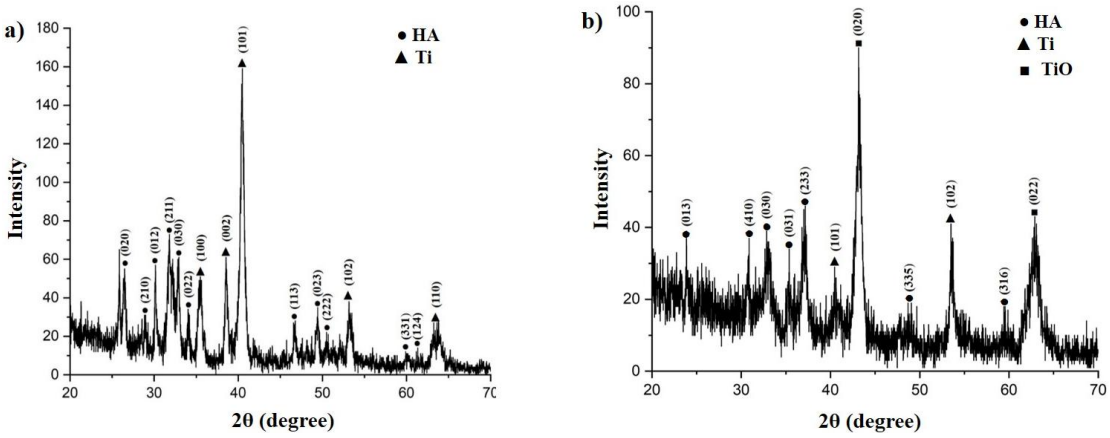

Figure 3. Diffractogram of composite powder and coating HATi.

The microstructure study of the composite coating cross-section showed a layered structure with a thickness of 60 microns (figure 4). According to the microstructure results of the coating cross-section, no visible cracks were found at the coating/substrate interface, which indicates good surface contact. A thorough microstructure study showed that most of the small grey stripes have a dense structure. The grey areas are a non-compact structure with some irregularly shaped micropores. These paid shallow grey stripes were formed due to compaction caused by the impact of falling HA particles that occurred in a dense area on the upper and lower surfaces of HA splashes. In addition, there was also a porous layer on the coating's upper surface. This may result from limited deformation of the HA spray due to little melting in the process GDS [21] and minor compaction of the coating surface layer caused by the impact of falling particles [27]. This porous structure on the top surface of coatings helps improve biological properties.

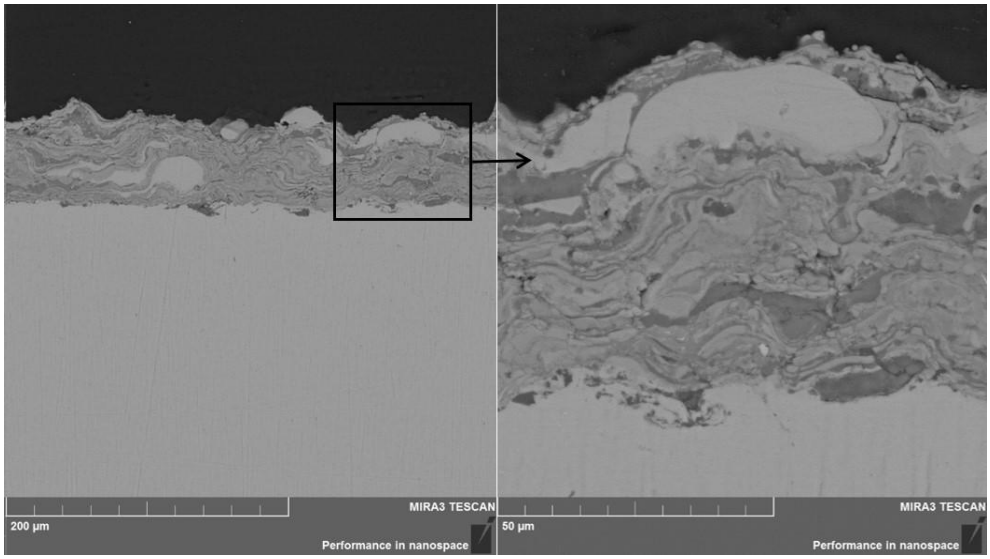

Figure 4. Microstructures of the HATi composite coating cross-section.

The EDS analysis showed that the white curved bands mainly consist of Ti and O, with a small content of Ca, P. The grey areas and shallow grey stripes are mainly Ca, P, O with some quantity Ti. In combination with the phase composition, it is recognized that the white curved stripes are mainly composed of TiO. Grey

areas and small grey stripes are mainly composed of HA. A thorough microstructure study showed that the white curved stripes shape differed from the initial Ti particles microstructure shape, demonstrating that during the HATi coating formation, significant plastic deformation and some oxidation of Ti spots occurred. There were few pores or cracks at the interface between the white curved stripes and the grey matrix, indicating suitable contact interfaces between the HA and TiO spots. Figure 5 shows the EDS analysis of the cross-section of the HATi composite coating.

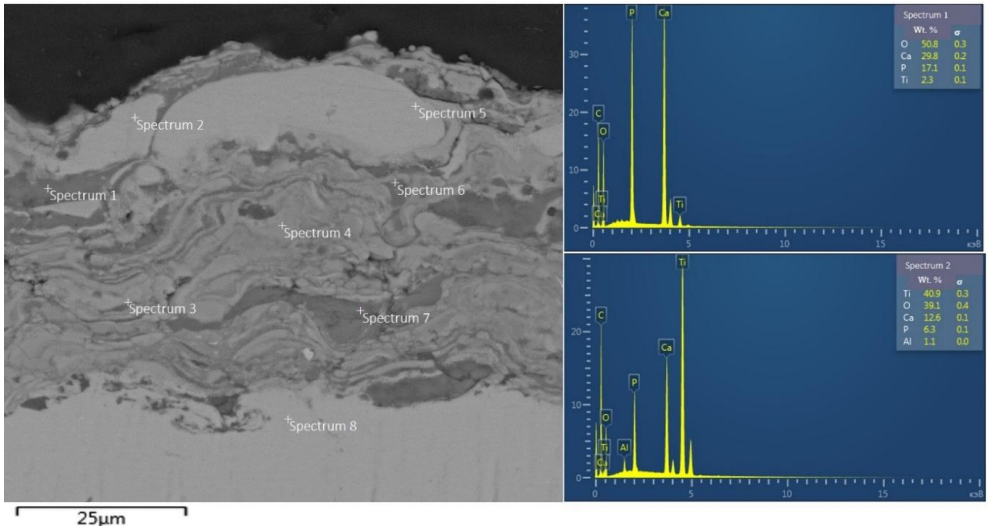

Figure 5. Cross-sectional microstructure and EDS analysis of the HATi composite coating.

Figure 6 illustrates the results of EDS analysis along the lines of the cross-section. The EDS analysis on the line showed that the HATi coverage comprises Ca, P, O, C and Ti. The SEM photos were taken in BSE mode, so areas with high brightness may indicate a high Ti content. Combined with the X-ray results, the bright white areas in the composite coating of the HATi are mainly composed of Ti, and the white regions are primarily formed of TiO. The above experimental results demonstrate that HATi coatings are dense microstructures with layered properties and compact interfaces with the Ti6Al4V substrate. During the HATi composite coating formation, strongly deformed and oxidized Ti spots led to the appearance of white curved stripes consisting of TiO and a certain amount of Ti. Limited deformation of HA spots formed a grey matrix and light grey stripes. During detonation spraying, Ti and TiO phases evolved from separate and white curved bands into interconnected and aggregated ones, forming improved frameworks in HATi composite coatings.

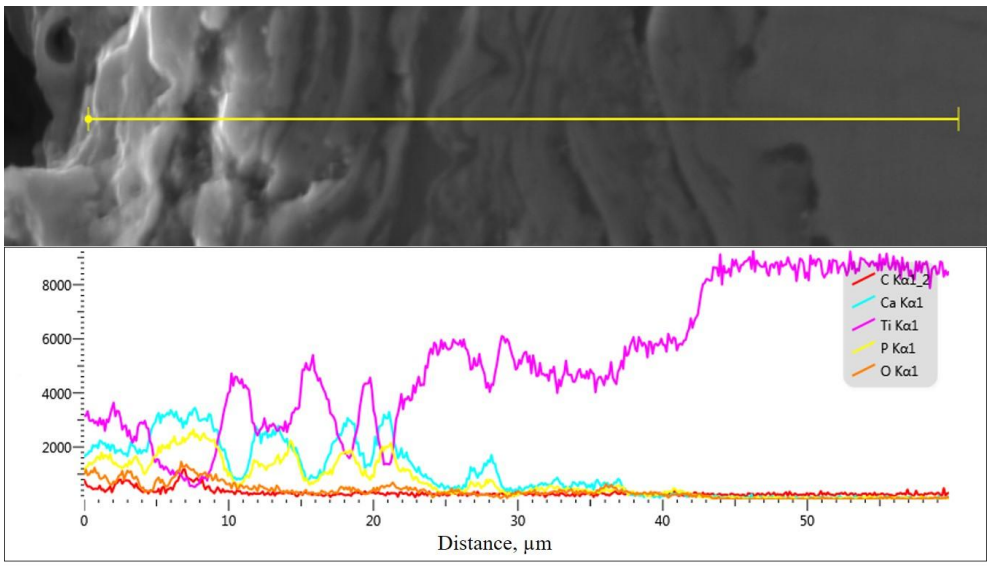

Figure 6. EDS analysis along the cross-sectional line of the HATi composite coating

Table 3 represents the measurement results of composite coatings' roughness. The coating surface has an inhomogeneous structure with pores, and typical layered wavelike arrangements of structural components are also observed. The surface roughness of composite coatings was measured using a model 130 profilometer on a 7 mm length segment on the sample surface. From the data obtained, it is established that the roughness of composite coatings by parameter has a value of Ra = 6.58.

Table 3

Measurement results of composite coatings roughness

	R_a (μm)	R_z (μm)	R_t (μm)	R_q (μm)	R_{pk} (μm)	R_k (μm)	R_v (μm)
HATi	6,58	44,3	46,6	8,42	19,9	20,3	27,6

To study the effect of Ti particles on the mechanical properties of coatings, the hardness and modulus of elasticity of composite coatings HATi were determined (Figure 7). The hardness and modulus of elasticity of composite coatings HATi were determined by nano-indentation using a triangular Berkovich pyramid. The nano-indentation curves analysis was carried out by the Oliver–Farr method. Figure 7 shows distribution graphs of hardness and modulus of elasticity over the coating depth. The average hardness and modulus of elasticity of HATi composite coatings were 7.11 = 0.16 GPa and 90.37 = 0.29 GPa, respectively. Thus, it can be argued that the formation of solid phases, TiO and Ti, can significantly improve the hardness and modulus of elasticity of coatings based on HATi. The microhardness of TiO and Ti is 9.3 GPa [17] and 4.4 GPa, respectively [38]. The interconnected textures of TiO and Ti in HATi composite coatings can increase the modulus of elasticity. The addition of Ti can increase deformable effects and enhance the impact effect of falling particles during impact, which helps to improve the phase ratio between the coating and the substrate. On the other hand, the formation of interconnected solid phases TiO by oxidation of Ti can enhance the interfacial connection of thin composite coatings HATi. The synergistic effect of these factors has significantly improved mechanical properties, including microhardness and modulus of elasticity.

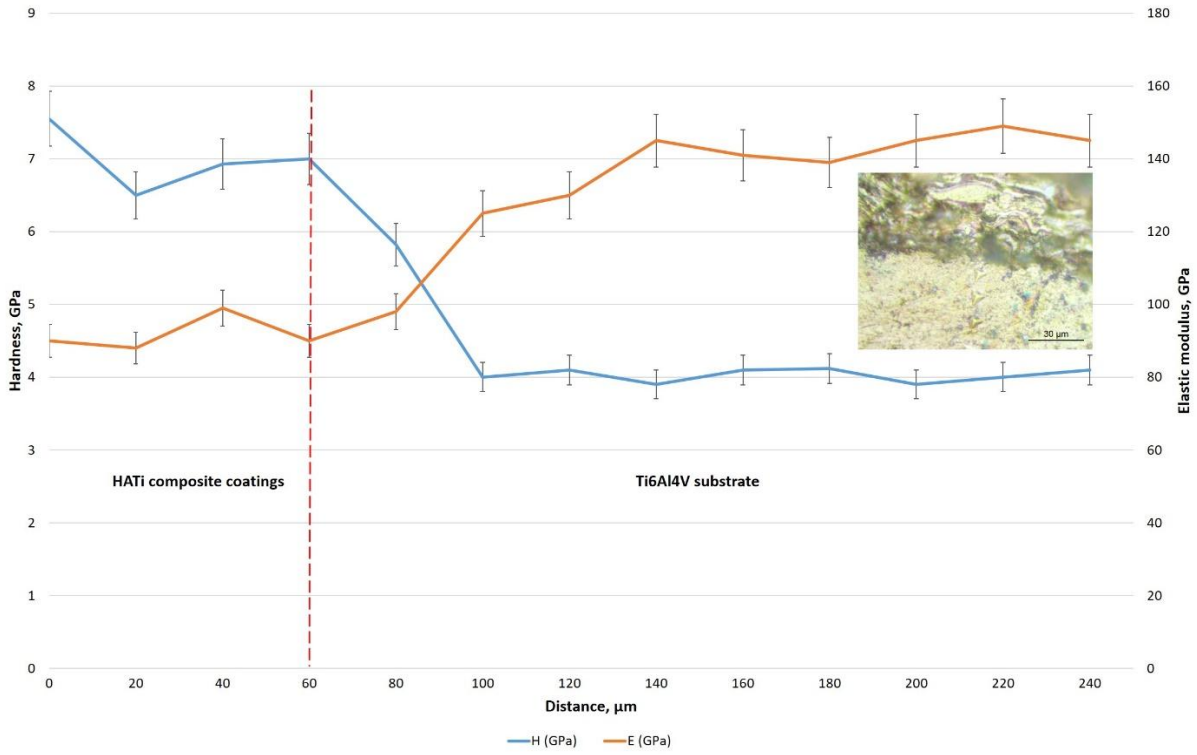

Figure 7. The hardness distribution graph and the modulus of elasticity over the depth of coatings..

Conclusions

The method of gas-detonation spraying makes it possible to successfully produce HATi composite coatings using mechanically mixed HATi powders without decomposition of the HA phase. HATi composite coatings with gas detonation spraying are a lamellar microstructure with a compact coating-substrate interface. The Ca/P ratio in composite coatings was comparable to the ratio of the initial powder. Composite coatings of HATi with gas detonation spraying showed significantly improved hardness, modulus of elasticity. The increased compactness explains these mechanical properties improvements and textures formed by well-deformed and oxidized Ti spots in HATi coatings obtained by gas-detonation spraying. According to the analysis of the results, the HATi based composite coatings obtained by gas detonation spraying demonstrate potential use as load-bearing implants in the biomaterial.

Acknowledgment

The research was funded by the Science Committee of the Ministry of Education and Science of the Republic of Kazakhstan (Grant No. AP09563455).

References

1 Corpe, R.S., Young, T.R., Steflik, D.E., Whitehead, R.Y., Wilson, M.D., & Jaramillo, C. (2000). Correlative experimental animal and human clinical retrieval evaluations of hydroxyapatite (HA)-coated and non-coated implants in orthopaedics and dentistry. *Journal of Critical Reviews in Biomedical Engineering. Prefac*, 28, 395–398.

2 Xuereb, M., Camilleri, J., & Attar, d N. (2015). Systematic review of current dental implant coating materials and novel coating techniques. *The International Journal of Prosthodontics*, 28, 51–59.

3 Singh, G., Singh, S., & Prakash, S. (2011). Surface characterization of plasma sprayed pure and reinforced hydroxyapatite coating on Ti6Al4V alloy. *Surface and Coatings Technology*, 205, 4814–4820.

4 Nawawi, N.A., Alqap, A.S.F., & Sopyan, I. (2011). Recent progress on hydroxyapatite-based dense biomaterials for load bearing bone substitutes. *Recent Patents on Materials Science*, 4, 63–80.

5 Zhao, G., Xia, L., Wen, G., Song, L., Wang, X., & Wu, K. (2011). Microstructure and properties of plasma-sprayed bio-coatings on a low-modulus titanium alloy from milled HA/Ti powders. *Surface and Coatings Technology*, 206, 4711–4719.

6 Yang, S., L, i W.H., & Man, H.C. (2013). Laser cladding of HA/Ti composite coating on NiTi *Surface Engineering of Light Alloys*. 29, 409–431.

7 Karimi, E., Khalil-Allafi, J., & Khalili, V. (2016). Electrophoretic deposition of double-layer HA/Al composite coating on NiTi. *Materials science engineering*, 58, 882–890.

8 Singh, B., Singh, G., Sidhu, B.S., & Bhatia, N. (2019). In-vitro assessment of HA-Nb coating on Mg alloy ZK60 for biomedical applications. *Materials Chemistry and Physics*, 231, 138–149.

9 Singh, B., Singh, G., & Sidhu B.S. (2019). Investigation of the in vitro corrosion behavior and biocompatibility of niobium (Nb)-reinforced hydroxyapatite (HA) coating on CoCr alloy for medical implants. *Journal of materials research and technology*, 34, 1678–1691.

10 Azari, R., Rezaie, H.R., & Khavandi, A. Investigation of functionally graded HA-TiO_2 coating on Ti–6Al–4V substrate fabricated by sol-gel method. Ceramics International, 2019, 45(14), 17545–17555.

11 Chen, H., Wang, C., Yang, X., Xiao, Z., Zhu, X., Zhang, K., Fan, Y., & Zhang, X. (2016). Construction of surface HA/TiO_2 coating on porous titanium scaffolds and its preliminary biological evaluation. *Materials Science and Engineering*, 70, 1047–1056.

12 Khazeni, D., Saremi, M., & Soltani, R. (2019). Development of HA-CNTs composite coating on AZ31 magnesium alloy by cathodic electrodeposition. Part 2: electrochemical and in-vitro behavior. *Ceramics International*, 45, 11186–11194.

13 Xiong, Y., Hu, X., & Song, R. (2017). Characteristics of CeO_2/ZrO_2-HA composite coating on ZK60 magnesium alloy. *Journal of Materials Research*, 32, 1073–1082.

14 Singh, G., Singh, H., & Sidhu, B.S. (2013). Corrosion behavior of plasma sprayed hydroxyapatite and hydroxyapatite-silicon oxide coatings on AISI 304 for biomedical application. *Applied Surface Science*, 284, 811–818.

15 Inagaki, M., Yokogawa, Y., & Kameyama, T. (2003). Bond strength improvement of hydroxyapatite/titanium composite coating by partial nitriding during rf-thermal plasma spraying. *Surface and Coatings Technology*, 173, 1–8.

16 Chengde, Gao., Shuping, Peng., Feng, Pei., & Cijun, Shuai. (2017). Bone biomaterials and interactions with stem cells. *Bone Research*, 5, 2017.

17 Hai-Long, Yao., Zhi-Hai, Yi., Chao, Yao., Meng-Xian, Zhang., Hong-Tao, Wang., Shi-Bin, Li., Xiao-Bo, Bai., Qing-Yu, Chen., & Gang-Chang, Ji. (2020). Improved corrosion resistance of AZ91D magnesium alloy coated by novel cold-sprayed Zn-HA/Zn double-layer coatings. *Ceramics International*, 46, 7687–7693.

18 Xiao, X.F., Liu, R.F., & Zhen, g Y.Z. (2005). Hydoxyapatite/titanium composite coating prepared by hydrothermal–electrochemical technique. *Materials Letters*. 59, 1660–1664.

19 Inagaki, M., Yokogawa, Y., & Kameyama, T. (2006). Effects of plasma gas composition on bond strength of hydroxyapatite/titanium composite coatings prepared by rf-plasma spraying. *Journal of the European Ceramic Society*. 26, 495–499.

20 Sun, R., Li, M., Lu, Y., & An, X. (2006). Effect of titanium and titania on chemical characteristics of hydroxyapatite plasma-sprayed into water. *Materials Science and Engineering*, 26, 28–33.

21 Rakhadilov, B.K., Baizhan, D.R., Sagdoldina, Z.B., Buitkenov, D.B., & Maulet, M. (2020). Phase composition and structure of composite Ti/HA coatings synthesized by detonation spraying. *AIP Conference Proceedings*, 2297(1), 020022.

22 Bulina, N.V., Rybin, D.K., Makarova, S..V, Dudina, D.V., Batraev, I.S., Utkin, A.V., & Ulianitsky, V.Y. (2021). Detonation spraying of hydroxyapatite on a titanium alloy implant. *Materials*, 14(17).

23 Erkmen, Z.E. (1999). The effect of heat treatment on the morphology of D-gun sprayed hydroxyapatite coatings. *Journal of Biomedical Materials Research*, 48(6), 861–868.

24 Inagaki, M., Yokogawa, Y., & Kameyama, T. (2001). Apatite/titanium composite coatings on titanium or titanium alloy by RF plasma-spraying process. *Thin Solid Films*, 222–226.

25 Qi, J., Chen, Z., Han, W., He, D., Yang, Y., & Wang, Q. (2017). Effect of deposition parameters and heat-treatment on the microstructure, mechanical and electrochemical properties of hydroxyapatite/titanium coating deposited on Ti6Al4V by RF-magnetron sputtering. Materials Research Express, 4(9), 0966409.

26 Gledhill, H.C., Turner, I.G., & Doyle, C. (1999). Direct morphological comparison of vacuum plasma sprayed and detonation gun sprayed hydroxyapatite coatings for orthopaedic applications. *Biomaterials*, 20, 315–322.

27 Gledhill, H. (2001). In vitro fatigue behaviour of vacuum plasma and detonation gun sprayed hydroxyapatite coatings. *Biomaterials*, 22, 1233–1240.

28 Kweh, S.W.K., Khor, K.A., & Cheang, P.(2002). High temperature in-situ XRD of plasma sprayed HA coatings. *Biomaterials*, 23, 381–387.

29 Buitkenov, D., Rakhadilov, B., Erbolatuly, D., & Sagdoldina, Z. (2020). Reserach of the mechanic-tribological characteristics of Ti3SiC2/TiC coatings after annealing. *Eurasian journal of physics and functional materials*, 4, 86–89.

30 Rakhadilov, B., Buitkenov, D., Idrisheva, Z., Zhamanbayeva, M., Pazylbek, S., & Baizhan, D. (2021). Effect of pulsed-plasma treatment on the structural-phase composition and tribological properties of detonation coatings based on Ti–Si–C. *Coatings*, 11(7), 795.

31 Popova, A.A., Yakovlev, V.I., Legostaeva, E.V., Sitnikov, A.A., &. Sharkeev, Y.P. (2013). The effect of the granulometric composition of a hydroxyapatite powder on the structure and phase composition of coatings deposited by the detonation gas spraying technique. *Russian Physics Journal*, 55, 1284–1289.

32 Tsygankov, P.A., Skriabin, A.S., Loktionov, E.Yu., Telekh, V.D., &Chelmodeev, R.I. (2017). On using of gas detonation for spraying of biocompatible films onto the carbon nanocomposites. *Journal of Physics: Conference Series*, 815, 12031.

33 Nosenko, V., Strutynska, N., Vorona, I., Zatovsky, I., Dzhagan, V., Lemishko, S., Epple, M., Prymak, O., Baran, N., Ishchenko, S., Slobodyanik, N., Prylutskyy, Y.,. Klyui, N, & Temchenko, V. (2015). Structure of biocompatible coatings produced from hydroxyapatite nanoparticles by detonation spraying. *Nanoscale Research Letters*, 10, 464.

34 Gryshkov, O., Klyui, N.I., Temchenko, V.P., Kyselov, V.S., Chatterjee, A., Belyaev, A.E., Lauterboeck, L., Iarmolenko, D., & Glasmacher, B. (2016). Porous biomorphic silicon carbide ceramics coated with hydroxyapatite as prospective materials for bone implants. *Materials Science and Engineering*, 68, 143–152.

35 Gryshkov, O., Klyui, N., Temchenko, V., & Glasmacher, B. (2004).Deposition of bioactive and bioinert ceramic coatings on magnesium using detonation. *Biomedical Technology*, 61, 198.

36 Ulianitsky, V., Batraev, I., Dudina, D., & Smurov, I. (2017). Enhancing the properties of WC/ Co detonation coatings using two-component fuels. *Surface and Coatings Technology, 318*, 244–249.

37 Rakhadilov, B., Maulet, M., Abilev. M., Sagdoldina, Z., & Kozhanova, R. (2021). Structure and tribological properties of Ni-Cr-Al-based gradient coating prepared by detonation spraying. *Coatings*, 11(2), 1–14.

38 Rakhadilov, B.K., Buitkenov, D.B., Tuyakbaev, B.T., Sagdoldina, Z.B., & Kenesbekov, A.B. (2019). Structure and properties of detonation coatings based on titanium carbosilicide. *Key Engineering Materials*, 821, 301–306.

Д.Р. Байжан, Б.Қ. Рахадилов, Л.Г. Журерова, Қ. Төребек

Газ-детонациялық тозаңдату әдісімен Ti6Al4V титан қорытпасында биокерамикалық композиттік жабындарды алу

Жұмыста биобелсенділік, биосәйкестік және механикалық қасиеттері үйлескен көтергіш имплантанттарды және газды-детонациялық тозаңдату әдісімен тозаңдату кезінде массалық құрамы 50:50 % болатын гидроксиапатит пен титан композитті ұнтақтарын дайындаудың жаңа тәсілін зерттеу ұсынылған. Көлденең қиманың беткі морфологиясы мен микроқұрылымының, ГаТі композиттік жабындарының фазалық құрамы мен механикалық қасиеттерінің эксперименттік зерттеу нәтижелері алынды. Эксперименттердің нәтижелері көрсеткендей, Ті композиттік жабындарының көлденең қимасының микроқұрылымдары жақсы деформацияланған және тотыққан Ті тақталарынан және шектеулі деформацияланған ГА тақталарынан құралған қисық жолақтардан тұратын типтік тақтайша құрылымдарды қамтиды. Растрлық электронды микроскопия және рентгендік дифрактометрия әдістерімен композиттік жабындардың морфологиясы мен фазалық күйлері зерттелді, оған сәйкес алынған жабындар негізінен ГА, Ті және TiO фазаларынан тұрады. Элемент құрамын зерттеу нәтижелері алынған жабындардағы кальций мен фосфордың атомдық қатынасы са/P~1,64 екені анықталды, бұл бастапқы ұнтақ — Ca/P 1,67 мәніне жақын, бұл өз кезегінде жабынды қалыптастыру кезінде химиялық құрамның шектеулі өзгеруін көрсетеді.

Кілт сөздер: газ-детонациялық тозаңдату, ГАТі композиттік жабындар, микроқұрылымдар және фазалық құрамы, механикалық қасиеттері.

Д.Р. Байжан, Б.К. Рахадилов, Л.Г. Журерова, К. Торебек

Получение биокерамических композитных покрытий на титановом сплаве Ti6Al4V методом газо-детонационного напыления

В работе представлены исследования нового подхода изготовления несущих имплантатов с сочетанием биоактивности, биосовместимости и механических свойств, композитных порошков гидроксиапатита и титана с массовым содержанием 50:50 % при напылении методом газо-детонационного напыления. Получены результаты экспериментальных исследований морфологии поверхности и микроструктуры поперечного сечения, фазового состава и механических свойств композитных покрытий ГАТi. Результаты экспериментов показывают, что микроструктуры поперечного сечения композитных покрытий ГАТi представляют собой типичные пластинчатые структуры, состоящие из изогнутых полос, образованных хорошо деформированными и окисленными пластинами Ti и ограниченными деформированными пластинами ГА. Методами растровой электронной микроскопии и рентгеновской дифрактометрии были исследованы морфология и фазовые состояния композитных покрытий, согласно которым установлено, что полученные покрытия в основном состоят из фаз ГА, Ti и TiO. Результаты исследования элементного состава показали, что атомное соотношение кальция и фосфора в полученных покрытиях составляет Ca/P~1,64, что близко к значению исходного порошка — Ca/P 1,67, что, в свою очередь, указывает на ограниченное изменение химического состава во время формирования покрытия.

Ключевые слова: газо-детонационное напыление, ГАТi композитные покрытия, микроструктуры и фазовый состав, механические свойства.

DOI 10.31489/2022PH1/99-106

UDC: 621.794

B.K. Rakhadilov[1,2], D.R. Baizhan[*2,3], Zh.B. Sagdoldina[1], K. Torebek[2]

[1]*Sarsen Amanzholov East Kazakhstan University, Ust-Kamenogorsk, Kazakhstan;*
[2]*Plasma Science LLP, Ust-Kamenogorsk, Kazakhstan*
[3]*Institute of Composite Materials, Kazakhstan*
[*]*E-mail: daryn.baizhan@mail.ru*

Research of regimes of applying coats by the method of plasma electrolytic oxidation on Ti-6Al-4V

In this work, ceramic coatings were formed on Ti6Al4V titanium alloy using a technique of plasma electrolytic oxidation. Plasma electrolytic oxidation was carried out in electrolytes with different chemical compositions and the effect of the electrolyte on the macro-and microstructure, pore size, phase composition and wear resistance of coatings was estimated. Three types of electrolytes based on sodium compounds were used, including phosphate, hydroxide, and silicate. The composition of the electrolyte affects the intensity and size of microcharges and the volume of gas release of various electrolytes. The plasma electrolytic oxidation processes were carried out at a fixed voltage (270 V) for 5 minutes. The results showed that the coating was mainly composed of rutile- and anatase TiO_2, but a homogeneous structure with lower porosity and a large number of crystalline anatase phases was obtained in the coating prepared in the silicate-based electrolyte. The diffractogram electrolytes did not reveal the peaks of the crystalline phases associated with the PO_4^{3-} and SiO_3^{2-} anions. This means that these anions included only oxygen in the coatings. The morphology and phase composition of the samples were studied using a scanning electron microscope and an X-ray diffractometer, respectively. Wear resistance was evaluated by the "ball-disc" method on the TRB^3 tribometer. The wear resistance of various coatings formed on Ti6Al4V titanium alloys showed completely different wear resistance. The lowest coefficient of friction ($\mu = 0.3$) was demonstrated by the coating obtained based on phosphate. This may be due to a large number of crystal phases of rutile. The sample prepared in a hydroxide-based electrolyte showed a high wear coefficient (μ=0.52). This effect can be obtained by eliminating surface defects (microcracks and micropores).

Keywords: plasma electrolytic oxidation, anatase, rutile, structure, phase.

Introduction

The manufacture of modern implants for traumatology and dentistry requires careful research and selection of the product material and surface treatment. Titanium alloys are the most widely used in surgery because of their bioinertness and corrosion resistance [1]. The disadvantage of using alloys, for example, Ti-6Al-4V is the content of harmful alloying components, and the use of pure titanium is hampered by insufficient strength. The solution to the problem of reducing the harmful alloying components of the metal can be found in introducing modern technology of nano-structuring into production [2]. Various methods of surface treatment have improved osseointegration and biocompatibility of titanium and titanium alloys [3], among which plasma electrolytic oxidation (PEO) has significant advantages. PEO — an ecologically pure and high-manufacturing process that makes it possible to obtain coatings with good adhesion, developed porosity for integrating osteoblast cells [4].

Recently, the PEO process has attracted considerable interest as an economically efficient, ecologically pure, and highly efficient technology for the deposition of porous and well-adhesive ceramic pellicles on Ti surfaces [5].

The features of PEO coatings lead to a process similar to anodizing of alternating current. In both processes, the metal substrate and counter electrode are conductively coupled to a power source and immersed in an aqueous electrolyte. However, in PEO, an alternating current is supplied under conditions of a higher voltage than during anodizing, which leads to the development of different surface morphologies [6].

The resulting porous oxide layer contains species obtained from the substrate and electrolytes [7]. Moreover, this porous oxide pellicle consists of an inner dense layer and an outer porous one [8]. The properties of formed PEO coatings depend on several factors, including processing time, electrical parameters, electrolyte composition, and substrate. One of these parameters, which have a great influence on the properties of PEO coatings, is the chemical composition of the electrolyte, which can be changed by changing the

concentration of the components or adding various additives. By adding various additives to the electrolyte (calcium hydroxide Ca $(OH)_2$, sodium phosphate Na_3PO_4, sodium hydroxide (NaOH), sodium phosphate silicate (Na_2SiO_3), sodium tetraborate ($Na_2B_4O_7$), and sodium fluoride (NaF) can be obtained on coatings based on hydroxyapatite and calcium phosphates [7–9].

The addition of nano– and microparticles in electrolytes can have a significant effect on the phase composition, microstructure, thickness and, consequently, on the corrosion properties of PEO coatings on titanium and its alloys. In most cases, particles can participate in PEO coatings by applying electrophoretic force and mechanical stirring. These two reinforcements transfer the negatively charged particles suspended in the electrolyte onto the oppositely charged conductive substrate. The particles are then incorporated into the PEO coating. Particles, entering, filling and sealing micropores, reduce the porosity of PEO coatings and modify the microstructure. This improved microstructure reduces the penetration of destructive ions from the coating into the substrate. It leads to an increase in the corrosion resistance of PEO coatings.

Changing the chemical composition of the electrolyte, oxidation time and electrical parameters (density, mode and frequency of current) in PEO contributes to obtaining films of biocompatible oxide — anatase (TiO_2) and to develop the surface relief in order to have a beneficial effect on the osseointegration of the implant surface in the recipient's body.

Experimental

As a substrate material for processing, we chose square-shaped samples of Ti6Al4V titanium alloy with a size of 20 mm × 20 mm × 3 mm. Table 1 illustrates the composition of the Ti6Al4V titanium alloy. The samples were ground and polished (using SiC paper with grain sizes from 100 to 2000 and using GOI paste (abrasive ability 0.3–0.1 μm)), washed with distilled water, and then dried before the PEO. For the deposition of coatings, PEO baths with different compositions were used (Table 2). In addition, 4 g of KOH (potassium hydroxide) was added to all baths to increase the conductivity of the electrolyte. The Ti6Al4V sample acted as an anode and a stainless steel container was used as a cathode. The PEO processes were performed using a constant voltage (270 V) for 5 minutes. The power source was a powerful rectifier, giving the maximum output value of 360V/100A as direct current. Using the cooling system, the temperature of the electrolyte during the experiments was cooled below 40°C. The samples were washed with distilled water and dried in a flow of cold air after each treatment. A schematic representation of the PEO installation is shown in Figure 1.

Table 1

Chemical composition of Ti6Al4V alloy (weight percent)

Ti	Al	V	Fe	C	O	N	H
88.5–92.5	5.5–6.5	3.5–4.5	<0.25	<0.08	<0.13	<0.05	<0.012

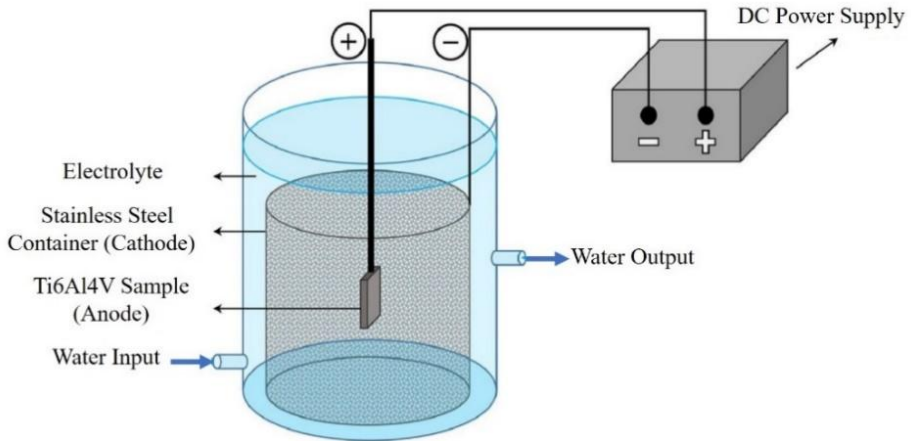

Figure 1. Schematic representation of the installation for PEO processing.

Table 2

Electrolyte composition for the PEO processes.

Electrolyte code	Electrolyte composition	Current density A/cm^2
H	20 g L^{-1} NaOH	26 A/cm^2
P	20 g L^{-1} Na_3PO_4	34 A/cm^2
S	20 g L^{-1} Na_2SiO_3	28 A/cm^2

The phase composition of the samples was studied by X-ray diffractometer X'PertPro (Philips Corporation, Netherlands) using CuKα radiation. Data processing and quantitative analysis were performed using PowderCell 2.4. The surface morphology was studied by scanning electron microscopy on a TESCAN MIRA scanning electron microscope with an electron-probe attachment for local microanalysis.

Results and Discussion

The chemical composition of the electrolyte significantly affects the acceleration of metal passivation and dielectric breakdown and, consequently, the formation of a thin insulating film [10]. Therefore, different electrolytes of different compounds (phosphate, silicate and hydroxide) were chosen here. In fact, a spark, known as a combustion phenomenon and an exothermic reaction containing an oxidizing agent, occurs as a result of absorption of a sufficient amount of oxygen. A micro-arc discharge leads to the eruption of molten substances from the discharge channels and the subsequent formation of micropores in the form of craters on the coating surface [11] (Figure 2).

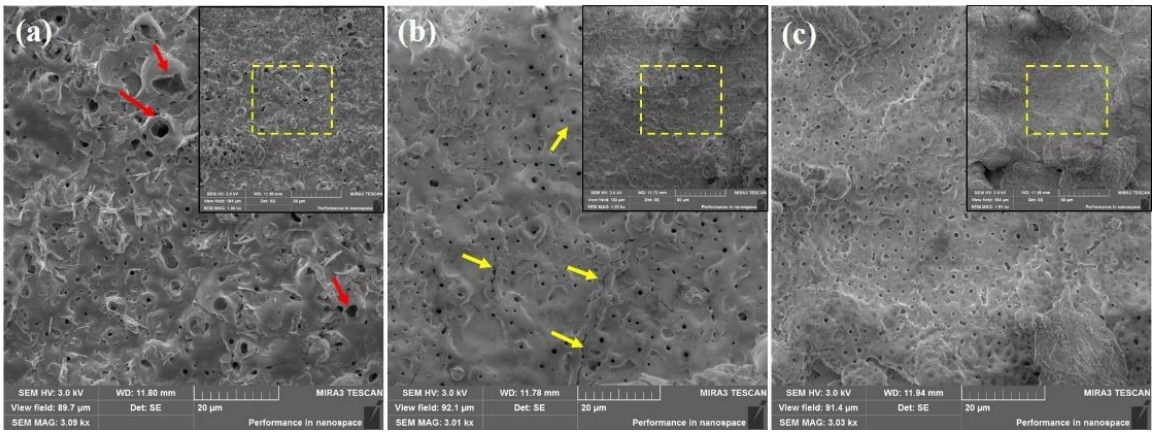

Figure 2. Surface morphology of PEO coatings of various electrolytes
(a) H, (b) P, (c) S

The spark voltages due to the nature of the electrolytes (electrolyte composition) were different for each electrolyte (Table 2). The composition of the electrolyte affects the intensity and size of microcharges and the volume of gas evolution of various electrolytes. On the surface of the sample prepared in electrolyte (H), there are several dark black spots, which can be caused by the large size and high intensity of the generated sparks at the points of low dielectric strength on the coating surface during the process.

The surface morphology of various coatings formed on Ti6Al4V titanium alloys is shown in Figures 2, 3. The coatings made with different electrolytes exhibited completely different microstructures. All coatings, due to the formation of micropores as a result of discharges accompanied by an avalanche of electrons at the interface between the electrolyte and the oxide layer, showed a typical structure of PEO, which contained micropores in the form of craters. When molten oxides leave the discharge channels and meet the surrounding electrolyte, they quickly solidify, and pores are formed on the coating surface [11]. On the other hand, a large amount of gas is formed on the discharge channels, which is then released into the electrolyte. At the early stage of the PEO process, the intensity of sparks and the amount of gas generated in the exhaust channels are much higher. Due to the gas ejection, molten oxides

are thrown out of the outlet channels, they cannot fill the outlet channels, and, accordingly, a large number of micropores are formed. Due to a decrease in the intensity of sparks, the volume of gases formed in the discharge channels decreases to some extent [12].

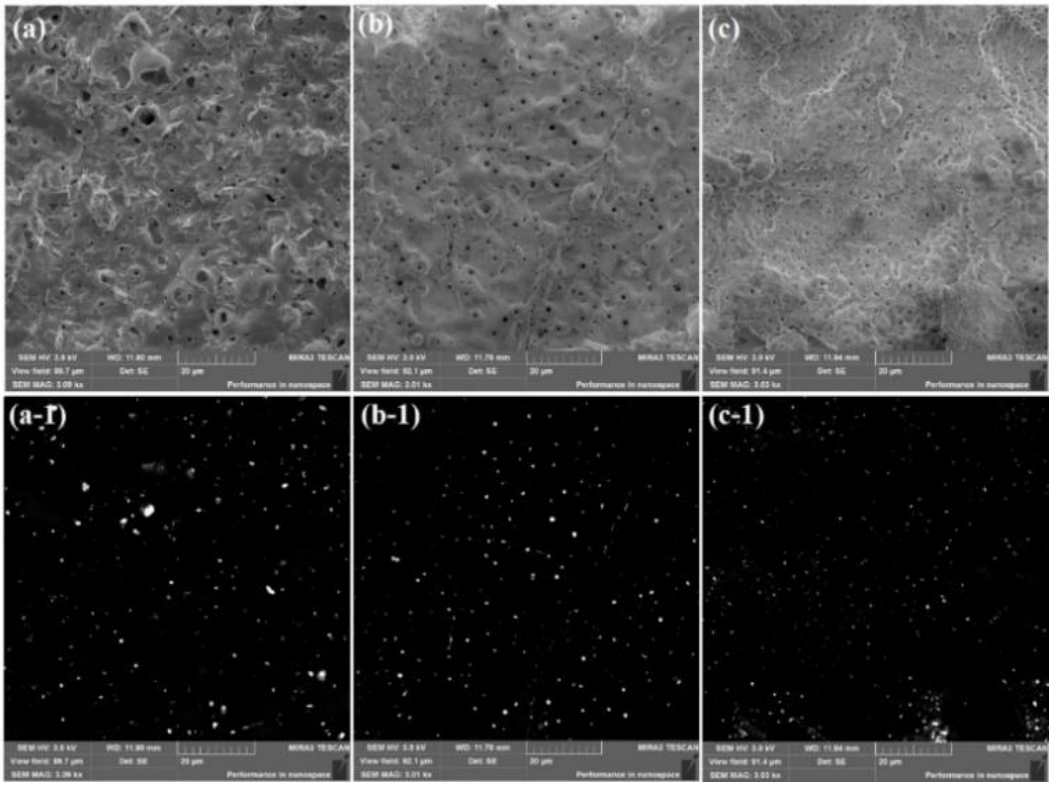

Figure 3. Pore distribution of PEO coatings in various electrolytes
(a, a-1) H, (b, b-1) P, (c, c-1) S.

In PEO processes, the characteristics of sparks and the amount of gas release affect the morphology of the coating surface. Larger sparks result in more and fewer micropores, while smaller sparks create more and smaller micropores and, consequently, form a more uniform structure. The average size of micropores and the percentage of porosity of the coatings are shown in Figure 4. According to Figures 3 and 4, it is obvious that due to the large number of small sparks and a small amount of gas evolution, the electrolyte coating (S) (Figure 3 (c, c-1)) possessed the smallest (with a porosity of 1.22 %), the smallest (with an average size of 0.48 microns) micropores. In this sample, the micropores are well distributed over the coating surface and are identical in size. The sample prepared in electrolyte (H) (Figure 3 (a, a-1)) had some large micropores with inhomogeneous dispersion, as well as large spherical condensation products formed by the rapid growth of the coating as a result of strong discharges [13]. In addition, the largest average micropore size (1.49 μm) was associated with electrolyte preparation (H). On the surface of the sample (P), several micropores and many microcracks were observed (Figure 3 (b, b-1)). Microcracks appear during the coating growth process due to the release of thermal stress and discharge activity [14]. Thus, the high temperature of the plasma discharges leads to the melting of oxides around the discharge channels, followed by rapid cooling with the electrolyte. Then, a rapid change in temperature causes the appearance of microcracks [15]. Although the average size of micropores in the sample (P) was smaller, and the percentage of porosity was higher compared to the sample (H).

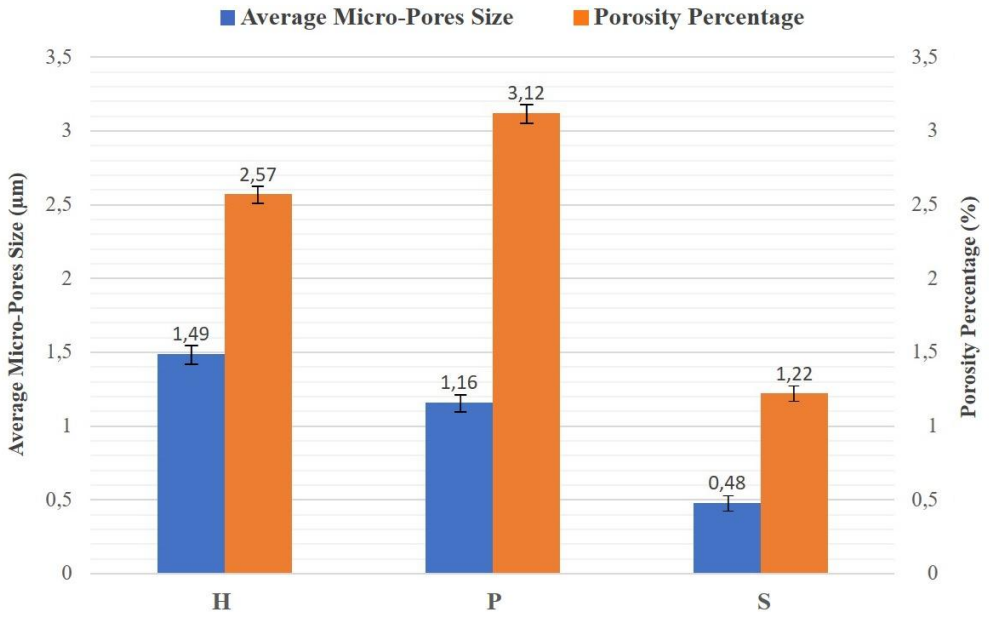

Figure 4. Average size of micropores and percentage of porosity of PEO coatings in various electrolytes.

Anatase, rutile, and brookite are the three main polymorphs of titanium oxide (TiO_2). In fact, TiO_2 and especially anatase are considered biocompatible. In addition, rutile has higher stability, high hardness, and, therefore, better mechanical properties and higher density than anatase. The temperature is low in the first stage of the PEO process. Thus, the anatase phase is formed earlier than rutile. With an increase in the applied voltage and current density, the temperature rises, and anatase is converted to rutile at 1461 °C, which is a more stable TiO_2 phase at high temperatures [16]. Diffraction patterns of coatings obtained in various electrolytes are shown in Figure 5. As can be seen in the figure, all coatings consisted of both rutile and anatase crystalline phases. The diffractogram of the (H), (P) and (S) electrolytes did not reveal the peaks of the crystalline phases associated with the PO_4^{3-} and SiO_3^{2-} anions. This means that these anions included only oxygen in the coatings.

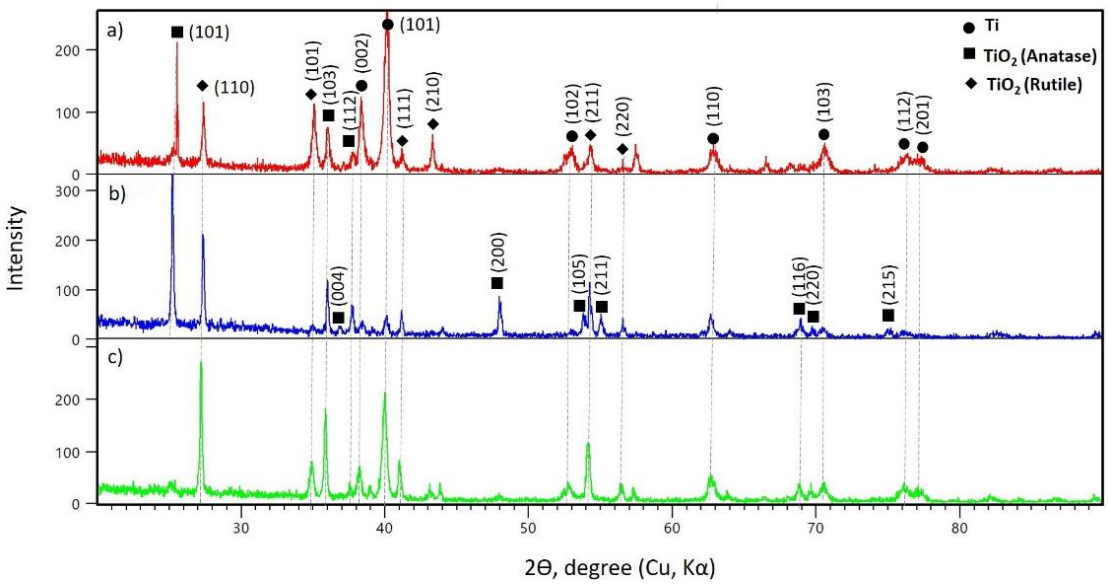

Figure 5. X-ray diffraction patterns of PEO coatings obtained in various electrolytes (a) H, (b) S, (c) P.

Quantitative analyses were performed using PowderCell 2.4. Table 3 shows the data of X-ray phase analysis.

Table 3

Results of X-ray phase analysis.

Sample	Detected Phases	Phase Structure Data in the Powder Cell Database		Structure Type	Phase Content wt.%
		Grid Type	Spatial Group		
P	Ti	hexagonal	P63/mmc (194)	D_{6h}^4	32
	TiO_2 (Anatase)	tetragonal	I41amd (141)	D_{4h}^{19}	15
	TiO_2 (Rutile)	tetragonal	P42/mnm (136)	D_{4h}^{19}	53
S	Ti	hexagonal	P63/mmc (194)	D_{6h}^4	46
	TiO_2 (Anatase)	tetragonal	I41amd (141)	D_{4h}^{19}	48
	TiO_2 (Rutile)	tetragonal	P42/mnm (136)	D_{4h}^{19}	6
H	Ti	hexagonal	P63/mmc (194)	D_{6h}^4	56
	TiO_2 (Anatase)	tetragonal	I41amd (141)	D_{4h}^{19}	18
	TiO_2 (Rutile)	tetragonal	P42/mnm (136)	D_{4h}^{19}	26

The wear resistance of various coatings formed on Ti6Al4V titanium alloys is demonstrated in Figure 6. The coatings made by different electrolytes showed completely different wear resistance. The lowest coefficient of friction (μ= 0.3) was indicated by the PEO coating (P). This may be due to many crystal phases of rutile. The sample prepared in electrolyte (H) represented a high wear coefficient (μ=0.52), this effect can be obtained by eliminating surface defects (micro-cracks and micropores).

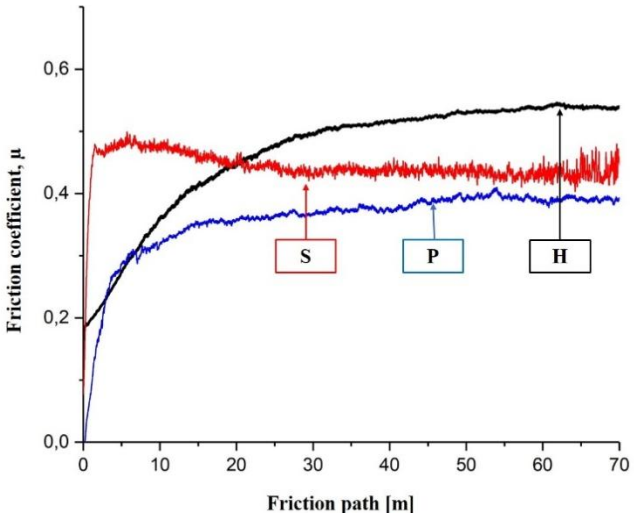

Figure 6. Results of tribological tests of PEO coatings of various electrolytes

Conclusions

The color and appearance, spark voltage and spark characteristics, surface morphology, phase composition and tribological behavior of coatings varied depending on the type of additive. The structures of the coatings formed using electrolytes containing Na_2SiO_3 additives were homogeneous and compact, with well-dispersed micropores. These technical characteristics were also associated with the formation of regular, uniform sparks during the coating process. The high electrical conductivity of the electrolyte containing Na_3PO_4 led to the formation of a coating containing relatively large micropores, with an irregular shape and distribution. Due to the release of thermal stresses during growth, this coating had micro-cracks. This coating has designated excellent wear resistance compared to other coatings. The good wear resistance of this coating is due to the high content of the rutile phase. The results of the PEO showed that the most homogeneous structure with lower porosity and numerous crystal phases of anatase were derived in a coating prepared in a silicate-based electrolyte. This mode is of practical interest from the point of view of obtaining a biocompatible coating.

Acknowledgment

This research was funded by the Science Committee of the Ministry of Education and Science of the Republic of Kazakhstan (Grant No. AP09563455).

References

1 Yao, Z.P., Jiang, Z.H., Wang, F.P., & Hao, G.D. (2007). Oxidation behavior of ceramic coatings on Ti–6Al–4V by micro-plasma oxidation. *Journal of Materials Processing Technology*, 190, 117–122.

2 Yerokhin, A.L., Nie, X., Leyland, A., Matthews A., & Dowey, S.J. (1999). Plasma electrolysis for surface engineering. Surface and Coatings Technology, 122, 73–93.

3 Yerokhin, A.L., Nie, X., Leyland, A., & Matthews, A. (2000). Characterization of oxide films produced by plasma electrolytic oxida-tion of a Ti–6Al–4V alloy. *Surface and Coatings Technology*, 130, 195–206.

4 Sun, X.T., Jiang, Z.H., Li, Y.P., Wang, F.P., & Lv, Y.D. (2005). Effect of the oxidation time on properties of ceramic coatings produced on Ti–6Al–4V by micro-arc oxidation. *Journal of Materials Processing Technology*, 21, 281–285.

5 Qaid, T.H., Ramesh, S., Yusof, F., Basirun, W.J., Ching, Y.C., Chandran, H., & Krishnasamy, S. (2019). Micro-arc oxidation of bioc-eramic coatings containing eggshell-derived hydroxyapatite on titanium substrate. *Ceramics International*, 45, 18371–18381.

6 Durdu, S., Deniz, Ö.F., Kutbay, I., & Usta, M. (2013). Characterization and formation of hydroxyapatite on Ti6Al4V coated by plasma electrolytic oxidation. *Journal of Alloys and Compounds*, 551, 422–429.

7 Liu, F., Wang, F., Shimizu, T., Igarashi, K., & Zhao, L. (2005). Formation of hydroxyapatite on Ti-6Al-4V alloy by microarc oxidation and hydrothermal treatment. *Surface and Coatings Technology*, 199, 220–224.

8 Arunnellaiappan, T. N., Kishore Babu, Rama Krishna, L., & Rameshbabu, N. (2015). Influence of frequency and duty cycle on micro-structure of plasma electrolytic oxidized AA7075 and the correlation to its corrosion behavior. *Surface and Coatings Technology*, 280, 136–147.

9 Dzhurinskiy, D., Gao, Y., Yeung, W.K., Strumban, E., Leshchinsky, V., Chu, P.J., Matthews, A., Yerokhin, A., & Maev, R.G. (2015). Characterization and corrosion evaluation of TiO2: n-HA coatings on titanium alloy formed by plasma electrolytic oxida-tion. *Surface and Coatings Technology*, 269, 258–265.

10 Rahadilov, B.K., Skakov, M.K., & Tulenbergenov, T.R. (2017). Tungsten surface erosion by hydrogen plasma irradiation. *Key Engineering Materials*, 736, 46–51.

11 Rakhadilov, B., Buitkenov, D., Sagdoldina, Z., Seitov, B., Kurbanbekov, S., & Adilkanova M. (2021). Structural features and tribological properties of detonation gun sprayed Ti–Si–C coating. *Coatings*, 11(2), 1–13.

12 Buitkenov, D.B., Rakhadilov, B.K., Sagdoldina, Z.B., & Erbolatuly, D. (2020). Reserach of the mechanic-tribological characteristics of Ti3SiC2/TiC coatings after annealing. *Eurasian Journal of Physics and Functional Materials*. 4(1), 86–92.

13 Buitkenov, D.B., Rakhadilov, B.K., Tuyakbaev, B.T., Sagdoldina, Z.B., & Kenesbekov, A.B. (2019). Structure and properties of detonation coatings based on titanium carbosilicide. *Key Engineering Materials*, 821, 301–306.

14 Buitkenov, D.B., Rakhadilov, B., Erbolatuly, D., & Sagdoldina, Zh. (2020). Influence of heat treatment on the phase composition and microhardness of coatings based on Ti_3SiC_2/TiC. *Key Engineering Materials*, 839, 137–143.

15 Rakhadilov, B., Buitkenov, D., Idrisheva, Z., Zhamanbayeva, M., Pazylbek, S., & Baizhan, D. (2021). Effect of pulsed-plasma treatment on the structural-phase composition and tribological properties of detonation coatings based on Ti–Si–C. *Coating*, 11(7), 795.

16 Rakhadilov, B.K., Baizhan, D.R., Sagdoldina, Zh.B., Buitkenov, D.B., & Maulet, M. (2020). Phase composition and structure of composite Ti/HA coatings synthesized by detonation spraying. *AIP Conference Proceedings*, 2297(1), 020022.

Б.К. Рахадилов, Д.Р. Байжан, Ж.Б. Сагдолдина, К. Торебек

Ti-6Al-4V плазмалық электролиттік тотығу әдісімен жабындарды жағу режимдерін зерттеу

Мақалада плазмалық электролиттік тотығу әдісімен *Ti-6Al-4V* титан қорытпасындағы керамикалық жабындар алынғандығы сипатталған. Плазмалық электролиттік тотығу әртүрлі химиялық құрамы бар электролиттерде жүргізілді және электролиттің макро— және микроқұрылымға әсерін, кеуектілік мөлшерін, фазалық құрамын және жабындардың тозуға төзімділігін бағалады. Натрий қосылыстарына негізделген электролиттің үш түрі қолданылды, соның ішінде фосфат, гидроксид және силикат. Электролиттің құрамы микрозарядтардың қарқындылығы мен мөлшеріне және әртүрлі электролиттердің газшығару көлеміне әсер етеді. Плазмалық электролиттік тотығу процестері тіркелген кернеу кезінде (270 В) 5 минут ішінде жүргізілді. Нәтижелер жабынның негізінен рутилден және TiO_2, анатазасынан тұратындығын көрсетті, бірақ аз кеуектілігі және көп кристалды фазалары бар біртекті құрылым силикат негізіндегі электролитте дайындалған жабындыда алынды. Электролиттердің дифрактограммасында PO_4^{3-} және SiO_3^{2-} аниондарымен байланысты кристалды фазалардың шыңдары анықталған жоқ. Бұл аниондар жабындардың құрамына тек оттегі кіргенін білдіреді. Үлгілердің морфологиясы мен фазалық құрамы сәйкесінше сканерлейтін электронды

микроскоп пен рентгендік дифрактометр көмегімен зерттелді. Тозуға төзімділік TRB^3 трибометрінде «шар-диск» әдісімен бағаланды, сонымен қатар, *Ti6Al4V* титан қорытпаларында түзілген әртүрлі жабындардың тозуға төзімділігі мүлдем басқа дәрежелерді көрсетті. Үйкелістің ең кіші коэффициенті (μ=0,3) фосфат негізінде алынған жабынмен көрсетілген. Бұл рутилдің кристалдық фазаларының көп болуына байланысты болуы мүмкін. Гидроксид негізіндегі электролитте дайындалған үлгі жоғары тозу коэффициентіне (μ=0,52) ие болды, бұл эффектіні бетіндегі ақауларды (микрожарықтар мен микрокеуектер) жою арқылы алуға болады.

Кілт сөздер: плазмалық электролиттік тотығу, анатаза, рутил, құрылым, фаза.

Б.К. Рахадилов, Д.Р. Байжан, Ж.Б. Сагдолдина, К. Торебек

Исследование режимов нанесения покрытий методом плазменного электролитического окисления на Ti-6Al-4V

В статье получены керамические покрытия на титановом сплаве *Ti6Al4V* методом плазменного электролитического окисления. Плазменное электролитическое окисление проводили в электролитах с различным химическим составом и оценивали влияние электролита на макро- и микроструктуру, размер пор, фазовый состав и износостойкость покрытий. Использовались три типа электролита на основе соединений натрия, включая фосфат, гидроксид и силикат. Состав электролита влияет на интенсивность, размер микрозарядов и объем газовыделения различных электролитов. Процессы плазменного электролитического окисления проводились при фиксированном напряжении (270 В) в течение 5 мин. Результаты показали, что покрытие, в основном, состояло из рутила и анатаза TiO_2, но однородная структура с меньшей пористостью и большим количеством кристаллических фаз анатаза была получена в покрытии, приготовленном в электролите на основе силиката. Дифрактограмма электролитов не выявила пиков кристаллических фаз, связанных с анионами PO_4^{3-} и SiO_3^{2-}. Это означает, что эти анионы включали в состав покрытий только кислород. Морфологию и фазовый состав образцов изучали с помощью сканирующего электронного микроскопа и рентгеновского дифрактометра соответственно. Износостойкость оценивалась методом «шар–диск» на трибометре *TRB*^{3}, притом износостойкость различных покрытий, сформированных на титановых сплавах *Ti6Al4V*, показала совершенно разную степень. Наименьший коэффициент трения ($\mu=0,3$) продемонстрировало покрытие, полученное на основе фосфата. Это, может быть, связано с большим количеством кристаллических фаз рутила. Образец, приготовленный в электролите на основе гидроксида, оказался с высоким коэффициентом износа ($\mu=0,52$), этот эффект может быть получен за счет устранения дефектов поверхности (микротрещин и микропор).

Ключевые слова: плазменное электролитическое окисление, анатаз, рутил, структура, фаза, дефекты поверхности.

DOI 10.31489/2022PH1/107-116

UDC 539.893

T.M. Inerbaev[1,2*], T. Matsuoka[3], Y. Kawazoe[3,4,5]

[1]*V.S. Sobolev Institute of Geology and Mineralogy SB RAS, Novosibirsk, Russian Federation;*
[2]*L.N. Gumilyov Eurasian National University, Nur-Sultan, Kazakhstan;*
[3]*New Industry Creation Hatchery Center, Tohoku University, Japan;*
[4]*Physics and Nanotechnology, SRM Institute of Science and Technology, Tamil Nadu, India;*
[5]*School of Physics, Institute of Science, Suranaree University of Technology, Thailand;*
[*]*E-mail: inerbaevtm@igm.nsc.ru; inerbaev@yahoo.com*

Optical band gap energy values in wurtzite $In_xGa_{1-x}N$

The narrow bandgap in InN has been known as a notorious example of local density approximation or generalized gradient approximation (*LDA* or *GGA*) calculations to give a metallic state. Various density functional methods are applied to optimize the atomic structures of the systems. These numerical results are used as the input values for the subsequent GW calculations, which can be applied to estimate the band gap value without phenomenological parameters. It is found that *LDA* with GW_0 or the hybrid functional with self-consistent GW_0 approximation provides sufficient theoretical results for both of the investigated compounds of GaN and InN. Although they are still time-consuming, due to less computational cost the former method is selected as a trial to compute the electronic structure in the entire range in ternary $In_xGa_{1-x}N$ alloys without any arbitrary parameters. The present theoretical studies in ternary $In_xGa_{1-x}N$ alloy were carried out by *LDA* with GW_0. As a result, a good agreement between theoretical and experimental results is obtained, and it is also shown that zone bending could be well-approximated using a quadratic function with a constant, independent of x, parameter equal to 1.85 eV, which is close to the recent experimental results.

Keywords: $In_xGa_{1-x}N$ alloys, density functional theory, GW_0 modeling, band structure, bowing parameter, band gap tuning, ternary alloy.

Introduction

The application of optical and electronic properties in nitride semiconductors with wurtzite structure has been focused on optical devices such as blue and white light-emitting-diodes [1–3], and electronic devices such as high electron mobility transistors used in the base station of cellular phones. Transistors with high power and high breakdown-voltage are expected in automobile industries for highly efficient inverters in vehicles. In these industrial applications to be realized in short time, the precise theoretical study is required for nitride semiconductors. The fundamental band gap value in InN has been uncertain up to 1980s. In early experiments in 1972 and 1986, the band gap values of about 1.9 eV and 2.1 eV were reported by measuring polycrystalline InN which was epitaxially grown with the sputtering technique and non-leak tight molecular beam epitaxy system (MBE) [4, 5]. Matsuoka predicted that this value is too large from his experiments on InGaN and single crystalline InN showed much smaller band gap energy value [6]. These values are much larger than the value of 0.7 eV reported later, which was measured from single crystalline InN [7–10]. These single crystalline InN samples were prepared by using the Molecular Beam Epitaxy (MBE) and the metalorganic vapor phase epitaxy (MOVPE) methods. A possible explanation of the results is that polycrystal is oxidized and mixed crystals of InN and In_2O_3 which band gap is 2.7 eV. The purity in single crystalline InN mentioned above is also poor. Its residual carrier concentration of 10^{17} to 10^{18} cm^{-3} is too high to accurately determine the band gap energy value because there is the Burstein-Moss effect due to the presence of residual charge carriers. It is difficult to epitaxially grow InN with high quality because the equilibrium vapor pressure of nitrogen between solid and gas phases is exceptionally high, compared with AlN and GaN [6]. Therefore, it is essential to theoretically determine the absolute band gap energy value in InN. In the present paper, the values of the band gap energy for the entire range of $In_xGa_{1-x}N$ ternary alloys are calculated using *ab initio* calculations without any empirical fitting parameters.

Experimental

The density-functional theory (*DFT*) within the local density approximation (*LDA*) or the generalized gradient approximation (*GGA*) has been extensively employed to investigate various electronic properties in post-transition metal (TM) compounds including both oxides and nitrides. *DFT* is a complete many-body the-

ory, but it is basically applicable only to the non-degenerated ground state. When *DFT* is used to estimate the band gap, the main drawback of *DFT* is that the band gap value is seriously underestimated in the ranges over 50 %-70 % for most of the post-TM compounds and reaches the value of 80 % reduction in the case of ZnO [11].In the case of InN, *DFT* gives even the negative band gap, *i.e.*, predicts InN to be metallic [12,13, 14]. For gallium nitride, the *DFT* calculation yields a strongly underestimated band gap value [13, 15]. Basically this extensional usage of *DFT* for the band gap estimation is theoretically incorrect since it is a ground state theory, and higher level of theoretical methods such as *GW* approximation is requested.

The band gap underestimation in post-TM compounds could be addressed in part by considering the on-site electron correlation energy *U*. Such an empirical treatment tries to include the effect of correlations of *d*-electrons which increases in the band gap value. However,we note that the *DFT+U* method violates the necessary condition of the virial theorem (*2T+V=0*), and tends to give the effect on other physical parameters to be non-physical. For example, the lattice-constants are reduced and also contribute widening the band gap. Alternatively, the hybrid functional scheme incorporating the exact exchange term from Hartree-Fock approximation is used to improve the band gap. However, the fraction of the exact exchange energy again should be varied among post-TM compounds to fit the band gap and it is only a phenomenological treatment [11, 12].

Modern methods of the theoretical modeling allow predicting the fundamental band gap value with high accuracy without any parameter by combining *DFT* and the quasiparticle (*QP*) theory with the exchange-correlation self-energy in *GW* approximation [16]. Taking into account *QP* corrections, this band gap problem can be solved with an accuracy of about 0.1 eV [17]. The first attempt to calculate the electronic properties of $In_xGa_{1-x}N$ ternary alloys with parameter-free theoretical technique was made in Ref. [18] using the *LDA-1/2* method [19]. This method approximately includes the self-energy of excitations in semiconductors and gives results close to calculations by the *GW* method.

The many-body perturbation theory in the *GW* approach presents a *QP* theory that overcomes the deficiencies of *LDA* and *GGA* and provides a suitable description of the band structure for weakly correlated solids such as GaN and InN. The *GW* approximation is formallythe first term in an expansion of the nonlocal and energy-dependent self-energy in the screened Coulomb interaction [20]. The self-energy operator is described as follows:

$$\sum(r,r' \in) = \frac{i}{4\pi}\int_{-\infty}^{\infty} e^{i\omega'\delta} G(r,r' \in +\omega')W(r,r')d\omega' \quad (1)$$

where *G* is Green's function, *W* is screened Coulomb interaction, and δ is infinitesimal. The evaluation of self-energy requires the wave functions and corresponding eigenvalues. If these quantities are fixed to *DFT* results, it is usually called as single-shot G_0W_0 calculations. GW_0 and *GW* approximations correspond to the case of iterative updates of the eigenvalues in the computation of *G* and *W*, respectively. A full update of the orbitals can be performed by specifying self-consistent *GW* calculations. If the orbitals and eigenvalues are updated in *G* and *W*, it is *scGW* approximation whereas $scGW_0$ corresponds to orbitals and eigenvalues update only in *G* calculations. In addition to the level of self-consistency of calculations, the results also depend on the initial conditions, i.e., from which method the eigenvalues and orbitals are derived in *GW* calculations.

Numerous studies using *GW* method have shown that the numerical results strongly dependon the initial geometry of the structure as well as on the choice of the starting wave functions [12, 13, 21-30]. Thus, the use of source structures optimized with the help of various functionals leads to a variation of the resulting numerical values of the band gap, for example from 3.366 eV (*GGA-PBE*) to 3.847 eV (*LDA*) optimized GaN wurtzite structure [30].

The choice of starting wave function for *GW* calculations is also crucial. Kang et al. [11] tested various levels of self-consistency and starting conditions to establish the most proper *GW* calculation scheme for the best exact description of the band gap value for post-TM oxides. It was found that the GW_0 scheme with *GGA+U* as the *DFT* functional turned out to give the best results in every aspect of the band structures. In one specific case of ZnO, it was proposed a modified scheme where on-site term *U* on Zn-*d* orbital was used within GW_0 scheme. Higher level of self-consistent *scGW* and employment of hybrid Heyd-Scuseria-Ernzerhof (*HSE06*) functional [31] to calculate wave functions and eigenvalues as starting conditions for G_0W_0 calculations were found to overestimate the band gap value. Pure *DFT* calculations with *LDA* or *GGA* functionals predict metallic state for InN [12, 21]. Kumar et al. [27] used the *DFT+U* to calculate the starting wave function, which made it possible to open the optical gap in the electron structure of indium nitride.

In the present paper, we tested various *GW* approaches on GaN and InN to compare their validity and accuracy. One important point is to minimize the computational time required forelectronic structure calculations, since we should use an extra-ordinally high demand computing resources for the ternary systems of InxGa1-xNas. With all of these careful theoreticalconsiderations, the optimal computational method was employed to calculate the accurate valueof the band gap energy for the InxGa1-xN ternary alloy. To investigate the electronic structure in InGaN alloys, we used 2×2×2 supercells containing 32 atoms. Supercells with 25 %, 50 %, and 75 % concentration of In atoms were considered and should provide a good approximation for the random alloy [12].

To obtain the initial calculations, all numerical calculations were performed using HSE06, Perdew-Burke-Ernzerhof (*PBE*) [32] and local density approximation (*LDA*) functionals by employing the projector augmented wave (*PAW*) method [33] as implemented in the Vienna *Abinitio* Simulation Package, *VASP* [34, 35]. The atomic structures of both InN and GaN were modeled by a fully relaxed wurtzite structure of 4 atoms (C^4_6v-*P63mc*: space group number 186) [36, 37]. The In-4*d* and Ga-3*d* electrons were treated as valence electrons. The electronic wavefunctions are described using a plane wave basis set with an energy cut-off of 600 eV. Γ-point centered k-point meshes of 6×6×6 are used throughout the calculations to obtain well-converged results for GaN and InN. Since the *DFT* calculations predict a metallic state for InN,to open the optical gap, the additional on-site correlation *DFT+U* in the Dudarev parameterization [37] was taken into account with the value of $U = 3.5$ eV.

In Ref. [21], the dependencies of theoretical band gap values were calculated depending on the choice of cutoff energies and k-space partitions. It was shown that the convergence of the calculated band gap occurs at the cut-off energy of 600 eV. By selecting a 4×4×4 k-point mesh, the calculated fundamental band gap values differ from thoseobtained on a 6×6×6 by 1.5 %. For this reason, the present numerical calculations are performed using the 2×2×2 k-point mesh.

From the theoretical point of view, state-of-the-art calculations within many-body perturbation theory allow to rigorously obtain band gap energy values. The *GW* approximation method used to compute self-energy corrections is a quite well-established and standard technique, giving energy levels generally in good agreement with experiments, even for complicated systems like reconstructed surfaces and clusters [39]. Due to high complexity and large computational require ments of *ab initio* calculations of the self-energy, this approach has rare been used to study systems with a large number of atoms in a unit cell. In the present study, were performed the investigation of the $In_xGa_{1-x}N$ alloy to estimate the band gap value in the entire composition range with GW approximation, predicting its properties without any experimental/fitting parameters.

Previous studies of $In_xGa_{1-x}N$ compounds showed poor agreement of the *DFT* band gap values with experimental data [12, 22, 40–44]. To improve consistency between theory and experiment, hybrid functionals in *DFT* have been used as an empirical simulation method. In the case of zinc blende $In_xGa_{1-x}N$ alloys, the overestimation of the band gap in the In-rich region was found [45]. For AlN, GaN, and InN with wurtzite structure, the resulting band gap values depend on the mixing ratio of the exact exchange energy functional, Mixing ratio is required to match the experimental band gaps increases with experimental band gaps [12].

Result and Discussion

To solve the problem of describing the band gap in the ternary alloy system, it is necessary to choose a suitable theoretical method that would equally accurately describe both compounds of GaN and InN. The available results in published literatures on InN and GaN *GW* band gap calculations are summarized in Table 1. It is astonishing to recognize that to date, only one study has been published in the literature which shows that the optimized effective potential (*OEP*) calculations predict well both the lattice geometry and the band gap for both nitrides.

[13] Unfortunately, this method requires enormous computational effort and cannot be applied to the study of large model cells as required by the present research on ternary alloys. Base onthis reason, we tested different approaches as initial stages to *GW* calculations in the framework of *GGA*, *LDA*, and hybrid functionals.

Besides choosing the initial wave function for calculating *GW*, which means selecting the appropriate density functional, the geometric structure of the model cells also largely determines the theoretical values of the band gap. The lattice constants of $In_xGa_{1-x}N$ ternary alloys can be obtained both as a result of theoretical calculations for lattice optimization and using interpolation formulae if we assume that the lattice parameters

of the alloys are governedby Vegard's laws. Another potential source of calculation errors is the inability to perform structural optimization in a real calculation process using the *GW* method.

In the present study, in contrast to Ref. [13], where experimental values of lattice constants were used, we explore various functionals concerning their accuracy in predicting the geometry of the unit cells. The lattice geometry found in this way is then used for GW calculations with the initial wave functions obtained with various functionals. The functional that provides the best agreement between the calculated bandgap values and the experimental ones were used for calculations using a model supercell of $In_xGa_{1-x}N$ (x=0.5) compound with lattice constants calculated according to Vegard's law for comparison.

The results of the present numerical results on the lattice parameters in GaN and InN in comparison with the experimental data are given in Table 2. The data obtained are typical for calculations carried out by DFT. In the case of InN, the hybrid functional predicts almost exactlattice-constant values, whereas the *PBE* functional overestimates, while the *LDA* functional overestimates the value of the parameter a and underestimates c. In the case of GaN, the best values of the lattice-constants are given by the calculation using the *PBE* functional, while the *HSE06* and *LDA* functionals underestimate these parameters. Thus, none of the selected methods for the optimization of the crystal lattice is preferable in comparison with experimentaldata for both considered compounds.

Table 1

Summary of the literature available high-accuracy calculations of fundamental band gap value for InN and GaN of wurzite structure

Compound	Band gap, eV	Method (based on the WF obtained with thismethod)	Reference
InN	0.71	*GW0+RPA (HSE3)*	[24]
	0.99	*scGW (LDA)*	[25]
	0.74	Hybrid approach[a)]	
	0.66	*HSE06*	[12]
	0.58	*LDA* with *SIC*[b)]	[22, 23]
	0.74	Simplified *Gc*[c)]	
	1.50	*GW SIC* (*LDA*)	
	0.82	*GW SIC* (*LDA*)	[26]
	0.8	*scGW0*	[27]
	0.7 (0.8 correction factor was applied)	*GW+RPA (LDA)*	[28]
	0.638, 0.765; 0.494[d)]	*G0W0+SOC*[e)] (*HSE*)	[30]
	0.711	*HSE06*	[21]
	0.694	*G0W0 (HSE06)*	
	0.805	*scGW0*	
	0.7	*OEPx*[6]*+G0W0(LDA)*	[13]
	0.0	*PBE*	[14]
	0.5	*HSE06*	[14]
	0.95	*LDA-1/2*	[19]
GaN	3.5	*GW*	[29]
	3.23	*HSE06*	[12]
	3.81	*scGW (LDA)*	[25]
	3.42	Hybrid approach[a)]	
	3.6 (0.8 correction factor was applied)	*GW+RPA (LDA)*	[28]
	3.659; 3.847; 3.366[d)]	*G0W0+SOC*[e)] (*HSE*)	[30]
	3.24	*OEPx*[f)]*+G0W0(LDA)*	[13]
	3.52	*LDA-1/2*	[19]

a) Combines 80 % of the *GW* self-energy with 20 % of the *LDA* self-energy as it is described in Ref. [53]; [b)] Self-interaction corrections; [c)]Quasi-particle corrections to *DFT* within a simplified *GW* approximation; [d)] Data obtained for geometries optimized using different methods (*AM05, LDA, PBE*); [e)] Spin-orbit coupling; [f)]exact-exchange optimized effectivepotential

Further, all obtained equilibrium lattice geometries were used to calculate the band gap values. For each structure, three possible wave functions were used as the starting values for the numerical calculations within

GW approximation. The results are shown in Table 3. From the presented data it can be seen that only two approaches provide sufficiently good values was an error less than 0.1 eV for both indium and gallium nitrides; namely, (case 1) $scGW_0$ approach with optimized geometry by *HSE06* and starting wave functions by *LDA*, and (case 2) GW_0 calculations with *LDA* for both geometry optimization and starting wave functions.

Table 2

The equilibrium values of the lattice-constants for InN and GaN at atmospheric pressure calculated by various methods in comparison with experimental data. Parentheses indicate the relative error of calculations

Compound	*a*, Å (error, %)	*c*, Å (error, %)	Unit cell volume, Å^3	*c/a*	*u*	Method
InN	3.533	5.693	61.50	1.611	0.375	Exp. [36]
	3.530 (-0.08)	5.700 (0.1)	61.52	1.614	0.379	*HSE06*
	3.578 (1.3)	5.777 (1.5)	64.06	1.614	0.379	*PBE*
	3.503 (0.8)	5.655 (-0.7)	60.09	1.614	0.379	*LDA*
	3.62	5.83		1.61		*PBE/HSE06* [14]
GaN	3.19	5.28	46.53	1.655	0.375	Exp. [54]
	3.176 (-0.4)	5.173 (-2.0)	45.20	1.628	0.377	*HSE06*
	3.214 (0.8)	5.235 (0.9)	46.84	1.628	0.377	*PBE*
	3.156 (-1.1)	5.140 (-2.7)	44.34	1.628	0.377	*LDA*

Thus, two theoretical approaches provide approximately the same values of the perception of both the lattice geometry and the band gap in both nitrides under study. Moreover, for the calculated values of the cell parameters, the use of the hybrid functional is somewhat closer to experimental values. On the other hand, the inclusion of the Hartree-Fock exchange in the hybrid functional raises the computation cost very significantly, especially when one uses the plane-wave basis sets [46, 47]. Besides, for the exact prediction of the width of the band gap, in this case, the $scGW_0$ method is used, which includes an additional self-consistency procedure in comparison with GW_0, which also significantly increases computational costs. Thus, based on consideration of the balance of the ability of prediction and the required computational costs, in the present study, we employed the *LDA* for structure optimization and wave functions calculation for GW_0. In the latter case, the *LDA+U* method was used on indium atoms, as indicated in "Computational method" section.

Table 3

The values of the band gap for nitrides, calculated using various methods. The valuesthat most closely coincide with the experimental values for both considered compounds are highlighted in bold

Compound	Input geometry	Input wavefunction	Bang gap calculation method			
			DFT	*G0W0*	*GW0*	*scGW0*
			Band gap, eV			
1	2	3	4			
InN	*HSE06*	*HSE06*	0.76	0.71	0.71	0.89
		PBE+U	0.09	0.21	0.27	0.50
		LDA+U	0.11	0.43	0.51	**0.73**
	PBE	*HSE06*	0.60	0.49	0.48	0.66
		PBE+U	0.04	0.07	0.30	0.30
		LDA+U	0.03	0.14	0.14	0.40
	LDA	*HSE06*	0.85	2.65	2.59	2.63
		PBE+U	0.16	0.29	0.36	0.25
		LDA+U	0.26	0.67	**0.76**	0.94
GaN	*HSE06*	*HSE06*	3.30	3.77	3.85	3.97
		PBE	1.97	3.13	3.33	3.50

1	2	3	4			
		LDA	1.99	3.16	3.38	**3.44**
	PBE	*HSE06*	3.02	3.47	3.67	3.67
		PBE	1.73	4.66	5.00	5.26
		LDA	3.03	3.47	3.57	3.63
	LDA	*HSE06*	3.46	3.93	4.01	4.14
		PBE	2.10	3.29	3.51	3.74
		LDA	2.12	3.33	**3.55**	3.69

The estimated lattice-constant values for the $In_xGa_{1-x}N$ ternary alloy as a function of x are shown in Figure 1. The present numerical calculations were carried out for a 2×2×2 supercell and the data presented was reduced to a single cell. When creating model structures, the atoms in the cases x = 0.25 and = x = 0.5, the substitution of gallium atoms was carried out in such a way as to distribute the indium atoms uniformly throughout the cell, while avoiding both the clustering of indium atoms and their ordering. The latter could lead to the appearance of periodic superstructures. Earlier results show that the clustering of indium InGaN alloy leads to a greater curvature of the curve of the band gap dependence on *x* value [51]. The case x = 0.75 is identical to x = 0.25 up to the mutual permutation of indium and gallium atoms. Test calculations on three different supercells with x = 0.5 showed a weak (< 2 %) dependence of the band gap on the choice of the atomic configuration. The geometries of all supercells have been optimized. The optimization concerned both the positions of the ions inside the supercells and the volume of the supercells. In this case, the lattice constants changed so that the volume of the optimized cell corresponded to the system at zero external pressure. The lattice symmetry was maintained constant.

It can be seen that the cell parameters are linearly dependent on the In content according to Vegard's law. The resulting atomic structures were used to calculate the band gap using the start wave functions obtained using the *LDA* functional. The obtained data are presented in Figure 2 in comparison with the available experimental data and earlier calculations using hybrid *HSE06* functional [12]. The present theoretical results, without any parameters are in excellent agreement with the experimental results.

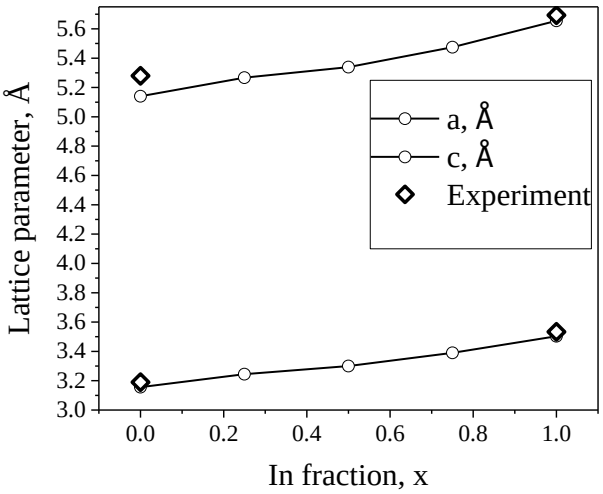

Figure 1. Calculated lattice parameters of $In_xGa_{1-x}N$ within *LDA* in comparison with experimental values [35, 53]

We also investigated the dependence of the theoretical band gap on the starting geometry of the model cell, implying that the lattice constants depend on the concentration of In and Ga according to Vegard's law. The obtained band gap for the ternary alloy of the composition $In_{0.5}Ga_{0.5}N$, obtained using *GW* calculations based on the *LDA* functional, is 1.36eV. This value is 0.29 eV less than the corresponding value calculated for a structure whose lattice constants are theoretically obtained.

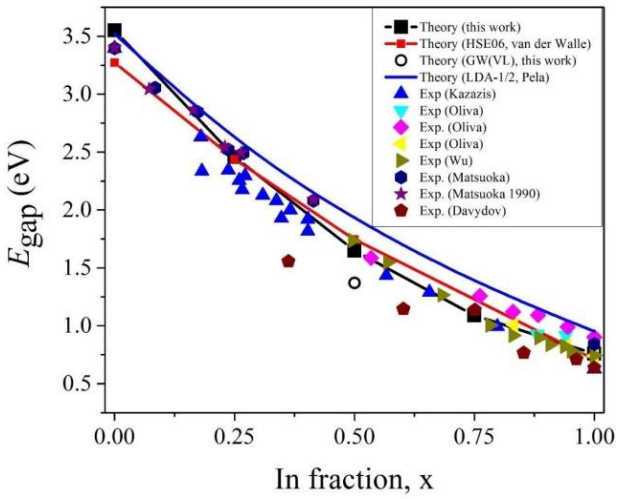

Figure 2. Theoretical and experimental values of the fundamental band gap values in Ga1-xInxNternary alloy as a function of the indium molar fraction. Theoretical results are obtained using *GW0* method (this work), *HSE06* hybrid functional [12] and *LDA*-1/2 method [18]. The band gap *GW*(VL) value was obtained for a model cell with lattice constants calculated using the Vegard's law. Experimental values are adopted from Refs. [6, 8–10, 55, 56]

The band gap in $In_xGa_{1-x}N$ as a function of the In content is of key importance for the analysis and design of efficient electronic devices. Qualitatively, there is an agreement that the band gap in $In_xGa_{1-x}N$ is a nonlinear function of the alloy composition. Conventionally, alloy band gap values are expressed as

$$E_g\,(In_x\,Ga_{1\,-\,x}N)\;=\;(1-x)\,E_g(GaN)\;+\;x\,E_{g(}InN)\,-\,bx(1-x), \qquad (2)$$

where *b* is the so-called bowing parameter. Since the most important parameter in the semiconductor alloy system is the band gap and its deviation from linear dependence characterized by the band gap bowing parameter *b*, which generally is a function of concentration. The various studies [22, 40, 43, 48–51] have disagreed on the magnitude and In concentration dependence of the bowing parameter. Some investigations show that the bowing cannot accurately be described by a composition-independent bowing parameter [12, 22, 40, 48, 52]. Wu *et al.* by optical absorption and photoluminescence measurements showed that band gap versus composition is well-described by a constant bowing parameter of 1.4 eV [10]. However, McCluskey *et al.*, obtained the bowing parameter value of 2.6 eV by carrying out optical absorption spectroscopy measurements [51]. Kazazis *et al.* measured that the intrinsic band gap value dependency on the In content is adequately expressed, for the entire range, by a bowing parameter value of 1.66±0.08 eV [8]. Fitting of our numerical results gives *b*=1.85 eV with a maximal absolute error less than 0.04 eV that is a good agreement with the most recent experiment of Kazazis *et al.*.

The above analysis corresponds to the use of a single parameter bowing calculating would be fitting (2). Moses et al. demonstrated that the bowing parameter varies with indium concentration. Namely, with an increase in the indium content, its value decreases [12]. Our results confirm this trend, although to a much lesser extent, and give *b* equal to 1.92, 1.85, and 1.79 eV for 25, 50, and 75 % of the indium content.

Conclusions

To solve the problem of band gap values in ternary InxGa1-xN alloys theoretically without phenomenological parameters, various functionals have been preliminarily tested both concerning using them to optimize the geometry of model cells and to calculate the initial wave functions for *GW* calculations applied to binary nitrides. For both InN and GaN, the acceptable accuracy is achieved either by *GW0* approximation with *LDA* or by *scGW0* method with hybrid HSE06 functional, especially the narrow band gap of InN was successfully reproduced without using the phenomenological parameters. With *LDA* the optical band gap in InN is estimated to be negative (metallic). To open it, it is necessary to use the *LDA+U* method. Since the former approach requires less computational costs, the present theoretical studies in ternary InxGa1-xN alloy were carried out by *LDA* with *GW0*. As a result, a good agreement between theoretical and experimental results was obtained, and it is also shown that zone bending could be well-approximated using a quadratic

function with a constant, independent of *x*, parameter equal to 1.85 eV, which is close to the recent experimental results.

Acknowledgements

The authors are grateful to JHPCN project as "jh190019-NAJ" on the supercomputer at Research Institute for Information Technology Kyushu University and the Center for Computational Materials Science, Institute for Materials Research, Tohoku University for their continuous support of the supercomputing system to be used for our simulation works.

References

1 Okamoto, K., Kashiwagi, J., Tanaka, T., & Kubota, M. (2009). Nonpolar *m*-plane InGaN multiple quantum well laser diodes with a lasing wavelength of 499.8 nm. *Appl. Phys. Lett.*, 94, 071105. https://doi.org/10.1063/1.3078818

2 Enya, Y., Yoshizumi, Y., Kyono, T., Akita, K., Ueno, M., Adachi, M., T. Sumitomo, T., Tokuyama, S., Ikegami, T., Katayama, K., & Nakamura, T. (2009). 531 nm Green Lasing of InGaN Based Laser Diodes on Semi-Polar {20$\bar{2}$1} Free-Standing GaN Substrates. *Appl. Phys. Express*, 2, 082101. https://doi.org/10.1143/APEX.2.082101

3 Wang, T. (2016). Development of overgrown semi-polar GaN for high efficiency green/yellow emission. *Semicond. Sci. Tech.*, No. *31*. -P. 093003. https://doi.org/10.1088/0268-1242/31/9/093003

4 Tansley T.L., & Foley, C.P. (1986). Optical band gap of indium nitride. *J. Appl. Phys.*, 59, 3241. https://doi.org/10.1063/1.336906

5 Guo, Q., & Yoshida, A. (1994) Temperature Dependence of Band Gap Change in InN and AlN. *Japanese J. Appl. Phys.*, 33, 2453. https://doi.org/10.1143/JJAP.33.2453

6 Matsuoka, T., Tanaka, H., Sasaki, T., & Katsui, A. (1990). Wide-Gap Semiconductor (In,Ga)N. *Inst. Phys. Conf. Ser.*, 199(106), 141–146.

7 Wu, J., Walukiewicz, W., Shan, W., Yu, K. M., Ager, J. W., Li, S. X., Haller, E. E., Lu, H., & Schaff, W. J. (2003). Temperature dependence of the fundamental band gap of InN. *J. Appl. Phys.*, 94, 4457. https://doi.org/10.1063/1.1605815

8 Kazazis, S. A., Papadomanolaki, E., Androulidaki, M., Kayambaki, M., & Iliopoulos E. (2018). Optical properties of InGaN thin films in the entire composition range. *J. Appl. Phys.*, 123, 125101. https://doi.org/10.1063/1.5020988

9 Oliva, R., Zelewski, S.J., Serafinczuk, L., Rudzunski, M., Ozbay, E., & Kudrawiec, R., (2018). Determination of the band gap of indium-rich InGaN by means of photoacoustic spectroscopy. *Semicond. Sci. Tech.*, 33, 035007. https://doi.org/10.1088/1361-6641/aaa908

10 Wu, J., Walukiewicz, W., Yu, K.M., Ager, J.W., Haller, E.E., & Lu, H. et al. (2002). Unusual properties of the fundamental band gap of InN. *Appl. Phys. Lett.*, 80, 3967. https://doi.org/10.1063/1.1482786

11 Kang, Y., Kang, G., Nahm, H.-H., Cho, S.-H., Park, Y.-S., & Han, S.-W. (2014). GW calculations on post-transition-metal oxides. *Phys. Rev. B*, 89, 165130. https://doi.org/10.1103/PhysRevB.89.165130

12 Moses, P.G., Miao, M.-S., Yan, Q.-M., & Van de Walle, C.G. (2011). Hybrid functional investigations of band gaps and band alignments for AlN, GaN, InN, and InGaN. *J. Chem. Phys*, 134, 84703. https://doi.org/10.1063/1.3548872

13 Rinke, P., Winkelnkemper, M., Qteish, A., Bimberg, D., Neugebauer, J., & Scheffler, M. (2008). Consistent set of band parameters for the group-III nitrides AlN, GaN, and InN. *Phys. Rev. B*, 77, 075202. https://doi.org/10.1103/PhysRevB.77.075202

14 Liang, D., Quhe, R., Chen, Y., Wu, L., Wang, Q., Guan, P., & Wangef, S. et al. (2017). Electronic and excitonic properties of two-dimensional and bulk InN crystals. *RSC Adv.*, 7, 42455. DOI 10.1039/c7ra07640a

15 Rani, A., & Kumar, R. (2017). LDA+U Study of Induced Half Metallicity in Cr-Doped GaN. *J. Supercond. Nov. Magn.*, 30, 1483. https://doi.org/10.1007/s10948-016-3938-8

16 Hybertsen, M. S., & Louie, S. G. (1986). Electron correlation in semiconductors and insulators: Band gaps and quasiparticle energies. *Phys. Rev. B*, 34, 5390. https://doi.org/10.1103/PhysRevB.34.5390

17 Bechstedt, F. (1992). *In Festkörperprobleme 32: Plenary Lectures of the Divisions of the German Physical Society (DPG)*. Berlin: Springer, 177. https://link.springer.com/book/10.1007/BFb0108617

18 Pelá, R.R., C. Caetano, C., Marques, M., Ferreira, L. G., Furthmüller, J., & Teles, L. K. (2011). Accurate band gaps of AlGaN, InGaN, and AlInN alloys calculations based on LDA-1/2 approach. *Appl. Phys. Lett., 98*, 151907. https://doi.org/10.1063/1.3576570

19 Ferreira, L. G., Marques, M., & Teles, L. K. (2008). Approximation to density functional theory for the calculation of band gaps of semiconductors. *Phys. Rev. B*, 78, 125116. https://doi.org/10.1103/PhysRevB.78.125116

20 Hedin, L., & Lundqvist, S. (1969). In Solid State Physics. *Academic Press*, 23, 1-181.

21 Duan, Y.-F., Qin, L.-X., Shi, L.-W., & Tang, G. (2015). More accurate predictions of band gap tuned by pressure in InN using HSE06 and GW approximations. *Comput. Mater. Sci.*, 101. 56. https://doi.org/10.1016/j.commatsci.2015.01.019

22 Bechstedt, F., Furthmuller, J., Ferhat, M., Teles, L.K., Scolfaro, L. M. R., & Leite, J. R. et al. (2003). Energy gap and optical properties of $In_xGa_{1-x}N$. *Phys. Status Solidi A*, 195, 628. https://doi.org/10.1002/pssa.200306164

23 Bechstedt, F., & J. Furthmuller (2002). "Do we know the fundamental energy gap of InN? *J. Cryst. Growth*, Vol. 246, 315. https://doi.org/10.1016/S0022-0248(02)01756-6

24 Piper, L.F.J., Colakerol, L., Learmonth, T., Glans, P.-A., Smith, K. E., & Fuchs, F. et al. (2007). Electronic structure of InN studied using soft x-ray emission, soft x-ray absorption, and quasiparticle band structure calculations. *Phys. Rev. B, 76*, 245204. https://doi.org/10.1103/PhysRevB.76.245204

25 Svane, A., Christensen, N.E., Gorczyca, I., van Schilfgaarde, M., Chantis, A.N., & Kotani, T. (2010). Quasiparticle self-consistent GW theory of III-V nitride semiconductors: Bands, gap bowing, and effective masses. *Phys. Rev. B,* 82, 115102. https://doi.org/10.1103/PhysRevB.82.115102

26 Furthmuller, J., Hahn, P. H., Fuchs, F., & Bechstedt, F. (2005). Band structures and optical spectra of InN polymorphs: Influence of quasiparticle and excitonic effects. *Phys. Rev. B, 72*, 205106. https://doi.org/10.1103/PhysRevB.72.205106

27 Kumar, M., Baldissera, G., Persson, C., David, D. G. F., da Silva, M. V. S., & Freitas, J. A., Tischler, Jr., J. G., Chubaci, J. F. D., Matsuoka, M., Ferreira da Silva, A. (2014). Bulk properties of InN films determined by experiments and theory. *J. Cryst. Growth*, 403, 124. https://doi.org/10.1016/j.jcrysgro.2014.06.001

28 Punya, A., & Lambrecht, W.R.L. (2012). Valence band effective-mass Hamiltonians for the group-III nitrides from quasiparticle self-consistent GW band structures. *Phys. Rev. B,* 85, 195147. https://doi.org/10.1103/PhysRevB.85.195147

29 Rubio, A., Corkill, J. L., Cohen, M. L., Shirley, E. L., & Louie, S. L. (1993). Quasiparticle band structure of AlN and GaN. *Phys. Rev. B,* 48, 11810. https://doi.org/10.1103/PhysRevB.48.11810

30 de Carvalho, L.C., Schleife, A., & Bechstedt, F. (2011). Influence of exchange and correlation on structural and electronic properties of AlN, GaN, and InN polytypes. *Phys. Rev. B, 84*, 195105. DOI:10.1103/PHYSREVB.84.195105

31 Heyd, J., Scuseria, G. E., & Ernzerhof, M. (2003). Erratum: Hybrid Functionals Based on a Screened Coulomb Potential. *J. Chem. Phys.* 118, 8207. DOI: 10.1063/1.2204597

32 32 Paier, J., Hirschl, R., Marsman, M., & Kresse, G. (2005). The Perdew-Burke-Ernzerhof exchange-correlation functional applied to the G2-1 test set using a plane-wave basis set. *J. Chem. Phys.*, 122, 234102. DOI:10.1063/1.1926272

33 Blöchl, P. E. (1994). A Projector augmented-wave method. *Phys. Rev. B,* 50, 17953. DOI:10.1103/PHYSREVB.50.17953

34 Kresse, G., & Furthmüller J., (1996). Efficient iterative schemes for ab initio total-energy calculations using a plane-wave basis set. *Phys. Rev. B*, 54, 11169. DOI: 10.1103/physrevb.54.11169

35 Kresse G., & Joubert, D. (1999). From Ultrasoft Pseudopotentials to the Projector Augmented-Wave Method. Phys. Rev. B. 59, 1758. doi:10.1103/PhysRevB.59.1758

36 Juza, R., H. Hahn, H., & Anorg, Z. (1938). Über die Kristallstrukturen von Cu3N, GaN und InN Metallamide und Metallnitride. *Allg. Chem.*, 239, 282. https://doi.org/10.1002/zaac.19382390307

37 Hellwege, K. H., & Madelung, O. (1982). *Numerical data and functional relationships in science and technology*. New York: Springer. .P. 342.

38 Dudarev, S. L., Botton, G. A., Savrasov, S. Y., Humphreys, C. J., & Sutton, A. P. (1998). Electron-energy-loss spectra and the structural stability of nickel oxide: An LSDA+U study. *Phys. Rev. B,* 57, 1505. DOI:10.1103/PHYSREVB.57.1505

39 Aryasetiawan, F., & Gunnarsson, O. (1998). The GW Method. *Rep. Prog. Phys.*, 67, 237. https://doi.org/10.1088/0034-4885/61/3/002

40 Ferhat, M., & Bechstedt, F. (2002). First-principles calculations of gap bowing in In x Ga 1 − x N and In x Al 1 − x N alloys: Relation to structural and thermodynamic properties. *Phys. Rev. B,* 65, 075213. DOI:10.1103/PHYSREVB.65.075213

41 Bellaiche, L., Mattila, T., Wang, L. W., S. H. Wei, S. H., & Zunger, A. (1999). *Appl. Phys. Lett.*, 74, 1842. DOI:https://doi.org/10.1103/PhysRevB.57.1505

42 Wright, A. F., Leung, K., & Van Schilfgaarde, M. (2001) Effects of biaxial strain and chemical ordering on the band gap of InGaN. *Appl. Phys. Lett.*, 78, 189. https://doi.org/10.1063/1.1338490

43 Teles, L. K., Furthmuller, J., Scolfaro, M. R., Leite, J. R., & Bechstedt, F. (2001). Phase separation and ordering in group-III nitride alloys. *Phys. Rev. B,* 63, 085204. DOI: 10.1590/S0103-97332004000400014

44 Kim, K., Limpijumnong, S., Rambrecht, W. R. L., & Segall, B. (1997). Elastic constants and related properties of tetrahedrally bonded BN, AlN, GaN, and InN. *Phys. Rev. B,* 449, 929. DOI:https://doi.org/10.1103/PhysRevB.53.16310

45 Wu, X., Walter, E. J., Rappe, A. M., Car, R., & Selloni, A. (2009). Hybrid density functional calculations of the band gap of GaxIn1−xN. *Phys. Rev. B,* 80, 115201. DOI:https://doi.org/10.1103/PhysRevB.80.115201

46 Hafner, J. (2008). Ab-initio simulations of materials using VASP: Density-functional theory and beyond. *J. Comput. Chem.*, 29, 2044. DOI:10.1002/jcc.21057

47 Marsman, M., Paier, J., Stroppa, A., & Kresse, G. (2008). Hybrid functionals applied to extended systems. *J. Phys. Condens. Matter*. 20, 064201. DOI: 10.1088/0953-8984/20/6/064201

48 McCluskey, M. D., Van de Walle, C. G., Romano, L. T., Krusor, B. S., & Johnson, N. M. (2003). Effect of composition on the band gap of strained InxGa1ÀxN alloys. *J. Appl. Phys.*, 93, 4340. DOI: 10.1063/1.1560563

49 Caetano, C., Teles, L. K., Marques, M., & Dal Pino, A., Ferreira, Jr., L. G. (2006). Phase stability, chemical bonds, and gap bowing of InxGa1−xN alloys: Comparison between cubic and wurtzite structures. *Phys. Rev. B,* 74, 045215. https://doi.org/10.1103/PhysRevB.74.045215

50 Gorczyca, I., Suski, T., Christensen, N. E., & Svane, A. (2010). Limitations to band gap tuning in nitride semiconductor alloys. *Appl. Phys. Lett.*, 96, 101907. https://doi.org/10.1063/1.3357419

51 Gorczyca, I., Lepkowski, S. P., Suski, T., Christensen, N. E., & Svane, A. (2009). Band gap bowing in quaternary nitride semiconducting alloys. *Phys. Rev. B,* 80, 075202. https://doi.org/10.1063/1.3597795

52 Van de Walle, C. G., McCluskey, M. D., Master, C. P., Romano, L. T., & Johnson, N. M. (1999). Large and composition-dependent band gap bowing in $In_xGa_{1-x}N$ alloys. *Mat. Sci. Eng. B-Adv.*, 59, 274. https://doi.org/10.1016/S0921-5107(98)00340-7

53 Chantis, A. N., Van Schilfgaarde, M., & Kotani, T. (2006). Ab Initio Prediction of Conduction Band Spin Splitting in Zinc Blende Semiconductors. *Phys. Rev. Letters*, 96, 086405. doi:10.1103/PhysRevLett.96.086405

54 Petkov, V., Gateshki, M., Choi, J., Gillan, E. G., & Ren, Y. (2005). Structure of nanocrystalline GaN from X-ray diffraction, Rietveld and atomic pair distribution function analyses. *J. Mater. Chem.*, 15, 4654. DOI https://doi.org/10.1039/B509577H

55 Matsuoka, T., Okamoto, H., Nakao, M., Harima, H., & Kurimoto E. (2002). Optical bandgap energy of wurtzite InN. *Appl. Phys. Lett.* 81, 1246. https://doi.org/10.1063/1.1499753

56 Davydov, V. Y., Klochikhin, A. A., Emtsev, V.V., Kurdyukov, D. A., Ivanov, S. V., & Vekshin, V. A. et al. (2002). Band Gap of Hexagonal InN and InGaN Alloys. *J. Phys. Status Solidi B Basic Res.*, 234, 787. https://doi.org/10.1002/1521-3951(200212)234:3<787::AID-PSSB787>3.0.CO;2-H Изменила название учитывая смысл: Selection inoculated additives for modifying nickel alloys ---> Selection of inoculant additives for modifying nickel alloys

Т. Инербаев, Т. Матсиока, И. Кавазое

$In_xGa_{1-x}N$ вуртциттегі оптикалық жолақ саңылауының энергия мәндері

InN тар тыйым салынған аймақ жергілікті тығыздыққа жақындағанда немесе жалпыланған градиент жақындағанда (*LDA* немесе *GGA*) есептеулер жартылай өткізгіштің орнына заттың металдық күйін болжайтын белгілі мысал болып табылады. Бұл жұмыста зерттелетін жүйелердің геометриясын оңтайландыру үшін тығыздық функционалының әртүрлі әдістері қолданылды және бұл сандық нәтижелер феноменологиялық параметрлерсіз тыйым салынған аймақ енінің мәнін бағалау кезінде болуы мүмкін *GW* әдісімен кейінгі есептеулер үшін кіріс мәндері ретінде пайдаланылды. *LDA* комбинациясын GW_0 есептеулерімен немесе гибридті функционалды GW_0 өзіне сәйкес келетін жуықтауымен пайдалану зерттелген *GaN* және *InN* қосылыстары үшін жеткілікті дәл теориялық нәтижелер беретіні анықталды. Мұндай есептеулер әлі де компьютердің көп уақытын қажет ететініне қарамастан, есептеу құнының төмен болуына байланысты, бірінші әдіс $In_xGa_{1-x}N$ үштік қорытпаларындағы барлық диапазондағы электрондық құрылымды кез келген реттеу параметрлерінсіз есептеудің сынақ әдісі ретінде таңдалды. $In_xGa_{1-x}N$ үштік қорытпасының нақты теориялық зерттеулері *LDA* GW_0 жуықтау комбинациясында орындалды. Нәтижесінде теориялық және эксперименттік нәтижелер арасында өте жақсы келісім алынды, сонымен қатар тыйым салынған аймақтың енін *x* функциясы ретінде иілу квадраттық функцияны қолдана отырып, *x*-ге тәуелді емес, 1,85 эВ параметрімен жақсы жақындастыруға болатындығы көрсетілген, бұл соңғы эксперименттік нәтижелерге жақын.

Кілт сөздер: $In_xGa_{1-x}N$ қорытпалары, тығыздықтың функционалдық теориясы, GW_0 модельдеу, жолақ құрылымы, иілу параметрі, жолақ саңылауын орнату, үштік қорытпа.

Т. Инербаев, Т. Матсиока, И. Кавазое

Значения энергии оптической запрещенной зоны в вюрците $In_xGa_{1-x}N$

Узкая запрещенная зона *InN* представляет собой известный пример, когда расчеты в приближении локальной плотности или приближении обобщенного градиента (*LDA* или *GGA*) предсказывают металлическое состояние вещества вместо полупроводникового. В настоящей работе для оптимизации геометрии исследуемых систем применены различные методы функционала плотности, и эти численные результаты использованы в качестве входных значений для последующих вычислений методом *GW*, которые могут быть при оценке значения ширины запрещенной зоны без феноменологических параметров. Установлено, что применения комбинации *LDA* с GW_0 расчетами или гибридного функционала с самосогласованным GW_0 приближением дают достаточные точные теоретические результаты для обоих исследованных соединений *GaN* и *InN*. Хотя такие расчеты по-прежнему занимают очень много компьютерного времени, из-за меньшей вычислительной стоимости первый метод выбран в качестве пробного для расчета электронной структуры во всем диапазоне в тройных сплавах $In_xGa_{1-x}N$ без каких-либо подгоночных параметров. Настоящие теоретические исследования тройного сплава $In_xGa_{1-x}N$ были выполнены в комбинации *LDA* с GW_0 приближением. В результате получено очень хорошее согласие между теоретическими и экспериментальными результатами, а также показано, что изгиб ширины запрещенной зоны как функции *x* можно хорошо аппроксимировать с помощью квадратичной функции с постоянным, не зависящим от *x*, параметром, равным 1,85 эВ, что близко к последним экспериментальным результатам.

Ключевые слова: сплавы $In_xGa_{1-x}N$, теория функционала плотности, моделирование GW_0, зонная структура, параметр изгиба, настройка запрещенной зоны, тройной сплав.

DOI 10.31489/2022PH1/117-122

UDC 538.9

N.A. Mazhenov[1], Z.R. Syzdykova[*1]

[1]*Karaganda Technical University, Kazakhstan*
[*]*E-mail: zika_0885@mail.ru*

The formation of the mixed anions $PAsO_7$ in solid solutions $Mg_2P_2O_7$ – $Mg_2As_2O_7$

The article presents structural features at formation of solid solutions of the isostructural $Mg_2P_2O_7$ and $Mg_2As_2O_7$ connections. In these compounds, complex $P_2O_7^{4-}$ anions, $As_2O_2^{4-}$, as well as the formation of complex $PAsO_7^4$ anions, is not natural. The formation of solid solutions is confirmed by the linear dependence of x-ray debaegram and optical refractive indices, depending on the concentration of P/As. In the article, phosphates are involved in energy processes in cells. For the first time, the formation of mixed anions in polyphosphates has been proven. The oscillatory spectra of pyro anions have intervals of localization of terminal and bridging groups of atoms that have no intersection regions. Strip at 662–670 cm^{-1} (between structures from P: As=0.8:0.2 to 0.1–0.9), located between v_sPOP frequency in $_\beta$ — $Mg_2P_2O_7$ at 737 cm^{-1} and the frequencies about 550 cm^{-1} characteristic of fluctuations of v_sAsOAs in alkaline pyroarsenates, is interpreted as a strip of fluctuations of v_sPOAs of the mixed $PAsO_7$ ions. In the area, the strip at 925–902 cm^{-1} is located between frequencies of fluctuations of v_{as}POP and v_{as}AsOAs. The fluctuations of mastic group P-O found in ranges of infrared absorption allow establishing knowledge of the adjacent anions $(PAsO_7)^{4-}$ that it is possible to confirm with quantum-chemical calculations in the subsequent.

Keywords: pyrophosphate, pyroarsenate, debaegram, empirical, refractometric, valence-force field, linear approximation.

Introduction

Solid solutions of Mg_2 (P, As)$_2O_7$ with molar contents of pyrophosphate and pyroarsenate varying in 10 % were obtained by thermal decomposition of the corresponding mixtures of $MgHPO_4$ and $MgHAsO_4$ at 900^0C and characterized by refractometric analysis. The obtained solid solutions are colorless, the refractive indices change linearly, with a composition from 1.585 for $Mg_2As_2O_7$ to 1.680 for α-$Mg_2P_2O_7$ (Figure 1). Debaegrams are characterized by clear reflexes, and the values of interplane distances change smoothly as the composition changes.

IR spectra of solid solutions (Specord-75 spectrometer, samples with a constant molar concentration for all compositions obtained by pressing powders with KVG) are shown in Figure 2. The assignment of frequencies in the $Mg_2P_2O_7$ spectrum has already been discussed in the literature [1, 2]. The spectrum of $Mg_2As_2O_7$ resembles that of isostructuredtorteuitite $Sc_2Si_2O_7$ [3] and the assignment of the frequencies of valence oscillations of a complex anion can be carried out by analogy with interpretating the latter spectrum (Table 1).

The structures of $Mg_2As_2O_7$ and α-$Mg_2P_2O_7$ are not identical: if the first is structurally quite similar to thortveitite [4], the second differs from it by "curved" groups of P_2O_7 ($P2_1/c$, Z=2), but already under 68^0C undergoes an α_β transformation, and the structure of the type of thortveitite for the $_\beta$ — form may be carried out by statistical averaging over the configurations of P_2O_7 groups, each of which separately may remain non — centrosymmetric [5]. Judging by the sharp broadening of the bands characteristic of the спектра-$Mg_2P_2O_7$ spectrum, it is possible to switch to this type of structure from α-$Mg_2P_2O_7$ already at 10 % arsenate content in solid solution (Figure 2).

In the spectra of solid solutions, it is possible to distinguish only three bands that have no analogues in the spectra of the extreme members of the series: 925–902, 670–662, 625–623 cm^{-1}. The last of the bands is selected (despite the presence of a band with the same frequency in the spectrum of α-$Mg_2P_2O_7$, table) based on the dependence of its intensity on the concentration of the solid solution: this band appears when adding 10 % phosphate to the arsenate, and already with the composition of P: As=0.3:0.7 practically disappears: the band $_\beta$-$Mg_2P_2O_7$ with the same frequency appears at P: As=0.5:0.5 and then monotonously increases.

The band at 662–670 cm^{-1} (in the range of compositions from P: As=0.8:0.2 to 0.1–0.9), located between the v_sPOP frequency at $Mg_2P_2O_7$ at 737 cm^{-1} and frequencies of the order of 550 cm^{-1} characteristic of v_sAsOAs oscillations in alkaline pyroarsenates [6], is interpreted as the v_sAsOAs oscillation band of mixed

$RAsO_7$ ions. In the area between the vibration frequencies of v_sPOP and v_sAsOAs, the band at 925–902 cm^{-1} is located, which can be attributed to the antisymmetric oscillation of the ROAs bridge. It should be noted that the lower value of the frequency v_sAs 829 cm^{-1}, obtained earlier when calculating the oscillations of the $PAsO_7$ ion [7], can be explained by the excessively small value of the angle ROAs (120^0) adopted for the calculation, and by the rather low force constants of the P-O (As) and As-O (P) bonds.

Table 1

Anion vibration frequencies in the IR spectra of solid solutions$Mg_2P_2O_7$ – $Mg_2As_2O_7$

Frequency assignment		Frequencies of absorption maxima in the IR spectrum (cm^{-1}) at various phosphorus contents							
Type of anion	Waveform	1,0	0,9	0,8	0,6	0,4	0,2	0,1	0,0
I, III	$v_{as}PO_3$	1206	1210	1210	1203	1200	1190	1190	1006
I, III	$v_{as}PO_3$	1185	1115	1108	1100	1090	1089	1089	900
		1136	1055	1050	1043	1042	1042	1000	879
II	$v_{as}AsOAs$	1101	1005	1003	1003	1002	1000	880	845
I	$v_{as}POP$	1080	985	970	975	975	910	845	820
III	$v_{as}POAs$	1040	975	921	916	902	883	623	505
II, III	$v_{as}AsO_3$	990	925	732	850	850	845	592	440
		970	735	620	727	665	660	505	406
II, III	$v_{as}AsO_3$	737	620	588	665	590	625	440	405
I	$v_{as}POP$	620	588	550	624	508	590	405	403
III	$v_{as}POAs$	600	550	510	590	402	505	402	405
II	$v_{as}AsOAs$	588	510	440	550	400	405	400	400

*I — P_2O_7; II — As_2O_7; III — $PAsO_7$.

Thus, the appearance of vibration bands v_sPOAs and $v_{as}POAs$ of mixed $PAsO_7$ ions convincingly proves their formation in solid solution.

It should be noted that the band at 737–727 cm^{-1} remains in the spectra of solid solutions up to the composition P: As=0.5:0.5, indicating the preservation of the curved configuration of pyrophosphate groups. The presence of this band in the spectra of compositions characterized, apparently, by the structure of the type β-$Mg_2P_2O_7$ allows us to presumably explain the appearance of a band about 625 cm^{-1} in the spectra of solid solutions with P contents from 10 to 20 % by activating the v_sAsOAs oscillation due to a violation of the statistical centrosymmetry of the $Mg_2As_2O_7$ structure. Thus, we can assume a curved configuration of the As_2O_7 groups individually and in pure $Mg_2As_2O_7$. Similarly, if the oscillation band of vAs-As is correctly identified in the spectra of solid solutions, then the comparison of its frequency with the frequency of vAs-As indicates (taking into account the results of calculating the oscillations of the $RAsO_7$ ion [8]) rather the curved shape of the p-O-As bridge in this ion, i.e. the uniformity of the structure of complex anions of any composition in the considered series of solid solutions.

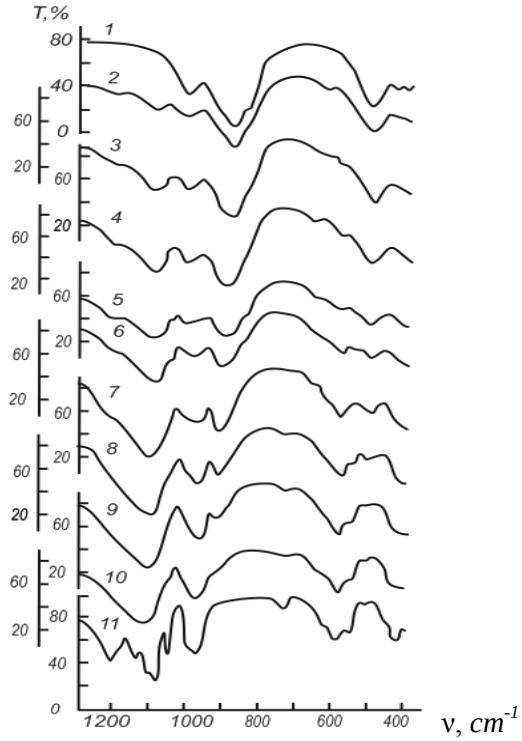

Figure 1. Change in light refraction index N of solid solution $Mg_2(P, As)_2O_7$

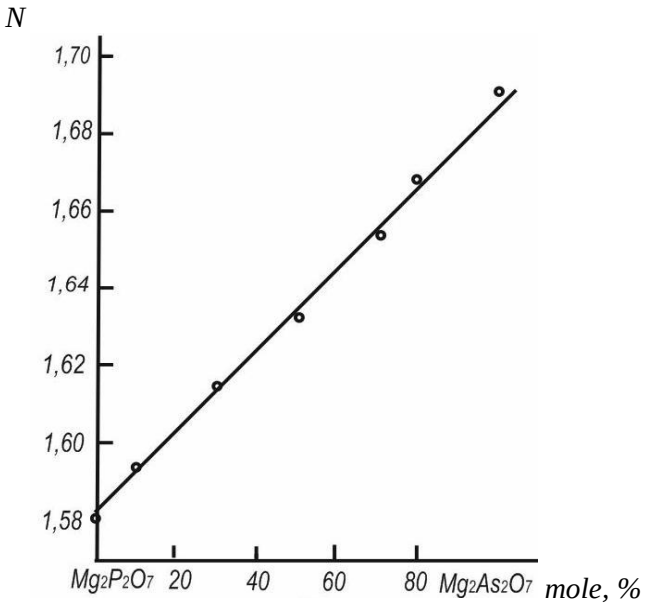

Figure 2. IR spectra of solid solutions in system $Mg_2P_2O_7$ — $Mg_2As_2O_7$

Relation P: As: 1–0,0:1,0; 2–0,1:0,9; 3–0,2:0,8; 4–0,3:0,7; 5–0,4:0,6; 6–0,5:0,5; 7–0,6:0,4; 8–0,7:0,3; 9–0,8:0,2; 10–0,9:0,1; 11–1,0:0,0

Oscillations of the crystal lattice and deformation properties of the crystal.

The structure of an ideal crystal with N atoms in a unit cell is described by specifying vectors a_1, a_2, a_3 that determine the size and shape of the unit cell, and N vectors r_i that specify the coordinates of the atoms in the cell. Homogeneous deformations are described by changes in the vectors and the increments of the vectors Δr_i form a basis convenient for describing the limit oscillations (long-wave) and the internal structural relaxation of the lattice caused by its homogeneous deformations under external influences.

For compactness of formula writing, generalized vectors are used. So, it is convenient to combine the coordinates of atoms in a cell into a 3N-dimensional vector r = (x_1, y_1, z_1, ...z_n), and describe small shifts of sub-lattices with the vector Δr.

In the valence-force field (VFF) model, so-called natural coordinates defined as small increments of valence bond lengths, angle values there between, etc. are selected as a coordinate basis for setting a potential function and for describing deformation. The whole set of translational — non-equivalent natural coordinates q_n, is described by the generalized vector $q_n = (q_1, q_2, ..., q_M)$. The dimension of this vector M is generally chosen to be greater than 3N, allowing the proposed nature of interatomic interactions in the VFF model and taking into account the symmetry properties of natural coordinates with respect to crystal factor-group operations.

The calculation of normal coordinates in the VFF model is based on the linear approximation between q and Δr, described using the matrix B:

$$q = B\Delta r$$

The potential energy of the lattice in the valence-force field model in natural coordinates is expressed as a quadratic form:

The elements of the matrix F are force constants-fitting parameters for solving the inverse spectral problem.

The elements of which determine the relative amplitudes of changes in individual natural coordinates in different normal oscillations.

From the above definitions, the relationship between the force constants, frequencies, and forms of normal oscillations follows,

$$\Lambda = Q_l^{+} F Q_l,$$

which is necessary for the analysis of various contributions to the elasticity of normal vibrations.

The elastic constants of the crystal are described by a matrix C (6 x 6), whose elements are defined as the second derivatives of the energy density for various components of the vector of homogeneous deformations: where Ω is the volume of the unit cell.

The expression for elastic constants can be obtained by directly differentiating the expression for energy if we introduce the concept of the uniform deformation form described in the linear approximation by the Q_u matrix:

$$q = Q_u u.$$

To calculate IR intensities and piezoelectric constants, information is needed about the change in the polarization of the crystal under various lattice deformations. To do this, depending on the nature of the structure of the object, different model representations are used (rigid or deformable ions, variable charges on atoms, a valence-optical scheme, etc.), which describe the dependence of the dipole moment of the cell P on the deformations Δr and u.

Conclusions

Structural features at formation of solid solutions of the isostructural $Mg_2P_2O_7$ and $Mg_2As_2O_7$ connections are considered. In these compounds, there are complex $P_2O_7^{4-}$ anions, $As_2O_2^{4-}$, as well as the formation of complex $PAsO_7^{4-}$ anions, is not natural.

Infrared absorption spectra depend on the composition of P/As. For removal of IR spectrums of solid $Mg_2P_2O_7$ solutions — $Mg_2As_2O_7$ was used the modern Specord-75 spectrophotometer, samples with constant molar concentration for all structures are received by pressing of powders with KBR. The oscillatory spectra of pyro anions have intervals of localization of terminal and bridging groups of atoms that have no intersection regions. Strip at 662–670 cm^{-1} (in the range of structures from P: As=0,8:0,2 to 0,1–0,9), located between v_sPOP frequency in β — $Mg_2P_2O_7$ at 737 cm^{-1} and the frequencies about 550 cm^{-1} characteristic of fluctuations of v_sAsOAs in alkaline pyroarsenates, is interpreted as a strip of fluctuations of v_sPOAs of the mixed $PAsO_7$ ions. The strip at 925–902 cm^{-1} is located between frequencies of fluctuations of v_{as}POP and v_{as}AsOAs. The fluctuations of mastic groups P-O found in ranges of infrared absorption — As allow to establish reliably education the adjacent anions $(PAsO_7)^4$-that it is possible to confirm with quantum-chemical calculations in the subsequent.

In the $Mg_2P_2O_7$-$Mg_2As_2O_7$ system, a continuous series of solid solutions is formed, whose IR spectra indicate the presence of mixed $[RAsO_7]^{4-}$ ions, characterized by a nonlinear configuration of P-O-As bridges.

References

1 SuFuhai, Ma Balei. Luminescence temperature and pressure studies of Zn_2SiO_4 doped by with Mn^{3+} and Eu^{3+} ions / Fuhai Su, Balei Ma // Lett. Journal Luminescence, 2006. — Vol. 116, No. 1–2. — P. 117–126.

2 Лазарев А.Н. Колебательные спектры и строение силикатов / А.Н. Лазарев. — Л.: Наука, 2001 — 348 с.

3 Sheludko V.I. Post-annealing green luminescence of sulphate crystals / V.I. Sheludko, S.G. Nedilko, V.V. Bojko // Lett. Functional Materials, 2003. — 10, 1. — P. 93–97.

4 Wang J. The atteanuation peak and elastic anomaly of $LiKSO_4$ crystal under low temperature / J.Wang, R.Wang, L. Zhang., F.Li, S.Lin // Lett. Journal Low Temperature Physics, 2002. — Vol. 11, 2. — P. 135–140.

5 Лазарев А.Н. Колебательные спектры сложных окислов / А.Н. Лазарев, А.П. Миргородский, И.С. Игнатьев. — Л.: Наука, 2000. — 296 с.

6 Alybakov A.A. Optical absortion and EPR spectra of Cu^{2+} ions in $LiKSO_4$ single crystals / A.A. Alybakov, V.A. Gubanova, K. Kudabaev, K. Sharsheev // Lett. Physica Status Solidi (b), 1988. — Vol. 146. — P. 135–139.

7 Маженов Н.А. Расчет колебаний иона [(P, As)$2O_7$] методом нормальных координат / Н.А. Маженов, О.А. Маженова, З.М. Мулдахметов // Изв. АН СССР. Неорганические материалы. — 2002. — Т. 13, № 2. — С. 391, 392.

8 Kityk I.V. Band energy calculation and optical constans of K_2SO_4 single crustals/ I.V. Kityk, B.V. Andrievckii, V.O. Yuvchenco // Lett. Physica Status Solidi (b), 1994. — Vol. 182. — P. 79–83.

Н.А. Маженов, З.Р. Сыздыкова

$Mg_2P_2O_7$ — $Mg_2As_2O_7$ қатты ерітінділерде $PASO_7$ аралас аниондарының пайда болуы

Мақалада $Mg_2P_2O_7$ және $Mg_2As_2O_7$ изоқұрылымдық қосылыстарының қатты ерітінділерінің түзілуіндегі құрылымдық ерекшеліктер қарастырылған. Олардың құрамында $P_2O_7^{4-}$ мен $As_2O_2^{4}$ күрделі аниондар бар, ал $PAsO_7^{4}$ аниондарының түзілуі табиғи емес. Қатты ерітінділердің түзілуі P/As концентрациясының функциясы ретінде рентгендік дебаеграммалардың және оптикалық сыну көрсеткіштерінің сызықтық тәуелділігімен расталады. Мақаланың өзіндік ерекшелігі мынада: фосфаттардың жасушалардағы энергетикалық процестерге қатысуы. Авторлар алғаш рет полифосфаттарда аралас аниондардың түзілуін дәлелдеген. Пироаниондардың тербелмелі спектрлерінде қиылысу аймақтары жоқ атомдардың соңғы және көпірлік топтарының локализация аралықтары болады. 662–670 $см^{-1}$ жолағы (аралық құрамы P: As=0,8:0,2-ден 0,1–0,9-ға дейін) ν_sPOP в β–$Mg_2P_2O_7$ у 737$см^{-1}$ жиілік аралығында және 550 $см^{-1}$ жиілік ретімен орналасқан, сілтілі пироарсенаттардағы ν_sAsOAs тербелістеріне тән, $PAsO_7$ аралас иондарының ν_sPOAs тербелістерінің жолағы ретінде түсіндіріледі. ν_{as}POP және ν_{as}AsOAs тербеліс жиіліктері арасындағы ауданда 925–902$см^{-1}$ жолағы орналасқан. Инфрақызыл сіңіру спектрлерінде анықталған P—O—As көпірлік топтарының тербелістері іргелес аниондардың $(PAsO_7)^{4-}$ түзілуін сенімді түрде анықтауға мүмкіндік береді, оны кейіннен кванттық химиялық есептеулермен растауға болады.

Кілт сөздер: пирофосфат, пироарсенат, дебаеграмма, эмпирикалық, рефрактометриялық, валенттік-күш өрісі, сызықтық жуықтау.

Н.А. Маженов, З.Р. Сыздыкова

Образование смешанных анионов в $PAsO_7$ в твердых растворах $Mg_2P_2O_7$ — $Mg_2As_2O_7$

В статье рассмотрены структурные особенности приобразования твердых растворов изоструктурных соединений $Mg_2P_2O_7$ и $Mg_2As_2O_7$. В них существуют сложные анионы $P_2O_7^{4-}$, $As_2O_2^{4-}$, и образование сложных анионов $PAsO_7^{4-}$ не является закономерным. Образование твердых растворов подтверждено линейной зависимостью рентгеновских дебаеграмм и оптических коэффициентов преломления в зависимости от концентрации P/As. Оригинальность статьи заключается в том, что фосфаты участвуют в энергетических процессах в клетках. Авторами впервые доказано образование смешанных анионов в полифосфатах. Колебательные спектры пироанионов имеют интервалы локализации концевых и мостиковых групп атомов, которые не имеют областей пересечения. Полоса у 662–670$см^{-1}$ (в интервале составов от P: As=0,8:0,2 до 0,1–0,9), расположенная между частотой ν_sPOP в β–$Mg_2P_2O_7$ у 737$см^{-1}$ и частотами порядка 550 $см^{-1}$, характерными для колебаний ν_sAsOAs в щелочных пироарсенатах, с оче-

видностью интерпретируется как полоса колебаний v_sPOAs смешанных ионов $PAsO_7$. В области между частотами колебаний v_{as}POP и v_{as}AsOAs расположена полоса у 925–902 $см^{-1}$. Обнаруженные в спектрах инфракрасного поглощения колебания мостиковых групп P–O–As позволяют установить надежно образование смеженных анионов $(PAsO_7)^{4-}$, что можно подтвердить квантовохимическими расчетами в последующем.

Ключевые слова: пирофосфат, пироарсенат, дебаеграмма, эмпирический, рефрактометрический, валентно-силовое поле, линейная приближения.

References

1 Su Fuhai, Ma Balei (2006). Luminescence temperature and pressure studies of Zn_2SiO_4 doped by with Mn^{3+} and Eu^{3+} ions.Lett., *J. Luminescence, 116, 1–2,* 117–126.

2 Lazerov, A.N. (2001). *Kolebatelnye spektry i stroenie silikatov [Oscillatory spectra and structure of silicates]*. Moscow: Nauka [in Russian].

3 Sheludko, V.I., Nedilko, S.G., & Bojko, V.V. (2003). Post-annealing green luminescence of sulphate crystals. *Lett., Functional Materials, 10,1,* 93–97.

4 Wang, J., Wang, R., Zhang, L., Li, F., & Lin, S. (2008). The atteanuation peak and elastic anomaly of $LiKSO_4$ crystal under low temperature. Lett., *Journal Low Temperature Physics, 11,2,* 135 — 140.

5 Lazerev, A.N., Mirgorodski, A.P., & Ignatev, I.S. (2000). Kolebatelnye spektry slozhnykh okislov [Oscillatory spectra of complex oxides]. Leningrad: Nauka, 5, 270–354 [in Russian].

6 Alybakov, A.A., Gubanova, V.A., Kudabaev, K., & Sharsheev, K. (1988). Optical absortion and EPR spectra of Cu^{2+} ions in $LiKSO_4$ single crystals. *Lett. Physica Status Solidi (b), 146,* 135 — 139.

7 Mazhenov, N.A., Mazhenova, O.A., & Muldahmetova, Z.M. (2002). Raschet kolebanii iona [$(P, As)2O_7$] metodom normalnykh koordinat [Calculation of vibrations of the [$(P, As)2O_7$] ion by the normal coordinate method]. *Izvestiia AN SSSR. Neorganicheskie materialy — Bulletion of ANSSSR. Inorganic materials, 13,* 391 [in Russian].

8 Kityk, I.V., Andrievckii, B.V., & Yuvchenco, V.O. (1994). Band energy calculation and optical constans of K_2SO_4 single crustals. Lett. *Physica Status Solidi (b), 182,* 79–83.

DOI 10.31489/2022PH1/123-129

UDC 544.14

A.B. Kuanyshbekova*, T.M. Serikov, P.A. Zhanbirbayeva,
A.E. Sadykova, G.T. Beisembaeva, A.S. Baltabekov

Karaganda University of the name of academician E.A. Buketov, Kazakhstan
**E-mail: kuanyshbekovaaya@mail.ru*

The influence of the solution of their amount on the process of water splitting by the electrolysis method

The article presents the results of an experimental study of the effect of the solution and their concentration on the process of splitting water by electrolysis under the action of a direct electric current using a Hoffman device. As solutions, we used sodium hydroxide, sodium phosphoric acid, sodium carbonate, sodium sulfate, sodium metaborate, sodium phosphoric acid 2 — substituted and potassium hydroxide. The number of salts in the solution varied from 0.2 mol to 0.8 mol. The study showed that the splitting water at constant current and voltage is influenced by both the nature of salts and their quantity. So, it was found that with the same amount of substances in the solution, the process of splitting water occurs faster in a solution containing potassium hydroxide. When using an aqueous KOH solution in an amount of 0.2 mol, the volume of hydrogen released was 15 ml, and at 0.8 mol, 19.5 ml. Using an aqueous solution of sodium metaborate with a similar concentration, the volume of hydrogen released was 2 ml and 4.5 ml, respectively. The obtained results allow to choose the solution and its amount during the process of photocatalytic splitting of water.

Keywords: water splitting, Hofmann apparatus, electrolysis, hydrogen, salt, solution, reactions, electrochemical process.

Introduction

Hydrogen is considered the ideal fuel of the future. Hydrogen fuel can be produced from clean and renewable energy sources, which will make it environmentally friendly. The sun and wind are the two main sources of renewable energy, as well as promising sources for the production of renewable hydrogen. Currently, the production of hydrogen by the above methods is not yet popular due to the high cost. Photovoltaic electrolysis of water can become more competitive, since the cost of hydrogen produced decreases with the development of technologies and materials used [1].

The photocatalytic splitting of water was first mentioned by Giacomo Ciamitian in the early 1900s [2]. Later, in 1970, Honda and Fujishima experimentally proved the possibility of splitting water by using a wide-band semiconductor and solar energy. Since then, revolutionary research by scientists on the photoelectrochemical decomposition of water has been published [3–9]. The works are mainly devoted to the study of the photocatalyst and its modification to improve the ability to split water [10–14]. However, it is necessary to take into account that even using a highly efficient photocatalyst, the splitting of distilled water is extremely difficult. Therefore, it becomes necessary to add sources of donor electrons to the purified water, which can serve as organic compounds methanol, ethanol and lactic acid, which significantly enhances the interaction of the electron/hole of the semiconductor and the solution used, leading to higher quantum efficiency [15, 16]. The addition of carbonate salts Na2CO3, HCO2–, C2O2- to water also increases the production of hydrogen and oxygen [17]. It can be concluded that the process of photo-splitting of water is affected not only by the high performance of the photocatalyst but also by the solution where the splitting of the water molecule into hydrogen and oxygen occurs, which makes this work relevant.

This paper presents the results of a study of the effect of the solution (sodium hydroxide, sodium phosphoric acid, sodium carbonate, sodium bicarbonate, sodium sulfate, sodium metaborate, sodium phosphoric acid 2 — substituted and potassium hydroxide) and their amounts on splitting water.

Experimental

To determine the effect of the solution on the water-splitting process, the following were used: sodium hydroxide (NaOH), sodium phosphoric acid 3 substituted (Na3PO4), sodium carbonate (Na2CO3), sodium bicarbonate (NaHCO3), sodium sulfate (Na2SO4), sodium metaborate (NaBO2), sodium phosphoric acid 2 substituted (Na2HPO4), potassium hydroxide (KOH). All the salts were dissolved in distilled water in a

volume of 150 ml. The requirement for all samples was presented in the same way. The amount of the substance varied from 0.2 mol to 0.8 mol. The amount of hydrogen released at the cathode and oxygen at the anode was recorded every 5 minutes, with a total duration of 60 minutes.

All experimental work was carried out by electrolysis at constant voltage using the Hoffmann apparatus. The diagram of the working chamber of the Hoffmann apparatus is shown in Figure 1. The device consists of three vessels, each with a volume of 50 ml. Three vertical, glass communicating vessels, one of which is open and designed to inject an aqueous solution. Platinum electrodes are placed in the lower part of the vertical vessels. The electrodes are connected to the positive and negative poles of the current source. The electrolysis voltage is 3 V. When a voltage source is connected to the network, the electrolysis process takes place. The volume of hydrogen and oxygen released is recorded by the volume of the solution displaced by the gas. A universal power supply PHYWE with direct and alternating current was used as a voltage source.

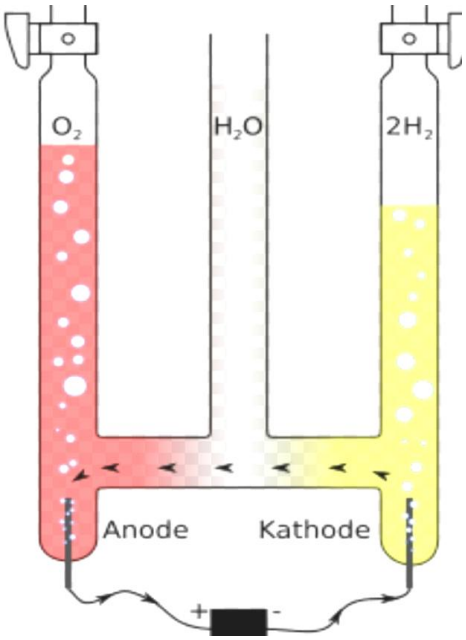

Figure 1. Scheme of the Hoffmann apparatus of three vessels

Sodium hydroxide NaOH is a solid substance, that dissolves well in water and emits a large amount of heat. Solubility in water 108.7 g per 100 ml temperature + 15 ^{0}C. KOH potassium hydroxide-solubility in water 107 g per 100 ml temperature +15 ^{0}C. Na2HPO4 sodium hydrophosphate-forms colorless crystals. It is well soluble in water. Solubility temperature +100 0C. Na2SO4 sodium sulphate g / 100ml at 0 °C -4.5 g, at 20 °C — 19.2 g, at 32.4 °C — 49.8 g at 100 °C — 42.3 g. Sodium acid Na2CO3 is insoluble in acetone and carbon disulfide, slightly soluble in ethanol, well soluble in glycerin and water. NaHCO3 has a low solubility of sodium bicarbonate in carbon dioxide water and increases slightly with increasing temperature: from 6.87 g per 100 g of water at 0 °C to 19.17 g per 100 g of water at 80 °C. Due to its low solubility, the density of saturated aqueous solutions of sodium bicarbonate differs little from the density of pure water. Sodium metabolate NaBO2 forms colorless hygroscopic crystals of trigonal syngony, dissolves well in water, easily forms saturated solutions. Na3PO4 sodium phosphate acid is highly soluble in water — 12.1 g / 100 ml. Together with water, a crystallohydrate with the general formula Na3PO4 ·12H2O is formed.

Results and Discussion

The effects of solutions of sodium hydroxide (NaOH), sodium phosphoric acid 3 substituted (Na3PO4), sodium carbonate (Na2CO3), sodium bicarbonate (NaHCO3), sodium sulfate (Na2SO4), sodium metaborate (NaBO2), sodium phosphoric acid 2 substituted (Na2HPO4), potassium hydroxide (KOH) at various amounts are illustrated in Figure 2.

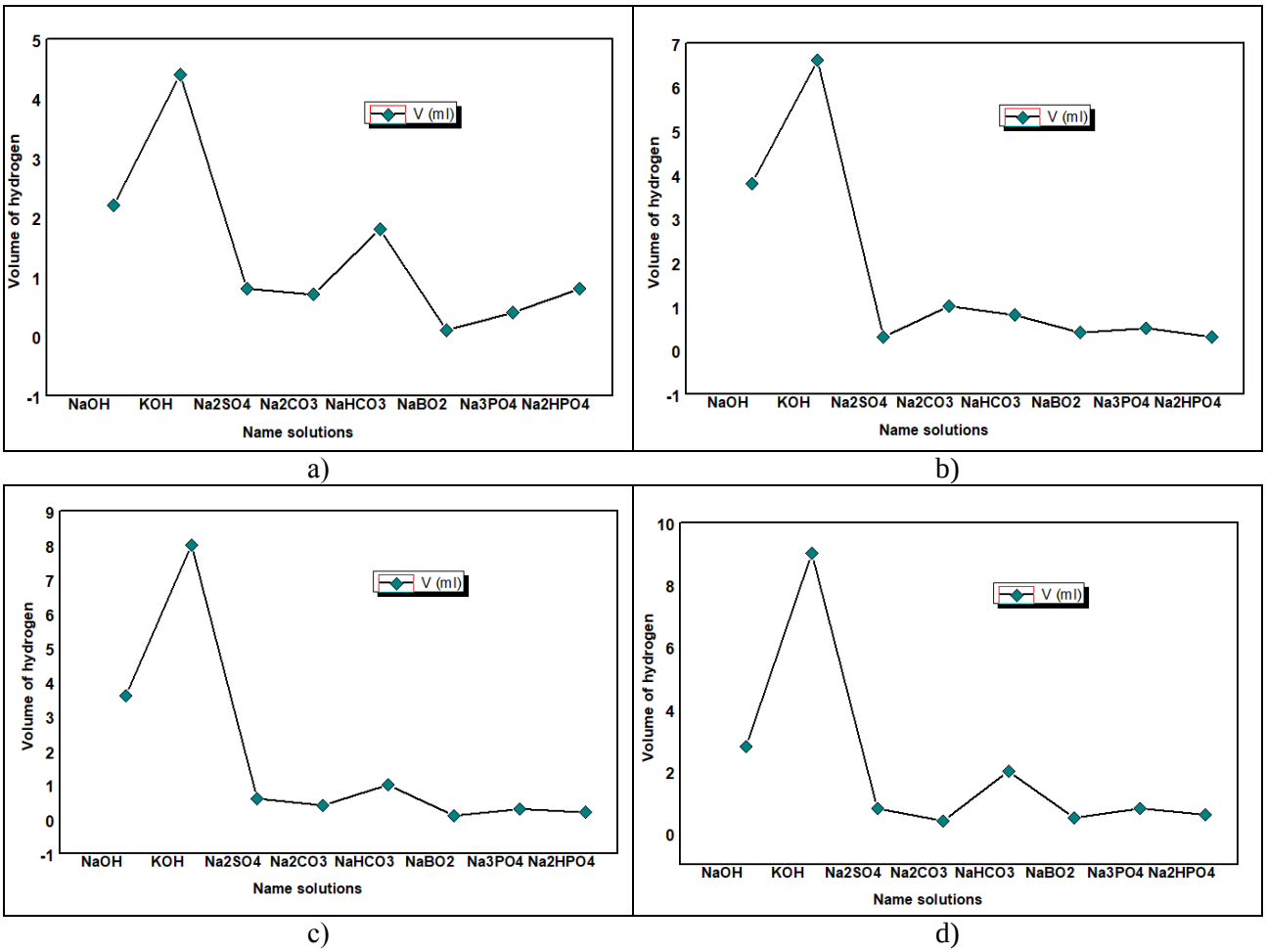

a– (0,2 mol); b — (0,4 mol); c — (0,6 mol); d — (0,8 mol)

Figure 2. The effect of solutions on the process of splitting water by electric riveting.

Figure 2a demonstrates that when using hydroxide groups, carbonate salts and phosphates in the amount of 0.2 mol, the volume of hydrogen gas released is different. Moreover, when using a solution containing potassium hydroxide (KOH), the volume of hydrogen released is higher than with the other groups. For example, the volume of hydrogen released for him was 4.5 ml. The highest value of the released hydrogen belongs to a solution containing sodium metaborate NaBO2 (v= 0.2 mol) and is 0.2 ml. The remaining solutions occupy an intermediate value. Figure 2b represents that when the number of salts in the distilled water increased to 0.4 mol, the volume of hydrogen released increased 1.5 times for potassium hydroxide (KOH) and sodium hydroxide (NaOH), and when using Na3PO4, Na2CO3, NaHCO3, Na2SO4, NaBO2, Na2HPO4 remained practically unchanged and was in the range from 0 to 1 ml. A further increase in the number of salts in water to 0.6 mol showed (Figure 2c) that when using potassium hydroxide, the volume of hydrogen released increased by 2 times compared to 0.2 mol, while sodium hydroxide practically remained unchanged. An increase in the number of salts in the solution to 0.8 mol led to a decrease compared to 0.4 mol, and amounted to 2.8 ml (Figure 2 d). From the data obtained, it can be concluded that the best medium for splitting hydrogen is a solution containing 0.8 mol of potassium hydroxide, and the worst is sodium metaborate NaBO2. An increase in the amount of the substance in the water to 1 mol did not lead to an increase in the volume of hydrogen released.

Figure 3 shows the dependence of the volume of hydrogen released on the duration of electrolysis, with the amount of potassium hydroxide in the solution varying from 0.2 to 0.8 mol.

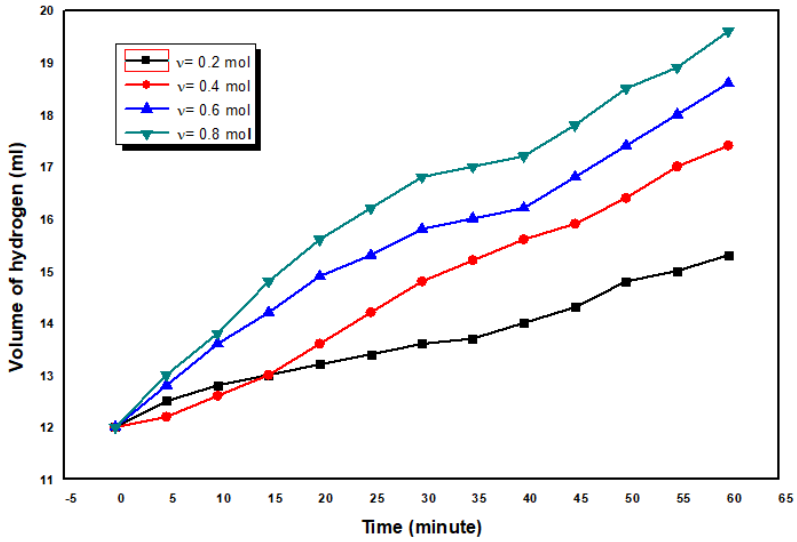

Figure 3. The effect of the amount of potassium hydroxide on the process of splitting water by electric riveting

One can see that during the electrolysis process lasting 60 minutes, the volume of hydrogen released increases with the amount of potassium hydroxide in water from 0.2 mol to 0.8 mol. So, at 0.2 mol, the volume of gas was 15 ml, and at 0.8 mol, 19.5 ml.

The solutions that we used in the experiment are called colloidal. Colloidal solutions are systems that comprise a solid dispersed phase distributed in a liquid or solid dispersion medium. Solutions are always single-phase, which are homogeneous gas, liquid or solid. This means that one of the substances is distributed in the mass of the other in the form of molecules, atoms, or ions.

Electrolysis of solutions is a complex process because, besides metal ions and acid residue, water molecules and H^+ and OH^- ions are present in the solution, which can also participate in the redox process during passaging electric current. To correctly determine the products formed in the electrodes during the electrolysis of hydrophytic solutions of electrolytes, it is necessary to adhere to the following important rules, which occur in the cathode and anode.

The passing process at the cathode depends on the position of the metal in the electrochemical series. Our solutions are part of the active metal activity: K, Ba, Ca, Na in which water is reduced to hydroxide ion to hydrogen, and only hydrogen is released at the cathode because of the reduction of water molecules.

$$2H_2O + 2\bar{e} = H_2 + 2OH^-$$

The strongest reducing agent is oxidized at the anode. During electrolysis of solutions of acid-containing salts oxygen is released on the anode O_2

$$2H_2O — 4\bar{e} = O_2 + 4H^+$$

Electrolysis Na_2So4.

(-) Cathode $\longleftarrow$ $2Na^+ + SO_4^{2-} \longrightarrow$ Anode (+)

Cathode: $2H_2O + 2e^- = \mathbf{H_2}\uparrow + 2OH^-$

Anode: $2H_2O — 4e^- = \mathbf{O_2}\uparrow + 4H^+$

Total: $2H_2O = 2H_2\uparrow + O_2\uparrow$

Conclusion: the electrolysis of this salt is reduced to the decomposition of water; salt is necessary to increase electrical conductivity, since pure water is a weak electrolyte.

Electrolysis KOH.

Cathode (-) $\longleftarrow$ $K^+ + OH^- \longrightarrow$ Anode (+)

Potassium cations will not be restored at the cathode since potassium is in the metal voltage range to the left of aluminum, instead, water molecules will be restored:

Cathode: (-) $2H_2O + 2e = H_2 + 2OH^-$

Anode: (+) $4OH^- — 4e = 2H_2O + O_2$

Total: $4H_2O + 4OH^- = 2H_2 + 4OH^- + 2H_2O + O_2$ $2H_2O = 2H_2 + O_2$

Electrolysis NaOH.

$4NaOH = 4Na + O_2 + 2H_2O$
Cathode: $2H_2O + 2e = H_2 + 2OH^-$
Anode: $4OH^- — 4e^- = O_2 + 2H_2O$
Water molecules are restored at the cathode. The growth of sodium hydroxide is reduced to the electrolysis of water.
Electrolysis Na_2CO_3.
Water electrolysis occurs:
$H_2O = H^+ + OH^-$
Cathode (K^-): $2H_2O + 2e^- = H_2 + 2OH^-$
Anode (A^+): $4OH^- — 4e^- = 2H_2O + O_2$
Total: $2H_2O = 2H_2 + O_2$
Sodium, as an alkaline metal, is not released at the cathode, and the CO_3^{2-} ion is also not discharged, as an acidic residue of an oxygen-containing acid.
Electrolysis $NaHCO_3$.
Cathode (-) $H_2O+2e=H_2+2OH^-$
Anode (+) $2H_20–4e=O_2 +4H^+$
The equation: $NaHCO_3+2H_2O = O_2+2H_2+NaHCO3$
In the equations of solution electrolysis $NaHCO_3$ there will be water electrolysis reactions, the oxidation of the bicarbonate ion does not occur.
Electrolysis Na_3PO_4.
Cathode: $2 H^+ +2e= H_2$
Anode: $4OH^- — 4e= 2H_2O + O_2$
The equation: $Na_3PO_4 +5H_2O= 3NaOH +2H_2 + O_2 +H_3PO_4$

Hydrogen is released at the cathode and oxygen is released at the anode due to the electrolysis of water. Sodium cations are not reduced, since the electrode potential is lower than that of hydrogen. An excess of sodium hydroxide is formed in the near-cathode space. Hydroxide anions (water) are oxidized at the anode, oxygen is released. Phosphate anions are not oxidized, since their potential is higher. There is an excess of weak orthophosphoric acid in the near-anodyne space. In general, sodium orthophosphate salt is not subjected to electrolysis in this case.

The process at the cathode depends on the position of the metal in the electrochemical series. Our solutions belong to the range of activity of active metals: K Ba Ca Na, in which water is reduced to the hydroxide ion to hydrogen, and only hydrogen is released at the cathode due to the reduction of water molecules. It can be said that the electrolysis of salts is reduced to the decomposition of water, and salt is necessary to increase electrical conductivity since pure water is a weak electrolyte.

Conclusions

In the presence of substances in various amounts, such as sodium hydroxide, sodium phosphoric acid, sodium carbonate, sodium sulfate, sodium metaborate, sodium phosphoric acid 2 — substituted and potassium hydroxide, water electrolysis was carried out. At different time intervals, the volume of hydrogen released was recorded using the Hoffmann apparatus. The study designated that in the presence of potassium hydroxide, regardless of its amount, the electrolysis process occurs faster, as evidenced by the volume of gas released. Sodium hydroxide turned out to be less effective, as the remaining substances showed a low ability to generate hydrogen. In addition, the effect of the amount of substance per unit volume of water on the process of electrolysis of water was demonstrated, where the best result was recorded for a solution with an amount of 0.8 mol. Low efficiency is demonstrated by sodium metaborate NaBO2 at an amount of 0.2 mol.

Acknowledgement

The study was performed within the framework of grant of the Scientific Committee of the Ministry of Education and Science of the Kazakhstan Republic (AP08052675).

References

1 Ni M., Leung M.K.H., Sumathy K., Leung DYC. (2004). Water electrolysis—a bridge between renewable resources and hydrogen. Proceedings of the International Hydrogen Energy forum, 1, 475–480.

2 Ciamician, G. (1912). The photochemistry of the future. *Chemistry of Materials, 36,* 385–94.

3 Fujishima, A, & Honda, K. (1972). Electrochemical Photolysis of Water at a Semiconductor Electrode. *Nature, 238,* 37–8.

4 Asahi, R, Morikawa, T., Ohwaki, T., Aoki, K., & Taga, Y. (2001). Visible-light photocatalysis in nitrogen-doped titanium oxides. *Science, 293-269,* 71.

5 Khaselev, O., Turner, J.A. (1998). A monolithic photovoltaic-photo-electrochemical device for hydrogen production via water splitting, *Science,* 425–7.

6 Zou, Z.G., Ye, J.H., Sayama, K., & Arakawa, H. (2001). Direct splitting of water under visible light irradiation with a 10 n oxide semiconductor photocatalyst. *Nature, 414,* 625–7.

7 Khan, SUM, Al-Shahry, J.M., & Ingler, W.B. (2002). Efficient photochemical water splitting by a chemically modified n12-TiO_2. *Science, 297-2243,* 5.

8 Herrmann, J.M. (1999). Heterogeneous photocatalysis: fundamentals and applications to the removal of various types of aqueous pollutants. *Catal Today, 1,* 115–29.

9 Fox, M.A, & Dulay, M. (1993). Heterogeneous photocatalysis. *Chem Rev, 93,* 341–57.

10 Hoffmann, M.R., Martin, S.T., Choi, W.Y., & Bahnmann, D.W. (1995). Environmental applications of semiconductor photocatalysis. *Chem Rev, 95,* 69–96.

11 Mills, A., & Hunte, S.L. (1997). An overview of semiconductor photocatalysis. *Chem, 108,* 1–35.

12 Jing, L.Q., Sun, X.J., Shang, J., Cai, W.M., Xu, Z.L., & Du, Y.G. (2003). Review of surface photovoltage spectra of nanosized semiconductor and its applications in heterogeneous photocatalysis. *Sol Energy Mater Sol Cells, 79,* 133–51.

13 Fujishima, A., Rao, T.N., Tryk, D.A. (2000). Titanium dioxide photocatalysis. *Photochem Rev, 1,* 1–21.

14 Alfano, O.M., Bahnemann, D., Cassano, A.E., Dillert, R., & Goslich, R. (2000). Photocatalysis in water environments using artificial and solar light. *Catal Today, 58,* 199–230.

15 Bamwenda, G.R., Tsubota, S., Nakamura, T., & Haruta, M. (1995). Photoassisted hydrogen production from a water ethanol solution: a comparison of activities of Au-TiO2 and Pt-TiO2. *Chemistry of Materials, 89, 2,* 177–89.

16 Lee, S.G., Lee ,S.W., & Lee, H.I. (2001). Photocatalytic production of hydrogen from aqueous solution containing CN_ as a hole scavenger. *Appl Catal A, 207,* 173–81.

17 Sayama, K., & Arakawa, H. (1994). Effect of Na2CO3 addition on photocatalytic decomposition of liquid water over various semiconductors catalysis. *Chemistry of Materials, 77,* 243–7.

А.Б. Куанышбекова*, Т.М. Сериков, П.А. Жанбирбаева,
А.Е. Садыкова, Г.Т. Бейсембаева, А.С. Балтабеков

Суды электролиз әдісі арқылы ыдырату кезінде ерітіндінің және оның мөлшерінің әсері

Мақалада Гофман құрылғысын қолдана отырып, тұрақты электр тогының әсерінен электролиз арқылы судың бөліну процесіне ерітіндінің әсері мен оның концентрациясын эксперименттік зерттеу нәтижелері келтірілген. Ерітінді ретінде натрий гидроксиді, фосфорқышқылды натрий, көмірқышқыл натрийі, көмірқышқылды қышқыл натрий, күкіртқышқылды натрий, натрий метабораты, фосфорқышқылды натрий және 2— алмастырылған калий гидроксиді пайдаланылды. Ерітіндідегі тұздардың мөлшері 0,2 моль мен 0,8 моль аралығында болды. Зерттеу көрсеткендей, тұрақты ток пен кернеу кезінде судың ағу процесіне тұздардың табиғаты да, олардың мөлшері де әсер етеді. Сонымен, ерітіндідегі заттардың бірдей мөлшерімен судың ыдырау процесі калий гидроксиді бар ерітіндіде тезірек жүретіні анықталды. 0,2 моль мөлшерінде KOH ерітіндісін қолданған кезде бөлінетін сутектің көлемі 15 мл, ал 0,8 моль кезінде 19,5 мл болды. Осыған ұқсас концентрациясы бар натрий метаборатының сулы ерітіндісін пайдаланған кезде, бөлінген сутектің көлемі тиісінше 2 мл және 4,5 мл құрады. Алынған мәліметтер судың фотокаталитикалық ыдырауы кезінде ерітінді мен оның мөлшерін таңдауға мүмкіндік береді.

Кілт сөздер: суды ыдырату, Гофман аппараты, электролиз, сутегі, тұздар, ерітінді, реакциялар, электрохимиялық процесс.

А.Б. Куанышбекова, Т.М. Сериков, П.А. Жанбирбаева,
А.Е. Садыкова, Г.Т. Бейсембаева, А.С. Балтабеков

Влияние раствора и его количества на процесс расщепления воды методом электролиза

В статье приведены результаты экспериментального исследования влияния раствора и и его концентрации на процесс расщепления воды путем электролиза под действием постоянного электрического тока с применением устройства Гофмана. В качестве растворов нами были использованы гидроксид натрия, натрий фосфорнокислый, натрий углекислый, натрий углекислый

кислый, натрий сернокислый, метаборат натрия, натрий фосфорнокислый 2-замещенный и гидроксид калия. Количество солей в растворе варировалось от 0,2 до 0,8 моль. Результаты исследования показали, что на процесс ращепления воды при постоянном токе и напряжения влияет как природа солей, так и их количество. Так, было установлено, что при одинаковом количестве веществ в растворе, процесс расщепления воды происходит быстрее в растворе содержанием гидроксида калия. При использовании водного раствора KOH в количестве 0,2 моль, объем выделяемого водорода составил 15 мл, а при 0,8 моль — 19,5 мл. При использовании водного раствора метабората натрия с аналогичной концентрацией, объем выделенного водорода составил 2,0 и 4,5 мл соответственно. Полученные данные позволяют сделать выбор раствора и его количества при процессе фотокаталитического расщепления воды.

Ключевые слова: расщепление воды, аппарат Гофмана, электролиз, водород, соль, раствор, реакция, электрохимический процесс.

АВТОРЛАР ТУРАЛЫ МӘЛІМЕТТЕР
СВЕДЕНИЯ ОБ АВТОРАХ
INFORMATION ABOUT AUTHORS

Akasheva, Zh.K. — Researcher, Research Laboratory «Computational modeling and information technology» at Satbayev University, Almaty, Kazakhstan, e-mail: zhibek_akasheva@mail.ru.

Akhazhanov, S.B. — PhD, Associate Professor, Karagandy University of the name of academician E.A. Buketov, Kazakhstan; e-mail: stjg@mail.ru

Aniskin A. — Candidate of technical sciences, Assistant Professor, University North, Varazhdin, Croatia; e-mail: aaniskin@unin.hr

Assilbekov, B.K. — PhD, Leading Researcher, Head of the Research Laboratory «Computational modeling and information technology» at Satbayev University, Almaty, Kazakhstan; e-mail: assilbekov@mail.ru

Baizhan, D.R. — Engineer, Scientific Research Center "Surface engineering and tribology" at Sarsen Amanzholov East Kazakhstan University, Ust-Kamenogorsk, Kazakhstan; daryn.baizhan@mail.ru

Baltabekov, A.S. — Candidate of physical and mathematical sciences, Karagandy University of the name of academician E.A. Buketov, Kazakhstan;

Beisembaeva, G.T. — Engineer, Karagandy University of the name of academician E.A. Buketov, Kazakhstan;

Bolysbek, D.A. — Researcher, Research Laboratory «Computational modeling and information technology» at Satbayev University, PhD-student at al-Farabi Kazakh National University, Almaty, Kazakhstan; e-mail: bolysbek.darezhat@gmail.com.

Bulkairova, G.A. — 1st year doctoral student, Karagandy University of the name of academician E.A. Buketov, Kazakhstan; e-mail: gulden2111@mail.ru

Cherepanska, I.Yu. — DSc, Professor, the Department of Automation and non-destructive testing; National Technical University of Ukraine "Igor Sikorsky Kyiv Polytechnic Institute"; Kyiv, Ukraine; +380682191497; e-mail: cherepanskairina@gmail.com.

Dyusembayeva, A.N. — Master of science, Senior Lecturer, Karagandy University of the name of academician E.A. Buketov, Kazakhstan;

Eremin, E.N. — Doctor of Technical Sciences; Professor; Dean of the Mechanical Engineering Institute, Head of the Department of Mechanical Engineering and Materials Science; Omsk State Technical University; Omsk; Russia; weld_techn@mail.ru

Inerbaev T.M. — Candidate of physical and mathematical sciences, L.N. Gumilyov Eurasian National University, Kazakhstan; e-mail: talgat.inerbaev@gmail.com

Kalchuk, S.V. — PhD, Associate Professor, Zhytomyr Polytechnic State University, Zhytomyr, Ukraine.

Kantay, N. — Junior Researcher at the "National Scientific Laboratory for Collective Use" at Sarsen Amanzholov East Kazakhstan University, Ust-Kamenogorsk, Kazakhstan; e-mail: nurgan85@mail.ru

Karabekova, D.Zh. — PhD, Docent, Karagandy University of the name of academician E.A. Buketov, Kazakhstan; e-mail: karabekova71@mail.ru

Kawazoe Y. — Professor and Professor Emeritus in New Industry Creation Hatchery Center, Tohoku University, Sendai, Japan; e-mail: kawazoe@e-workshop.co.jp

Khassenov, A.K. — PhD, Assistant professor, Karagandy University of the name of academician E.A. Buketov, Kazakhstan; e-mail: ayanbergen@mail.ru

Kotov, B.I. — Dr.Tech. Sc., Prof., State Agrarian and Engineering University in Podilya, Ukraine.

Kuanyshbekova, A.B. — Engineer, Karaganda University of the name of academician E.A. Buketov, Kazakhstan; e-mail: kuanyshbekovaaya@mail.ru

Kucheruk, V.Yu. — Professor, Doctor of science (Engineering), Head of the Department of Metrology and Industrial Automation Vinnytsia National Technical University, Ukraine, E-mail: vladimir; e-mail: kucheruk@gmail.com

Kudaikulov, A.A. — PhD, Leading Researcher, Research Laboratory «Computational modeling and information technology» at Satbayev University, Almaty, Kazakhstan; e-mail: aziz.kudaikulov@gmail.com.

Matsuoka, Y. — Professor Institute for Materials Research, Tohoku University, Japan; e-mail: matsuoka@imr.tohoku.ac.j

Mazhenov, N.A. — Candidate of physical and mathematical sciences, Professor, Karaganda state technical university, Faculty of power engineering, automation and telecommunications, department of physics, Karaganda, Kazakhstan; e-mail: mazhenov@mail.ru.

Minkov, L.L. — Doctor of Physical and Mathematical Sciences, Professor, National Research Tomsk State University, Tomsk, Russia.

Nabioldina, A. — 4rd year student of the specialty Materials Science and technology of new materials, Sarsen Amanzholov East Kazakhstan University, Ust-Kamenogorsk, Kazakhstan; e-mail: aiym.nabioldina@mail.ru

Nussupbekov, B.R. — Full Professor, Karagandy University of the name of academician E.A. Buketov, Kazakhstan; E-mail: bek_nr1963@mail.ru

Paszkowski, M. — DSc, PhD, Associate Professor, Faculty of Mechanical Engineering, Wroclaw Polytechnic University; e-mail: maciej.paszkowski@pwr.edu.pl

Rakhadilov, B.K. — PhD, Associate Professor, Senior Researcher, Scientific Research Center "Surface engineering and tribology" at Sarsen Amanzholov East Kazakhstan University, Director of Plasma Science LLP, Ust-Kamenogorsk, Kazakhstan; e-mail: rakhadilovb@mail.ru.

Razina, O.V. — PhD, Associate Professor, Department of General and Theoretical Physics, L.N. Gumilyov ENU, Nur-Sultan, Kazakhstan; e-mail: olvikraz@mail.ru

Sadykova, A.E. — Master of Science, Teacher, Karaganda University of the name of academician E.A. Buketov, Kazakhstan.

Sagdoldina, Zh.B. — PhD, Associate Professor, Leading Researcher, Scientific Research Center "Surface engineering and tribology" at Sarsen Amanzholov East Kazakhstan University; e-mail: sagdoldina@mail.ru

Sazonov, A.Yu. — PhD, Associate Professor, the Department of Hardware and Software of Automation, National Technical University of Ukraine "Igor Sikorsky Kyiv Polytechnic Institute", Kyiv, Ukraine; +380682186148; e-mail: a.sazonov@kpi.ua.

Serikov, T.M. — PhD, Karaganda University of the name of academician E.A. Buketov, Kazakhstan; e-mail: serikov-timur@mail.ru;

Shaimerdenova, K.M. — Professor, Karaganda University of the name of academician E.A. Buketov, Kazakhstan.

Shashubay, B.U. — Undergraduate 2nd year, Karagandy University named after academician E.A. Buketov, Kazakhstan; e-mail: balnur.shashubay@g.mail.com

Sivaieva, O.S. — Senior Lecturer, the Foreign Languages Department, Polissya National University, Zhytomyr, Ukraine.

Sokolovskyi, O.F. — PhD, Associate Professor, Polissya National University, Zhytomyr, Ukraine.

Spirin, A.V. — Cand. of tech. Sciences, Associate Professor, Separate structural subdivision "Ladyzhyn vocation college of Vinnytsia National Agrarian University", Ukraine.

Stepanenko, S.P. — Dr.Tech. Sc., National Scientific Center "Institute of Agricultural Engineering and Electrification", Ukraine; e-mail: stepanenko_s@ukr.net

Suikimbayeva, N.T. — senior lecturer, Department of Physics, Dulaty University, Taraz, Kazakhstan; e-mail: nurgul-1708@mail.ru

Syzdykova, Z.R. — Master of physics, teacher. Karaganda state technical university, Faculty of power engineering, automation and telecommunications, department of physics, Karaganda, Kazakhstan; e-mail: zika_0885@mail.ru.

Tanasheva, N.K. — PhD, Associate Professor, Karaganda University of the name of academician E.A. Buketov, Kazakhstan.

Tleubergenova, A.Zh. — PhD-1styear student, Karaganda of the name of academician E.A. Buketov, Kazakhstan; e-mail: shymkent.a7@mail.ru

Torebek, K. — Engineer of Plasma Science LLP, Ust-Kamenogorsk, Kazakhstan; e-mail: kiztore98@mail.ru

Tsyba P.Yu. — PhD, Associate Professor, Department of General and Theoretical Physics, L.N. Gumilyov ENU, Nur-Sultan, Kazakhstan; e-mail: pyotrtsyba@gmail.com

Tulebekova, A.S. — PhD, Senior Researcher, CSI Research & Lab (LLP), Associate Professor, L.N. Gumilyov Eurasian National University, Nur-Sultan, Kazakhstan; e-mail: krasavka5@mail.ru

Utepov, Ye.B. — PhD, Head of R&D at the CSI Research & Lab (LLP), Acting Professor, L.N. Gumilyov Eurasian National University, Nur-Sultan, Kazakhstan; e-mail: utepov-elbek@mail.ru

Uzbergenova, S.Zh. — Master of Logistics and Supply Chain Management, Senior Lecturer, the Department of Engineering Technologies and Transport, Sh. Ualikhanov Kokshetau University, Kokshetau, Kazakhstan.

Zhanbirbayeva, P.A. — Engineer, Karaganda University of the name of academician E.A. Buketov, Kazakhstan.

Zharassov, Sh.Zh. — PhD Student, L.N. Gumilyov Eurasian National University, Nur-Sultan, Kazakhstan; e-mail: zhshzh95@gmail.com

Zhurerova, L.G. — PhD, Senior Researcher, Scientific Research Center “Surface engineering and tribology” at Sarsen Amanzholov East Kazakhstan University; e-mail: leila_uka@mail.ru